Diss. ETH NO. 25057

MORPHOLOGICAL GRADIENTS FOR PROTEIN-ADSORPTION AND BLOOD-COAGULATION STUDIES

A thesis submitted to attain the degree of

DOCTOR OF SCIENCES of ETH ZURICH

(Dr. sc. ETH Zurich)

presented by

REBECCA PATRIZIA HUBER

MSc ETH Materials Science

born on 15.12.1986

citizen of Emmen (LU)

accepted on recommendation of

Prof. Dr. Nicholas D. Spencer, examiner

Prof. Dr. Katharina Maniura, co-examiner

Dr. Simon Berner, co-examiner

Prof. Dr. Janos Vörös, co-examiner

2018

Abstract

Gradient surfaces with a continuously changing surface parameter allow rapid, high-throughput investigations and systematic studies in tribology, adhesion and biology. Surface roughness is an important surface parameter on both micrometer and nanometer scales. In this thesis, different methods for the fabrication of micro- and/or nano-featured morphology gradients and their applications in biology are described.

Nanoparticle-density gradients were produced by a simple dip-coating process of a positively charged poly(ethylene imine) (PEI)-coated silicon wafer into a negatively charged silica-nanoparticle suspension. To ensure firm anchoring of the particles to the surface the gradients were sintered at 1050 °C. All fabricated gradients were extensively characterized by SEM and AFM. Gradients were coated with TiO_2 to mimic the surface of bone implants.

A step-by-step *in vivo* like model that follows the natural processes occurring after implantation of an osseous implant was chosen to study the effect of nano-rough surfaces on protein adsorption, blood coagulation as well as cell behavior.

TiO_2-coated nanoparticle-density gradients were used for protein-adsorption studies. For gradients with 39- and 72-nm-diameter nanoparticles no influence of nano-features on the amount of adsorbed proteins could be found. In contrast, for gradients with 12-nm-diameter nanoparticles, fibrinogen in competition with albumin and fibronectin or serum, showed a higher adsorption at the high-particle-density end of the gradient.

Blood-coagulation studies revealed that nanostructures involving 39-nm-diameter nanoparticles seem to enhance blood coagulation. With an increase in 39 nm particle-density, faster fibrin-network formation was observed, while smaller (12 nm) and bigger (72 nm) nanoparticles did not influence the activation of platelets or the fibrin-network formation.

Monoclonal-antibody binding specific for the dodecapeptide sequence of the fibrinogen γ chain was measured on fibrinogen adsorbed onto nanoparticle-density gradients to gain further insight into the correlation between the protein and blood experiments. The ratio of antibody to adsorbed fibrinogen decreased by approximately 65% with increasing nanoparticle density for 39 nm particles, indicating conformational changes of adsorbed fibrinogen along the gradient.

Human-bone-cell (HBC) experiments performed on nano-roughness gradients exhibited a gradual change in the cell behavior along the gradient with decreasing proliferation with decreasing inter-particle distance. Ten days post seeding, the number of HBCs on 39 nm particle-density gradients was six times higher at positions without particles compared to the high-density end of the gradient.

Since biological experiments require a large number of substrates, different replication techniques were used to create copies of master gradients. Injection molding from polymer inserts was shown to be a successful replication technique for the mass production of samples with 72 nm features. For smaller nanoparticle, a novel replication method called substrate conformal imprint lithography (SCIL) demonstrated the replication of nanofeatures down to a size of 12 nm and was proven to be able to replicate combined nano- and micro-featured structures.

Lastly, silver-particle gradients with changing particle size, height and density along the gradient were prepared by dewetting of gradients in silver thickness. Replication of the silver-particle gradients in PDMS and epoxy was

shown to be a possible way to produce identical particle-size gradients and TiO_2 coated epoxy replicas could be used for biological applications.

Zusammenfassung

Oberflächengradienten mit sich kontinuierlich ändernden Oberflächeneigenschaften ermöglichen systematische Studien mit hohem Durchsatz in Tribologie, Adhäsion und Biologie. Oberflächenrauigkeit ist eine wichtige Oberflächeneigenschaft im Mikrometer- und Nanometerbereich. In dieser Arbeit werden verschiedene Methoden für die Herstellung von Rauheitsgradienten mit Mikro- und Nanostrukturen und deren Anwendung in biologischen Studien beschrieben.

Nanopartikeldichte-Gradienten wurden durch einen einfachen Tauchbeschichtungsprozess von einem positive geladenen, Polyethylenimin (PEI) beschichteten Siliziumwafer in eine negative geladenene Siliziumoxid-Nanopartikelsuspension, hergestellt. Um eine feste Verbindung der Partikel mit der Oberfläche zu erreichen, wurden die Gradienten bei 1050 °C gesintert. Alle hergestellten Gradienten wurden ausführlich mit SEM und AFM charakterisiert. Um die Oberfläche von Knochenimplantaten zu imitieren wurden die Gradienten mit Titanoxid beschichtet.

Um den natürlichen Prozessen zu folgen, die nach der Implantation von Knochenimplantaten auftreten, wurde ein *in vivo* ähnliches Schritt-für-Schritt Modell gewählt. Dabei wurde der Effekt von nanorauen Oberflächen auf die Proteinadsorption, Blutkoagulation und das Zellverhalten studiert.

Titanoxid beschichtete Nanopartikeldichte-Gradienten wurden für Proteinadsorptions-Studien verwendet. Gradienten mit Partikeln von einem Durchmesser von 39 oder 72 nm zeigten keinen Einfluss auf die Menge von adsorbierten Proteinen. Im Gegensatz dazu zeigten Gradienten mit Partikeln von 12-nm-Durchmesser eine erhöhte Fibrinogen-Adsorption an Stellen des

Gradienten mit maximaler Partikeldichte bei der Adsorption von Fibrinogen im Wettbewerb mit Albumin und Fibronektin oder Serum Proteinen.

Blutkoagulation-Studien zeigen, dass Nanostrukturen mit einem Durchmesser von 39 nm die Blutkoagulation steigern. Mit einer höheren Partikeldichte der 39-nm-Partikel wurde eine schnellere Fibrin-Netzwerk-Bildung beobachtet, während kleinere (12 nm) und grössere (72 nm) Nanopartikel keinen Einfluss auf die Aktivierung von Blutplättchen oder die Fibrin-Netzwerk-Bildung zeigten.

Um einen weiteren Einblick in die Korrelation von Protein- und Blutexperimenten zu bekommen, wurde die monoklonale Antikörperbindung spezifisch für die dodecapeptide Sequenz der Fibrinogen γ-Kette an Fibrinogen, welches auf Nanopartikeldichte-Gradienten adsorbiert wurde, gemessen. Das Verhältnis von Antikörper zu adsorbiertem Fibrinogen nahm mit der Zunahme der Nanopartikeldichte für 39-nm-Partikel ungefähr 65% ab, was eine Indikation für die Änderung der Konformation von adsorbiertem Fibrinogen entlang des Gradienten ist.

Humane Knochenzellenexperimente die auf Nanorauheits-Gradienten durchgeführt wurden, zeigten eine graduelle Änderung des Zellverhaltens entlang des Gradienten, mit reduzierter Proliferationsrate bei abnehmendem Partikelabstand. Zehn Tage nach dem Aussähen der Zellen wurde eine sechsfach höhere Anzahl Zellen an Orten ohne Partikel gezählt, als an Orten mit maximaler Partikeldichte.

Da Zellversuche eine grosse Anzahl Proben benötigen, wurden verschiedene Replikationsmethoden angewandt um Kopien der Originalgradienten herzustellen. Es wurde gezeigt, dass Spritzguss von einem Polymerformstück eine erfolgreiche Replikationstechnik für die Massenfertigung von Proben mit 72 nm Strukturen ist. Eine neue Replikationsmethode, genannt Substrate Conformal Imprint Lithography (SCIL), zeigte die erfolgreiche Replikation von Nanostrukturen mit einer Grösse von 12 nm oder grösser und

erwies sich als geeignet für die Replikation von kombinierten Nano- und Mikrostrukturen.

Abschliessend wurden Silberpartikelgradienten mit unterschiedlicher Partikel-Grösse, Höhe und Dichte entlang des Gradienten durch die Entnetzung eines Silber-Schicht-Gradienten, hergestellt. Es war möglich die Silberpartikelgradienten in PDMS und Epoxidharz zu replizieren und Titanoxid beschichtete Epoxidharzkopien wurden für biologische Experimente verwendet.

Table of Contents

Chapter 1

Introduction

1.1 General introduction

With the development of implants for modern medicine the design of the implant surface became more and more important, since the success of a surgical implant is dependent on an appropriate cellular response [1] for which the surface roughness plays an important role. Cell growth, proliferation and attachment are influenced by the roughness [2]. Especially for medical bone implants, roughness is important, since osteoblasts have been shown to have different behavior according to the roughness of the surface they were cultured on [3-5].

Typical experiments on this topic are focused on bone cells, but wound healing around implants is a complex process in which water molecules from the surrounding blood first come in contact with the surface. In the next step, ions and proteins adsorb, before platelets and cells respond to the protein-covered surface [6]. This rapid adsorption of proteins from blood acts as a translation of the implant surface into a biological language to which the cells can respond. The surface-induced arrangement and conformation mediate the biological reactions at the interface and are crucial for subsequent cell response [1]. (Figure 1.1)

Previous studies showed that not only cell behavior [7, 8], but also protein [7] and blood-component adsorption [9] onto surfaces is influenced by micro- as well as nanoscale surface topography.

The adsorption of proteins from blood onto the implant surface is a dynamic and complex process that involves noncovalent interactions, such as van der Waals forces, hydrogen bonding, hydrophobic and electrostatic interactions [10]. On the one hand protein adsorption is influenced by the protein properties, such as protein size, composition and structural stability, [11] while on the other hand, surface properties, such as surface chemistry [12, 13], and topography [7, 14, 15] come into play. The physical and chemical surface properties can affect the kinetics and thermodynamics of protein adsorption, orientation and denaturation [10, 16].
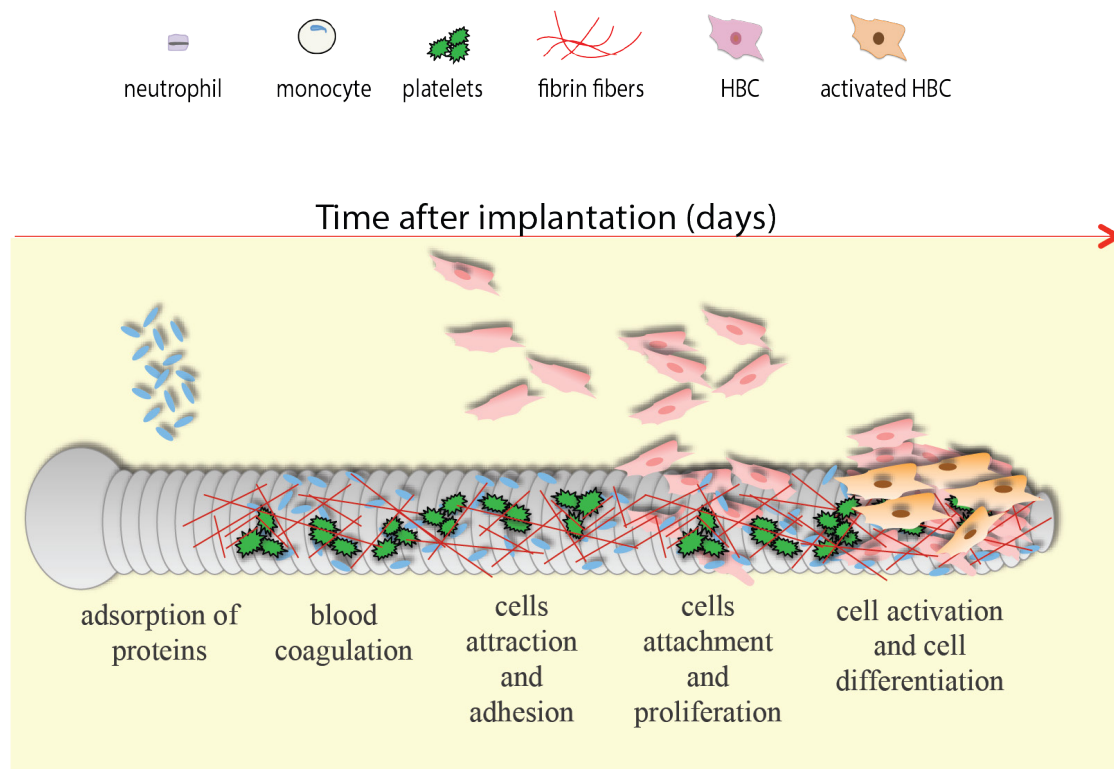
Figure 1.1: Schematic illustration of in vivo processes after implantation. The surface of the implant is initially contacted by water molecules, followed by the adsorption of blood proteins and in a last step cells will respond to the protein covered surface. Image adapted from [17].

When adding the influence of protein concentration, protein type and adsorption time, the complexity of interpreting protein adsorption further increases. At low protein concentrations the mass transfer from the solution to the surface is slow and individual proteins can spend longer times spreading and adapting to the lowest energy conformation. At high protein concentrations, proteins compete for available spots on the surface and there is no time for the

individual protein to spread, resulting in a high surface density of proteins with low binding strength and fewer conformational changes [18, 19].

An implant material is not only exposed to one specific protein but to a huge variety of plasma proteins, among them fibrinogen, fibronectin and albumin. Fibrinogen plays a fundamental role in blood coagulation, platelet aggregation and cell binding [20]. Fibronectin is known to affect cell-cell and cell-surface adhesion [21] and mediates cell and protein attachment to extracellular matrix during wound healing [22]. Albumin, the most abundant component of blood plasma, serves as a transport medium and maintains the osmotic pressure [23]. Initially, smaller proteins of high solution abundance diffuse to the implant surface and rapidly adsorb. Later, the less abundant but more surface-active proteins displace the smaller proteins. This sequential adsorption/replacement of proteins is described as the *Vroman effect* [24].

Protein adsorption onto surfaces is a common event and the first step in many biological processes such as blood coagulation on materials [11]. Trindade *et al.* [25] claim that it is the first step of the path to osseointegration. Since blood-protein adsorption and blood coagulation are greatly influenced by the topography of titanium surfaces [7, 9, 26], the initial interaction of blood components and proteins with titanium implant surfaces may affect the eventual adhesion, migration and differentiation of primary human osteogenic cells. It is of major importance for implantology to understand the early interaction between blood and the implant and how this steers osseointegration.

To investigate the influence of a surface parameter on a given process, working with individual samples requires many repetitions, with the associated challenge of maintaining the experimental conditions constant. This approach is laborious and cost-ineffective. Roughness gradients are a very promising tool to investigate the effect of surface topography on a biological system, as a wide range of parameters can be covered in a single experiment. Additionally, homogenous conditions are ensured during all the measurements [8, 27].

1.2 Aim of the thesis

The aim of this thesis was to study the effect of controlled nanoscale topographies on the adsorption of blood proteins, the adhesion and activation of blood cells and the influence of the pre-adsorbed blood clot on the behavior of osteoblasts. The study should enhance the understanding of the early interaction between blood and the implant and how this further steers osseointegration by following the natural processes that occur after implantation of an osseous implant. Ultimately, this understanding could facilitate the design of new implant surfaces.

Aims of this thesis were:
1) Fabrication and characterization of morphological gradients.
2) Replication of morphological gradients.
3) To study the role of nanoscale surface topography on the adsorption of blood proteins.
4) To determine morphology influence on blood-cell adsorption and activation, in correlation with the behavior of adhesion proteins.
5) To study the interaction of bone cells with adsorbed blood proteins and cells.

1.3 Overview of the thesis chapters

Chapter 2 introduces the techniques used in this thesis to form one- and two-dimensional roughness gradients. The fabrication method for nano-particle density gradients with silica particles of diameters 12, 39 and 72 nm is explained. Additionally, an approach to micro-featured roughness gradient and a method for the fabrication of 2D-orthogonal gradients are shown.

In **Chapters 3-6** the nanoparticle-density gradients were used to study the effect of nano-rough surfaces on protein adsorption, blood coagulation as well as cell behavior in a step-by-step *in vivo* like model. First, in **Chapter 3**, the

protein adsorption was studied by incubating TiO_2-coated nanoparticle-density gradients in protein mixtures or single protein solutions incorporating fluorescently labeled albumin and fibrinogen. In the second step, the influence of nano-roughness on blood coagulation was investigated in **Chapter 4**. The gradients were incubated for 2 to 10 min with partially heparinized (0.5 IU/ml) whole human blood from healthy donors before characterizing the blood-material interaction by scanning electron microscopy. In **Chapter 5** antibody-experiments were carried out to get insight into the influence of nano-rough surfaces on the conformation of fibrinogen that might change the platelet binding-site availability and blood coagulation behavior. Subsequently, in **Chapter 6**, the effect of pre-adsorbed blood components on human bone cell behavior was studied. Gradient samples with pre-adsorbed blood components were seeded with human bone cells (HBC) prior to analysis by ALP/Actin/DAPI staining and fluorescence microscopy on day 7 and 10.

For the replication of micro-, nano- and combined micro- and nanostructures three different replication methods were examined in **Chapter 7**. Micro-roughness was replicated with an epoxy replica technique; nanoparticle-density gradients were replicated with a two-step PDMS-epoxy based technique, injection molding and a novel technique called substrate conformal imprint lithography (SCIL). And lastly, the SCIL method was adapted to replicate 2D-orthogonal gradients.

Chapter 8 deals with the preparation and characterization of silver particle-size gradients prepared through solid-state dewetting of silver thickness gradients. The silver particle-size gradients were used for protein adsorption experiments and a two-step PDMS-epoxy technique was applied to replicate the gradients.

The conclusions of the thesis and the outlook are given in **Chapter 9**.

References:

[1] C.J. Wilson, R.E. Clegg, D.I. Leavesley, M.J. Pearcy, Mediation of biomaterial-cell interactions by adsorbed proteins: a review, Tissue engineering 11(1-2) (2005) 1-18.

[2] D.M. Brunette, P. Tengvall, M. Textor, T. P., Titanium in Medicine, Springer, Berlin2001.

[3] C. Huwiler, T.P. Kunzler, M. Textor, J. Vörös, N.D. Spencer, Functionalizable Nanomorphology Gradients via Colloidal Self-Assembly, Langmuir 23(11) (2007) 5929-5935.

[4] T.P. Kunzler, C. Huwiler, T. Drobek, J. Vörös, N.D. Spencer, Systematic study of osteoblast response to nanotopography by means of nanoparticle-density gradients, Biomaterials 28(33) (2007) 5000-5006.

[5] T.P. Kunzler, T. Drobek, M. Schuler, N.D. Spencer, Systematic study of osteoblast and fibroblast response to roughness by means of surface-morphology gradients, Biomaterials 28(13) (2007) 2175-2182.

[6] B. Kasemo, Biological surface science, Surface Science 500(1–3) (2002) 656-677.

[7] M.S. Lord, M. Foss, F. Besenbacher, Influence of nanoscale surface topography on protein adsorption and cellular response, Nano Today 5(1) (2010) 66-78.

[8] C. Zink, H. Hall, D.M. Brunette, N.D. Spencer, Orthogonal nanometer-micrometer roughness gradients probe morphological influences on cell behavior, Biomaterials 33(32) (2012) 8055-8061.

[9] V. Milleret, S. Tugulu, F. Schlottig, H. Hall, Alkali treatment of microrough titanium surfaces affects macrophage/monocyte adhesion, platelet activation and architecture of blood clot formation, European Cells and Materials 21 (2011) 430-444.

[10] P. Roach, D. Farrar, C.C. Perry, Interpretation of Protein Adsorption: Surface-Induced Conformational Changes, Journal of the American Chemical Society 127(22) (2005) 8168-8173.

[11] M. Rabe, D. Verdes, S. Seeger, Understanding protein adsorption phenomena at solid surfaces, Advances in Colloid and Interface Science 162(1) (2011) 87-106.

[12] T.A. Horbett, Adsorption to Biomaterials from Protein Mixtures, Proteins at Interfaces, American Chemical Society1987, pp. 239-260.

[13] C.G. Gölander, Y.S. Lin, V. Hlady, J.D. Andrade, Wetting and plasma-protein adsorption studies using surfaces with a hydrophobicity gradient, Colloids and Surfaces 49 (1990) 289-302.

[14] M.S. Lord, B.G. Cousins, P.J. Doherty, J.M. Whitelock, A. Simmons, R.L. Williams, B.K. Milthorpe, The effect of silica nanoparticulate coatings on serum protein adsorption and cellular response, Biomaterials 27(28) (2006) 4856-4862.

[15] E. Jansson, P. Tengvall, Adsorption of albumin and IgG to porous and smooth titanium, Colloids and Surfaces B: Biointerfaces 35(1) (2004) 45-51.

[16] P. Roach, D. Farrar, C.C. Perry, Surface Tailoring for Controlled Protein Adsorption: Effect of Topography at the Nanometer Scale and Chemistry, Journal of the American Chemical Society 128(12) (2006) 3939-3945.

[17] M. Obarzanek-Fojt, Y. Elbs-Glatz, E. Lizundia, L. Diener, J.-R. Sarasua, A. Bruinink, From implantation to degradation — are poly (l-lactide)/multiwall carbon nanotube composite materials really cytocompatible?, Nanomedicine : nanotechnology, biology, and medicine (2014).

[18] C.F. Wertz, M.M. Santore, Effect of Surface Hydrophobicity on Adsorption and Relaxation Kinetics of Albumin and Fibrinogen: Single-Species and Competitive Behavior, Langmuir 17(10) (2001) 3006-3016.

[19] E.A. Vogler, Protein adsorption in three dimensions, Biomaterials 33(5) (2012) 1201-1237.

[20] L. Feng, J.D. Andrade, Structure and adsorption properties of fibrinogen, Proteins at Interfaces Ii 602 (1995) 66-79.

[21] M. Malmsten, Ellipsometry studies of fibronectin adsorption, Colloids and Surfaces B: Biointerfaces 3(6) (1995) 371-381.

[22] D.E. MacDonald, N. Deo, B. Markovic, M. Stranick, P. Somasundaran, Adsorption and dissolution behavior of human plasma fibronectin on thermally and chemically modified titanium dioxide particles, Biomaterials 23(4) (2002) 1269-1279.

[23] M. Pegueroles, C. Tonda-Turo, J.A. Planell, F.J. Gil, C. Aparicio, Adsorption of fibronectin, fibrinogen, and albumin on TiO_2: time-resolved kinetics, structural changes, and competition study, Biointerphases 7(1-4) (2012) 48.

[24] M.C.D. R.J. Green, C.J. Roberts, S.J.B. Tendler, Competitive protein adsorption as observed by surface plasmon resonance, Biomaterials 20 (1999) 385—391.

[25] R. Trindade, T. Albrektsson, P. Tengvall, A. Wennerberg, Foreign Body Reaction to Biomaterials: On Mechanisms for Buildup and Breakdown of Osseointegration, Clinical Implant Dentistry and Related Research 18(1) (2016) 192-203.

[26] J. Hong, K. Nilsson Ekdahl, H. Reynolds, R. Larsson, B. Nilsson, A new in vitro model to study interaction between whole blood and biomaterials. Studies of platelet and coagulation activation and the effect of aspirin, Biomaterials 20(7) (1999) 603-611.

[27] S. Morgenthaler, C. Zink, N.D. Spencer, Surface-chemical and -morphological gradients, Soft Matter 4(3) (2008) 419-434.

Chapter 2

Fabrication and characterization of one- and two-dimensional gradients

2.1 Introduction

The investigation of the influence of a surface parameter on a given process is often performed by working with individual samples that require many repetitions, with the challenge of maintaining the experimental conditions constant. This approach is laborious and cost-ineffective. Gradients with one gradually changing parameter are a very promising tool to investigate the influence of a particular phenomenon in one single experiment in the minimum amount of time. Such a method reduces sample-to-sample error and ensures homogenous conditions throughout the experiment.

Different fabrication approaches for gradients have already been described in the literature [1]. Due to their high-throughput nature, gradients have been applied in a large variety of studies over the past decade. They have led to interesting results in the areas of protein adsorption [2-4], cell adhesion [5, 6] and a variety of other fields [1].

In the early 90s, Chaudhury et al. [7] showed that a drop of water could move uphill using a chemical gradient. They evaporated decyltrichlorosilane next to a silicon surface; the silane then diffuses along the surface, adsorbs partially and creates a concentration gradient. Since then, more work has been carried out and new techniques have been used to prepare gradients, such as

electrochemical desorption, contact printing, gradual immersion into a diluted solution, polymer-based techniques and irradiation-based methods [1].

In materials science, not only is the surface chemistry an important parameter, but also the surface roughness. It plays an important role in tribology by changing the coefficient of friction and/or the adhesion [8, 9]. It also effects the biological response to a surface, as cell attachment, proliferation and cell fate are influenced by the roughness [10]. Especially for medical bone implants, roughness is important, since osteoblasts have been shown to have different behavior according to the roughness of the surface they were cultured on [11-13].

This chapter introduces the techniques used in this thesis to form one- and two-dimensional roughness gradients. All the methods were developed at ETH Zürich. Originally, the method for nanoparticle-density gradients as described in Section 2.2 was designed by Christoph Huwiler and Tobias Künzler [11], the approach for micro-featured roughness gradients (Section 2.3) was developed by Tobias Künzler [14] and the method for the fabrication of 2D-orthogonal gradients (Section 2.4) was established by Christian Zink [15]. Much of this work is based on these three methods and hence, a detailed introduction to the procedures is given below.

2.2 Nanoparticle-density gradients

Nanoparticle-density gradients were prepared by the method developed by Tobias Künzler and Christoph Huwiler [11]. The adsorption of silica particles is a kinetically controlled process. Based on the adsorption of the negatively charged nanoparticles onto a positively charged substrate, a simple dip-coating process can create gradients.

2.2.1 Experimental

2.2.1.1 Gradient fabrication

Silicon wafers (<100> orientation, Si-mat, Germany) were cut into samples of 25 x 25 mm², cleaned in toluene (puriss. P.a., ≥ 99.7%, Fluka Chemicals, Germany) in an ultrasonic bath for 20 minutes, with a change of solvent after 10 minutes and ultra-sonicated again for 20 min in 2-Propanol (ACS grade, min 99.8%, Fluka Chemicals, Germany), exchanging the solvent after 10 minutes. The samples were then dried with a jet of dry nitrogen and stored in well plates until further use. As a last cleaning step and to activate the surface, the samples were further cleaned in a radio-frequency (RF) oxygen plasma (PDC_32G, Harrick Plasma, USA), pumping the plasma chamber down to 2.5×10^{-2} mbar, and maintaining a constant pressure at $3 \cdot 10^{-2}$ mbar under oxygen. The plasma was ignited at high RF level (100 W) for 2 min.

The clean samples were subsequently immersed into a freshly prepared poly(ethylene imine) (PEI) solution (M_w = 750'000, 50 wt% in water, Sigma Aldrich, Switzerland) at 1 mg/ml for one hour to render the surface positively charged. Finally the substrates were rinsed with ultrapure water and blown dry with nitrogen.

The nanoparticle-density gradients were prepared by dipping the pre-treated silica wafers into highly diluted particle suspensions of diameters 12 nm

(Microsphere-Nanospheres, Corpuscular Inc., USA), 39 nm (Klebesol, Clarient, France) and 72 nm (Klebesol, Clarient, France). The particles were delivered as a 30 wt% stock solution. To prepare the silica-particle suspension, the 30 wt% stock solution was homogenized for 10 minutes in an ultrasonic bath and diluted with ultra-pure water to a 1 wt% intermediate stock solution. Just before the particle adsorption, the 1 wt% solution was sonicated for 10 min and further diluted with deionized water to a 0.002 wt% working suspension for 12 nm particles and to 0.004 wt% for 39 and 72 nm particles. The working suspension was sonicated for 20 min prior to use to reduce particle clustering.

For the gradient fabrication, the suspension was stirred with a mechanical stirrer (200 rpm) and was kept agitated in a cooled ultrasonic bath. First, the PEI coated Si-wafer was immersed to the starting point of the gradient (about 5 mm from the lower edge) and kept there for 2 minutes to ensure homogenous condition for the adsorption. The samples were then slowly immersed into the suspension using a linear-motion drive (OWIS Staufen, Germany). The immersion profile was set to $s(t) = -3.09 \times 10^{-6} \times t^2$, where s [mm] is the position on the gradient at time t [s]. This profile led to a 10 mm long gradient after 1800 seconds of immersion. At the end of this process, the samples were immediately removed from the suspension and dipped into a 200 ml beaker containing ultrapure water and rinsed 5 times with ultrapure water to remove non-adsorbed particles and dried with a jet of nitrogen.

The gradient was subsequently heat-treated in order to attach the silica particles firmly to the surface and to burn off the organic PEI layer, leaving a pure silicon oxide surface behind. The samples were sintered at temperatures between 1050 and 1100 °C under ambient conditions for 1 hour using a high temperature oven (Heraeus K114, Thermo Scientific, USA). The heating and cooling rate was set to 4 °C/min.

For biological experiments, the gradients were coated with 6 nm of TiO_2 to mimic the surface of titanium implants. The coating was performed at the Paul Scherrer Institute by magnetron sputtering and a growing rate of 1 nm/min.

A schematic of the whole particle-density fabrication process can be seen in Figure 2.1.
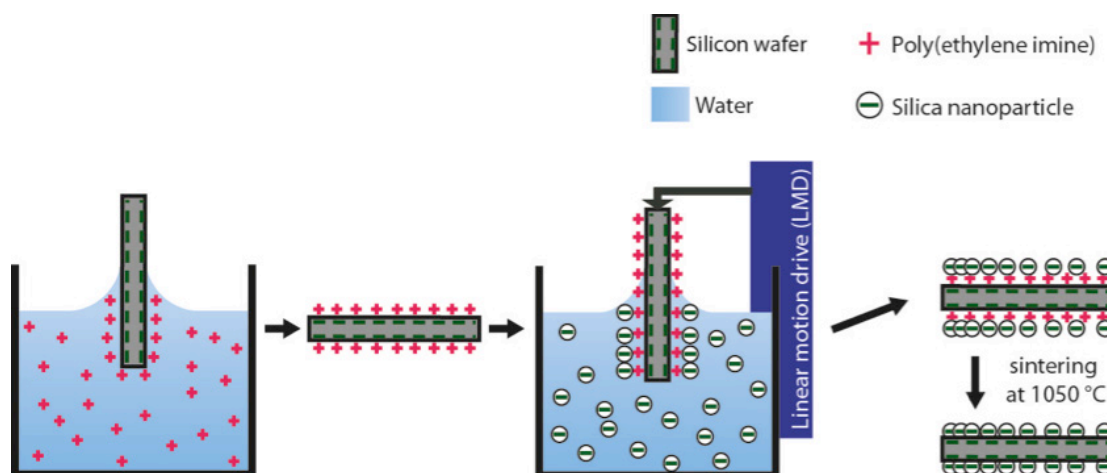
Figure 2.1: A silicon wafer is rendered positively charged with a PEI coating and subsequently slowly immersed into a colloidal suspension. The particle density depends on the immersion time, longer immersion results in a higher density.

2.2.1.2 Characterization

Particle-density gradient samples were analyzed by the use of scanning electron microscopy (SEM, LEO 1530, Zeiss, Germany) by taking SEM pictures along the gradient with an acceleration voltage of 3 kV with the in-lens detector. To avoid any charge effects the samples were coated with 3 nm of platinum.

To take cross-sectional images, the samples were places in a cross-section holder (G301S, Plano GmbH, Germany) and coated for a second time with 3 nm of platinum. To improve image quality the stage was tilted by 5 °.

Atomic force microscopy (AFM) analysis (Dimension Icon with ScanAsyst, Bruker Nano Surfaces Division, USA) in tapping mode was used as a second method to characterize the gradients and to measure the height of the particles after sintering. AFM tips with resonance frequencies in the range of 200-400 kHz (OMCL-AC, 160TS-R3, Olympus, Japan) were used.

The particle density for each position was determined with the Particle Size Analyzer (PSA) macro (https://code.google.com/archive/p/psa-macro/) for Image J (version 1.44p for Mac).

2.2.2 Results and Discussion

It has been shown previously that nanoparticle adsorption follows a random sequential adsorption (RSA) model, where the adsorption is proportional to $\sqrt{t}$ and a theoretical particle coverage of 54.7% cannot be exceeded [16, 17]. In reality the coverage limit might not be reached, as an electrical double layer, which adds to the actual particle diameter, surrounds the particles. In order to generate linear particle-density gradient the immersion profile was set to $s(t) = -3.09 \times 10^{-6} \times t^2$. SEM images were used to quantify the particle density along the gradient. The particle density steadily decreases along the gradient with shorter immersion times.

72 nm particle gradient
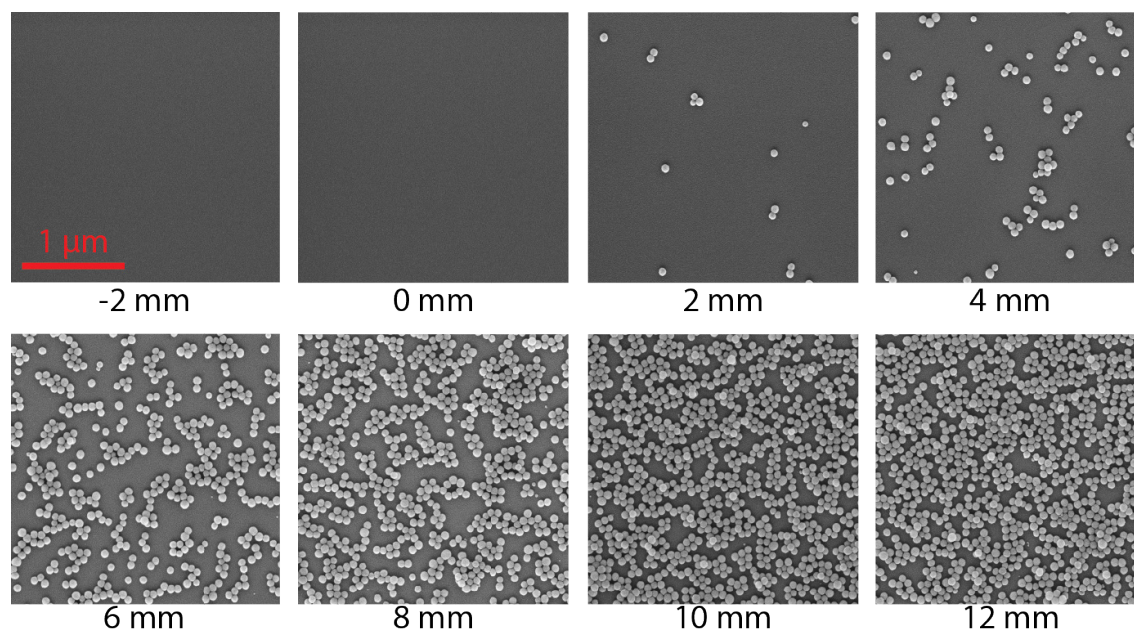
Figure 2.2: SEM images taken every 2 mm along a 72 nm nanoparticle-density gradient.

SEM images of 72 nm particle-density gradients are shown in Figure 2.2. The images were taken every 2 mm along the gradient. The analysis of the particle density averaged over gradients from 9 different gradient batches reveals a nearly linear increase along the gradient (Figure 2.3). The initial density at the high coverage end is around 60 particles/ m² and goes down to no particles at a distance of 00 mm. The particle density rises approximately linear and best fit resulted in the functional equation: $\delta = 5.9x - 5.4\ [\mu m^{-2}]$ with δ the particle density and x the position along the gradient in mm. The functional graph for the calculated particle density is shown as red line.
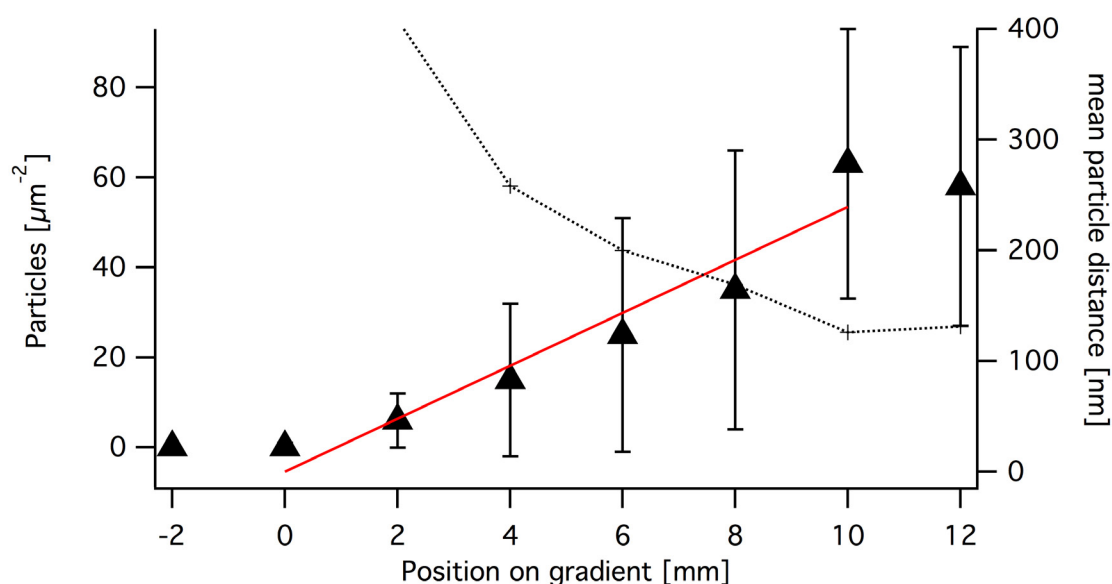
Figure 2.3: Measured particle density (black triangle) and mean particle distance between two particles (black cross) along the 72 nm nanoparticle-density gradient. (Mean ± standard deviation, n = 9)

39 nm particle gradient
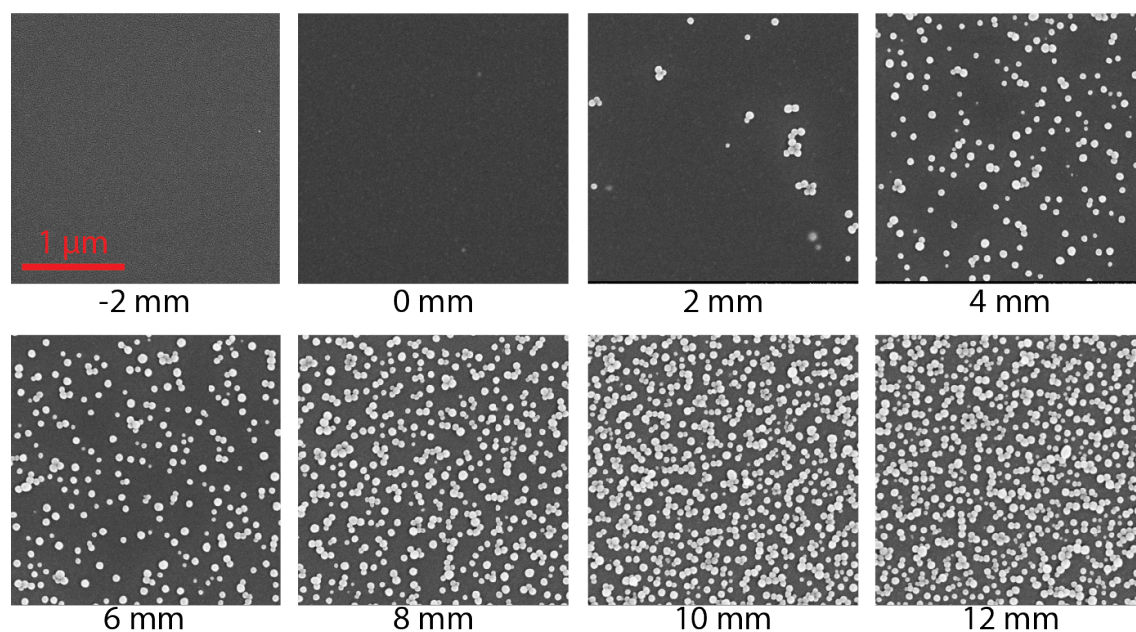
Figure 2.4: SEM images taken every 2 mm along a 39 nm nanoparticle-density gradient.

SEM images of 39 nm particle-density gradients are shown in Figure 2.4. The images were taken every 2 mm along the gradient. The analysis of the particle density averaged over gradients from 14 different gradient batches reveals a nearly linear increase along the gradient from 0 to 8 mm on the gradient (Figure 2.5). The initial density at the high coverage end is around 150 particles/ m² and goes down to no particles at a distance of 0 mm. The particle density rises approximately linear and best fit resulted in the functional equation: $\delta = 17.9x - 1\ [\mu m^{-2}]$ with δ the particle density and x the position along the gradient in mm. The functional graph for the calculated particle density is shown as a red line.
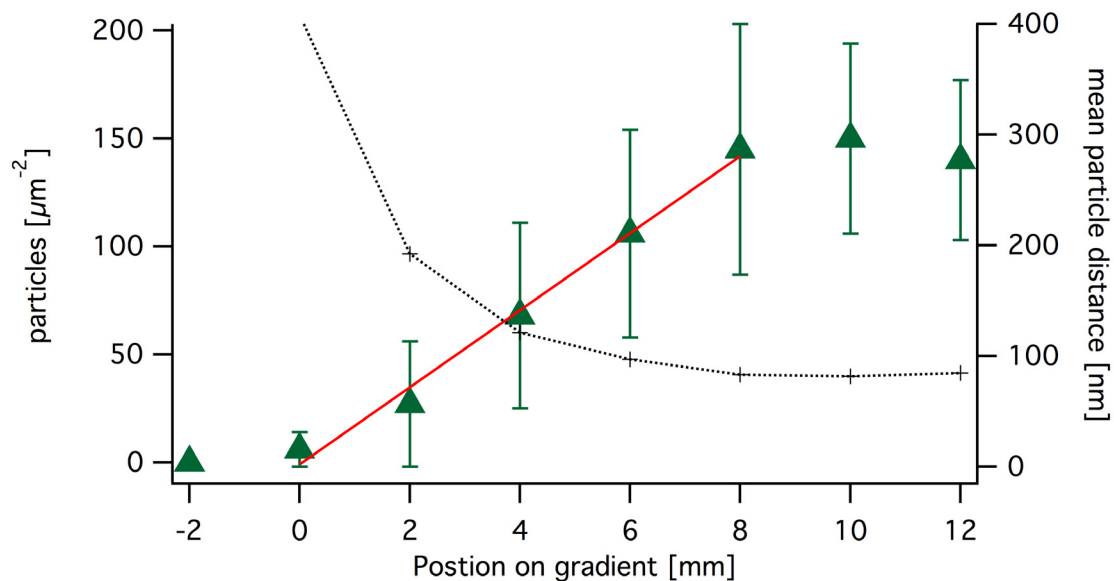
Figure 2.5: Measured particle density (green triangle) and mean particle distance between two particles (black cross) along the 39 nm nanoparticle-density gradient. (Mean ± standard deviation, n = 14)

12 nm particle gradient
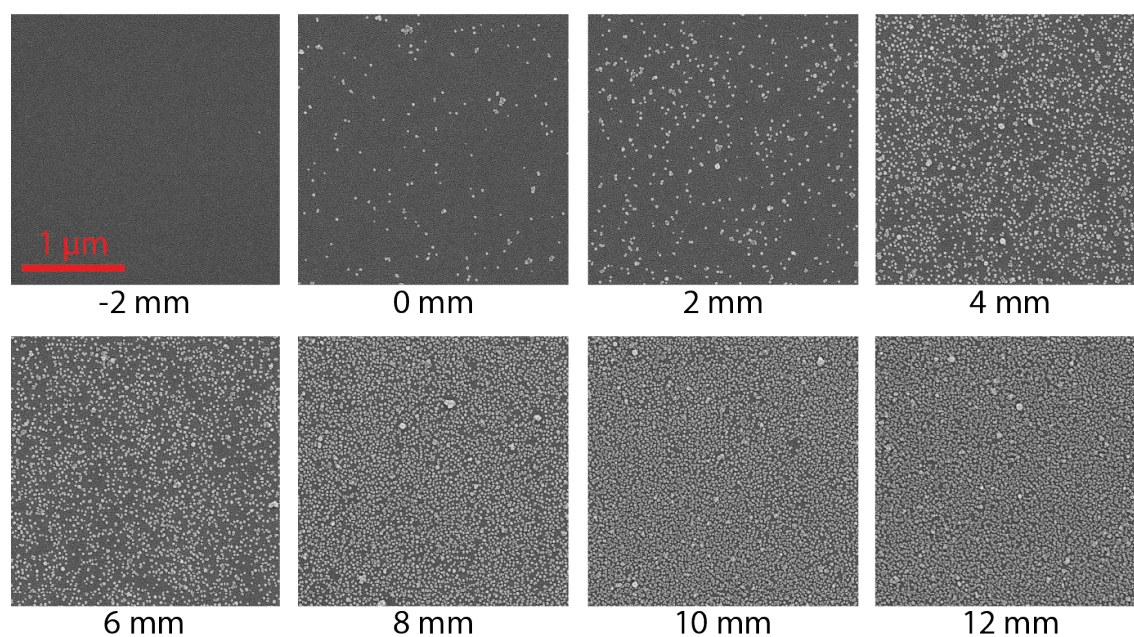
Figure 2.6: SEM images taken every 2 mm along a 12 nm nanoparticle-density gradient.

SEM images of 12 nm particle-density gradients are shown in Figure 2.6. The images were taken every 2 mm along the gradient and were used to quantify the particle density along the gradient. Some particles on the surface form clusters, but most of them adsorb individually on the substrate in a random

pattern. Along the gradient, the density steadily increases with longer immersion times. The analysis of the particle density averaged over gradients from 9 different gradient batches reveals a nearly linear increase along the gradient (Figure 2.7). The initial density at the high coverage end is around 1300 particles/ m² and goes down to no particles at a distance of -2 mm. The blue triangles indicate the particle densities in average number of particle per m², and the black crosses represent mean particle distance along the gradient. The particle density rises approximately linear and best fit resulted in the functional equation: $\delta = 99x - 160 \,[\mu m^{-2}]$ with δ the particle density and x the position along the gradient in mm. The functional graph for the calculated particle density is shown as red line.
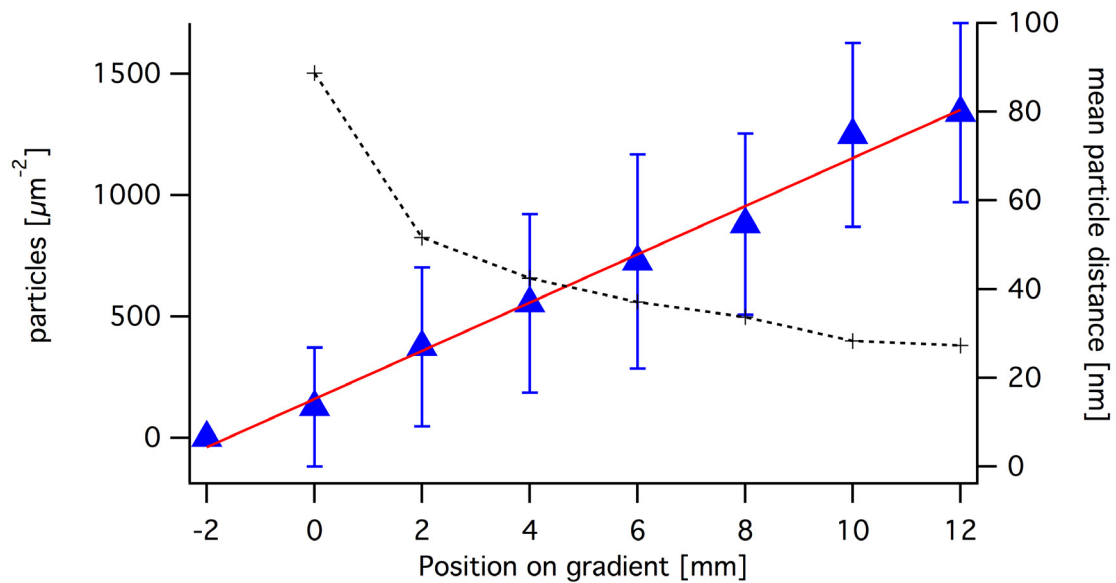
Figure 2.7: Measured particle density (blue triangle) and mean particle distance between two particles (black cross) along the 12 nm nanoparticle-density gradient. (Mean ± standard deviation, n = 9)

AFM data and SEM cross-sections (Figure 2.8) show that the particle height can be adjusted by the heat treatment. With an increasing sintering temperature, the particles are sintered more into the substrate, depending on the sintering temperature any height between the particle size and zero can be chosen. In order to keep the shrinking of the particles to a minimum a sintering temperature of 1050 °C was chosen; with higher temperatures the sintering of

the 12 nm particles is too advanced. At 1075 °C the particle height for 12 nm particles was decreased by 50% to approximately 6 nm.
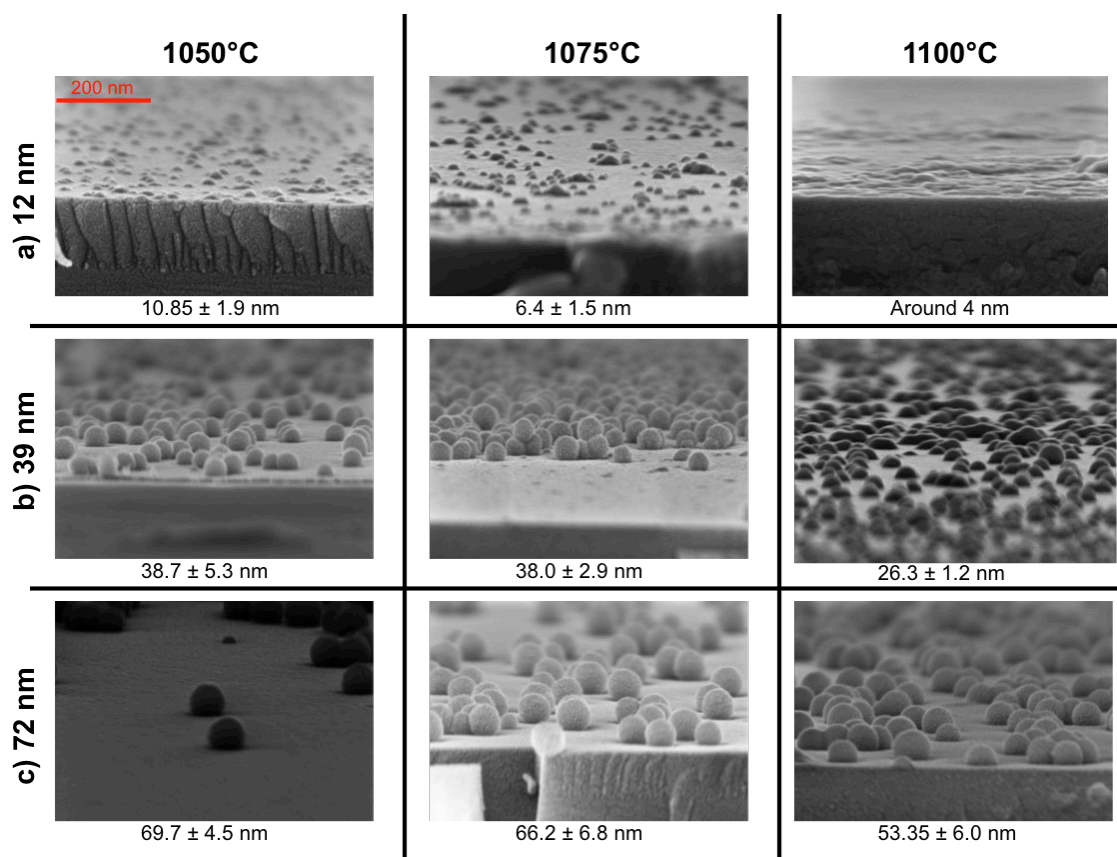
Figure 2.8: Effect of the sintering temperature on the a) 12 nm, b) 39 nm and c) 72 nm particles. Cross-sections SEM images showing the particles and substrates and the height of the particles measured by AFM are displayed.

The method described in this section allows the creation of nanoparticle-density gradients by a simple dip-coating process. The gradient slope and gradient profile change depending on the immersion profile. By differing the heat treatment the morphology of the particles can be changed.

The technique is not limited to the materials mentioned above, as long as the general principle of using oppositely charged particles and substrates is followed. For example, Cremmel *et al.* [18] produced particle-height vs. –density gradients using polystyrene particles (535 nm, microparticles GmbH, Germany).

2.3 Micro-roughness gradients

To create microscale-featured roughness gradients, Künzler *et al.* [14] developed a two-step process. First, an aluminum substrate was sandblasted (SB) with corundum particles to achieve a uniformly rough surface morphology. In a second step, the roughened substrate was fully immersed into a chemical polishing solution and then withdrawn in a kinetically controlled manner by means of a linear-motion drive (LMD), resulting in a roughness gradient with microscale features. (See Figure 2.9)
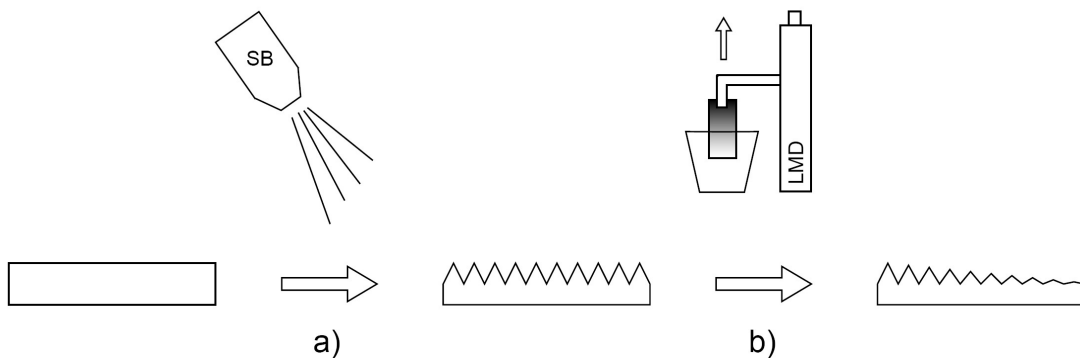
Figure 2.9: A sketch for the generation of morphological gradients with micro-features. (a) First a homogenously rough surface is generated by sandblasting (SB). (b) The rough features are then gradually removed by withdrawing the sample from a chemical-polishing solution with a linear motion drive (LMD). Figure taken from [19].

2.3.1 Experimental

2.3.1.1 Gradient fabrication

Pure aluminum sheets (Reinalu HH, purity higher than 99.5%, Metall Service Menzikon AG, Switzerland) were cut into $2 \times 20 \times 40$ mm^3 or $2 \times 60 \times 60$ mm^3 substrates. Both surfaces were roughened in a conventional sand-blasting cabinet (Modell 65, SABLUX, Switzerland) using fractured corundum particles (81500-826-074, SABLUX, Switzerland) with a diameter of 297 - 420 m. Following sandblasting, the substrates were cleaned with ethanol for 10 min in an ultrasonic bath and subsequently dried in a stream of nitrogen.

In a second step the roughness is reduced as a function of distance along the substrate by chemical polishing. The chemical polishing solution consist of 77.5% (v/v) phosphoric acid, 16.5% (v/v) sulphuric acid, and 6% (v/v) nitric acid (all from Merck, Germany) and was heated in a round-bottom flask to 80 ± 1 °C in an oil bath. Figure 2.10 shows the detailed experimental setup. To prevent the evaporation of the polishing solution, the vapors were condensed in a Dimroth cooler and returned to the bath. A magnetic stirrer with a moderate mixing speed was used to keep the solution agitated. In order to create a homogenous aluminum oxide layer on the surface, the substrate was first dipped into the polishing solution for 10 s and then immersed for 3 min in boiling ultrapure water. In the second step, the aluminum substrate was fully immersed in the polishing bath and slowly withdrawn with a computer-controlled linear-motion drive (OWIS Staufen, Germany) to fabricate the gradient. During the polishing process gas bubbles can be generated that can adhere to the aluminum surface and obstruct the polishing. In order to move the gas formation away from the substrate, a platinum electrode was immersed into the solution and a potential of + 6 V was applied. The gradient fabrication was stopped by rinsing the sample with boiling ultra-pure water and dried in a jet of nitrogen.
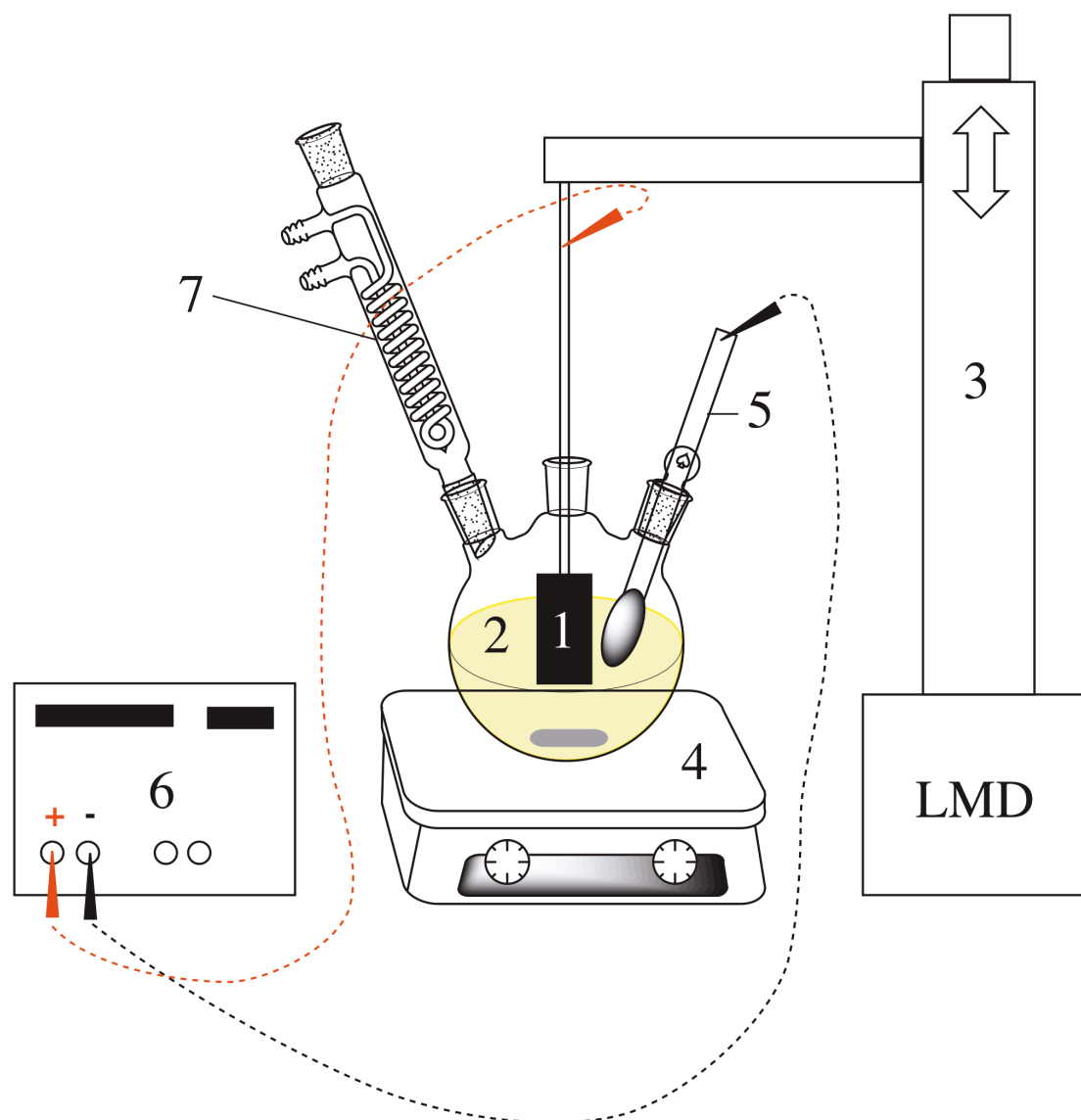
Figure 2.10: Experimental setup for micrometer-roughness gradient fabrication. A roughened aluminum substrate (1) is slowly withdrawn from the chemical-polishing solution (2) by means of a linear-motion drive (3). The polishing bath is kept slightly agitated by a magnetic stirrer (4). To shift the gas formation away from the substrate, a platinum electrode (5) is immersed into the solution, linked to a power supply (6) and a potential of 6 V is applied. The vapors were condensed in a Dimroth cooler (7) and returned to the bath, in order to maintain the composition of the solution constant. Reprinted from [20], Copyright (2018), with permission from Elsevier.

To achieve a linear roughness gradient, the withdrawing profile has to be set to $x(t) = a \times t^b$, where x corresponds to the position after time t, a is length factor and $b = 0.5$. To implement this routine, LabView (National Instruments, USA) was used. By adjusting the length factor a, different gradient length can be produced over a period of 40 min. For a 10-mm-long gradient, a was set to 0.2042, for a 20-mm-long gradient, a =0.4084 and for a 50-mm-long gradient, a =1.0206.

2.3.1.2 Characterization

The micro-roughness gradients were qualitatively characterized by SEM (LEO 1530, Zeiss, Germany) by taking pictures along the gradient with an acceleration voltage of 3 kV with the in-lens detector. To avoid any charge effects the samples were coated with 3 nm of platinum.

Optical profilometry (Plu NEOX, Sensofar, Spain) in confocal mode was used for quantitative characterization. The ISO standard 4287 and the ASME B46 require a profile of at least 2.5 mm length. To meet these standards, the stitching option was chosen to measure 2.75 mm long segments perpendicular to the gradient on different positions along the gradient. The software SensoMap (version 6.0.0.5883 incl. 3D Fourier Analysis Module, DigitalSurf, France) was used to analyze the data. The measurement was leveled and non-measured data points were filled in (measured data points > 95%). The 2.75 mm long profiles were then extracted and used for the calculation of roughness values (R_a, S_k).

To describe surface topographies in more detail, a wavelength-dependent evaluation, introduced by Wieland *et al.* [21], was used to separate the data into different roughness windows (1.5 - 3 m, 3 - 10 m, 10 - 50 m and 50 - 250 m) by using the FFT filter module. All roughness parameters are calculated for every window individually and contain only the information of the corresponding wavelength.

2.3.2 Results and Discussion

In Figure 2.11 stitched SEM images along a 10 mm long micro-roughness gradient can be seen. On the right the coarse structure consisting of deep grooves, cracks and sharp peaks from the sand-blasting process is visible. The chemical polishing time increases towards the left. With increasing polishing time, the sharp and fine features were polished away and only the bigger, more

pronounced structures remain. In the end after a total polishing time of 40 min only a smooth waviness is left behind.
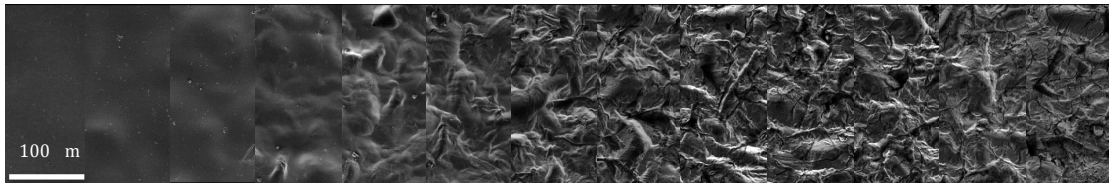
Figure 2.11: Stitched SEM images along a 10 mm long micro-roughness gradient.

The maximum topographical variations of the sample are determined in the sandblasting step by choosing the particle size and shape, angle of impact and air pressure, while the parameters of withdrawing determine the slope and profile of the gradient. In Figure 2.12, it can be seen that the roughness amplitude increases monotonically along the 50 mm long gradient. By applying the FFT method, the original profiles were split up into four different wavelength windows (1.5 - 3, 3 - 10, 10 - 50, 50 - 250 µm) and the arithmetic average, R_a, was calculated individually. A comparison of the roughness values in the different windows shows that the surface features with a short wavelength are removed faster by chemical polishing, whereas larger features remain longer on the surface. Features with a wavelength of 1.5 to 3 µm disappeared halfway along the gradient (25 mm), features with a wavelength of 3-10 µm approach a value close to zero at 10 mm and the only contribution to the surface roughness at the polished end are features with a wavelength between 50 and 250 µm. The chemical polishing solution initially attacks small features, such as peaks and sharp ridges, whereas larger features such as protuberances are removed only after longer polishing times.
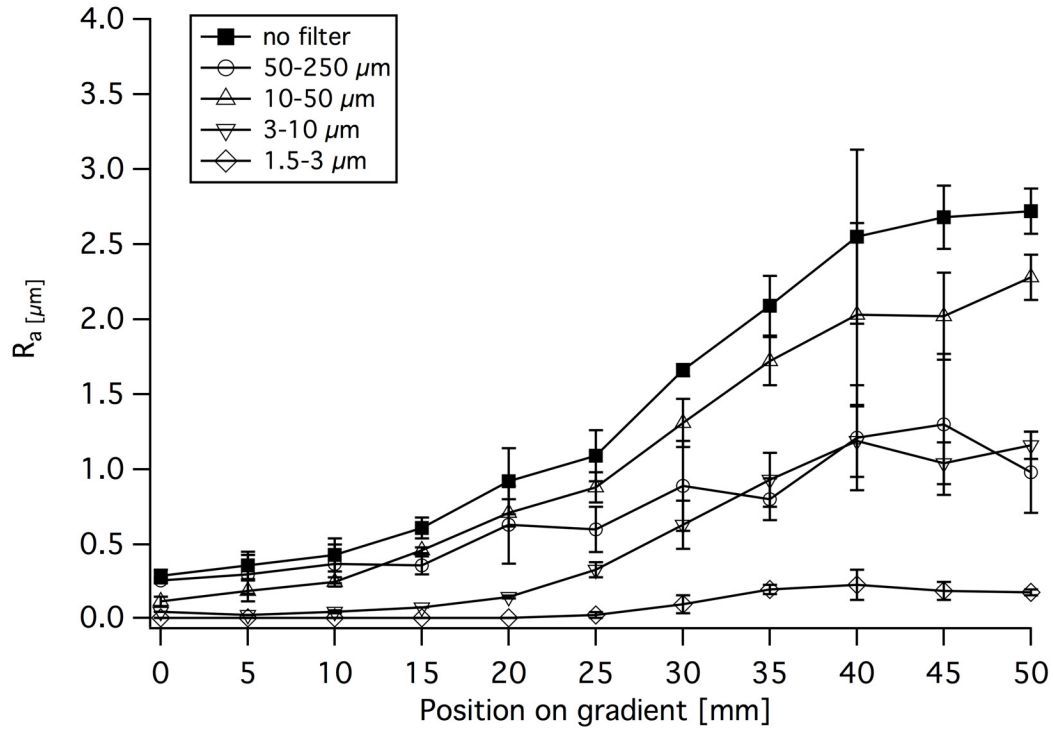
Figure 2.12: Roughness values R_a, acquired by optical profilometry. The unfiltered values (no filter) show that the roughness varies from 0.3 m to just under 3 m along the gradient. Data was evaluated by wavelength-dependent analysis applying FFT. Roughness values, R_a, calculated for different wavelength windows (1.5 - 3, 3 - 10, 10 - 50, 50 - 250 m).

2.4 2-Dimensional orthogonal nanometer-micrometer roughness gradients

2-dimensional micrometer-roughness vs. nano-feature density gradients were prepared by the method developed by Zink *et al.* [15]. By combining the two methods mentioned above, a two-dimensional orthogonal gradient with nano- and micro-features could be produced (Figure 2.13). Such sample types allow the investigation of the combined effect of both nano- and micro-scale surface structures in a single experiment.
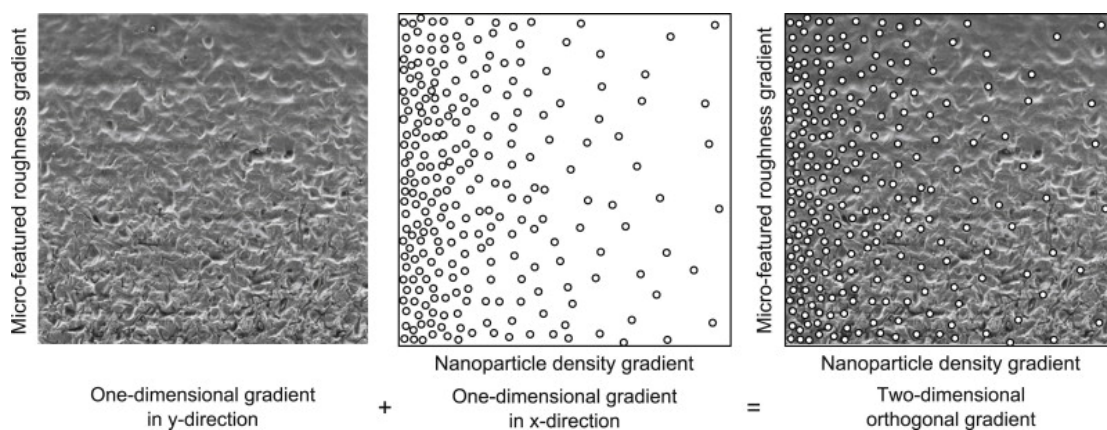
Figure 2.13: Sketch showing the formation of a two-dimensional orthogonal gradient: A micro-featured roughness gradient on one axis is combined with a nanoparticle density gradient on the other axis to form a 2D gradient that combines roughness on the m and nm scales. Reprinted from [15], Copyright (2018), with permission from Elsevier.

2.4.1 Experimental

2.4.1.1 Gradient Fabrication

In order to sustain the high-temperature sintering step required in the nanoparticle-density-gradient fabrication process, the aluminum substrate was replaced by a highly temperature-resistant material. Zink *et al.* [15] developed a ceramic-based approach: First a polyvinylsiloxane (POVIL novo light, Heraeus-Kulzer, Switzerland) negative was prepared. A high-solids-loading alumina slurry (57 vol% solids loading) was prepared by slowly adding alumina powder (200 nm grain size, C517475, Ceralox, USA) in deionized water, ball-milling the

suspension for 18 h to break up agglomerates, and to homogenize the slurry and subsequently degassed under constant stirring in a mild vacuum. The alumina positive was produced by casting the slurry into the polyvinylsiloxane negative (PVS) and drying at room temperature for at least 48 h. The green bodies were sintered for 4 h at 1500 °C in a high-temperature oven (HT08/17, Nabertherm, Switzerland). After sintering, the alumina positives were subsequently sputtered with 200 nm SiO_2 by PECVD (Plasma Enhanced Chemical Vapor Deposition, FIRST Laboratory, ETH Zürich) to mimic the chemistry of the silicon wafer prior to PEI adsorption and then used as substrate for the attachment of nanoparticles by dip coating. (See Figure 2.14)
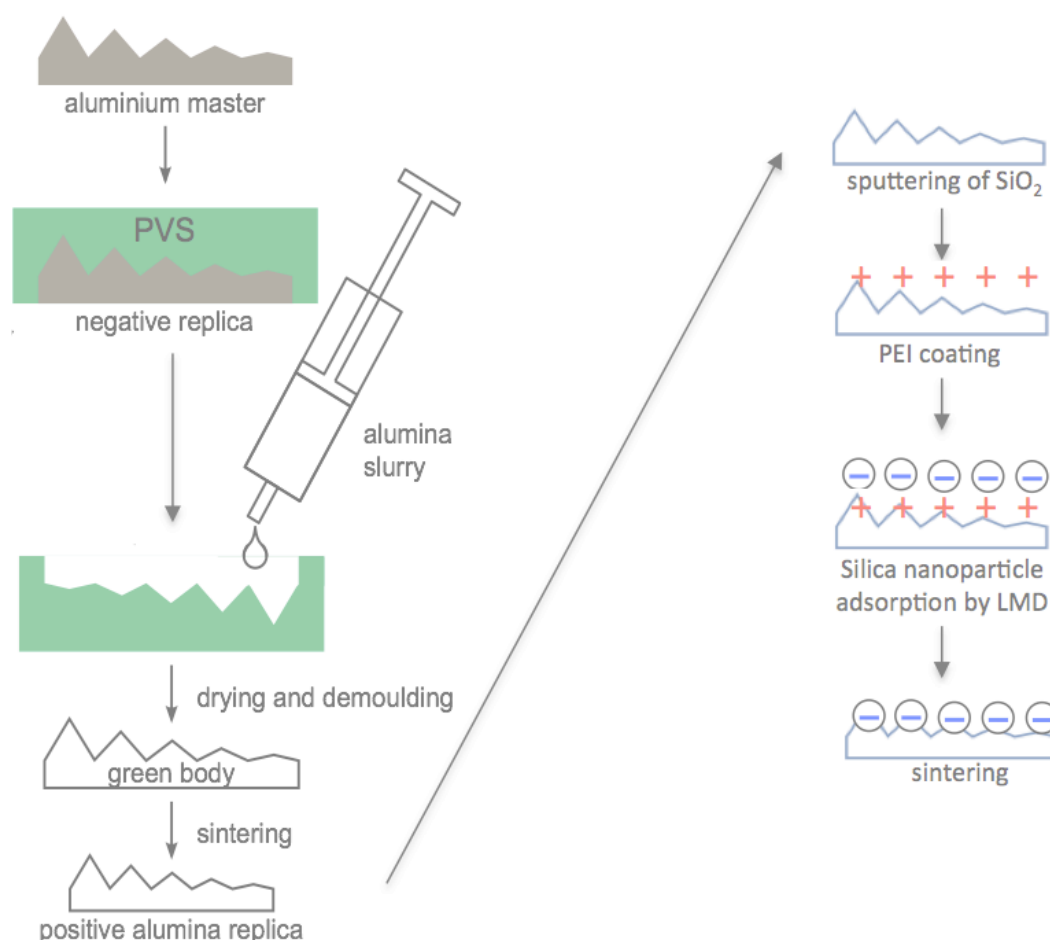
Figure 2.14: Two-step fabrication process for 2D-orthogonal gradients. Left: replication of the microscale gradient with alumina. Right: Adsorption of silica nanoparticles with a linear motion drive to produce a nanoscale gradient orthogonal to the microscale gradient.

The silica-particle adsorption required a few adjustments in order to adsorb the particles even at the bottom of deep grooves. This was solved by increasing the silica particle concentration to 0.005 wt%, degassing the suspension for 5 min in a light vacuum and keeping the suspension agitated with a magnetic stirrer (100 rpm) and an ultrasonic horn (UP 200, Hielscher GmbH, Germany) at the lowest settings (Cycle = 0.2, Amplitude = 20%).

2.4.1.2 Characterization

The particle-coated alumina master was characterized by SEM (Zeiss LEO 1500, Germany), the surface of the 2D-gradient was scanned in a 1 mm wide grid in the *x*- and *y*-directions, while images were taken with a magnification of 50,000X. From these images the particle density was determined with ImageJ software (version 1.44 for Windows, http:/rsbweb.nih.gov/ij/) with the particle-analysis plugin.

Optical profilometry in confocal mode was used to analyze the micrometer roughness. 2.5 mm long strips were stitched together, perpendicular to the gradient direction by using the 20X objective every millimeter along the gradient. The evaluation was carried out with the SensoMap software (Version 6.0.0.5832 incl. 3D Fourier Analysis Module, DigitalSurf, France) according to the ASME B46.1 standard.

2.4.2 Results and Discussion

The SEM analysis was very important to ensure that the particles covered the micro-features homogenously. As shown in Figure 2.15, grooves of the micro-rough surface can only be covered homogenously with nanoparticles by introducing ultrasonic pulses during the adsorption.
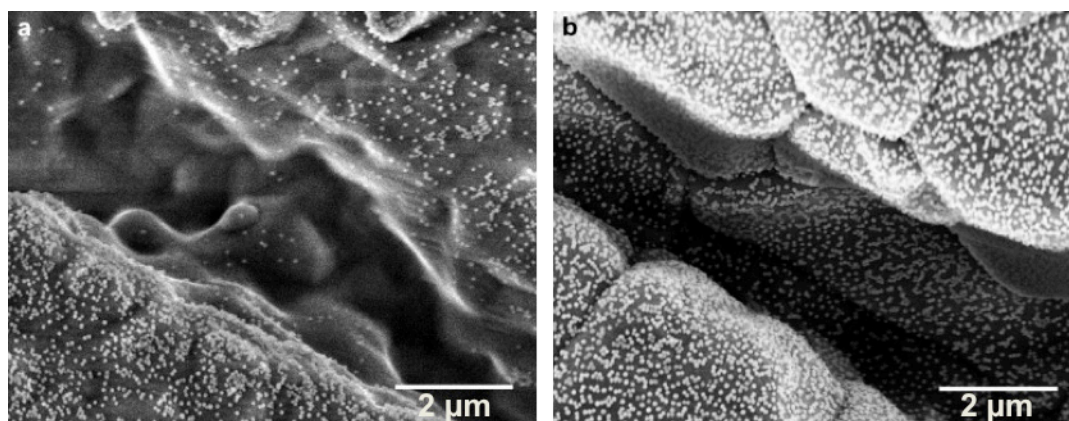
Figure 2.15: Nanoparticle attachment in deep grooves of micro-rough surface: SEM micrograph of grooves of particle adsorption without a) and with b) sonication. By additionally using the ultrasonic pulses during the adsorption, deep grooves become homogenously coated with particles. Adapted from [15], Copyright (2018), with permission from Elsevier.

As can be seen in Figure 2.16 (a), the R_a value linearly increases along the gradient from 0.8 to 4.1 m. The original 10-mm-long micro-roughness gradient shrank by 20% to 8 mm due to the shrinking of the alumina master during sintering. Figure 2.16 (b) shows that the particle number decreased linearly from 74 to 0 particles per m². Each value is averaged perpendicular to the nanoparticle density gradient.
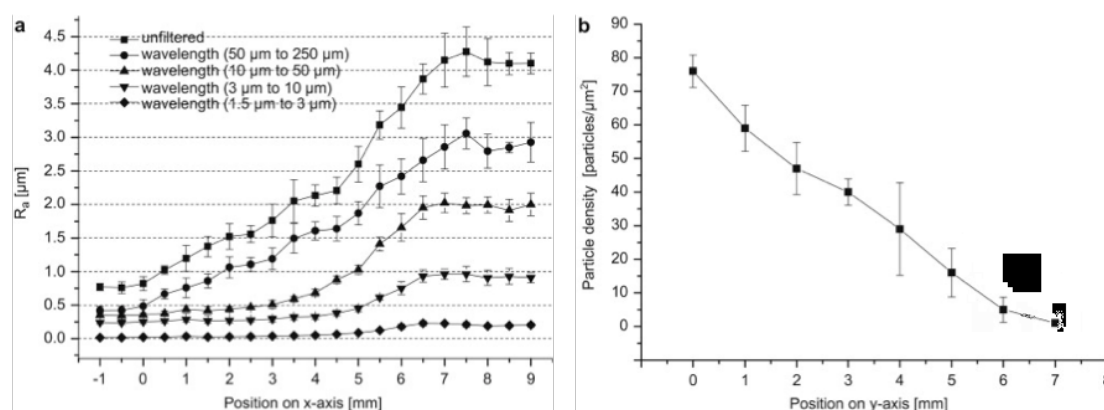
Figure 2.16: Analysis of the two-dimensional orthogonal gradient: a) the R_a-values (unfiltered) decrease linearly on the x-axis. Roughness with shorter wavelengths disappears faster, while bigger features are more persistent along the micro-roughness gradient. The error bars are the standard deviation of the R_a values from three-line profiles at this point. The nanoparticle-density b) decreases linearly along the y-axis. Reprinted from [15], Copyright (2018), with permission from Elsevier.

References:

[1] S. Morgenthaler, C. Zink, N.D. Spencer, Surface-chemical and-morphological gradients, Soft Matter 4(3) (2008) 419-434.

[2] H. Elwing, C.-G. Golander, Protein and detergent interaction phenomena on solid surfaces with gradients in chemical composition, Advances in Colloid and Interface Science 32(4) (1990) 317-339.

[3] L.M. Karlsson, P. Tengvall, I. Lundström, H. Arwin, Adsorption of human serum albumin in porous silicon gradients, physica status solidi (a) 197(2) (2003) 326-330.

[4] G.P. Rockwell, L.B. Lohstreter, J.R. Dahn, Fibrinogen and albumin adsorption on titanium nanoroughness gradients, Colloids and Surfaces B: Biointerfaces 91(0) (2012) 90-96.

[5] S.J. Lee, G. Khang, Y.M. Lee, H.B. Lee, The effect of surface wettability on induction and growth of neurites from the PC-12 cell on a polymer surface, Journal of Colloid and Interface Science 259(2) (2003) 228-235.

[6] S.B. Kennedy, N.R. Washburn, C.G. Simon Jr, E.J. Amis, Combinatorial screen of the effect of surface energy on fibronectin-mediated osteoblast adhesion, spreading and proliferation, Biomaterials 27(20) (2006) 3817-3824.

[7] M.K. Chaudhury, G.M. Whitesides, How to Make Water Run Uphill, Science 256(5063) (1992) 1539-1541.

[8] S.N. Ramakrishna, L.Y. Clasohm, A. Rao, N.D. Spencer, Controlling Adhesion Force by Means of Nanoscale Surface Roughness, Langmuir 27(16) (2011) 9972-9978.

[9] S.N. Ramakrishna, P.C. Nalam, L.Y. Clasohm, N.D. Spencer, Study of Adhesion and Friction Properties on a Nanoparticle Gradient Surface: Transition from JKR to DMT Contact Mechanics, Langmuir 29(1) (2013) 175-182.

[10] D.M. Brunette, P. Tengvall, M. Textor, T. P., Titanium in Medicine, Springer, Berlin2001.

[11] C. Huwiler, T.P. Kunzler, M. Textor, J. Vörös, N.D. Spencer, Functionalizable Nanomorphology Gradients via Colloidal Self-Assembly, Langmuir 23(11) (2007) 5929-5935.

[12] T.P. Kunzler, C. Huwiler, T. Drobek, J. Vörös, N.D. Spencer, Systematic study of osteoblast response to nanotopography by means of nanoparticle-density gradients, Biomaterials 28(33) (2007) 5000-5006.

[13] T.P. Kunzler, T. Drobek, M. Schuler, N.D. Spencer, Systematic study of osteoblast and fibroblast response to roughness by means of surface-morphology gradients, Biomaterials 28(13) (2007) 2175-2182.

[14] T.P. Kunzler, T. Drobek, C.M. Sprecher, M. Schuler, N.D. Spencer, Fabrication of material-independent morphology gradients for high-throughput applications, Applied Surface Science 253(4) (2006) 2148-2153.

[15] C. Zink, H. Hall, D.M. Brunette, N.D. Spencer, Orthogonal nanometer-micrometer roughness gradients probe morphological influences on cell behavior, Biomaterials 33(32) (2012) 8055-8061.

[16] J.W. Evans, Random and cooperative sequential adsorption, Reviews of Modern Physics 65(4) (1993) 1281-1329.

[17] E.L. Hinrichsen, J. Feder, T. Jøssang, Geometry of random sequential adsorption, Journal of Statistical Physics 44(5) (1986) 793-827.

[18] C.V.M. Cremmel, C. Zink, K. Maniura-Weber, L. Isa, N.D. Spencer, Orthogonal Morphological Feature Size and Density Gradients for Exploring Synergistic Effects in Biology, Langmuir 31(30) (2015) 8446-8452.

[19] T.P. Kunzler, Surface Morphology Gradients, ETH Zürich, 2007.

[20] N.V. Venkataraman, C.V.M. Cremmel, C. Zink, R.P. Huber, N.D. Spencer, Chapter 6 - Patterning Gradients, in: M. Piel, M. Théry (Eds.), Methods in Cell Biology, Academic Press2014, pp. 91-121.

[21] M. Wieland, P. Hänggi, W. Hotz, M. Textor, B.A. Keller, N.D. Spencer, Wavelength-dependent measurement and evaluation of surface topographies: application of a new concept of window roughness and surface transfer function, Wear 237(2) (2000) 231-252.

Chapter **3**

Protein-adsorption studies on nanoparticle-density gradients

3.1 Introduction

Nanoscale surface topographical features with dimensions less then 100 nm may resemble the pores and fibers found in the natural extracellular matrix (ECM) that controls the function of cells. Therefore, it is hypothesized that nanoscale surface features of similar dimensions of the protein modulate the proteins' behavior most strongly and can be tailored to control and direct interactions with proteins and cells [1, 2].

During the last decade, protein adsorption on nanoparticles and nanostructured surfaces has been studied intensively, but the overall reported effect of nano-roughness on the amount of adsorbed protein and the protein behavior, remains unclear from the reports currently available in the literature [1, 3].

Cai *et al.* [4] reported that the amount of neither albumin nor fibrinogen adsorption is altered by statistically nano-rough titanium surfaces with a root mean square (RMS) roughness of 2 to 21 nm. Similarly, the amount of collagen adsorbed on gold-coated nano-rough substrates (polystyrene particles with a diameter of 23 nm) was not altered compared to smooth controls [5]. In contrast, the amount of adsorbed albumin and fibrinogen showed a 50% increase with roughness on titanium roughness gradients with an RMS roughness varying linearly from 1 to 16 nm [6]. Rechendorff *et al.* [7] found that

the amount of adsorbed fibrinogen on tantalum surfaces increases with increasing RMS roughness (from 2 to 32.9 nm), the increase being greater than what might have been predicted from the corresponding increase in surface area.

The different outcomes of the studies might not only come from differences in the type of nanostructures studied but also from differences in the protein adsorption protocol. In 1988 Meltzer *et al.* [8] showed that the result of protein adsorption studies is highly path-dependent. The kind of protein film formed on surfaces sequentially exposed to proteins with different concentrations strongly depends on the sequence of events that the surface experienced. Meltzer *et al.* [8] concluded that "frustration could be expected when the adsorption of proteins is studied as a field". It is the exception that a system is obtained which is in thermodynamic equilibrium and most adsorbed protein layers are history-dependent artifacts.

Not only the size and spacing of surface structures, but also the curvature of surface asperities, plays a role in protein adsorption. Nanoparticles with a radius of less than 20 nm promote the adsorption of globular proteins (e.g. albumin) in their native conformation, while the conformation of large proteins (e.g. fibrinogen) is altered by high surface curvature [9]. Changes in protein conformation depending on the surface nanostructure have been confirmed by other studies [2, 4, 7, 10]

It can thus be seen that the relationship between protein adsorption and surface roughness needs further investigation.

To investigate how size, curvature and spacing of nanoparticles influence protein adsorption, nanoparticle-density gradients as described in Section 2.2 were used. The gradients were incubated with individual proteins or protein mixtures incorporating fluorescently labeled albumin and fibrinogen and analyzed by means of a fluorescent microarray scanner.

3.2 Experimental

3.2.1 Substrates - nanoparticle-density gradients

Nanoparticle gradients were produced as described in Section 2.2. In brief, a flat silicon wafer was first rendered positively charged with a coating of poly(ethyleneimine), and then slowly immersed into a highly diluted silica-particle suspension (average particle size: 12, 39 or 72 nm in diameter), to generate a linear particle-density gradient on the surface. The gradient was subsequently heat-treated at 1050 °C to sinter the particles to the surface and adjust their shape. Additionally, all organic compounds were burned out at this temperature.

Particle density was calculated from SEM images with the Particle Size Analyzer (PSA) macro (https://code.google.com/archive/p/psa-macro/) for ImageJ (version 1.44p for Mac).

In order to mimic the surface of titanium implants, the gradients were sputter-coated with 6 nm of TiO_2. Prior to all biological experiments, the gradients were oxygen-plasma cleaned for 2 minutes (PDC_32G, Harrick Plasma, USA), pumping the plasma chamber down to 2.5×10^{-2} mbar, and maintaining the pressure constant at 3×10^{-2} mbar with oxygen.

3.2.2 Protein solutions for adsorption tests

Labeled proteins:
- Albumin (Albumin from bovine serum (BSA), Alexa Fluor® 647 conjugate, Invitrogen, USA)
- Fibrinogen (Fibrinogen from human plasma (HPF), Alexa Fluor® 546 conjugate, Invitrogen, USA)

Unlabeled proteins:

- Albumin (Albumin from bovine serum (BSA), Sigma-Aldrich, USA)
- Fibrinogen (Fibrinogen from human plasma (HPF), Sigma-Aldrich, USA)
- Fibronectin (Fibronectin from bovine plasma (BSF), Sigma-Aldrich, USA)
- Fetal bovine serum (FBS, Invitrogen, USA, 10270-106, sterile-filtered)

Protein stock solution:

Stock solutions of 0.5 mg/ml albumin and 0.5 mg/ml fibrinogen were made according to the product manuals. For storage, the stock solutions were divided into 0.5 ml aliquots and frozen at -20 °C. Fibronectin solutions were made directly from the as-purchased 20 g vials, without making a stock solution.

Protein solutions:

Protein solutions for protein adsorption studies were prepared with HEPES 2 buffer with 10 mM 4-(2-hydroxylethyl)-piperazine-1-ethanesulfonic acid (HEPES) and 150 mM NaCl with pH 7.4 (both from Sigma, Switzerland) or fetal bovine serum (FBS). Prior to use, the HEPES 2 buffer was filtered (Whatman FP 30/0.2 CA-S, size 0.2 m, maximum pressure 7 bar). To enhance the solubility of proteins, HEPES 2/FBS was heated to 37 °C (water bath, INCO 2/108, Memmert GmbH&Co, Germany) prior to the preparation of the solution.

For low-protein-concentration experiments, the protein solution consisted of filtered HEPES 2 and fluorescently labeled protein of defined concentration (Table 3.1). For high-concentration experiments, unlabeled protein was additionally added (Table 3.1).

Table 3.1: Protein solutions for single-protein adsorption.

	Albumin	Fibrinogen	Fibronectin	Solution in
low protein concentration				
single BSA low	3 g/ml	-	-	HEPES 2
single HPF low	-	5 g/ml	-	HEPES 2
high protein concentration				
single BSA high	3 g/ml + 1 mg/ml*	-	-	HEPES 2
single HPF high	-	5 g/ml + *1 mg/ml**	-	HEPES 2

* = unlabeled protein

In addition to single-protein adsorption, the adsorption of specific proteins in competition with others was studied by adding fluorescently labeled proteins to a mixture of unlabeled proteins or FBS (Table 3.2). It was assumed that labeled proteins behave like the unlabeled ones that are already present in the mixture/serum.

The protein solutions were always freshly prepared right before the adsorption experiments and incubations were performed for 10, 30 and 120 min at room temperature in the dark.

Table 3.2: Protein solutions for competitive protein adsorption.

	Albumin	Fibrinogen	Fibronectin	Solution in
high protein concentration				
BSA + HPF high	5 g/ml + *30 mg/ml**	5 g/ml + *5 mg/ml**-	-	HEPES 2
BSA + HPF + FN high	5 g/ml + *30 mg/ml**	5 g/ml + *5 mg/ml**	30 g/ml *	HEPES 2
BSA + HPF in FBS	5 g/ml	5 g/ml	-	FBS

* = unlabeled protein

3.2.3 Protein-adsorption tests

Before use, the nanoparticle-density gradients were cleaned in the oxygen plasma cleaner (PDC-32G) for 2 min to remove hydrocarbon contamination from air and to obtain a clean, hydrophilic TiO_2 surface.

The whole gradient was incubated for 10, 30 or 120 min in 5 ml protein solution using a 50 ml glass beaker (Figure 3.1 a). After the adsorption time, the samples were transferred into 5 ml HEPES 2 buffer followed by rinsing with 15 ml HEPES 2 buffer. The samples were then transferred into a 400 ml beaker with ultrapure water, rinsed with 5 ml ultrapure water and dried in a stream of nitrogen.

An easy and rapid data read-out was achieved by using a fluorescence microarray scanner (Axon Genepix 4200A, Molecular Devices, USA) to map both fibrinogen and albumin separately (Figure 3.1 b and c).

The microarray scanner was originally constructed for use with microscope slides of dimension $(24.8-26.9) \times (74.5-76.5) \times (0.90-1.20)$ mm^3. The size of the silicon wafers used for the nanoparticle-density gradient was chosen to be $25 \times 25 \times 0.5$ mm^3 in order for them to lie flat on top of the three quartz holding-balls of the microarray scanner.
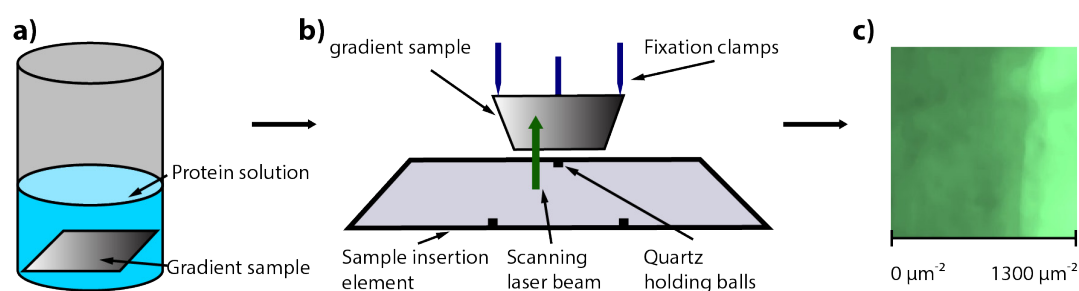
Figure 3.1: Scheme of the protein-adsorption process and read-out. a) Adsorption of fluorescently labeled proteins on the entire gradient surface. b) Schematic of microarray scanner set-up. c) Microarray scanner image of albumin on a 12 nm-particle-density gradient.

The resolution was set to 100 m/pixel for intensity read out. To minimize bleaching, only one scan per line was carried out. The photo-multiplier tube (PMT) of the fluorescence scanner was specified to be linear between a gain of 350 to 600. For that reason, all scans were performed in this gain range. The gain was kept constant for all measurements with one type of protein solution in case saturation was not reached. Typically in one experiment, three samples of each nanoparticle-density gradient type (12, 39 and 72 nm) were measured for each protein solution and incubation time and the experiment was repeated 1-5 times.

Table 3.3 presents the wavelength of the two lasers applied and the adsorption/emission wavelength of the protein conjugates tested.

Table 3.3: Wavelength of microarray scanner laser, filter windows and protein adsorption/emission maxima.

Protein	Excitation laser	Protein abs. max.	Scanner filter window	Protein em. Max.
Fibrinogen, Alexa Fluor® 546	532 nm	556 nm	550-600 nm	573 nm
Albumin, Alexa Fluor® 647	635 nm	650 nm	655-695 nm	669 nm

The resulting images were processed with Adobe Photoshop to alleviate the effect of small protein aggregations; the brightness of the images was interpolated within a radius of 5 pixels. Image analysis was performed using Image J (version 1.44p for Mac) a line plot of intensity along the particle-density gradient was created by averaging the grey values of all pixels along the lines perpendicular to the gradient. The measured intensity values were normalized to the intensity on the smooth region of the gradient and corrected for the increase in surface area by the presence of nanoparticles by assuming that the nanoparticles are half-spheres with a diameter of 12, 39 or 72 nm, respectively.

3.3 Results

3.3.1 Nanoparticle-density gradients

Detailed results for the used nanoparticle gradients can be found in Section 2.2.2. Nanoparticle-density gradients were produced with 12, 39 and 72 nm silica particles and coated with 6 nm TiO_2 to mimic the surface of a titanium implant. Every batch of gradients was analyzed extensively with SEM and AFM on different positions on the gradient to check particle densities and distribution. It was assumed that all gradients of one batch show the same properties.

The scaling of the particle density with the gradient position can be described by functional equations for the three different particles sizes:
The particle density increases approximately linearly along the 10 mm long gradient and is given by the equation:

- 72 nm: $\delta = 5.9x - 5.4[\mu m^{-2}]$, increase from 0 to 60 particles/ m^2 along 10 mm gradient.
- 39 nm: $\delta = 17.9x - 1[\mu m^{-2}]$, increase from 0 to 150 particles/ m^2 along 10 mm gradient
- 12 nm: $\delta = 99x + 160[\mu m^{-2}]$, increase from 0 to 1300 particles/ m^2 along 10 mm gradient.

where, δ is the particle density and x the position along the gradient in mm.

3.3.2 Protein-adsorption studies

3.3.2.1 Single adsorption of albumin or fibrinogen with low concentration (single BSA/ HPF low)

First the gradients were exposed to a low-concentration solution of 3 g/ml fluorescently labeled albumin or 5 g/ml fluorescently labeled fibrinogen in HEPES 2 buffer for 10 min (single BSA/HPF low).

Line plots of relative intensities measured with the micro-array scanner and averaged over three samples showed that the nano-roughness gradients with 12 nm particles have an influence on albumin and fibrinogen adsorption. For both proteins, the intensity decreases by about 50% on the high-particle-density end of the gradient. A smaller influence of the 39 and 72 nm particles was found for the adsorption behavior of albumin and fibrinogen; the amount of both proteins gradually decreases to approximately 75% at the high-particle-density end of the gradient (Figure 3.2).

Figure 3.2: Relative intensities of albumin (green) and fibrinogen (red) adsorption measured with the microarray scanner. Results from single low concentration protein adsorption (single BSA/HPF low) for 72 nm, 39 nm and 12 nm particle-density gradients. (Mean ± standard deviation, n = 3)

3.3.2.2 Single adsorption of albumin or fibrinogen with high concentration (single BSA/ HPF high)

The next set of experiments was carried out with higher protein concentrations by spiking 1 mg/ml of unlabeled albumin or fibrinogen with 5 g/ml fluorescently labeled albumin or 3 g/ml fluorescently labeled fibrinogen, respectively (single BSA/HPF high). Line plots of relative intensities measured with the micro-array scanner and averaged over six samples showed that the nano-roughness gradients with 12, 39 and 72 nm particles have no significant influence on protein adsorption (Figure 3.3).

Figure 3.3: Relative intensities of albumin (green) and fibrinogen (red) adsorption measured with the microarray scanner. Results from single high-concentration protein adsorption (single BSA/HPF high) for 72 nm, 39 nm and 12 nm particle-density gradients. (Mean ± standard deviation, n = 3)

3.3.2.3 Competitive adsorption of albumin and fibrinogen with high concentration (BSA + HPF high)

Experiments with high protein concentrations for albumin and fibrinogen in competition were carried out by spiking unlabeled albumin (30 mg/ml) and fibrinogen (5 mg/ml) with 5 g/ml fluorescently labeled albumin and 5 g/ml fluorescently labeled fibrinogen (BSA + HPF high). No significant influence of the 12, 39 and 72 nm particles on the adsorption behavior of albumin and fibrinogen in competition for 10 min (Figure 3.4), 30 min and 120 min protein incubation was found (Figure 3.5).

Figure 3.4: Relative intensities of albumin (green) and fibrinogen (red) adsorption measured with the microarray scanner. Results from competitive protein adsorption of albumin and fibrinogen with high-concentration (BSA + HPF high) for 72 nm, 39 nm and 12 nm particle-density gradients. (Mean ± standard deviation, n = 9)

Figure 3.5: Relative intensities of albumin (green) and fibrinogen (red) adsorption measured with the microarray scanner. Averaged results from competitive protein adsorption of albumin and fibrinogen with high-concentration (BSA + HPF high) for 72 nm, 39 nm and 12 nm particle-density gradients. Protein incubation for 10 min ——, 30 min - - - - - and 120 min ·········.

3.3.2.4 Competitive adsorption of albumin, fibrinogen and fibronectin with high concentration (BSA + HPF + FN high)

Adsorption behavior in competition with albumin, fibrinogen and fibronectin was tested by adding 30 g/ml unlabeled fibronectin to the high concentration albumin and fibrinogen solution (BSA + HPF + FN high). No significant influence of the 39 and 72 nm particles was found on the adsorption behavior of albumin, fibrinogen and fibronectin in competition. However, for 12 nm gradients, fibrinogen in competition with albumin and fibronectin, showed an increase of approximately 50% adsorption at the high-particle-density end of the gradient. (Figure 3.6)
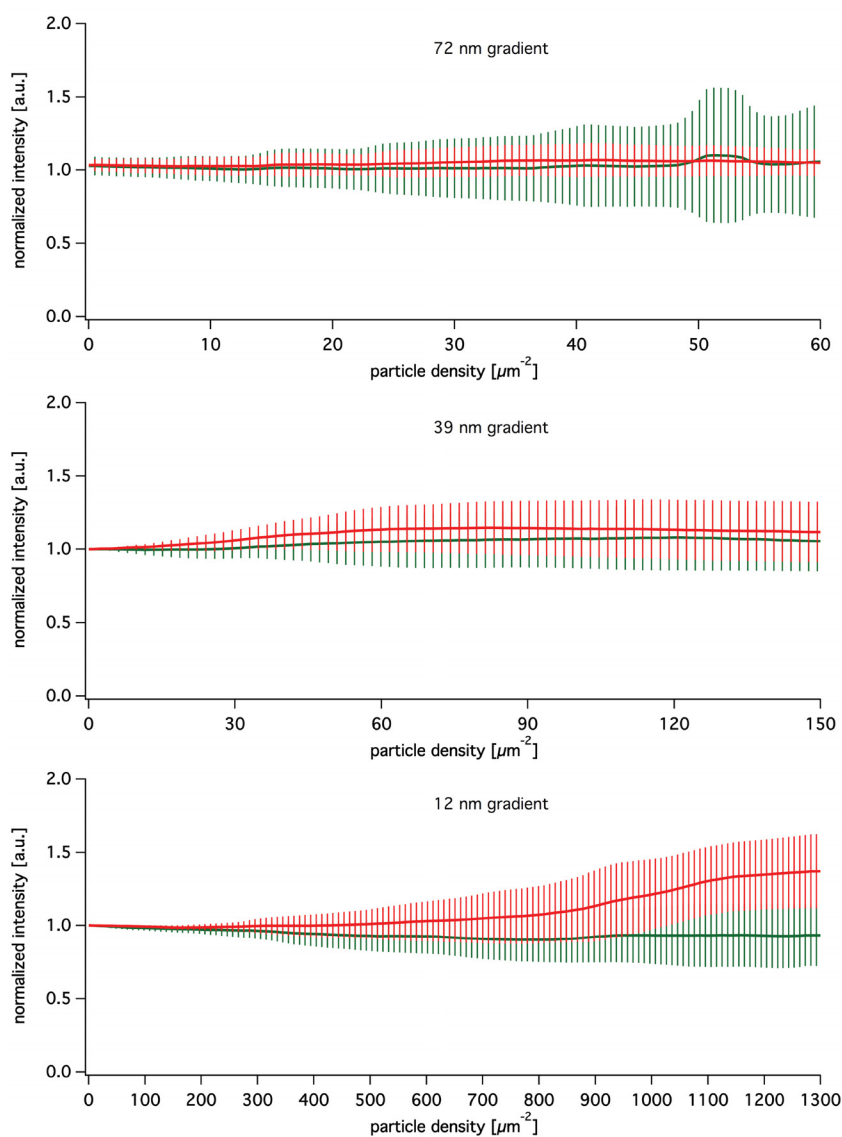
Figure 3.6: Relative intensities of albumin (green) and fibrinogen (red) adsorption measured with the microarray scanner. Results from competitive protein adsorption of albumin, fibrinogen and fibronectin with high-concentration (BSA + HPF + FN high) for 72 nm, 39 nm and 12 nm particle-density gradients. (Mean ± standard deviation, n = 6)

Adsorption experiments with longer incubation times showed that the increase in fibrinogen adsorption on the high-particle density region of the 12 nm gradient levels off with longer incubation times. No significant influence of the 12 nm particle on fibrinogen adsorption was observed after 120 min of incubation.

No change in adsorption behavior of albumin and fibrinogen was detected for longer incubation times (30 and 120 min) on 39 and 72 nm particle-density gradients for albumin, fibrinogen and fibronectin in competition (Figure 3.7).
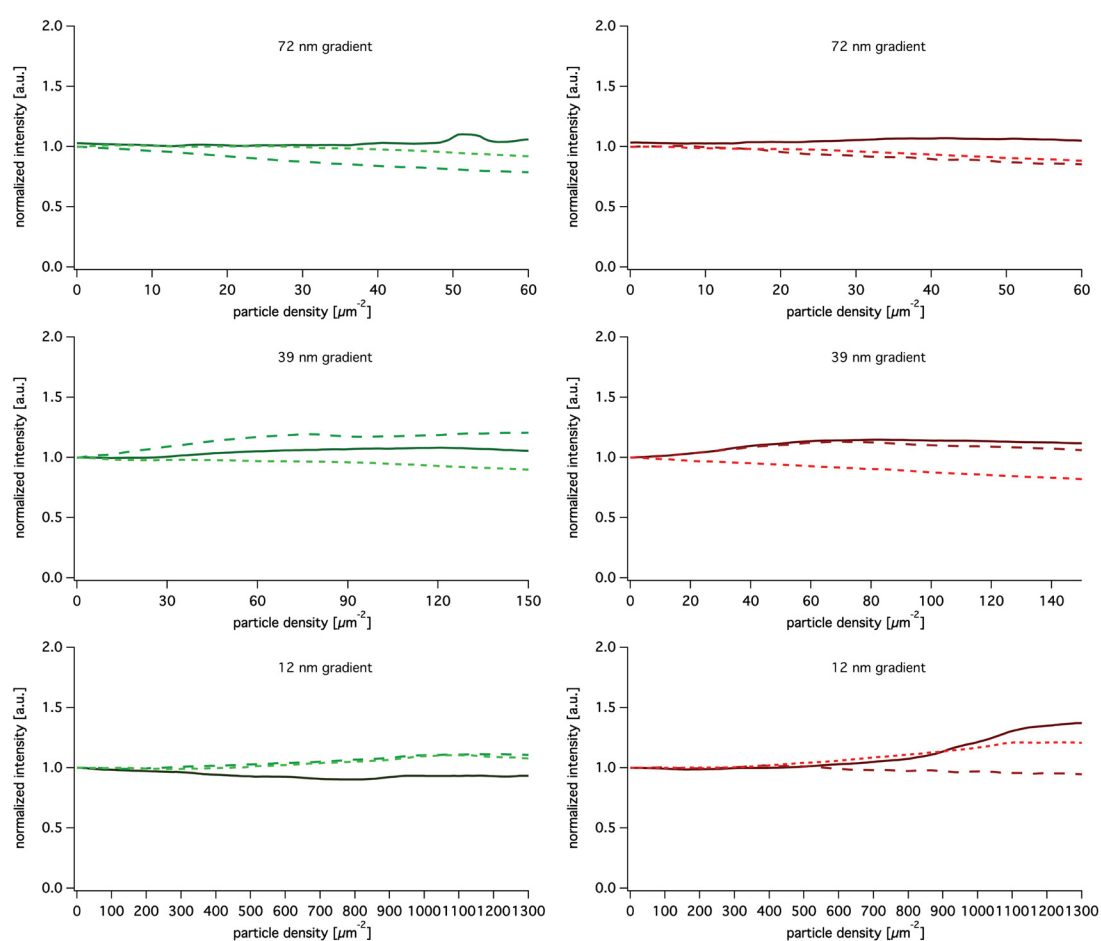
Figure 3.7: Relative intensities of albumin (green) and fibrinogen (red) adsorption measured with the microarray scanner. Averaged results from competitive protein adsorption of albumin, fibrinogen and fibronectin with high-concentration (BSA + HPF + FN high) for 72 nm, 39 nm and 12 nm particle-density gradients. Protein incubation for 10 min ———, 30 min- - - - and 120 min······.

3.3.2.5 Competitive adsorption of albumin and fibrinogen with fetal bovine serum (BSA + HPF in FBS)

To mimic the real physiological situation, experiments were carried out in competition with fetal bovine serum (FBS) by spiking pure FBS with 5 g/ml fluorescently labeled albumin and 5 g/ml fluorescently labeled fibrinogen (BSA + HPF in FBS).

Line plots of relative intensities measured with the microarray scanner and averaged over fifteen samples showed no significant influence of nano-features on protein adsorption for gradients with 39 and 72 nm nanoparticles. On the contrary for 12 nm gradients, the adsorption of fibrinogen in competition with serum increased with increasing particle coverage, and the adsorption was about 2 times higher at the high-particle-density end of the gradient compared to the smooth region. (Figure 3.8)

Spiked serum adsorption experiments with longer incubation times showed that the increase in fibrinogen adsorption on the high-particle density region of the 12 nm gradient levels off with longer incubation times. No significant influence of the 12 nm particle on fibrinogen adsorption was observed after 120 min of incubation. (Figure 3.9)

For 72 nm gradients, an increase in fibrinogen adsorption with higher particle density was found for 30 min incubation but this effect leveled off after 120 min (Figure 3.9).

The same effect was visible for 39 nm gradients, where 10 min protein incubation showed no influence of nanoparticle density on albumin and fibrinogen adsorption, 30 min incubation showed an increase in protein adsorption for both proteins with increasing particle density. But this effect was leveling-off after 120 min (Figure 3.9).
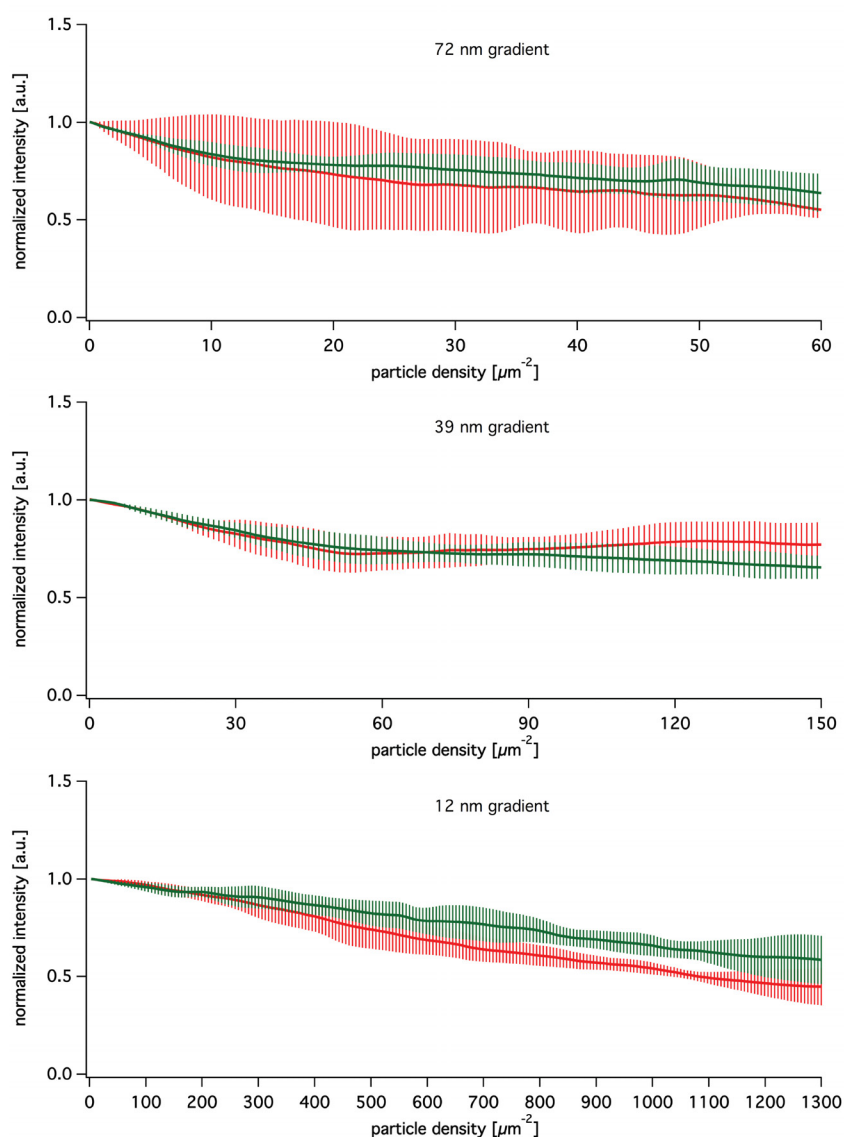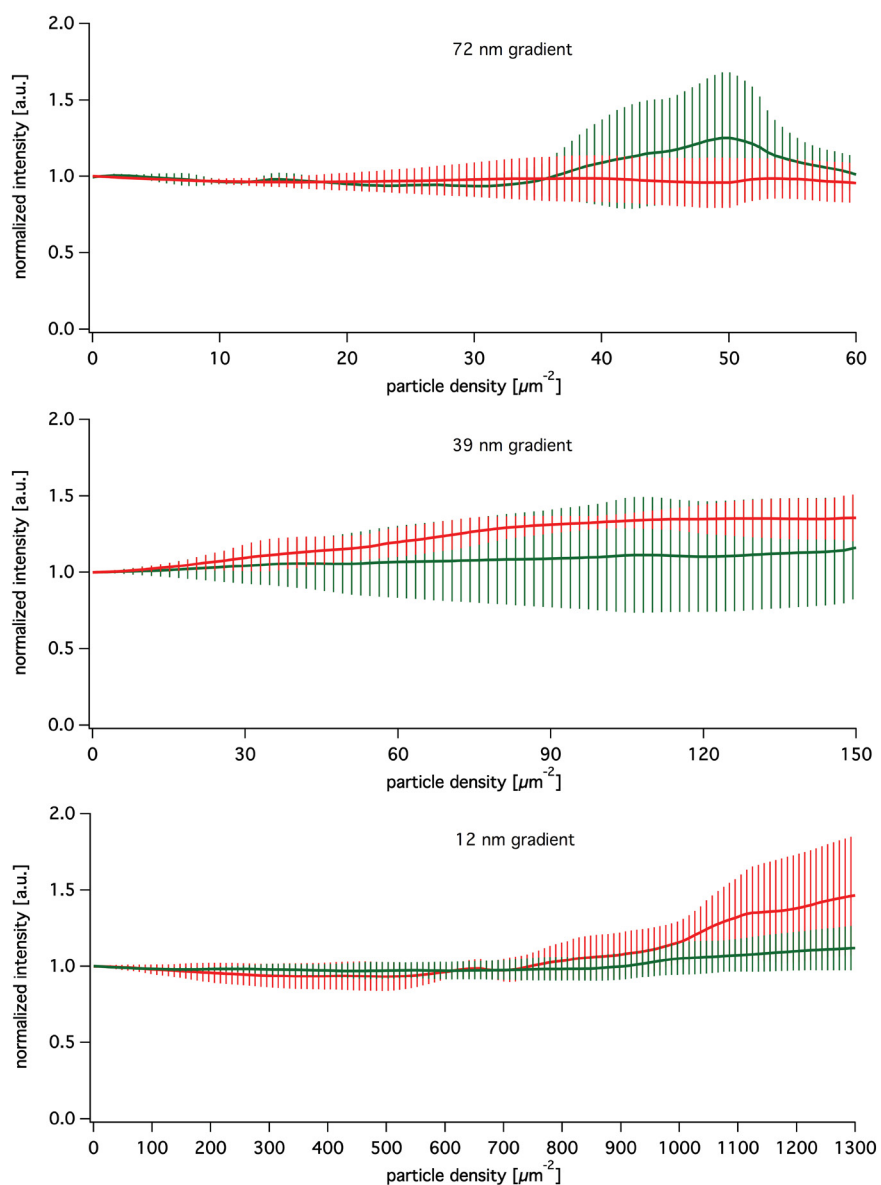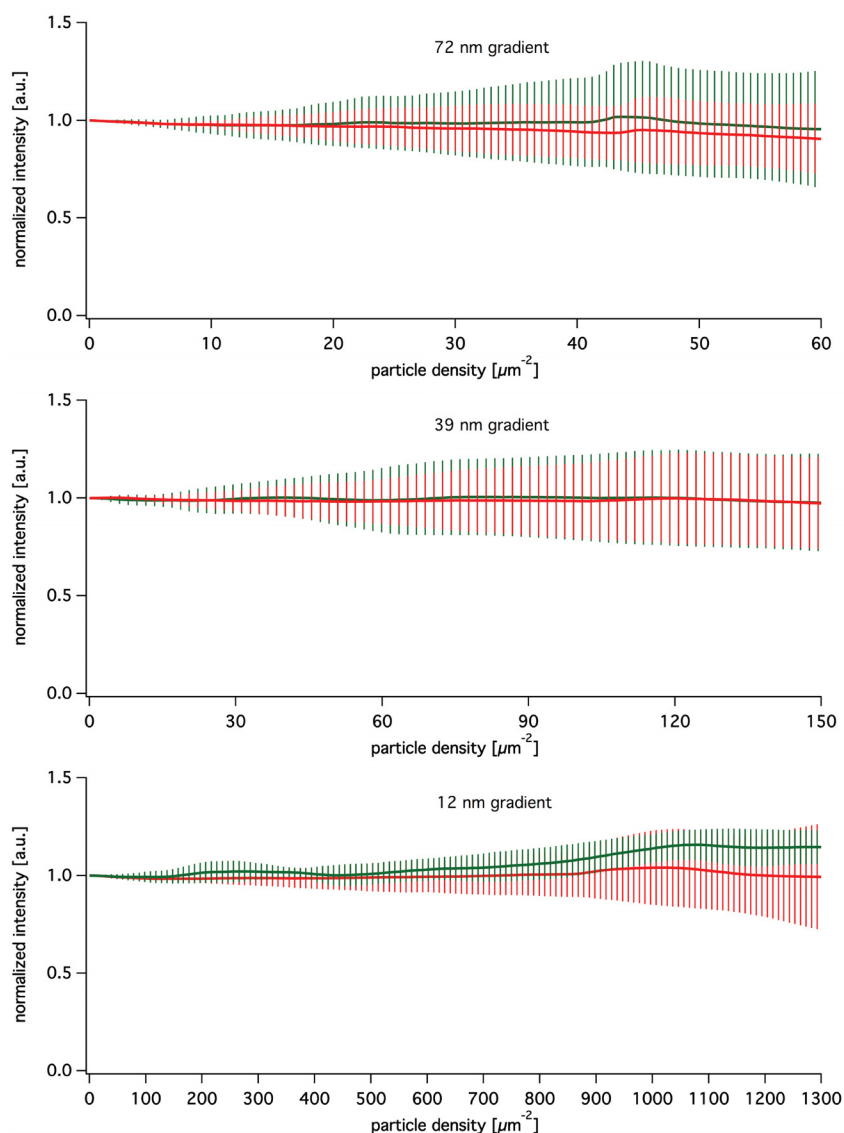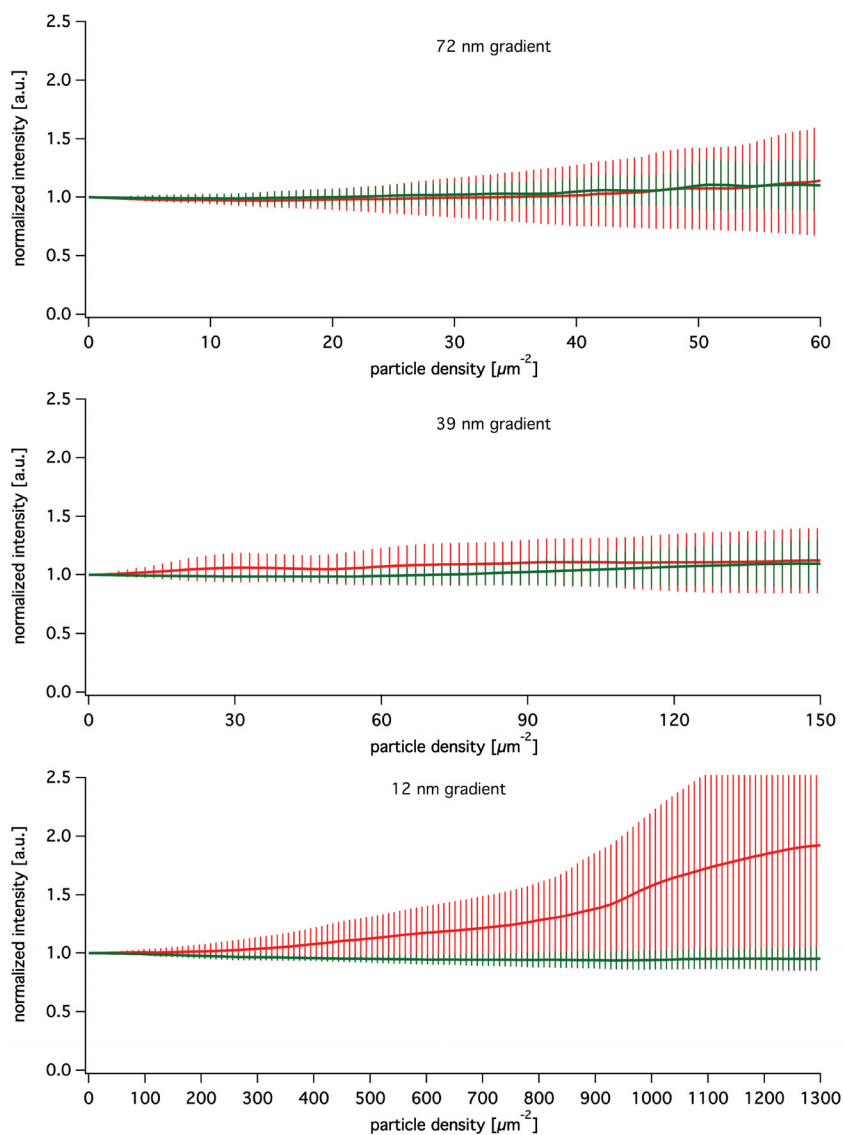
Figure 3.8: Relative intensities of albumin (green) and fibrinogen (red) adsorption measured with the microarray scanner. Results from competitive protein adsorption in fetal bovine serum (BSA + HPF in FBS) for 72 nm, 39 nm and 12 nm particle-density gradients. (Mean ± standard deviation, n = 15)
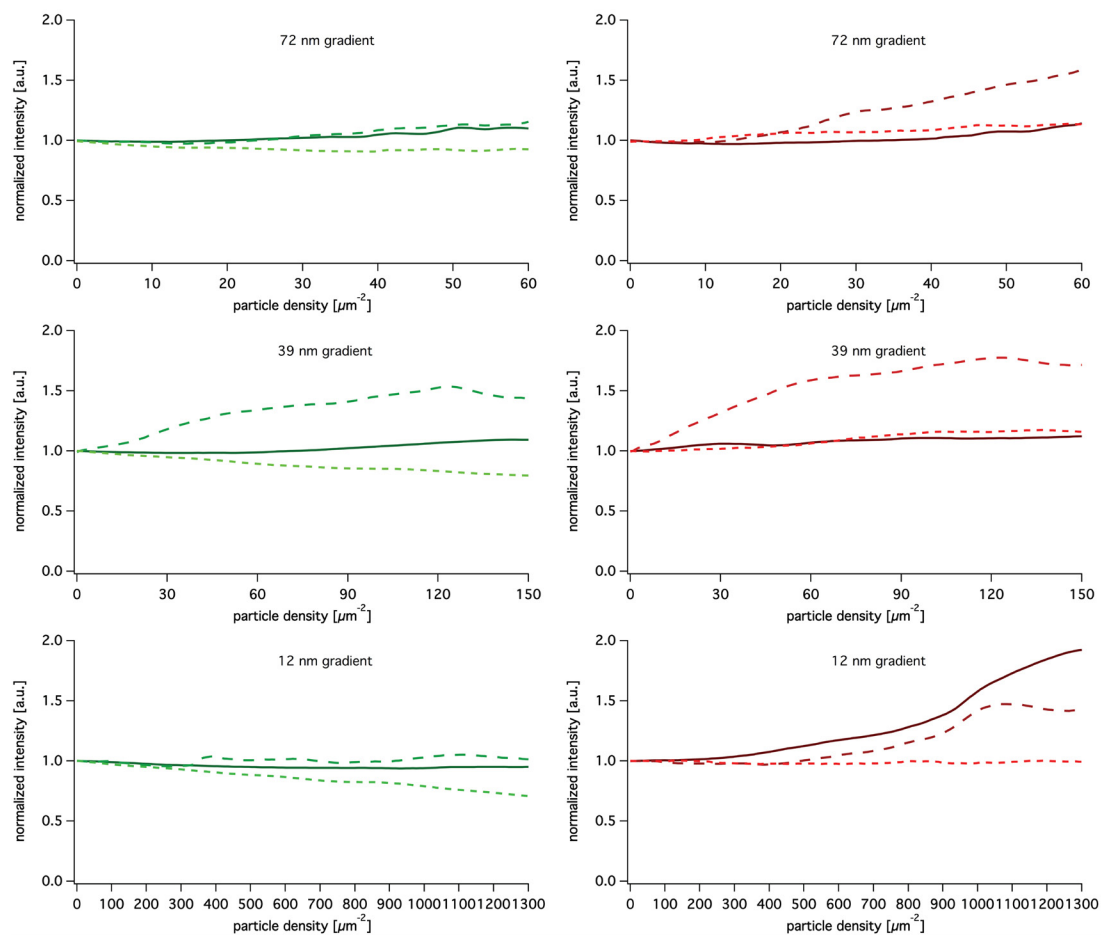
Figure 3.9: Relative intensities of albumin (green) and fibrinogen (red) adsorption measured with the microarray scanner. Averaged results from competitive protein adsorption in fetal bovine serum (BSA + HPF in FBS) for 72 nm, 39 nm and 12 nm particle-density gradients. Protein incubation for 10 min ——— , 30 min - - - - and 120 min ⋯⋯.

3.3.2.6 Summary of nanoparticle-density gradients incubated for 10 min in different protein solutions

In this study the influence of nanoparticle size and density on the adsorption of the blood proteins fibrinogen and albumin was systematically investigated. Figure 3.10 shows the summary of the three nanoparticle-density gradients incubated for 10 min in different protein solutions. Nano-roughness from spherical nanoparticles appears to have only little influence on the amount of protein that adsorbs from solutions; only 12 nm particles seem to influence the adsorption behavior of fibrinogen in competition with albumin, fibrinogen and fibronectin or full serum.
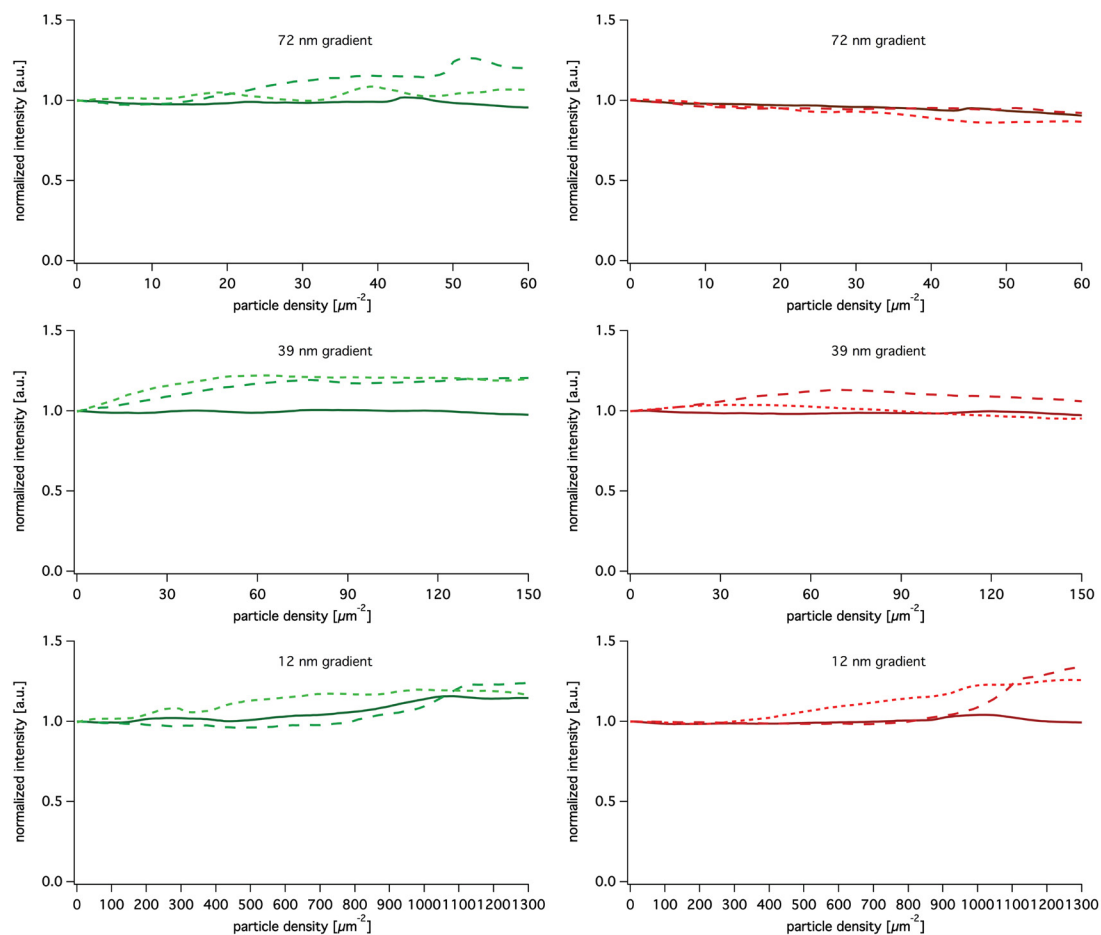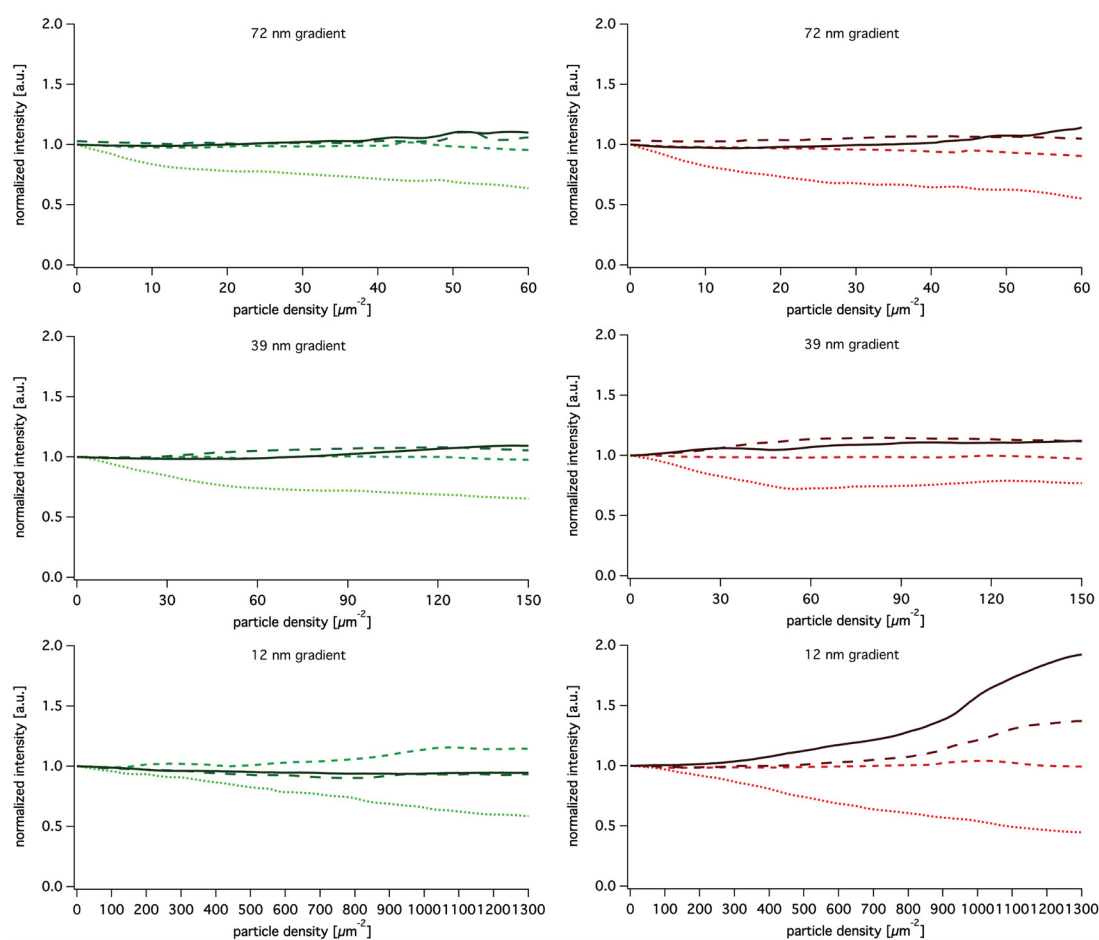

Figure 3.10: Relative intensities of albumin (green) and fibrinogen (red) adsorption measured with the microarray scanner. Averaged results from 10 min protein incubation in different protein solutions: ·········· low concentration single protein adsorption (single BSA/HPF low); - - - - - - - high concentration albumin and fibrinogen in competition (BSA + HPF high); — — — high concentration albumin, fibrinogen and fibronectin in competition (BSA + HPF + FN); ——— spiked - fetal bovine serum (BSA + HPF in FBS); on 12 nm, 39 nm and 72 nm particle-density gradients.

3.4 Discussion

Several aspects need to be considered to discuss the influence of nano-roughness on protein adsorption: First, protein properties such as size, shape, charge and internal stability, play an important role in the outcome of adsorption and secondly, surface properties such as curvature and inter-particle distances can also have an effect. All nanoparticle-density gradients were sputter coated with 6 nm TiO_2, therefore the influence of surface chemistry on protein adsorption on nanoparticle-density gradients can be neglected.

Proteins under investigation were albumin, one of the most abundant proteins in the circulatory system, with a molecular weight of 66 kDa and a heart-shaped structure (14 nm x 4 nm) [11] and fibrinogen, a key structural glycoprotein in the blood clotting process, with a mass of 340 kDa and an elongated shape (47.5 nm x 6 nm) [12]. The proteins differ significantly in their size and shape. Roach *et al.* [13] demonstrated that the rod-like fibrinogen undergoes a multistep adsorption process, as the amount of adsorbed protein increases, the orientation changes from "side on" to "end on" type , while the globular albumin adsorbs in a single stage process (Figure 3.11).
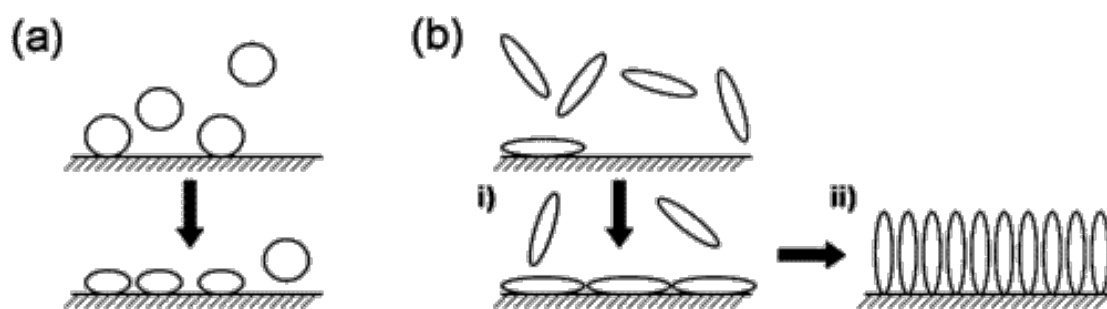
Figure 3.11: Schematic to show adsorption of (a) a globular protein (e.g. albumin), whose conformation can become slightly distorted on surfaces and (b) a rod-like protein (e.g. fibrinogen) that undergoes a multistage adsorption process, where it (i) initially adsorbs with a "side on" orientation and (ii) rearrangement occurs to "end on" orientation to increase protein-protein interaction. Reprinted with permission from [13]. Copyright (2018) American Chemical Society.

In terms of internal stability of protein structures, proteins can be differentiated as "soft" proteins with low thermodynamic stability (e.g. albumin, fibrinogen and immunoglobulin) that undergo structural alterations upon

surface adsorption and adsorb more easily and "hard" proteins (e.g. lysozyme, ribonuclease), which are less prone to unfolding [14].

In another study Roach *et al.* [9] reported that both fibrinogen and albumin undergo greater conformational disordering while adsorbing onto hydrophobic rather than hydrophilic surfaces, but that they react very differently to changes in surface curvature. The native-like conformation of albumin was stabilized by high surface curvature, while a large change in fibrinogen conformation was observed on adsorption on to small particles (radius < 30 nm). An increase in protein-surface interaction can be expected for such a conformational change which probably also hinders surface rearrangement of the protein. A schematic drawing of albumin and fibrinogen orientation and conformation depending on surface curvature can be seen in Figure 3.12.
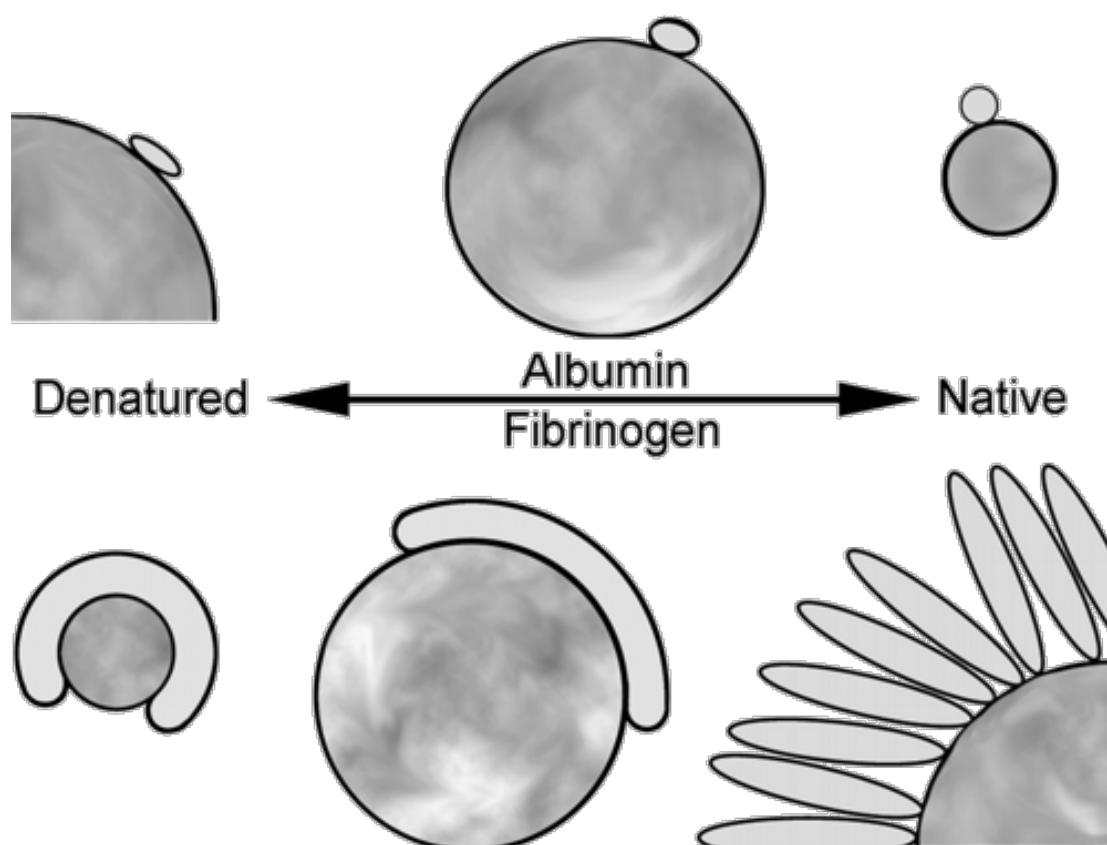
Figure 3.12: Schematic demonstrating control of conformation and orientation of albumin and fibrinogen by surface curvature. Reprinted with permission from [9]. Copyright (2018) AMERICAN CHEMICAL SOCIETY.

It can be assumed that fibrinogen adsorbs in a "side on" orientation on nanoparticles and loses secondary structure to a greater extent when adsorbing onto nanoparticles with high surface curvature. Fibrinogen in the "side on" orientation will occupy more space. Therefore, a decrease in fibrinogen adsorption with increase in nanoparticle density for all three nanoparticle-density gradients can be expected for low concentration single fibrinogen adsorption. (Figure 3.10 single HPF low)

As reported by Roach *et al.* [9] the structure of albumin gets stabilized by high surface curvature, inducing a decrease in protein-surface binding affinity and therefore lowers the probability for adsorption on a high curvature surface. For low concentration single albumin adsorption, a decrease in albumin adsorption with increase in nanoparticle density for all three nanoparticle-density gradients can be expected due to the lower adsorption probability of albumin on nanoparticles. (Figure 3.10 single BSA low)

At low protein concentration, mass transfer from the solution to the surface is slow and individual proteins are able to spread and reach a conformation that minimizes the energy after adsorption, which is leading to a lower coverage. This changes at high protein concentration, the rate of interfacial protein arrival increases, leading to competition for available binding sites on the surface, where no time is left for the individual protein to spread and alter its conformation. This results in a high surface coverage of proteins with low binding strength [15, 16].

For individual adsorption experiments at high protein concentration, the crowding effect obscures that of surface curvature and no significant change in protein adsorption along the particle-density gradients was observed. (Figure 3.3 single BSA/HPF high)

Multiple proteins in blood or serum compete for the surface. Initially small proteins with high mobility diffuse to an interface and rapidly adsorb and are later replaced by less abundant proteins with higher surface affinities [17]. In

1969, Vroman and Adams [18] observed that adsorbed plasma proteins were antibody detectable on Ta-oxide in a time-dependent order, albumin, IgG, fibrinogen, fibronectin, and high-molecular-weight kininogen (HMWK) [19]. Today, the early adsorption of fibrinogen onto negatively charged surfaces (i.e. TiO_2) and its replacement by HMWK and other plasma proteins is named the *Vroman effect* [19].

The *Vroman effect* combined with the findings of Roach *et al.* [9] can explain our observations, where fibrinogen adsorption was increased with an increase in 12 nm particle-density in competition with serum or albumin and fibronectin (Figure 3.10 BSA and HPF in serum; BSA + HPF +FN).

Fibronectin is a relatively big protein with a molecular weight of 450-500 kDa—higher than fibrinogen (340 kDa) [20]—and its high affinity towards titanium surfaces has been previously reported [21, 22]. Following the Vroman sequence, fibrinogen first adsorbs on the gradient, followed by fibronectin and other bigger serum proteins with higher surface affinity that will reach the surface later. In the low-nanoparticle-density regions of the gradient, fibrinogen adsorbs mostly in the "end-on" conformation and can easily be displaced by fibronectin and serum proteins. With higher particle coverage, more fibrinogen adsorbs in a "side-on" orientation in a denatured state, displaying a very high surface affinity and thus being less likely to be displaced by other proteins. At longer incubations times (30 min and 120 min) bigger proteins with higher surface affinity (i.e. fibronectin), have more time to diffuse to the surface and displace fibrinogen from the nanoparticle surface and the effects levels-off (Figure 3.7 and Figure 3.9).

In contrast to fibrinogen adsorbed on 12 nm particles, the surface affinity of fibrinogen adsorbed on 39 nm and 72 nm nanoparticle-density gradients was not high enough to resist the replacement by other proteins, most probably because the loss in native conformation is more pronounced for fibrinogen on substrates with a radius smaller than 20 nm on hydrophilic surfaces. Roach *et al.* [9] showed that fibrinogen displays a greater degree of structural change on

smaller spheres (radius < 20 nm), losing about 12% helical structure at the expense of an increasing random chain component (Figure 3.13c). With increasing radius, the variation in fibrinogen conformation decreases. With radii above 30 nm only little variation in fibrinogen conformation was seen.
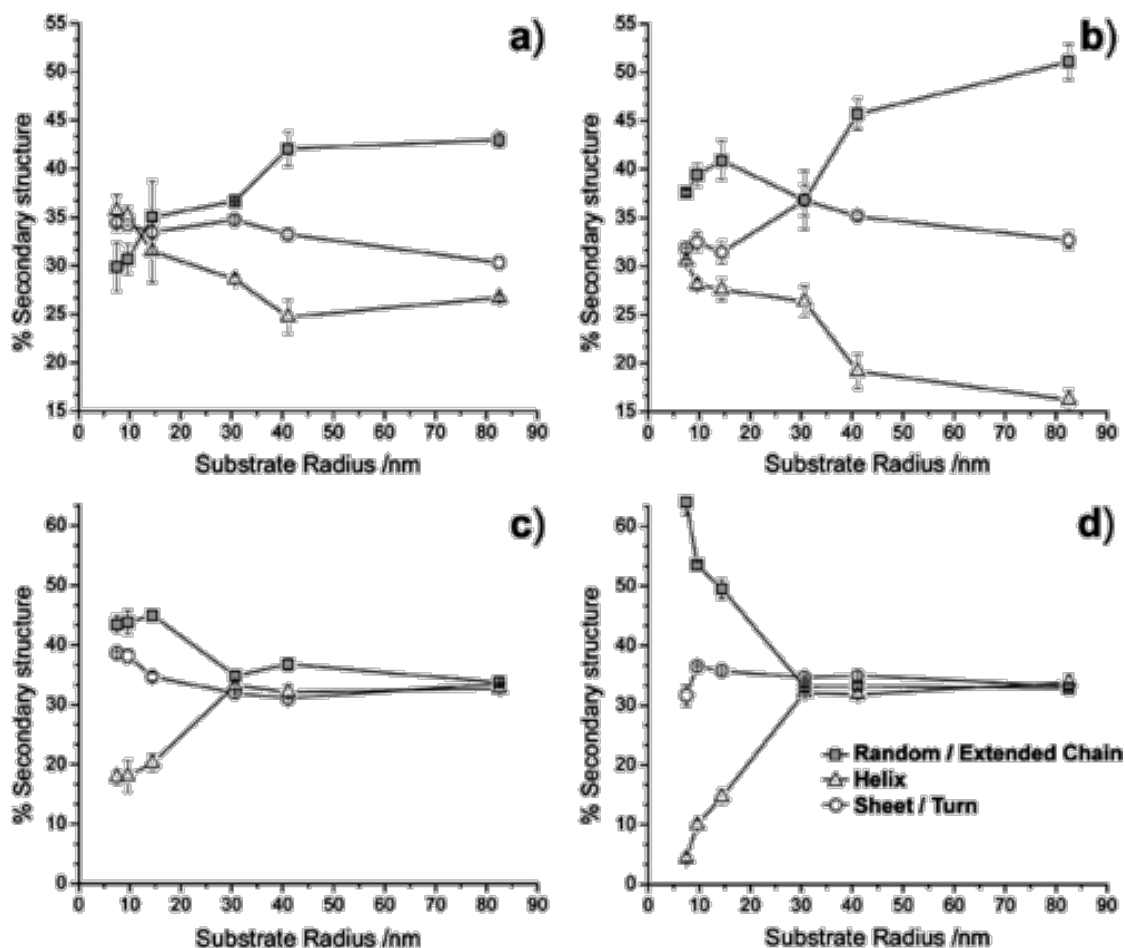
Figure 3.13: Conformational assessment of surface-bound BSA (a) and (b); fibrinogen (c) and (d) onto hydrophilic (a) and (c); and hydrophobic (b) and (d) substrates. Random coil/extended chain structure −□−; α-helix −△−; β-sheet/β-turn −○−. Reprinted with permission from [9]. Copyright (2018) American Chemical Society.

3.5 Conclusion

By using nanoparticle-density gradients and a fluorescence microarray scanner for analysis an easy and fast method was used to study protein-adsorption on surfaces with varying nano-roughness Nano-roughness from spherical nanoparticles appears to have only little influence on the amount of protein that adsorbs from solutions; only 12 nm particles seem to influence the adsorption behavior of fibrinogen in competition with albumin, fibrinogen and fibronectin or full serum.

On 12 nm gradients, the adsorption of fibrinogen in competition with serum increased with increasing particle coverage. At the high-particle-density end of the gradient (1300 particles/ m²) fibrinogen adsorption increased by about 200% compared to the smooth region. This cannot be explained by the effect of increased surface area as the results were corrected for this effect. It is suggested that the increase in fibrinogen adsorption is a consequence of the *Vroman effect* and the particle surface curvature induced "side on" adsorption of the fibrinogen in a denatured state. The denatured fibrinogen displays a very high surface affinity and is thus less likely to be displaced by other proteins that follow the *Vroman sequence*.

References:

[1] M.S. Lord, M. Foss, F. Besenbacher, Influence of nanoscale surface topography on protein adsorption and cellular response, Nano Today 5(1) (2010) 66-78.

[2] D.S. Sutherland, M. Broberg, H. Nygren, B. Kasemo, Influence of Nanoscale Surface Topography and Chemistry on the Functional Behaviour of an Adsorbed Model Macromolecule, Macromolecular bioscience 1(6) (2001) 270-273.

[3] P. Koegler, A. Clayton, H. Thissen, G.N.C. Santos, P. Kingshott, The influence of nanostructured materials on biointerfacial interactions, Advanced Drug Delivery Reviews 64(15) (2012) 1820-1839.

[4] K. Cai, J. Bossert, K.D. Jandt, Does the nanometre scale topography of titanium influence protein adsorption and cell proliferation?, Colloids and surfaces. B, Biointerfaces 49(2) (2006) 136-44.

[5] F.A. Denis, P. Hanarp, D.S. Sutherland, J. Gold, C. Mustin, P.G. Rouxhet, Y.F. Dufrêne, Protein Adsorption on Model Surfaces with Controlled Nanotopography and Chemistry, Langmuir 18(3) (2002) 819-828.

[6] G.P. Rockwell, L.B. Lohstreter, J.R. Dahn, Fibrinogen and albumin adsorption on titanium nanoroughness gradients, Colloids and Surfaces B: Biointerfaces 91(0) (2012) 90-96.

[7] K. Rechendorff, M.B. Hovgaard, M. Foss, V.P. Zhdanov, F. Besenbacher, Enhancement of Protein Adsorption Induced by Surface Roughness, Langmuir 22(26) (2006) 10885-10888.

[8] H. Meltzer, A. Silberberg, Adsorption of collagen, serum albumin, and fibronectin to glass and to each other, Journal of Colloid and Interface Science 126(1) (1988) 292-303.

[9] P. Roach, D. Farrar, C.C. Perry, Surface Tailoring for Controlled Protein Adsorption: Effect of Topography at the Nanometer Scale and Chemistry, Journal of the American Chemical Society 128(12) (2006) 3939-3945.

[10] M.S. Lord, B.G. Cousins, P.J. Doherty, J.M. Whitelock, A. Simmons, R.L. Williams, B.K. Milthorpe, The effect of silica nanoparticulate coatings on serum protein adsorption and cellular response, Biomaterials 27(28) (2006) 4856-4862.

[11] D.C. Carter, J.X. Ho, Structure of Serum Albumin, in: C.B. Anfinsen, J.T. Edsall, F.M. Richards, D.S. Eisenberg (Eds.), Advances in Protein Chemistry, Academic Press1994, pp. 153-203.

[12] C.E. Hall, H.S. Slayter, The Fibrinogen Molecule: Its Size, Shape, and Mode of Polymerization, The Journal of Biophysical and Biochemical Cytology 5(1) (1959) 11-27.

[13] P. Roach, D. Farrar, C.C. Perry, Interpretation of Protein Adsorption: Surface-Induced Conformational Changes, Journal of the American Chemical Society 127(22) (2005) 8168-8173.

[14] T.A. Horbett, B.D. Ratner, J.M. Schakenraad, F.J. Schoen, CHAPTER 3 - Some Background Concepts, Biomaterials Science, Academic Press, San Diego, 1996, pp. 133-164.

[15] E.A. Vogler, Protein adsorption in three dimensions, Biomaterials 33(5) (2012) 1201-1237.

[16] C.F. Wertz, M.M. Santore, Effect of Surface Hydrophobicity on Adsorption and Relaxation Kinetics of Albumin and Fibrinogen: Single-Species and Competitive Behavior, Langmuir 17(10) (2001) 3006-3016.

[17] M.C.D. R.J. Green, C.J. Roberts, S.J.B. Tendler, Competitive protein adsorption as observed by surface plasmon resonance, Biomaterials 20 (1999) 385—391.

[18] L. Vroman, A.L. Adams, Findings with the recording ellipsometer suggesting rapid exchange of specific plasma proteins at liquid/solid interfaces, Surface Science 16 (1969) 438-446.

[19] P. Tengvall, 4.6 Protein Interactions With Biomaterials, Comprehensive Biomaterials II, Elsevier, Oxford, 2017, pp. 70-84.

[20] M. Pegueroles, C. Tonda-Turo, J.A. Planell, F.J. Gil, C. Aparicio, Adsorption of fibronectin, fibrinogen, and albumin on TiO_2: time-resolved kinetics, structural changes, and competition study, Biointerphases 7(1-4) (2012) 48.

[21] D.E. MacDonald, B. Markovic, A.L. Boskey, P. Somasundaran, Physico-chemical properties of human plasma fibronectin binding to well characterized titanium dioxide, Colloids and Surfaces B: Biointerfaces 11(3) (1998) 131-139.

[22] S.R. Sousa, P. Moradas-Ferreira, M.A. Barbosa, TiO_2 type influences fibronectin adsorption, Journal of Materials Science: Materials in Medicine 16(12) (2005) 1173-1178.

Chapter 4

Blood-interaction studies on nanoparticle-density gradients

4.1 Introduction

Blood is the first medium that comes into contact with a bone implant, due to the vascular nature of bone. Clot formation, as well as the migration and differentiation of osteogenic cells into the healing compartment, may be influenced by the initial interactions of blood with the implant [1]. It has therefore been suggested that an understanding of the initial blood-implant surface interactions is crucial for the understanding of peri-implant healing and may lead to improved design strategies for bone implants [1, 2].

In an event of injury, the blood coagulation cascade gets activated to prevent blood loss, however the coagulation cascade can also be activated by contact with foreign surfaces. For a blood-contacting biomaterial like a vascular stent or prosthetic heart valves, thrombosis can have fatal consequences, while for osseous implant surfaces, a strong thrombogenic response is regarded as a crucial step in implant healing and is therefore often desired [2-4]. After implantation, rapid adsorption of plasma proteins occurs on the foreign material surface, which leads to platelet adhesion and triggers the coagulation of blood leading to thrombus formation [5].

Platelets are the first reactive blood cells to arrive at the implant interface after protein adsorption [6]. When the platelets get activated, they change shape from round spheres, to irregular spheres with spiny pseudopods, to a fully

spread state [7]. The activated platelets will then generate thrombin, initiating the thrombin-mediated conversion of fibrinogen to fibrin and the formation of a fibrin network/clot [8]. Platelets respond to proteins (e.g. fibrinogen, fibronectin, vitronectin, and von Willebrand factor) adsorbed on a biomaterial surface through binding to integrins. Surface-bound fibrinogen is by far the most important protein in mediating platelet adhesion and activation. It possesses three pairs of platelet binding sites, the RGDF sequence at Aα 95-98, the RGDS sequence at Aα 572-575 and the γ-chain dodecapeptide at γ 400-411 [9].

Whole blood has been shown to react differently to surfaces with different surface chemistries [6, 10] and topographies [11-13]. Platelet adhesion was more extensively studied from platelet-rich plasma (PRP). Recent publications have shown that a variety of nanostructures can indeed influence the degree of platelet adhesion and activation. Hulander *et al.* [14] studied the effect of surface nanotopography on the adhesion and activation of human platelets in vitro using nanoparticle-density gradients made by adsorbing gold nanoparticles with a diameter of 36 or 56 nm on smooth gold substrates. According to those authors, the activation of platelets correlates inversely with particle coverage; the highest number of activated platelets was found on the smooth control surface. The effect was more prominent on particle gradients with 56 nm than on 36 nm gold particles. Sutherland *et al.* [15] reported that fibrinogen bound to topographically structured surfaces (10 nm deep pits with 40 nm diameter) binds platelets significantly faster than fibrinogen bound to flat surfaces. Koh *et al.* [16] suggested that high aspect ratio nanostructures (> 3:1) with a small interspacing (< 200 nm) on poly-(lactic-co-glycolic-acid) (PLGA) films significantly reduce platelet activation, Stavridi *et al.* [17] reported that patterning poly(caprolactone) (PCL) with grooves (depth = 190 nm, width = 450 nm and ridge = 1000 nm) increases platelet adhesion and induces faster coagulation compared to smooth PCL samples. At this stage it is difficult to see a general trend for the influence of nanotopography on platelet adhesion and activation as the parameters varied have included aspect ratio, height, width and separation of nanofeatures.

In this study nanoparticle-density gradients as described in Section 2.2 were used to systematically investigate how size and spacing of nanoparticles influence the process of blood coagulation.

4.2 Experimental

Blood incubation studies have been carried out using a protocol previously established and reported by Brigitte S. Kopf [18].

4.2.1 Partially heparinized whole human blood

9 ml S-Monovette tubes (neutral S-Monovette®, Sarstedt, Switzerland) with 3 IU/ml sodium heparin (180 IU/mg; Carl Roth, Karlsruhe, Germany) were used for withdrawal of whole human blood from healthy volunteers (ethical approval was obtained from the ethics committee in St.Gallen; BASEC Nr. PB_2016-00816), resulting in a final concentration of 0.5 IU heparin/ml blood. Blood samples were kept at room temperature and used within 15 min after withdrawal.

4.2.2 Blood incubation of gradient samples in a teflon model

Before use, the nanoparticle-density gradients were cleaned in the oxygen plasma cleaner (PDC-32G) for 2 min to remove hydrocarbon contamination and to get a clean, hydrophilic TiO_2 surface.

Two custom-made polytetrafluoroethylene (PTFE, Teflon) devices were designed for the blood-incubation experiment. For experiments with one gradient, a round chamber with inner diameter of 50 mm and 4 mm height, containing a square cavity with a size of 26 mm and height of 0.7 mm was built. 7.8 ml of blood was added to the chamber and immediately closed with a PTFE lid, sealed with parafilm and placed on a wave shaker (Polymax, Heidolph®,

Germany) at 10 rpm and 37 °C. Three samples of the same nanoparticle size of nanoparticle-density gradients were incubated in three separate devices with blood from the same donor for 2, 5 and 7 min.

In order to be able to test the three different nanoparticle-sized gradients with blood from the same donor, a second incubation chamber was designed with a rectangular geometry with three separate inlets with a volume of 3 mL containing a square cavity with a size of 26 mm and height of 0.7 mm (see Figure 4.1). The inlets of the chamber were filled with 3 ml of blood, closed with a PTFE lid, sealed with parafilm and placed on a wave shaker (Polymax, Heidolph®, Germany) at 10 rpm and 37 °C. 72, 39 and 12 nm sized nanoparticle-density gradients were placed in the separate inlets of the same chamber and incubated with blood from the same donor for 2, 5 and 7 min.
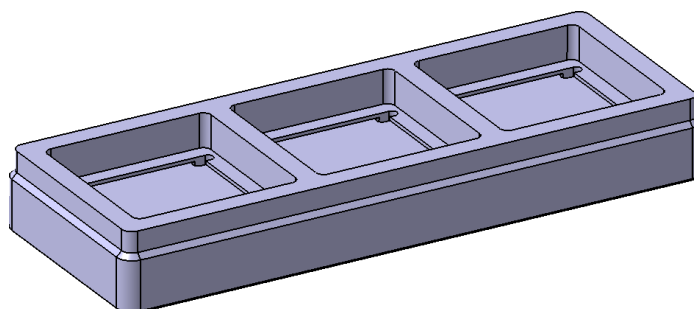
Figure 4.1: Schematic of the sample holder for simultaneous blood incubation of three gradient samples.

After incubation, the blood was carefully removed and the gradients were rinsed gently 4 times in pre-warmed phosphate-buffered saline (PBS, Sigma) before SEM preparation. Each experiment was carried out at least three times using blood from different donors.

4.2.3 SEM preparation

Samples were fixed in Karnovsky solution (4 g paraformaldehyde, 50 ml aqua bidest, 5 ml glutaraldehyde 50%, 45 ml PBS without glucose, pH 7.4) for 1 h at room temperature. The samples were dehydrated through an ethanol series with ethanol solution of 50%, 70% and 80% for 30 min each and 90% and 100% for

60 min each, followed by immersion in hexamethyldisilazane (HMDS, Sigma) for 30 min. Finally, samples were transferred into a new 6-well plate and left to dry overnight in air at room temperature under a hood. On the next day, samples were sputter-coated with 10 nm gold-platinum (high-vacuum coater Leica EM ACE 600, Switzerland). The blood-incubated gradient samples were analyzed by scanning electron microscopy (SEM) (LEO 1530, Zeiss, Germany) by taking SEM pictures every 2 mm along the gradient with an acceleration voltage of 3 kV with the in-lens detector.

4.3 Results

Whole human blood samples drawn from voluntary donors were used to study the adsorption of blood components on the three nanoparticle-density gradients.

First experiments carried out with 12, 39 and 72 nm particle-density gradients incubated for 10 min in whole human blood, showed promising results where an influence of the particle density on blood coagulation was seen (Figure 4.2). For 39 nm particle-density gradients, a higher density of fibrin clots and activated platelets could be found on the high-density end of the gradient (Figure 4.2b). Figure 4.2a) and c) showed that there is no significant influence of the 72 and 12 nm particle-density gradient on blood coagulation.

Repetitions with blood from other voluntary donors showed a different blood clotting speed and made it difficult to compare results from different experiments. In Figure 4.3 SEM images along a 12 nm particle-density gradient following a 10 min blood incubation experiment are presented. There was no clear tendency of a change in appearance of the blood clot along the gradient. This was due to the formation of a very dense blood clot where a lot of red blood cells were incorporated. The occurrence of very dense blood clots made it impossible to see differences in blood clotting behavior as the interface between blood clot and nanoparticle surface was not accessible by microscopy.
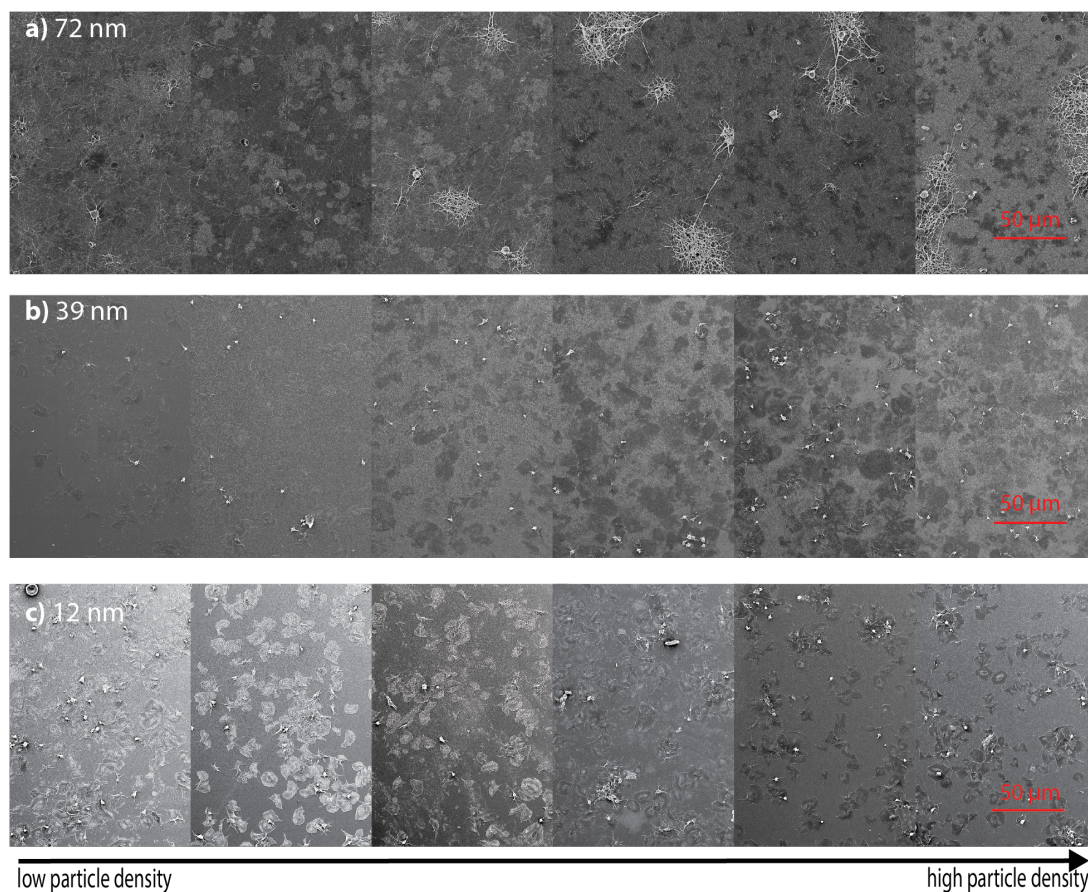
Figure 4.2: SEM images taken every 2 mm along the a) 12 nm, b) 39 nm and c) 72 nm nanoparticle-density gradient after blood incubation for 10 min.
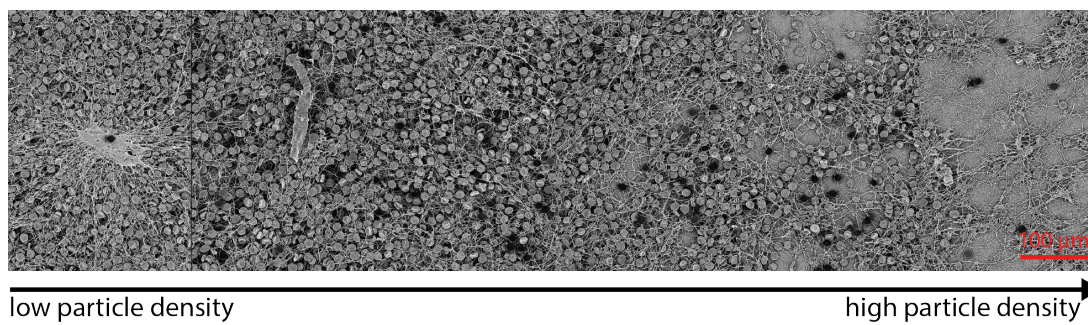
Figure 4.3: SEM images taken every 2 mm along a 12 nm nanoparticle density gradient after blood incubation for 10 min.

In order to avoid dense blood clots, shorter incubation times were used. In Figure 4.4, SEM images along a 39 nm nanoparticle density gradient following a 5 min blood-incubation experiment are presented. It can be seen clearly that the appearance of the blood clot changed along the particle-density gradient. While coagulation was observed everywhere on the sample, a denser fibrin network could be detected towards the high-density end of the gradient. The longer incubation for 7 min (Figure 4.4) led to a denser fibrin network with no visible activated platelets; no significant differences along the gradient were observed. On the other hand, the SEM images from the shorter incubation time of 2 min (Figure 4.4) showed activated platelets with only a few fibrin spots along the gradient.
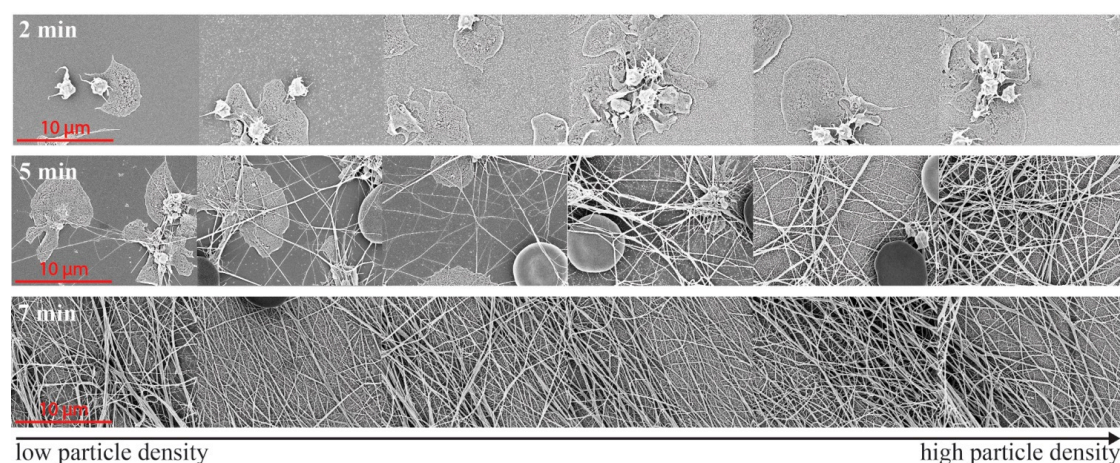
Figure 4.4: SEM images taken every 2 mm along 39 nm nanoparticle-density gradients. Gradients after incubation for 2 min, 5 min and 7 min with whole human blood.

The trend was also visible with the naked eye; Figure 4.5 shows photographs of the blood clot after preparation for SEM (before sputtering). After 2 min of blood incubation no blot clot was visible, while after 5 min a dense fibrin network was observed at the high-density end of the gradient; the fibrin network becoming thinner with decreasing particle-density on the gradient. 7 min post blood incubation, a dense fibrin network was observed over the entire gradient.
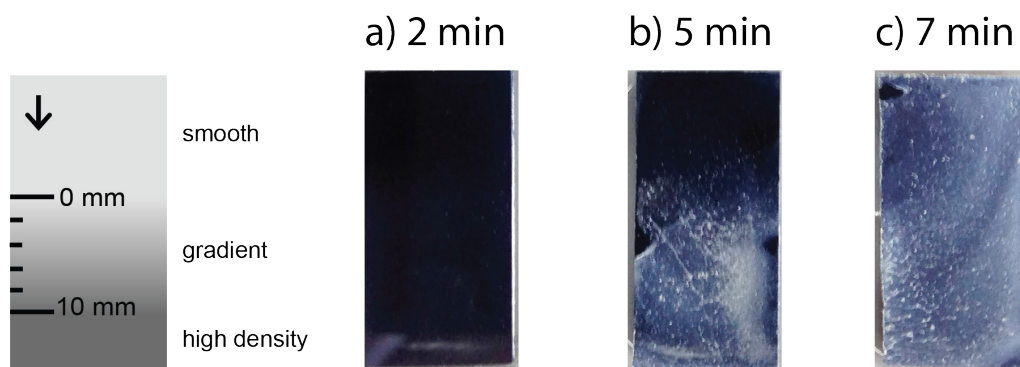
Figure 4.5: Photographs of dried blood clot on 39 nm particle-density gradients after incubation with whole human blood for a) 2 min, b) 5 min and c) 7 min.

Several repetitions with blood from different donors have been carried out to verify these results. Figure 4.6 and Figure 4.7 show the results from different donors on 39 nm particle-density gradients, a similar trend like in Figure 4.4 where a denser fibrin network could be detected towards the high-density end of the gradient was found, but the fibrin network formation started at a later time point (7 min).
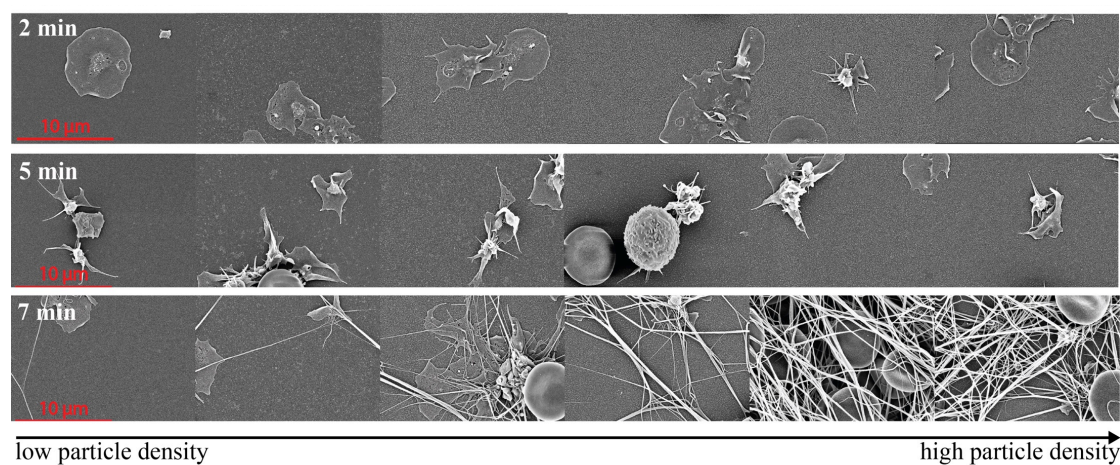
Figure 4.6: SEM images taken every 2 mm along 39 nm nanoparticle-density gradients. Gradients after incubation for 2 min, 5 min and 7 min with whole human blood

low particle density   high particle density
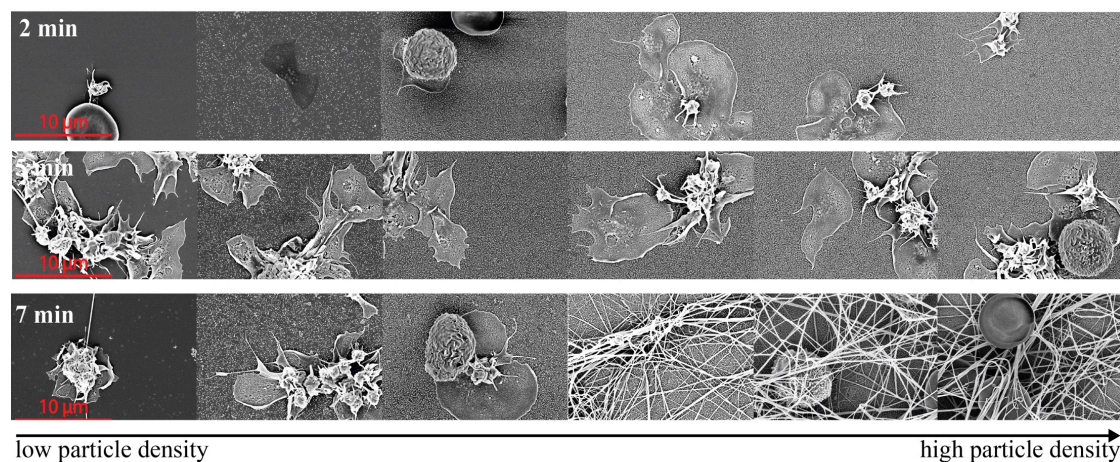
Figure 4.7: SEM images taken every 2 mm along 39 nm nanoparticle-density gradients. Gradients after incubation for 2 min, 5 min and 7 min with whole human blood.

Blood incubation of 72 and 12 nm particle-density gradients for 2, 5 and 7 min showed no significant influence of 72 nm (Figure 4.8) and 12 nm (Figure 4.9) particles on blood coagulation. Two repetitions for each nanoparticle size with blood from different donors led to the same observations (results not shown).

low particle density   high particle density
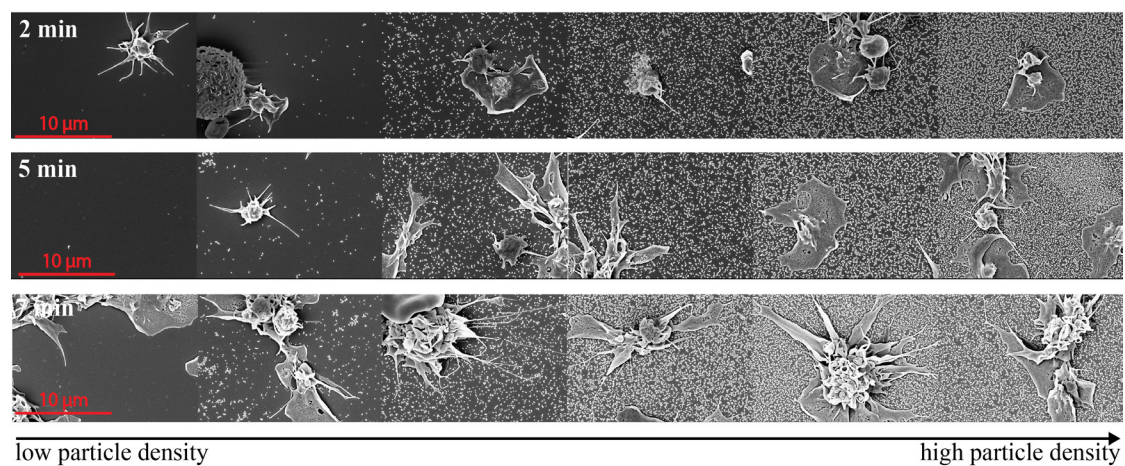
Figure 4.8: SEM images taken every 2 mm along 72 nm nanoparticle-density gradients. Gradients after incubation for 2 min, 5 min and 7 min with whole human blood.

low particle density   high particle density
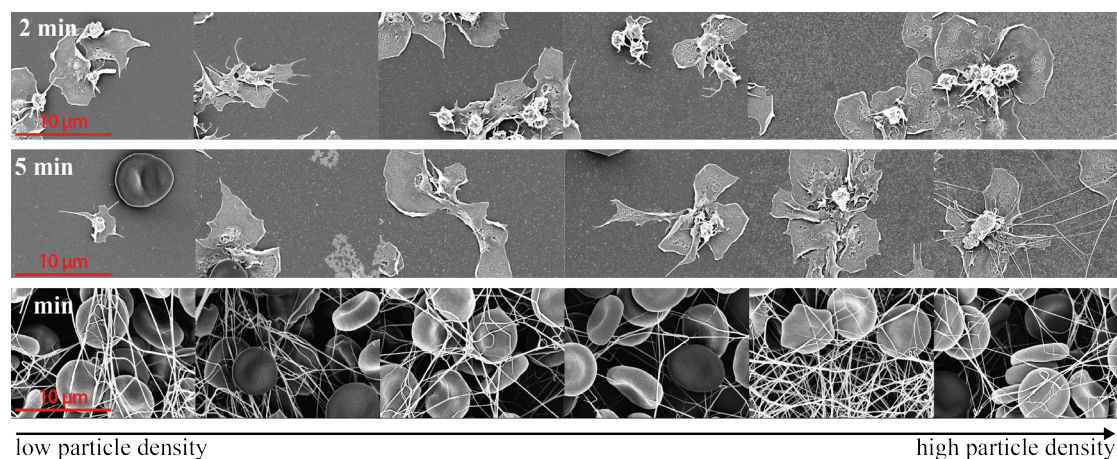
Figure 4.9: SEM images taken every 2 mm along the 12 nm nanoparticle-density gradient. Gradient after incubation for 12 min, 16 min and 20 min with platelets-enriched plasma.

4.4 Discussion and Conclusions

The main finding in this study was that nanostructures with a size of 39 nm seem to enhance blood coagulation. With an increase in 39 nm particle-density a faster fibrin network formation was visible, while smaller (12 nm) and bigger (72 nm) nanoparticles did not seem to influence the activation of platelets and the fibrin network formation.

Hulander *et al.* [14] reported that platelets respond differently to surfaces with a gradient in gold nanoparticle density. Spreading of the platelets was attenuated to a higher degree on surfaces with 56 nm particles than on surfaces with 36 nm particles. In contrast to our results they found that platelet activation decreased with increasing particle coverage for 56 nm particles and that 36 nm particles showed little or no effect. But based on their observations they also suggest that platelet adhesion and activation on nanostructured surfaces may depend more on the amount of available fibrinogen for the platelets than on the amount of adsorbed fibrinogen. They suggest that the relevant surface property for platelet response on nanostructured surfaces is the ratio of particle-height/inter-particle-distance. Fibrinogen adsorbed on top of nanoparticles is likely accessible for platelets, but a certain flexibility of the cell membrane would be necessary for integrins in the platelet membrane to reach and bind fibrinogen

located on the substrate surface between the particles. Platelets seeded on densely packed 56 nm particles were not able to reach the fibrinogen adsorbed on the substrate surface between the particles (Figure 4.10 a), while platelets on densely packed 36 nm particles showed a firm contact with the substrate surface (Figure 4.10 b). The firm contact with the substrate seemed to induce activation and flattening of the platelets.
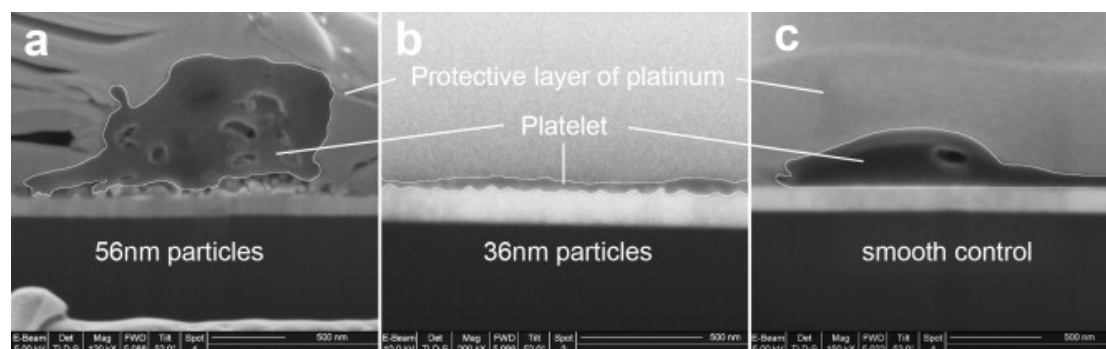
Figure 4.10: FIB-SEM sections analyzing the cell-substrate interface. a) Platelet seeded on surface with high density of 56 nm nanoparticles. The cell membrane is obstructed from reaching the area between the particles. b) When seeded on 36 nm nanoparticles the cell membrane can make contact with the surface between the particles. c) Platelet on smooth surface with a large cell-substrate contact. Reprinted from [14], Copyright (2018), with permission from Elsevier.

The change in accessibility of adsorbed fibrinogen for platelets due to the ratio of particle-height/inter-particle-distance alone cannot explain the findings in this study, where small (12 nm) and big (72 nm) nanoparticles did not seem to influence the activation of platelets and the fibrin network formation, while 39 nm particles did.

In Chapter 3 the influence of nanoparticle size and density on protein adsorption was investigated, an increase in the amount of adsorbed fibrinogen with increasing surface coverage of 12 nm particles along the gradient when fibrinogen was adsorbed in competition with fibronectin or full serum was found. This influence could not be found for 39 and 72 nm particle-density gradients. Fibrinogen was reported to be the key plasma protein mediating platelet adhesion [9], thus it was intuitively expected that the 12 nm particle-density gradients would show a bigger influence on platelet activation than 39 or 72 nm gradients. This finding might indicate that platelet adhesion and

activation on nanostructured surfaces may not only be dependent on the amount and accessibility of adsorbed fibrinogen, but also on the conformation of the fibrinogen and the amount of available binding sites for platelets.

The specific mechanism that mediates platelet adhesion to adsorbed fibrinogen is not fully understood. Recent publications cited that the amount of adsorbed fibrinogen is one of the most important factors for platelet activation [16, 19, 20], while others have found evidence that the conformational state of adsorbed fibrinogen may actually be more important for mediation of platelet response [21-26].

Further experiments are needed in order to gain insight if 39 nm particles induce a change in fibrinogen conformation that lead to an increase in platelet binding-site availability and therefore explain the enhanced blood coagulation that was found.

References:

[1] D.J. Park JY, Red blood cell and platelet interactions with titanium implant surfaces, Clinical oral implants research 11 (2000) 530-539.

[2] G.B. Shiu Hoi Ting, Lutton Cameron, Crawford Ross, and Xiao Yin, Formation of Blood Clot on Biomaterial Implants Influences Bone Healing Tissue Engineering Part B: Reviews 20(6) (2014) 697-712.

[3] M.B. Gorbet, M.V. Sefton, Biomaterial-associated thrombosis: roles of coagulation factors, complement, platelets and leukocytes, Biomaterials 25(26) (2004) 5681-5703.

[4] V. Milleret, S. Tugulu, F. Schlottig, H. Hall, Alkali treatment of microrough titanium surfaces affects macrophage/monocyte adhesion, platelet activation and architecture of blood clot formation, European Cells and Materials 21 (2011) 430-444.

[5] L.-C. Xu, J.W. Bauer, C.A. Siedlecki, Proteins, platelets, and blood coagulation at biomaterial interfaces, Colloids and Surfaces B: Biointerfaces 124(0) (2014) 49-68.

[6] N. Yayapour, H. Nygren, Interactions between whole blood and hydrophilic or hydrophobic glass surfaces: kinetics of cell adhesion, Colloids and Surfaces B: Biointerfaces 15(2) (1999) 127-138.

[7] S.L. Goodman, Sheep, pig, and human platelet–material interactions with model cardiovascular biomaterials, Journal of Biomedical Materials Research 45(3) (1999) 240-250.

[8] A.S. Wolberg, Thrombin generation and fibrin clot structure, Blood Reviews 21(3) (2007) 131-142.

[9] W.B. Tsai, J.M. Grunkemeier, C.D. McFarland, T.A. Horbett, Platelet adhesion to polystyrene-based surfaces preadsorbed with plasmas selectively depleted in fibrinogen, fibronectin, vitronectin, or von Willebrand's factor, J Biomed Mater Res 60(3) (2002) 348-59.

[10] K.M. Hansson, S. Tosatti, J. Isaksson, J. Wettero, M. Textor, T.L. Lindahl, P. Tengvall, Whole blood coagulation on protein adsorption-resistant PEG and peptide functionalised PEG-coated titanium surfaces, Biomaterials 26(8) (2005) 861-72.

[11] D. Di Iorio, T. Traini, M. Degidi, S. Caputi, J. Neugebauer, A. Piattelli, Quantitative evaluation of the fibrin clot extension on different implant surfaces: An in vitro study, Journal of Biomedical Materials Research Part B: Applied Biomaterials 74B(1) (2005) 636-642.

[12] C. Eriksson, J. Lausmaa, H. Nygren, Interactions between human whole blood and modified TiO$_2$-surfaces: influence of surface topography and oxide thickness on leukocyte adhesion and activation, Biomaterials 22(14) (2001) 1987-1996.

[13] A. Thor, L. Rasmusson, A. Wennerberg, P. Thomsen, J.M. Hirsch, B. Nilsson, J. Hong, The role of whole blood in thrombin generation in contact with various titanium surfaces, Biomaterials 28(6) (2007) 966-74.

[14] M. Hulander, A. Lundgren, L. Faxalv, T.L. Lindahl, A. Palmquist, M. Berglin, H. Elwing, Gradients in surface nanotopography used to study platelet adhesion and activation, Colloids and surfaces. B, Biointerfaces 110 (2013) 261-9.

[15] D.S. Sutherland, M. Broberg, H. Nygren, B. Kasemo, Influence of Nanoscale Surface Topography and Chemistry on the Functional Behaviour of an Adsorbed Model Macromolecule, Macromolecular bioscience 1(6) (2001) 270-273.

[16] L.B. Koh, I. Rodriguez, S.S. Venkatraman, The effect of topography of polymer surfaces on platelet adhesion, Biomaterials 31(7) (2010) 1533-1545.

[17] M. Stavridi, M. Katsikogianni, Y.F. Missirlis, The influence of surface patterning and/or sterilization on the haemocompatibility of polycaprolactones, Materials Science and Engineering C 23(3) (2003) 359-365.

[18] B.S. Kopf, S. Ruch, S. Berner, N.D. Spencer, K. Maniura-Weber, The role of nanostructures and hydrophilicity in osseointegration: In-vitro protein-adsorption and blood-interaction studies, Journal of Biomedical Materials Research Part A 103(8) (2015) 2661-2672.

[19] C.J. Nonckreman, S. Fleith, P.G. Rouxhet, C.C. Dupont-Gillain, Competitive adsorption of fibrinogen and albumin and blood platelet adhesion on surfaces modified with nanoparticles and/or PEO, Colloids and Surfaces B: Biointerfaces 77(2) (2010) 139-149.

[20] S.N. Rodrigues, I.C. Gonçalves, M.C.L. Martins, M.A. Barbosa, B.D. Ratner, Fibrinogen adsorption, platelet adhesion and activation on mixed hydroxyl-/methyl-terminated self-assembled monolayers, Biomaterials 27(31) (2006) 5357-5367.

[21] Y. Wu, F.I. Simonovsky, B.D. Ratner, T.A. Horbett, The role of adsorbed fibrinogen in platelet adhesion to polyurethane surfaces: a comparison of surface hydrophobicity, protein adsorption, monoclonal antibody binding, and platelet adhesion, Journal of biomedical materials research. Part A 74(4) (2005) 722-38.

[22] B. Sivaraman, R.A. Latour, The relationship between platelet adhesion on surfaces and the structure versus the amount of adsorbed fibrinogen, Biomaterials 31(5) (2010) 832-839.

[23] D.M. Hylton, S.W. Shalaby, R.A. Latour, Jr., Direct correlation between adsorption-induced changes in protein structure and platelet adhesion, Journal of biomedical materials research. Part A 73(3) (2005) 349-58.

[24] J.N. Lindon, G. McManama, L. Kushner, E.W. Merrill, E.W. Salzman, Does the conformation of adsorbed fibrinogen dictate platelet interactions with artificial surfaces?, Blood 68(2) (1986) 355-362.

[25] W.-B. Tsai, J.M. Grunkemeier, T.A. Horbett, Variations in the ability of adsorbed fibrinogen to mediate platelet adhesion to polystyrene-based materials: A multivariate statistical analysis of antibody binding to the platelet binding sites of fibrinogen, Journal of Biomedical Materials Research Part A 67A(4) (2003) 1255-1268.

[26] V. Milleret, S. Buzzi, P. Gehrig, A. Ziogas, J. Grossmann, K. Schilcher, A.S. Zinkernagel, A. Zucker, M. Ehrbar, Protein adsorption steers blood contact activation on engineered cobalt chromium alloy oxide layers, Acta Biomaterialia 24 (2015) 343-351.

Chapter 5

Availability of platelet-binding sites on fibrinogen adsorbed on nanoparticle-density gradients

5.1 Introduction

Surface-adsorbed proteins can bind to platelets via cell-membrane receptors such as GPIIb/IIa (known as integrin $\alpha_{IIb}\beta_3$) and other receptors. Such binding induces platelet adhesion. Adhered platelets become activated and mediate clotting events such as platelet aggregation and formation of thrombus [1]. Four adhesive plasma proteins are known to be capable of mediating platelet adhesion and aggregation, fibrinogen, fibronectin, vitronectin and von Willebrand factor [2]. Tsai and co-workers [3] showed that on surfaces of biomaterials previously incubated in plasma, platelet adhesion is mediated exclusively by surface-bound fibrinogen while the other adhesion proteins in plasma do not seem to be involved.

Fibrinogen is a symmetric molecule, composed of two sets of three non-identical polypeptide chains, termed Aα, Bβ and γ chains, with a total molecular weight of 340 kDa. [4]. Figure 5.1 shows the six polypeptide chains folding together in a tri-nodular structure with a center globular knot. The E domain, linked to this are the outer two D regions, containing one of the sets of three polypeptide chains [5].

Each fibrinogen molecule possesses three pairs of potential platelet-binding peptide sequences, two RGD sequences in each of the Aα chains (RGDF at Aα95-98, RGDS at Aα572-575) and a dodecapeptide sequence at the carboxyl-

terminus of each of the γ chains (HHLGGAKQAGDV at γ400-411) [1, 6]. Several studies showed that the γ chain C-terminal dodecapeptide is the most important ligand for platelet adhesion to adsorbed fibrinogen [7-9]. The corresponding platelet binding sites are not readily available on the fibrinogen molecule in the absence of thrombin cleavage [5]. It was shown that non-activated platelets do not strongly interact with soluble fibrinogen in its native state in the blood stream, but readily adhere and activate after contacting the same protein when fibrinogen is adsorbed on a surface [10]. Several groups proposed that surface-induced conformational changes in adsorbed fibrinogen molecules might alter fibrinogen such that different platelet binding domains become available and enables them to recruit platelets [11-13].

Figure 5.1: Schematic representation of fibrinogen with selected functional regions. Shown above are the three polypeptide chains, αCs tethered to the central E region near the fibrinopeptides (A and B), the outer D region and the terminal ends of each γ chain (drawn out of scale). The lower horizontal arrow indicates the possible platelet binding site of each γ chain. The two platelet binding sites on the Aα chains are indicated by the upper arrow. Reprinted from [5], Copyright (2018), with permission from Elsevier.

It is widely cited in the biomaterials field that the amount of adsorbed fibrinogen is one of the most important factors mediating platelet adhesion [14-17], but recently it is becoming more accepted that the conformation and availability of platelet-binding sites in fibrinogen are more important [7, 10, 18-21].

In Chapter 4 it was shown that nanostructures with a size of 39 nm seem to enhance blood coagulation, while protein studies on 39 nm particle-density gradients did not show any increase in fibrinogen amount with increasing particle coverage (Chapter 3). In order to get further insight if 39 nm particles induce a change in fibrinogen conformation that leads to an increase in platelet binding-site availability and enhances blood coagulation, monoclonal antibody binding specific for the dodecapeptide sequence of the fibrinogen γ chain was measured on fibrinogen adsorbed onto nanoparticle-density gradients.

5.2 Experimental

5.2.1 Substrates

Nanoparticle-density gradients (as described in Section 2.2) were split in half along the gradient; one half of the gradient was used as the sample and the other half as the control. After splitting, the gradients were cleaned for 20 min in ethanol (Fisher Chemical, UK) in an ultrasonic bath with an exchange of solvent after 10 min and dried in a steam of nitrogen.

Before their use, the nanoparticle-density gradients were cleaned in the oxygen plasma cleaner (PDC-32G) for 2 min to remove hydrocarbon contamination from air and to get a clean, hydrophilic TiO_2 surface.

5.2.2 Fibrinogen adsorption

HEPES 2 buffer was prepared with 10 mM 4-(2-hydroxylethyl)-piperazine-1-ethanesulfonic acid (HEPES) and 150 mM NaCl with pH 7.4 (both from Sigma, Switzerland). Prior to use, the HEPES 2 buffer was filtered (Whatman FP 30/0.2 CA-S, size 0.2 m, maximum pressure 7 bar).

Protein solution of 5 g/mL fibrinogen Alexa Fluor® 647 conjugate (F-35200, Molecular Probes, Switzerland) in HEPES 2 buffer was prepared. The fibrinogen-adsorption incubation was performed in a 6-well plate with 1.5 ml protein solution for 30 min at room temperature, in the dark and on a wave shaker (Polymax, Heidolph®, Germany) at 10 rpm. The control group was incubated in HEPES 2 for 30 min at room temperature, on a wave shaker (Polymax, Heidolph®, Germany) at 10 rpm.

After adsorption, the samples/controls were rinsed 4 times in phosphate-buffered saline (PBS, Sigma) and then blocked in 5% goat serum and 1% fetal calf serum (FCS; Lonza, Switzerland) in PBS for 1 h on the wave shaker in the dark.

5.2.3 Monoclonal antibody binding to surface-bound fibrinogen

Mouse monoclonal antibody [4H9] to the fibrinogen γ region was purchased from Genetex (USA, GTX60502) and goat anti-mouse IgG2a cross-adsorbed secondary antibody, Alexa Fluor® 488 was purchased from Thermo Fisher Scientific (USA, A21131). The antibodies were diluted in PBS supplemented with 1% FCS. All incubations were carried out on the wave shaker (10 rpm) at room temperature and in the dark.

After incubation of the samples in the blocking solution, they were rinsed 4 times in PBS and placed into a new 6-well plate. 1.5 ml of diluted fibrinogen gamma antibody (1:200) was added and incubated for 1 h. The samples were then rinsed 4 times with PBS. 1.5 ml of Alexa Fluor® 488 conjugated goat anti-mouse antibody (1:300) was added and incubated for 1 h. After incubation, the samples were rinsed 4 times with PBS followed by rinsing with ultrapure water. Finally, the samples were blown dry in a stream of nitrogen. The adsorption of protein/antibody on the substrates was assessed by fluorescence intensity measurements using a microarray fluorescence scanner (microarray laser scanner, LS reloaded, Tecan, Switzerland). The resolution was set to

10   m/pixel, a medium pinhole and an oversampling factor of 3 were chosen. The gain was set to 220 and 180 to read out the secondary antibody and fibrinogen, respectively.

Image analysis was performed using Image J (version 1.44p for Mac). Line plots of intensity along the particle-density gradient were created by averaging the grey values of all the pixels along the lines perpendicular to the gradient. The measured intensity values were normalized to the intensity on the smooth region of the gradient.

The surface area that is available for protein/antibody adsorption is larger in the presence of nanoparticles. Therefore the measured intensity values were always corrected for the increased surface area by assuming the nanoparticles as half-spheres with a diameter of 12, 39 or 72 nm.

5.3 Results

The reactivity of the main platelet-binding region of adsorbed fibrinogen was assessed by measurement of the binding of monoclonal antibodies to preadsorbed fibrinogen. The used antibody corresponds to a region within amino acids 210 and 437 of human fibrinogen and contains the dodecapeptide sequence at the carboxyl-terminus of the γ chain (HHLGGAKQAGDV at γ 400-411), that is known to be the most important ligand for platelet adhesion to adsorbed fibrinogen [7-9]. The binding of the monoclonal antibody to adsorbed fibrinogen was assessed by fluorescence-intensity measurements using a microarray fluorescence scanner.

Line plots of relative intensities measured with the micro-array scanner and averaged over three samples showed no significant influence of nano-features on protein adsorption and antibody binding for 72 nm nanoparticles Figure 5.2 a). The ratio of antibody to adsorbed fibrinogen stayed constant along the nanoparticle-density gradient (Figure 5.2 b).
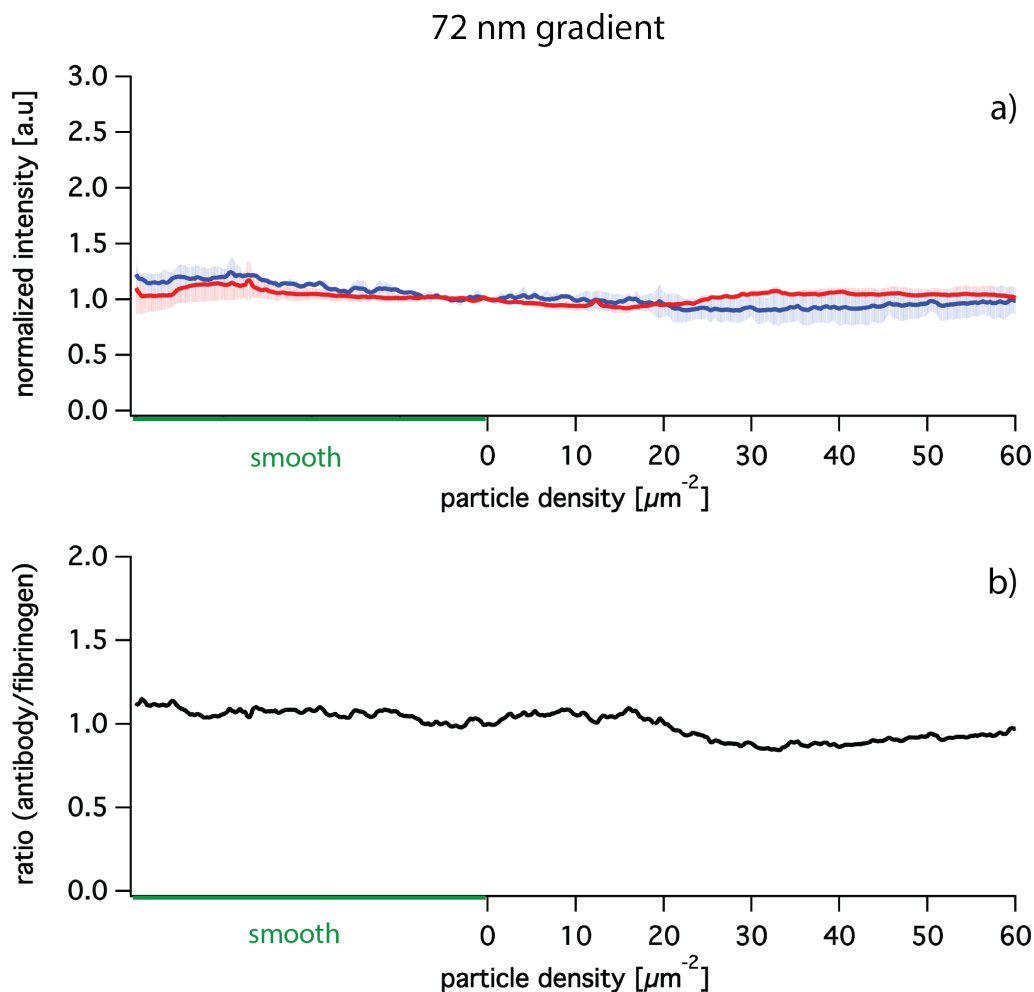
72 nm gradient

Figure 5.2: a) Relative intensities of adsorbed fibrinogen (red) and monoclonal antibody binding to surface bound fibrinogen (blue) on 72 nm particle-density gradients, measured with a microarray scanner. b) Ratio of bound antibody/ adsorbed fibrinogen. (Mean ± standard deviation, n = 3)

Figure 5.3 a) shows that at the high-density end of 39 nm particle-density gradients, the amount of adsorbed fibrinogen was 3 times higher than at the smooth part on the gradient, while the amount of bound antibody only increased slightly with increasing particle coverage. The ratio of antibody to adsorbed fibrinogen decreased by approximately 65% with increasing nanoparticle-density (Figure 5.3 b).
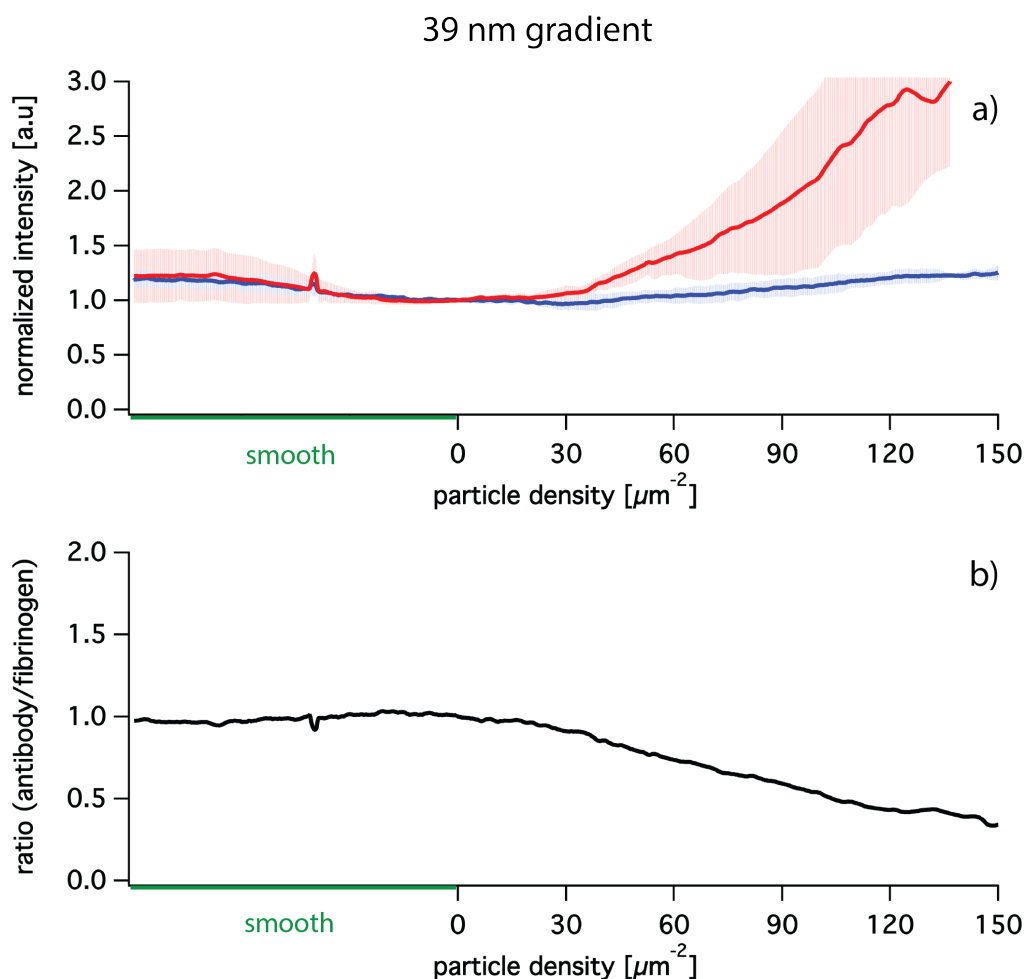
Figure 5.3: a) Relative intensities of adsorbed fibrinogen (red) and monoclonal antibody binding to surface bound fibrinogen (blue) on 39 nm particle-density gradients, measured with a microarray scanner. b) Ratio of bound antibody/ adsorbed fibrinogen. (Mean ± standard deviation, n = 3)

The amount of adsorbed fibrinogen at the high-density end of 12 nm particle-density gradients was about 2 times higher at the high-density position compared to the smooth part on the gradient (Figure 5.4 a). Also the amount of bound antibody increased with increasing particle coverage. Figure 5.4 b) shows that the ratio of antibody to adsorbed fibrinogen stayed constant along the gradient until a particle coverage of 800 particles/ m² where the ratio decreased by about 20 % with increasing particle-density.
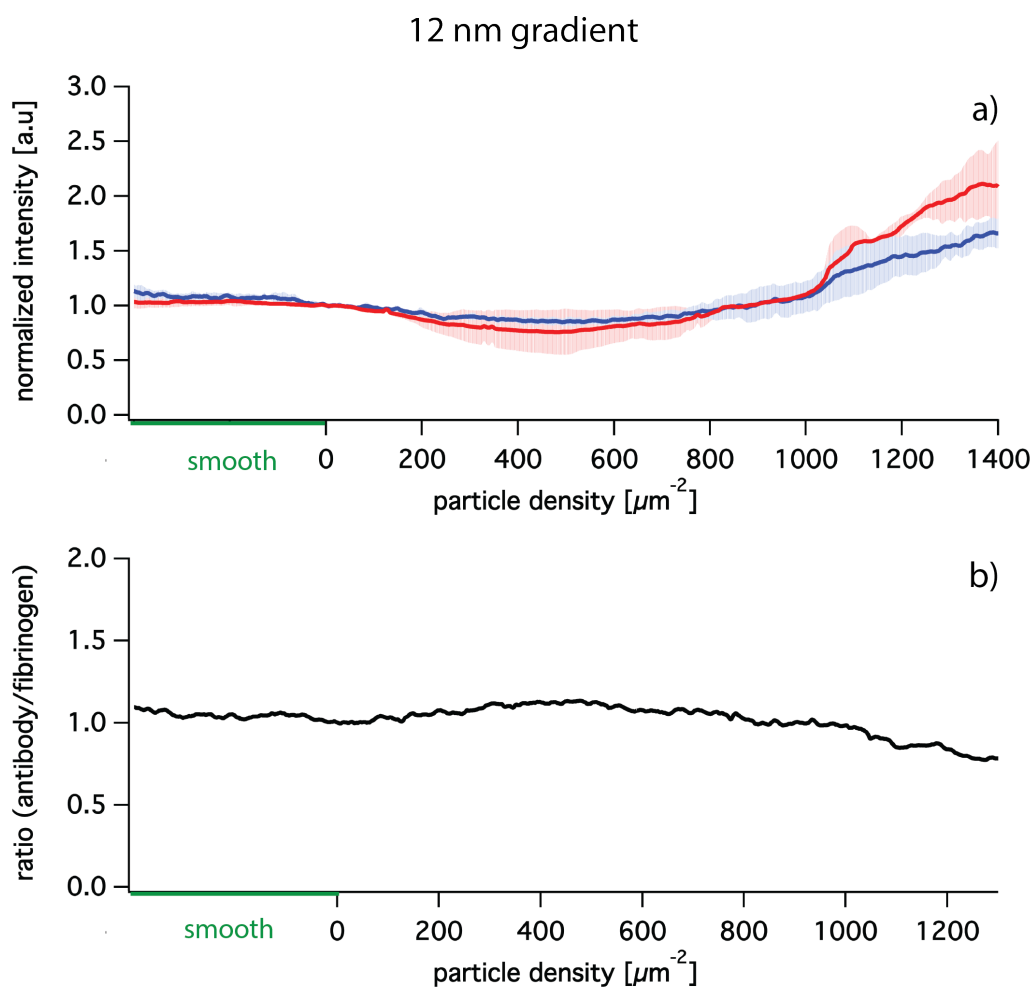
Figure 5.4: a) Relative intensities of adsorbed fibrinogen (red) and monoclonal antibody binding to surface bound fibrinogen (blue) on 12 nm particle-density gradients, measured with a microarray scanner. b) Ratio of bound antibody/ adsorbed fibrinogen. (Mean ± standard deviation, n = 3)

The monoclonal antibody binding to surface-bound fibrinogen on nanoparticle-density gradients showed that only 39 nm particles have a significant effect on the ratio of antibody/ surface-bound fibrinogen. With increasing coverage of 39 nm particles, the ratio of antibody/fibrinogen showed a decrease.

5.4 Discussion

The results presented above were obtained from one set of experiment with three samples of each gradient and are therefore only preliminary. Nevertheless, they showed significant differences in the antibody binding depending on the nanoparticle size. The ratio of antibody binding to adsorbed fibrinogen is an indicator of the conformation of the surface-bound fibrinogen. For 12 and 72 nm particles, the ratio stayed nearly constant along the gradient, meaning that that the amount of antibody binding was directly correlated to the amount of adsorbed fibrinogen and the fibrinogen conformation did not change with a change in particle-density; the antibody binding sites per fibrinogen remained constant. In contrast to that, 39 nm particles had an effect on the antibody/surface-bound fibrinogen ratio that decreased with increasing particle coverage, indicating that the conformation of adsorbed fibrinogen changed and less antibody binding sites were available.

Tsai *et al.* [7] studied the influence of surface-bound fibrinogen on platelet adhesion to different types of polystyrene-based microtiter plates. They found that platelet adhesion was positively correlated with the ability of adsorbed fibrinogen to bind three types of monoclonal antibodies, while no significant correlation between platelet adhesion and the absolute amount of adsorbed fibrinogen was found. The γ-chain C-terminal dodecapeptide of fibrinogen was shown to the most important platelet-binding site in adsorbed fibrinogen. In Chapter 4, enhanced fibrin network formation for surfaces with a high density of 39 nm particles was observed, while 12 and 72 nm particles did not have a significant influence on platelet activation and fibrin network formation. Therefore, an increase in antibody binding on gradients with 39 nm particles with increasing particle-density was expected. In contrast to our expectations, the antibody binding increased only slightly with increase in 39 nm particle-density, while it increased by about 50% with increasing 12 nm particle coverage, which did not induce enhanced blood coagulation. The amount of antibody binding to the surface is directly correlated to the amount of surface-bound fibrinogen and therefore the ratio of antibody and fibrinogen is a better

indicator for conformational changes in adsorbed fibrinogen. The experiments showed that for 39 nm particle-density gradients, the antibody/fibrinogen ratio decreases with increasing particle density while no changes were observed for 12 and 72 nm particles. This finding may indicate that not only the amount of available platelet binding sites but also the spacing of the binding sites might play an important role for platelet adhesion and blood coagulation. Further studies would be needed to conclusively prove this hypothesis.

The chosen monoclonal antibody corresponds to the region with amino acids 210-437, while the epitope of the platelet binding region has been localized to the sequence 400-411, therefore it would be possible that the antibody binding is hindered while the platelet binding site would be still accessible for platelets.

Horbett *et al.* [22] proposed that the availability of the platelet-binding regions of fibrinogen is not the only factor involved in mediating platelet adhesion. They found a similar time scale for changes in platelet adhesion and plasma displaceability of fibrinogen, which might indicate that platelet adhesion has a higher sensitivity to how tightly the fibrinogen molecule is bound to the substrate, than having much to do with the changes in the availability of the platelet binding domains in fibrinogen. Gaebel and Feuerstein [23] showed that adherent platelets cause redistribution of adsorbed fibrinogen, indicating that the tightness with which the fibrinogen is held could influence platelet behavior. Results from protein-adsorption studies in Section 3.2 and previous studies by Roach and co-workers [24] suggest that fibrinogen is bound tighter to 12 nm particles than to the 39 and 72 nm particles. The interplay between binding tightness of fibrinogen and platelet binding site availability might be the reason for enhanced platelet activation and fibrin network formation on surfaces with higher coverage for 39 nm particles. But more work has to be done to find direct evidence for the relationship between changes in the tightness of fibrinogen binding and platelet adhesion.

The observed fibrinogen adsorption on 39 nm gradients differed considerably from the findings in Chapter 3 where no increase in the amount of adsorbed fibrinogen was found with increasing particle-density. This difference can be explained by the differences in fibrinogen adsorption protocol. For the antibody experiments, samples were incubated in a solution of labeled fibrinogen in HEPES 2 buffer for 30 min and competition with diluted serum was only allowed afterwards. Chinn and co-workers have shown that fibrinogen adsorbed on surfaces and allowed to reside on the surface while it is kept in a buffer solution for a period of time undergoes post-adsorptive changes that decreases its displaceability by plasma, polyclonal antifibrinogen binding and the ability to support platelet adhesion [25, 26]. The decrease in reactivity of fibrinogen was prevented when stored in buffered albumin solution rather than buffer. Additionally, several studies have shown that the maximum in fibrinogen adsorption from plasma is a function of plasma dilution and contact time [27-29] and therefore the use of only 5% serum in PBS instead of full serum may also change the adsorption behavior.

5.5 Conclusions

The first results from these experiments show a significant change in the ratio of amount of antibody binding to amount of surface-bound fibrinogen for 39 nm particle-density gradients. The ratio of antibody to adsorbed fibrinogen decreased by approximately 65% with increasing nanoparticle-density of particles with a diameter of 39 nm. The decrease in ratio of antibody binding and adsorbed fibrinogen is an indicator for conformational changes in adsorbed fibrinogen and might explain the different platelet interaction and blood clotting behavior found on 39 nm particle-density gradients earlier (Chapter 4).

More experiments certainly have to be performed to verify the results. In order to be able to compare the protein data (Chapter 3), blood data (Chapter 4) and antibody binding data directly, antibody binding to nanoparticle-density gradients pre-adsorbed with full serum spiked with fluorescently labeled fibrinogen should be measured followed by platelet interaction studies on the very same substrates.

References:

[1] L.-C. Xu, J.W. Bauer, C.A. Siedlecki, Proteins, platelets, and blood coagulation at biomaterial interfaces, Colloids and Surfaces B: Biointerfaces 124(0) (2014) 49-68.

[2] T.A. Horbett, Chapter 13 Principles underlying the role of adsorbed plasma proteins in blood interactions with foreign materials, Cardiovascular Pathology 2(3, Supplement) (1993) 137-148.

[3] W.B. Tsai, J.M. Grunkemeier, C.D. McFarland, T.A. Horbett, Platelet adhesion to polystyrene-based surfaces preadsorbed with plasmas selectively depleted in fibrinogen, fibronectin, vitronectin, or von Willebrand's factor, J Biomed Mater Res 60(3) (2002) 348-59.

[4] J.W. Weisel, Fibrinogen and Fibrin, Advances in Protein Chemistry, Academic Press 2005, pp. 247-299.

[5] L. Zhang, B. Casey, D.K. Galanakis, C. Marmorat, S. Skoog, K. Vorvolakos, M. Simon, M.H. Rafailovich, The influence of surface chemistry on adsorbed fibrinogen conformation, orientation, fiber formation and platelet adhesion, Acta Biomaterialia 54 (2017) 164-174.

[6] J. Hawiger, S. Timmons, M. Kloczewiak, D.D. Strong, R.F. Doolittle, gamma and alpha chains of human fibrinogen possess sites reactive with human platelet receptors, Proceedings of the National Academy of Sciences 79(6) (1982) 2068-2071.

[7] W.-B. Tsai, J.M. Grunkemeier, T.A. Horbett, Variations in the ability of adsorbed fibrinogen to mediate platelet adhesion to polystyrene-based materials: A multivariate statistical analysis of antibody binding to the platelet binding sites of fibrinogen, Journal of Biomedical Materials Research Part A 67A(4) (2003) 1255-1268.

[8] D.H. Farrell, P. Thiagarajan, D.W. Chung, E.W. Davie, Role of fibrinogen alpha and gamma chain sites in platelet aggregation, Proceedings of the National Academy of Sciences of the United States of America 89(22) (1992) 10729-10732.

[9] D.H. Farrell, P. Thiagarajan, Binding of recombinant fibrinogen mutants to platelets, Journal of Biological Chemistry 269(1) (1994) 226-231.

[10] B. Sivaraman, R.A. Latour, The relationship between platelet adhesion on surfaces and the structure versus the amount of adsorbed fibrinogen, Biomaterials 31(5) (2010) 832-839.

[11] B. Sivaraman, R.A. Latour, Delineating the roles of the GPIIb/IIIa and GP-Ib-IX-V platelet receptors in mediating platelet adhesion to adsorbed fibrinogen and albumin, Biomaterials 32(23) (2011) 5365-5370.

[12] A. Chiumiento, S. Lamponi, R. Barbucci, Role of Fibrinogen Conformation in Platelet Activation, Biomacromolecules 8(2) (2007) 523-531.

[13] M. Tomikawa, M. Iwamoto, P. Olsson, S. Söderman, B. Blombäck, On the platelet-fibrinogen interaction, Thrombosis Research 19(6) (1980) 869-876.

[14] C.J. Nonckreman, S. Fleith, P.G. Rouxhet, C.C. Dupont-Gillain, Competitive adsorption of fibrinogen and albumin and blood platelet adhesion on surfaces modified with nanoparticles and/or PEO, Colloids and Surfaces B: Biointerfaces 77(2) (2010) 139-149.

[15] L.B. Koh, I. Rodriguez, S.S. Venkatraman, The effect of topography of polymer surfaces on platelet adhesion, Biomaterials 31(7) (2010) 1533-1545.

[16] S.N. Rodrigues, I.C. Gonçalves, M.C.L. Martins, M.A. Barbosa, B.D. Ratner, Fibrinogen adsorption, platelet adhesion and activation on mixed hydroxyl-/methyl-terminated self-assembled monolayers, Biomaterials 27(31) (2006) 5357-5367.

[17] K. Ishihara, K. Fukumoto, Y. Iwasaki, N. Nakabayashi, Modification of polysulfone with phospholipid polymer for improvement of the blood compatibility. Part 2. Protein adsorption and platelet adhesion, Biomaterials 20(17) (1999) 1553-1559.

[18] Y. Wu, F.I. Simonovsky, B.D. Ratner, T.A. Horbett, The role of adsorbed fibrinogen in platelet adhesion to polyurethane surfaces: a comparison of surface hydrophobicity, protein adsorption, monoclonal antibody binding, and platelet adhesion, Journal of biomedical materials research. Part A 74(4) (2005) 722-38.

[19] D.M. Hylton, S.W. Shalaby, R.A. Latour, Jr., Direct correlation between adsorption-induced changes in protein structure and platelet adhesion, Journal of biomedical materials research. Part A 73(3) (2005) 349-58.

[20] J.N. Lindon, G. McManama, L. Kushner, E.W. Merrill, E.W. Salzman, Does the conformation of adsorbed fibrinogen dictate platelet interactions with artificial surfaces?, Blood 68(2) (1986) 355-362.

[21] V. Milleret, S. Buzzi, P. Gehrig, A. Ziogas, J. Grossmann, K. Schilcher, A.S. Zinkernagel, A. Zucker, M. Ehrbar, Protein adsorption steers blood contact activation on engineered cobalt chromium alloy oxide layers, Acta Biomaterialia 24 (2015) 343-351.

[22] T.A. Horbett, K.R. Lew, Residence time effects on monoclonal antibody binding to adsorbed fibrinogen, Journal of Biomaterials Science, Polymer Edition 6(1) (1995) 15-33.

[23] K. Gaebel, I.A. Feuerstein, Platelets process adsorbed protein: a morphological study, Biomaterials 12(6) (1991) 597-602.

[24] P. Roach, D. Farrar, C.C. Perry, Surface Tailoring for Controlled Protein Adsorption: Effect of Topography at the Nanometer Scale and Chemistry, Journal of the American Chemical Society 128(12) (2006) 3939-3945.

[25] J.A. Chinn, S.E. Posso, T.A. Horbett, B.D. Ratner, Postadsorptive transition in fibrinogen adsorbed to polyurethanes: Changes in antibody binding and sodium dodecy1 sulfate elutability, Journal of Biomedical Materials Research 26(6) (1992) 757-778.

[26] J.A. Chinn, S.E. Posso, T.A. Horbett, B.D. Ratner, Postadsorptive transitions in fibrinogen adsorbed to Biomer: Changes in baboon platelet adhesion, antibody binding, and sodium dodecyl sulfate elutability, Journal of Biomedical Materials Research 25(4) (1991) 535-555.

[27] S.M. Slack, T.A. Horbett, Changes in the strength of fibrinogen attachment to solid surfaces: An explanation of the influence of surface chemistry on the Vroman effect, Journal of Colloid and Interface Science 133(1) (1989) 148-165.

[28] J.L. Brash, P. ten Hove, Effect of plasma dilution on adsorption of fibrinogen to solid surfaces, Thrombosis and haemostasis 51(3) (1984) 326-330.

[29] T.A. Horbett, Mass action effects on competitive adsorption of fibrinogen from hemoglobin solutions and from plasma, Thrombosis and haemostasis 51(2) (1984) 174-181.

Chapter 6

Human bone cells on nanoparticle-density gradients in presence of blood

6.1 Introduction

The importance of surface topography and roughness on cellular responses has been known from the very beginning of cell culture. In 1912 Ross G. Harrison [1] described how cells spread along the fibers of a mesh of spider silk. He also observed that cells move along the fibers.

It is well known that the success of a surgical implant is dependent on an appropriate cellular response to the implant surface [2]. The increasingly ageing population has led to a need for better-performing implants, making orthopaedics an area with a major research drive and the design of the implant surface becoming more and more important. For bone-anchored implants, a major requirement is rapid anchoring and attachment to the bone to ensure fast and long-term stability; this process is called osseointegration [3]. Roughness is known to have a significant influence on cell adhesion, proliferation and differentiation [4-11]. Several studies have shown that osteoblasts function more effectively on rough surfaces [4, 5] while other cells such as fibroblasts from the connective tissue actively select smooth surfaces [5, 12, 13].

In addition, it was shown that proliferation and growth of osteoblasts also depends on the roughness length scale. For micrometer roughness the osteoblast cell density increases with higher roughness [5] whereas for nano-featured roughness the cell density decreases with higher roughness [14]. At the interface

of the cell and the extra cellular matrix (ECM), interactions at the nanoscale take place – cells respond to textured cues in the ECM, which contains pits, pores, protrusions and fibers on a length-scale of 5-200 nm [11]. Therefore, nanoscale features may provide biomimetic cell-modulating cues.

The influence of nanoscale surface topographies on cellular response has been studied using a variety of surface topographies and cell types including fibroblasts, macrophages, endothelial cells and osteoblasts [15, 16]. It is well known that different cell types will exhibit a different behavior and that cellular response to nanotopography is cell-type and application specific. Nanotopography has been shown to modulate cell adhesion and spreading both positively and negatively. While Lim and co-workers [17] showed that osteoblast adhesion was positively affected by nanotopography on PLLA substrates with 3-45 nm nanofeatures, Cai *et al*. [18] found no major differences in cell proliferation on 2 vs. 20 nm titanium films.

In 2007, Dalby *et al.* [10] demonstrated that the dimensions of nanostructures alone do not control cellular response. Nanopits with a diameter of 120 nm were arranged in hexagonal, square, near-square and random placements. With an increase in nanoscale disorder, cellular adhesion and osteoblastic differentiation were increased.

With a simple oxidation treatment, Boyan *et al.* [19] created nanocrystallites (40 to 360 nm in diameter, 60 to 350 nm in height) on native titanium oxide surfaces. To combine nano-and microscale structures, they added the nanostructures on machined, sandblasted/acid-etched substrates. They reported that nanoscale roughness decreases the proliferation of osteoblasts, while it increases the bone-formation factors. The same is true for the microscale roughness. They concluded that a combination of micro- and nanostructures is synergetic for cell differentiation and bone formation and therefore reduces the time for osseointegration. Zink *et al*. [8] created a two-dimensional roughness gradient by combining a micro-roughness gradient with a 40 nm particle-density gradient. The results showed that high micro-roughness combined with an

intermediate nanoparticle-density (30-40 nanoparticles/ m^2) led to the highest degree of mineralization.

In vivo, osseointegration involves a complex chain of event at the implant surface. Protein adsorption and blood clotting are followed by site infiltration and biological recognition of the surface by mesenchymal stem cells (MSCs) and osteoblasts, finally leading to bone formation by these cells at the interface, creating a firm bond between the bone and the implant [20]. In *in vitro* evaluation of implant materials, the importance of the interaction between blood components and cells has been largely neglected in the past. Recently Kopf *et al*. [21] showed that pre-incubation with whole human blood leads to an increased number of attached cells, enhanced ALP and Col-I protein expression and strong mineralization. They suggest that blood pre-incubation of implant surfaces mimics a more physiological situation and might provide a more predictive *in vitro* model that can be used for the evaluation of novel implant surfaces.

In Section 2.2, a simple method has been presented to produce nanoparticle-density gradients with continuously changing particle-density, while the shape and size of the nano-features as well as the surface chemistry remain unchanged over the entire gradient. This section aims to systematically examine the effect of nanostructures and pre-adsorbed blood components on human bone cell behavior by means of particle-density gradients. For this, three different surfaces (smooth, homogenous and gradient) were incubated in partially heparinized whole human blood and human bone cells (HBC) were seeded on top of this pre-formed blood clot (Figure 6.1).
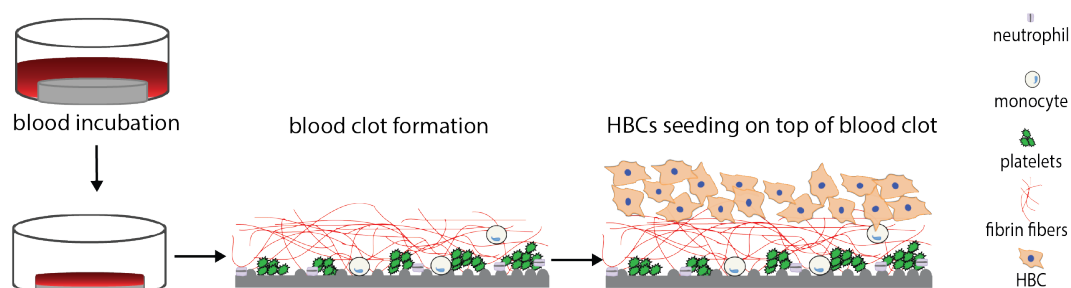
Figure 6.1: Schematic of human bone cell (HBC) culture in the presence of pre-adsorbed blot components.

6.2 Experimental

6.2.1 Substrates

To study the effect of pre-adsorbed blood components on human bone cell behavior, three different nanostructured surfaces with 39 nm particles (smooth, homogenous and gradient) were produced.

39 nm gradients were produced as described in Section 2.2. Homogenous high-density samples were produced with the same technique as the gradients, by dipping about 20 mm of the negatively rendered silicon wafer (25 x 25 mm^2) for 30 min into 0.004 wt% 39 nm particle suspension, but without withdrawing the wafer. For the smooth samples, 25 x 25 mm^2 silicon wafers were cleaned, treated and sintered with the same procedure as the gradients, but without the nanoparticle application.

In order to mimic the surface of titanium implants, the samples were coated with 6 nm of TiO_2.

Prior to use, the nanoparticle-density gradients were cleaned in the oxygen plasma cleaner (PDC-32G) for 2 min to remove hydrocarbon contamination and to obtain a clean, hydrophilic TiO_2 surface. Immediately

before use, the samples were sterilized for 30 min in 70% ethanol solution and washed 3 times in PBS.

6.2.2 Blood incubation

To study the effect of pre-adsorbed blood components on human bone-cell behavior, the three different nanostructured surfaces with 39 nm particles (smooth, homogenous and gradient) were incubated in partially heparinized whole human blood for 8 or 14 min (see Section 4.2). Prior to blood incubation the ideal incubation time for each donor was estimated by incubating a reference gradient sample in whole blood spiked with Alexa Fluor® 488 conjugated fibrinogen (final concentration 18 g/ml) and analyzed via epi-fluorescence microscopy (Axio Imager.M1, Carl Zeiss AG).

The different sample types were incubated in separate blood chambers. After incubation, the blood was carefully removed and samples were rinsed 3 times with pre-warmed PBS. 6 samples per sample type (smooth, homogenous and gradient) were used for each experiment. The experiment was carried out twice with blood from different donors.

6.2.3 Primary human bone cells

Bone-marrow samples were obtained as described in [21] from patients undergoing surgical hip replacement after informed consent (ethical approval was obtained from the local ethics committee; BASEC Nr. PB_2016-00816). All experiments were performed with HBCs of passage 3.

6.2.4 Cell seeding

Cells were seeded with an adapted protocol previously described by Brigitte Kopf and Angela Schipanski [21].

Sub-confluent primary HBCs were removed from cell-culture flasks with trypsin solution (0.5 g/l trypsin, 0.2 g/l EDTA, Sigma) for 4 min and re-suspended in proliferation medium before centrifugation at $110 \times g$ for 15 min at 4 °C. Prior to cell seeding, the samples previously incubated with blood for 8 or 14 min, were placed in 6-well cell-culture plates (TPP, Switzerland). Cells were seeded in proliferation medium on samples and tissue-culture polystyrene (TCPS) as a control, at a cell-seeding density of 1×10^4 cells/cm². After 24 h the samples were transferred into new wells with differentiation medium. α-MEM supplemented with 10% FCS, 1% PSN, 50 M ascorbic acid (Sigma), 2 mM β-glycerophosphate (Sigma), 10 nM dexamethasone and 10 nM 1,25-dihydroxy-vitamin D_3 was used as differentiation medium. Each time the medium was changed, dexamethasone and vitamin D_3 were freshly added to the medium. As a positive control, cells on TCPS were cultivated in differentiation medium and as a negative control in proliferation medium. All samples were incubated at 37 °C in humidified 5% CO_2 atmosphere.

6.2.5 Immunofluorescence staining

Immunofluorescence staining was carried out with an protocol adapted from that previously described in [21].

For confocal laser scanning microscopy, cells on samples were washed 3 times in PBS, fixed for 20 min in an aqueous solution of 4% PFA, 65 mM PIPES, 25 mM HEPES, 10 mM EGTA and 3 mM $MgCl_2$ and subsequently permeabilized for 10 min in Millipore water containing 0.1% Triton X-100.

Before staining, unspecific binding sites were blocked with PBS containing 5% goat serum and 1% BSA for 30 min. All stainings were performed at room temperature and antibodies were dissolved in 1% FCS in PBS. Secondary antibody incubation was always performed in the dark. After all incubations of samples with antibody solutions, samples were washed 3 times with PBS.

After 24 h of HBC culture, one sample of each type was stained with a fibrinogen-actin-nuclei staining procedure. Fibrin fibers were stained using the monoclonal anti-human fibrinogen antibody (1:500, mouse iGG1 isotype, F9902, Sigma) for 1 h followed by incubation with anti-mouse Alexa Fluor® 555 (1:300, A21422, Molecular Probes, Switzerland). Actin filaments and nuclei were stained with Alexa Fluor® 488 labeled phalloidin (1:200, Invitrogen, Switzerland) and 40,6-diamidino-2-phenylindole (DAPI, 1:1000, Sigma), respectively, for 1 h.

At day 7 and 10 of HBC culture, two samples of each type were stained with an ALP-actin-DAPI staining procedure. Alkaline phosphatase (ALP) was stained using anti-human bone alkaline phosphatase (bALP, 1:1000, Developmental Studies Hybridoma Bank, USA) for 1 h followed by Alexa Fluor® 546 goat anti-mouse (1:400, A11029, Invitrogen) for 1 h. Actin filaments and nuclei were stained with Alexa Fluor® 488 labeled phalloidin (1:200, Invitrogen, Switzerland) and 40,6-diamidino-2-phenylindole (DAPI, 1:1000, Sigma), respectively, for 1 h.

Surfaces were viewed using a laser scanning confocal microscope (LSM 780, Carl Zeiss AG, Switzerland) with filter sets corresponding to the fluorescence of interest, 24 h post-seeding and after 7 and 10 days of culture. Image analysis was performed using Image J (version 1.44p for Mac). Images were taken every 2 mm along the sample (two lines per sample); nuclei were counted per area (mm^2).

6.2.6 Scanning electron microscopy (SEM)

One sample of each substrate type was analyzed in SEM after 8/14 min blood incubation. The samples were analyzed using the same protocol as described in Section 4.2.3.

6.3 Results and Discussion

Experiments were carried out on a titanium oxide coated smooth surface, a homogenous surface with a high-density layer of 39 nm particles and 39 nm particle-density gradients.

SEM investigation of the three surfaces after whole human blood incubation for 8 min showed only a few adhering platelets and no fibrin network formation on the surface (Figure 6.2). More platelets adhered to the smooth control surface than to the nanostructured surface. Fibrin fiber network formation could not be observed on any of the surfaces.

Figure 6.2 shows laser scanning confocal microscope images of HBC, cultured on the different surfaces for 24 h. The images showed a similar cell number along all samples.

On day 7 of cell culture, qualitative (Figure 6.3) as well as quantitative (Figure 6.5) results showed a larger number of attached cells on smooth surfaces than on nanostructured (39 nm) surfaces. 7 days post seeding, the number of HBCs was 4 times higher at the smooth position on the gradient ($\sim$ 200 cells/mm^2) than at the high-density end of the gradient ($\sim$ 50 cells/mm^2).

On day 10 of cell culture, qualitative (Figure 6.4) as well as quantitative (Figure 6.5) results showed the same trend as on day 7 with a larger number of attached cells on smooth surfaces than on nanostructured (39 nm) surfaces. 10 days post seeding, the number of HBCs was 6 times higher at smooth positions ($\sim$ 300 cells/mm^2) than at the position with maximum particle coverage on the nanoparticle-density gradient ($\sim$ 50 cells/mm^2).
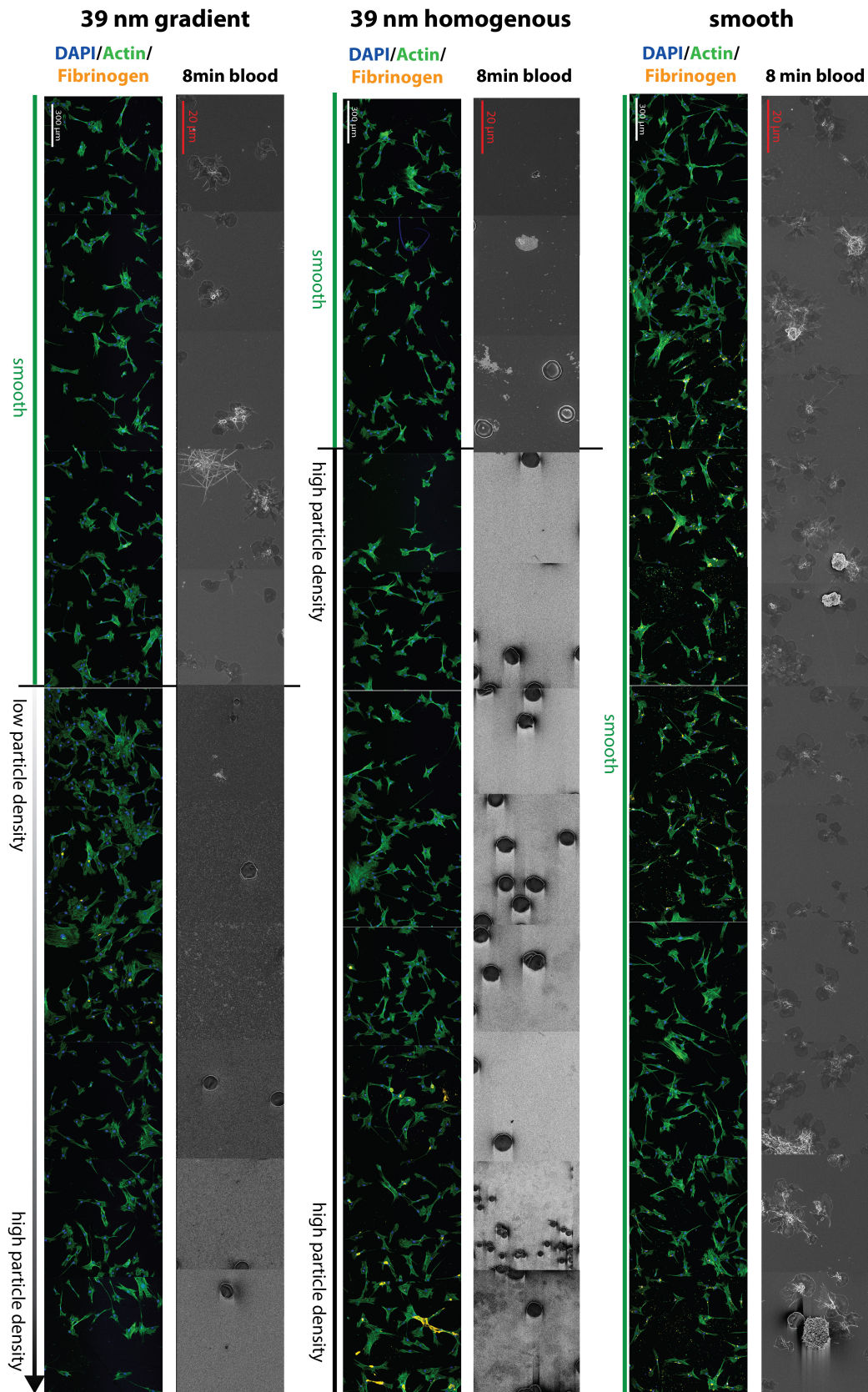
Figure 6.2: SEM images taken every 2 mm along smooth surface, homogenous high-density 39 nm surface and 39 nm particle-density gradient after incubation for 8 min with whole human blood. Laser scanning confocal microscope images of HBCs 24h post seeding, stained for f-actin (green), nuclei (blue) and fibrinogen (orange). Images where taken ever 2 mm along smooth surface, homogenous high-density 39 nm surface and 39 nm density gradient.

Figure 6.3: Laser scanning confocal microscope images of HBCs seeded on top of a preformed blood clot after incubation in whole human blood for 8 min on day 7, stained for f-actin (green), nuclei (blue) and ALP (red). Images where taken ever 2 mm along smooth surface, homogenous high-density 39 nm surface and 39 nm density gradient.

Figure 6.4: Laser scanning confocal microscope images of HBCs seeded on top of a preformed blood clot after incubation in whole human blood for 8 min on day 10, stained for f-actin (green), nuclei (blue) and ALP (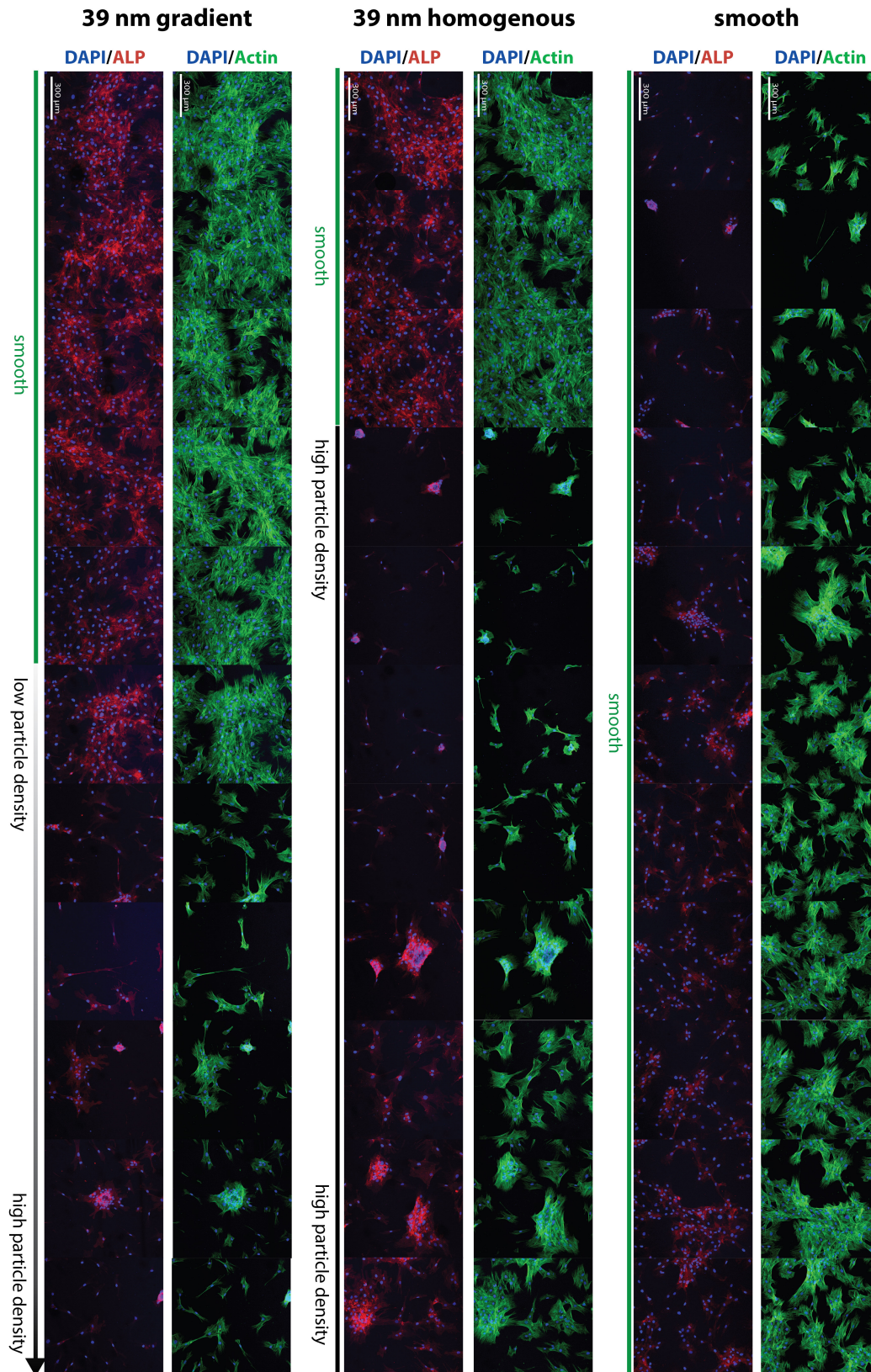red). Images where taken ever 2 mm along smooth surface, homogenous high-density 39 nm surface and 39 nm density gradient.

On day 7, cells on all surfaces showed positive alkaline phosphatase (ALP) staining (Figure 6.3) and had relatively increased intensity of alkaline phosphatase stain on day 10 of cell culture (Figure 6.4). The overall expression of ALP was increased on day 7 and day 10 on smooth surfaces compared to nanostructured surfaces (39 nm). As a control, cells were also cultured on TCPS in proliferation medium (negative control) and in differentiation medium (positive control). ALP expression was only seen in differentiation medium but not in proliferation medium (results not shown).
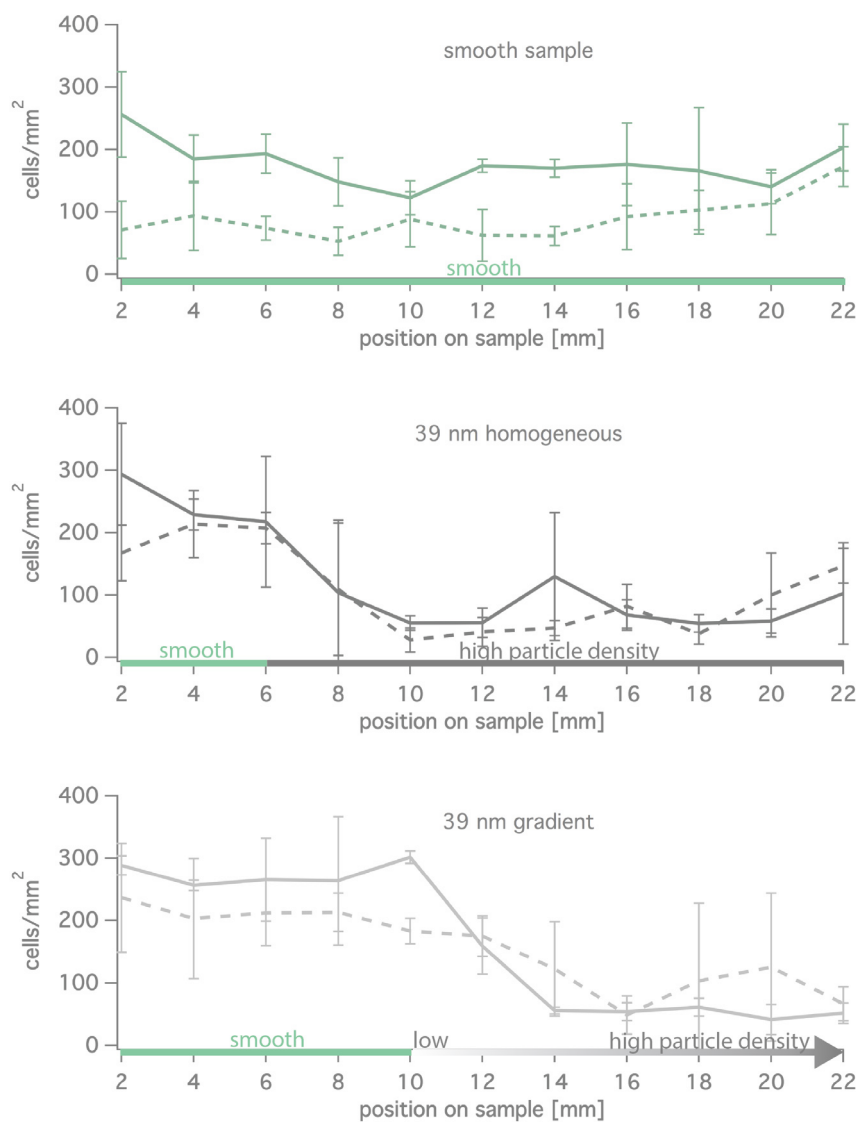
Figure 6.5: Cell adhesion on smooth samples, homogeneous 39 nm high-density samples and 39 nm particle-density gradients after whole blood incubation. Quantitative assessment of HBCs attached to the different surfaces after 7 (dashed) and 10 days (line). (Mean ± standard deviation, n = 4)
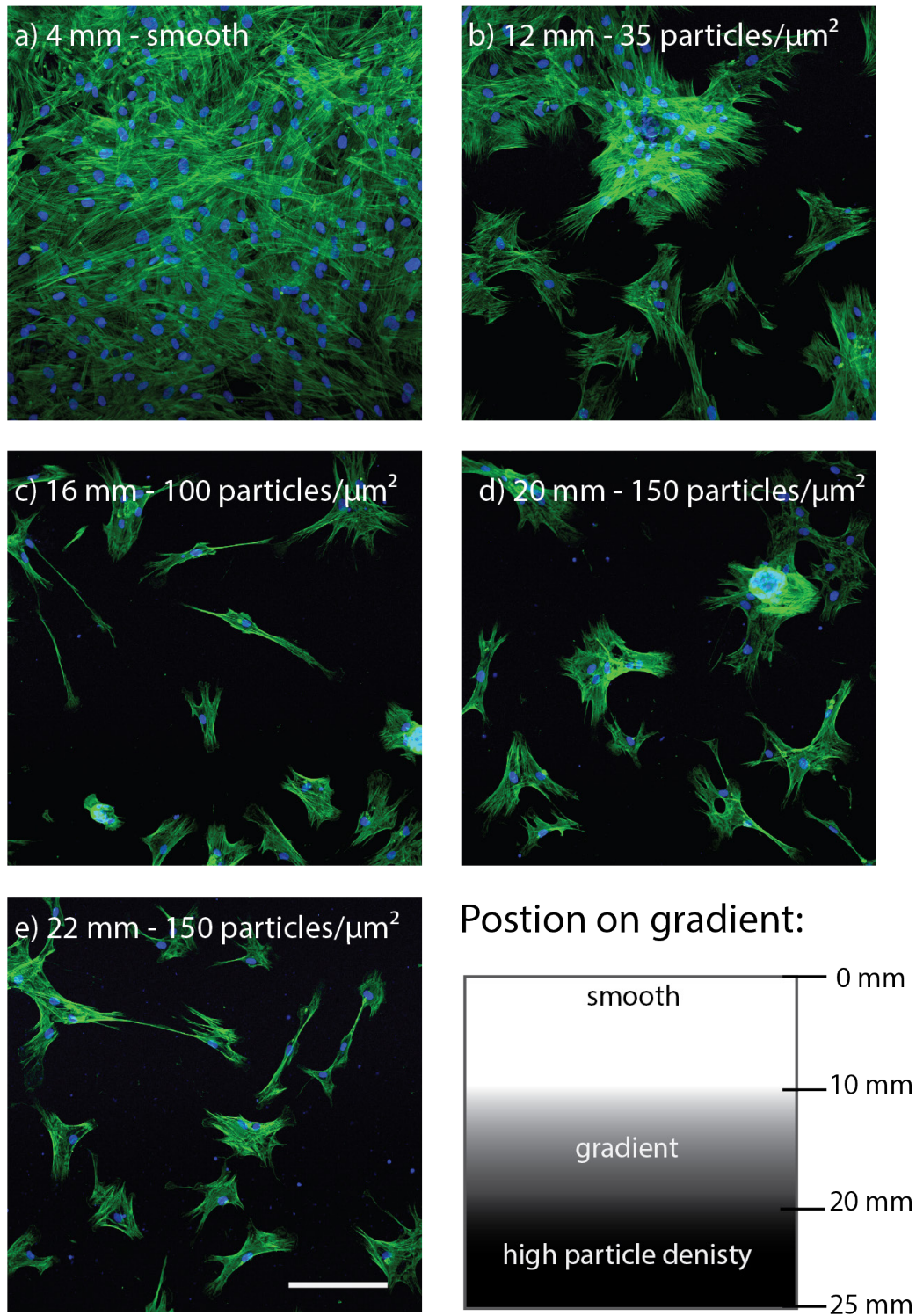
Figure 6.6: Fluorescence image of cell morphology at different position on the particle-density gradient. HBCs were cultured for 10 days and stained for actin (green) and nuclei (blue). Scale bar is 200 m.

The cell morphology changed with increasing particle coverage (Figure 6.6). At high particle coverage the HBCs were rather small in size and exhibit some long filopodia (Figure 6.6 c-e). With decreasing particle coverage, the cells were more spread ((Figure 6.6 b) and on the smooth surface, HBCs were well spread (Figure 6.6 a).

For experiments with 14 min blood incubation similar trends to those for the experiments with 8 min blood incubation were found for HBC culture after 24 h, 7 days and 10 days (results not shown).

Nanostructures formed by 39 nm particles seem to influence adhesion of HBC negatively. Laser scanning confocal microscope images of HBCs cultured on smooth, homogenous high-density 39 nm particle samples and 39 nm particle-density gradients on day 7 and 10 showed that cells adhere in larger numbers on the smooth surface than on the nanostructured surface; a low particle-density already decreased the amount of adhering HBCs.

SEM investigation of the three surfaces after whole human blood incubation for 8 min are shown in Figure 6.2. Contrary to our previous blood-adsorption experiments on the 39 nm gradients, more platelets adhered to the smooth control surface than to the nanostructured surface, while fibrin-fiber network formation could not be observed on all the surfaces. This might have been due to a delamination of the blood clot on the nanostructured surfaces. The pre-experiments to estimate the ideal blood incubation time with fluorescently stained fibrinogen showed a significant amount of fibrin network on a gradient sample after 8 min blood incubation. In Figure 6.7 it can be seen that the fibrin network lost the attachment to the surface and started to roll up and got accumulated at the edge of the sample. These findings led to the conclusion that due to the washing steps in PBS before HBC's seeding, the blood clot might delaminate from the surface and most of the blood components might get washed away prior the cell seeding. For the experiment with the 14 min blood incubation, we could observe how the blood clot delaminated after the cell

seeding on one of the gradients, leaving only a few cells on the surface (Figure 6.8).

The substrates used in the experiments were sputter coated on the topside with 6 nm TiO_2, while the bottom was covered with the native SiO_2 layer from the silicon wafer used to produce the substrates. The blood incubation chambers were designed such that only the top surface was directly exposed to the blood, but a small amount of blood can also get in contact with the bottom side of the substrate.
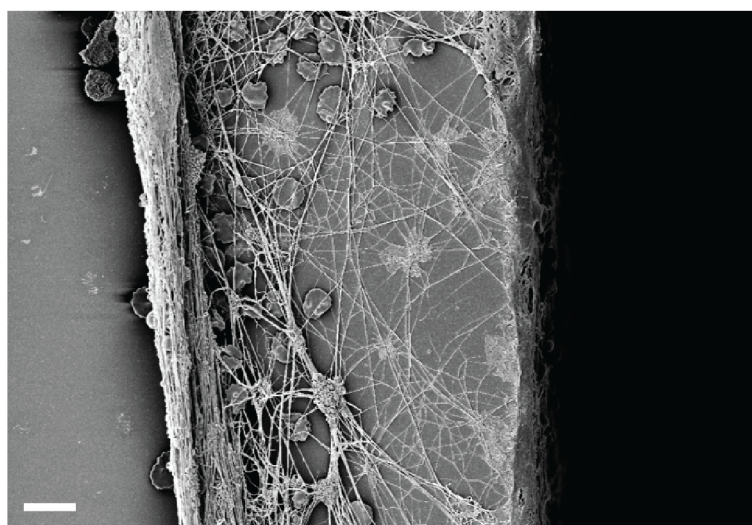
Figure 6.7: SEM image of the edge of a smooth sample after blood incubation for 14 min. It can be seen that the blot clot was not attached firmly to the surface and that it delaminated. Scale bar 10 m.
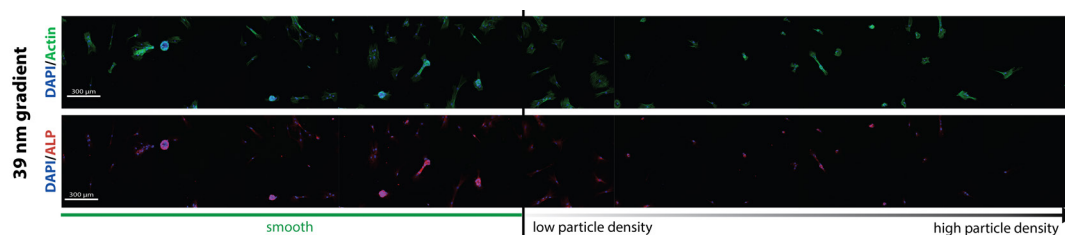
Figure 6.8: Laser scanning confocal microscope images of HBCs seeded on top of a preformed blood clot after incubation in whole human blood for 14 min on day 7. The blood clot got delaminated and only a few cells remained on the surface. Cells were stained for f-actin (green), nuclei (blue) and ALP (red). Images where taken ever 2 mm along a 39 nm particle-density gradient.

The observed accumulation of the blood clot at the sample edge (Figure 6.7) raised the question if the blood clot formation starts from the side/bottom of the sample instead of the TiO_2 coated surface. To answer this question, substrates with homogeneous high-density 39 nm particle coverage were sputter coated with 6 nm TiO_2 from both sides, just from the top or left uncoated (SiO_2 surface). The different substrates were incubated in whole human blood spiked with Alexa Fluor® 488 conjugated fibrinogen (final concentration 18 g/mL) for 9 min and analyzed via laser scanning confocal microscope (LSM 780, Carl Zeiss AG, Switzerland). No material-dependent effect on the blood-clot formation was observed (Figure 6.9).

It has been reported that implant surface properties influence the surface coverage and attachment strength of the fibrin clots on the implant surface [22]. It was suggested that increasing the surface roughness enhances the attachment strength of the fibrin clot, which is important to withstand the forces on the fibrin fibers during wound contraction [23]. The surface roughness of the used substrates is very low and cannot be changed; therefore, it is crucial to find the right blood incubation time for every donor to avoid the delamination of the blood clot due to contractions of the fibrin clot.

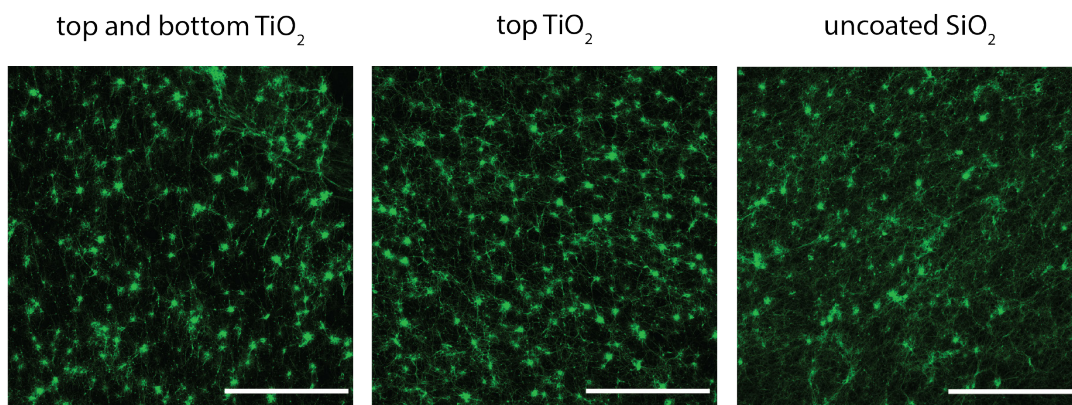top and bottom TiO_2 top TiO_2 uncoated SiO_2

Figure 6.9: Laser scanning confocal microscope images of stained fibrin network on substrates with a high-density 39 nm particle coverage sputter coated with 6 nm TiO_2 from both sides, just the top or left uncoated (SiO_2) after 9 min blood incubation.

A control experiment to compare the behavior of the HBCs seeded on top of the left-over blood clot that remains after delamination with HBCs on the same substrates without a prior incubation in whole human blood was carried out. Additionally, the experiment was carried out for 72 nm particle-density gradients and homogenous high-density particle samples with 72 nm particles (Figure 6.10).

Similar trends as for the blood-incubated substrates were seen; higher numbers of HBC's attached to the smooth control surface and to the smooth part of the gradients, while the number of cells decreased with increasing particle coverage, for 39 nm particles as well as for 72 nm particles.

The results presented in this study correlate well with previous *in vitro* studies from Kunzler *et al.* [14] which showed that rat calvarial osteoblasts (RCO) exhibit a significant decrease in proliferation on PLL-g-PEG-RGD-coated nanoparticle-density gradients with 72 nm particles at locations with higher particle coverage. Seven days post seeding, the number of osteoblasts was eight times higher at positions without particles compared to positions with maximum particle coverage.

The formation of focal adhesions is important for cell adhesion and is essentially controlled by the activation and clustering of the transmembrane protein integrin [24]. By controlling the position of single integrin binding sites, Arnold *et al.* [25] showed that focal contact requires an integrin binding site spacing of < 73 nm. For larger integrin spacings, cell attachment and spreading was limited.

For the highest particle density on gradients used in this work, the particle spacing was determined to be 132 and 85 nm for 72 and 39 nm particles, respectively. With decreasing particle density the particle spacing is even higher.
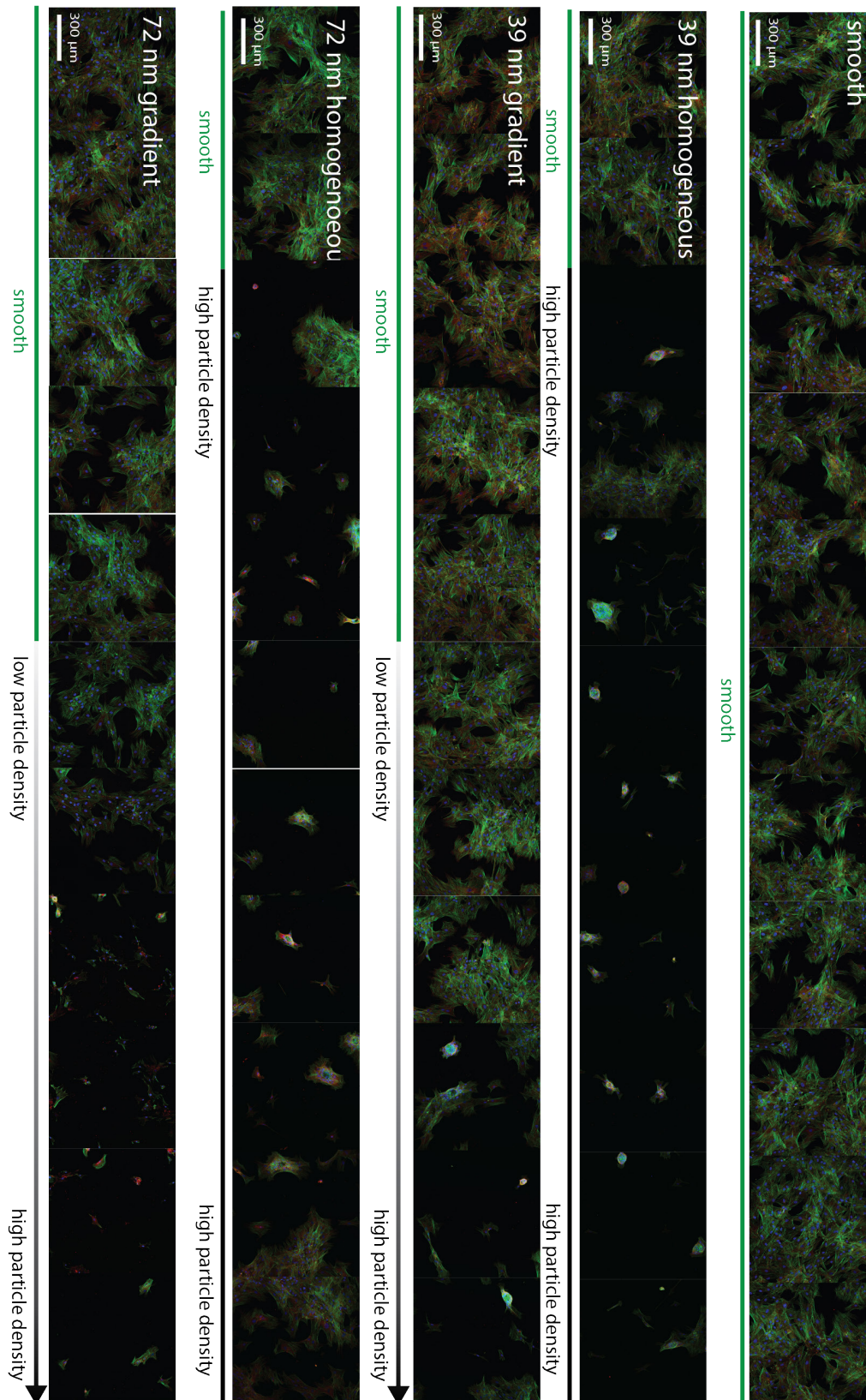
Figure 6.10: Laser scanning confocal microscope images of HBCs 7 days post seeding on top smooth, homogenous high-density nanoparticle (39 nm and 72 nm) and nanoparticle-density gradients (39 nm and 72 nm) substrates without prior blood incubation. Cells were stained for f-actin (green), nuclei (blue) and vinculin (red). Images where taken ever 2 mm along the substrates.

Kunzler and co-workers [14] explained that if it is assumed that a cell lies on top to the particles and integrins would solely bind to the particles, one would find only few cells all over the gradient. But on areas with lower particle coverage a higher number of cells with well-established focal adhesions were found. Therefore they suggested a mechanism whereby cell-binding sites (e.g. fibrinogen) on nanoparticles are likely to be accessible to cells, but a certain flexibility in the cell membrane would be needed to bind to cell-binding sites located at the surface between particles. The rigidity of the cell membrane hinders bulging of the membrane and prevents the integrins from reaching fibrinogen molecules between the nanoparticles when the inter-particle distance is small (Figure 6.11), while the proteins are easily accessible for the cell-membrane integrins when the inter-particle distance increases. At high particle density, the particles are close together and the effort of the cells to reach the bottom of the substrate by bulging down might cause a stress situation in the cell. In order to reduce the stress, the cell either minimizes the contact area with the substrate or moves to find another location with easier accessible binding sites. Both these behaviors could be observed for areas with high particle density (Figure 6.6 c-e). The filopodia might be an indication of cell migration. For proliferation, cells need to spread, and this is prevented by the nanoparticles in the high-particle-density area and might explain the low cell attachment.
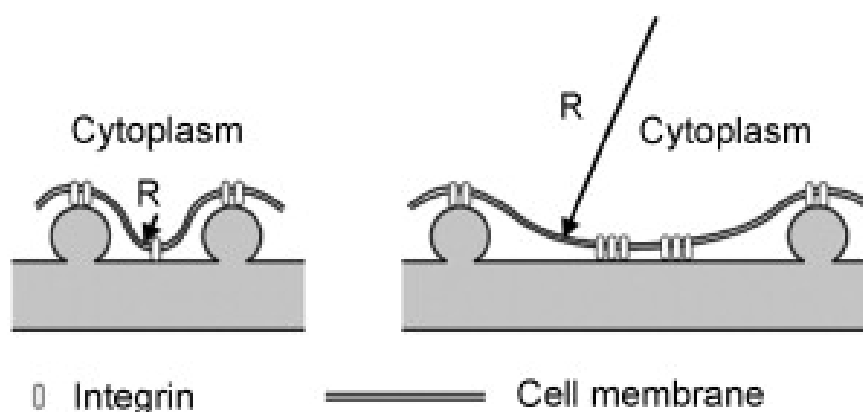
Figure 6.11: Schematic drawing of bending of the cell membrane for different inter-particle distances. On top of the particles the space for the attachment of integrins is limited. The cell has to distort to reach the substratum between the particles in order to establish more integrin bindings. Depending on the radius of curvature R the energy needed to bend the membrane changes. For a small radius of curvature (left) more energy is needed to form such a protrusion than for a larger radius of curvature (right). Additionally, there is more space to form integrin clusters between larger-spaced particles than between particles that are close together. Reprinted from [14], Copyright (2018), with permission from Elsevier.

A review by Biggs et al. [26] focused on the role of nanoscale structures on integrin-mediated adhesion and cellular function. They reported a decreased cellular adhesion for structures measuring 70-100 nm in height or with a feature diameter below 70 nm. But reducing the height of the nanofeatures to below 50 nm has been shown in numerous cell types to return the frequency of focal adhesion formation to that of cells cultured on planar controls.

In contrast to this finding, our study showed that particles with a diameter of 39 nm were also able to prevent adhesion and spreading of HBCs, to some extent also in the lower-particle-density area. The extent to which nanotopography influences cell behavior remains unclear, and further studies looking into the mechanism of cellular response to nanotopography are still needed.

6.4 Conclusions

Nanostructures formed by 39 nm particles seem to influence the adhesion and morphology of HBC. With decreasing inter-particle distance the number of HBCs decreased drastically and the spreading of HBCs was hindered. This indicates that the inter-particle distance plays a crucial role in the response of cells to nanofeatures. As suggested by Kunzler *et al.* [14] the observation of a decreased cell number on areas with high-particle coverage could be of interest in regard to potential applications in cell engineering and could be used as a simple approach to reduce cell adhesion on a surface in a permanent way.

The main goal of this study was to examine the effect of nanostructures and pre-adsorbed blood components on human bone cell behavior by means of particle-density gradients, but unfortunately due to the observed loss of blood clot prior to cell seeding, no conclusion about the influence of the pre-formed blood clot on the HBC behavior on nanostructured surfaces could be drawn. In order to examine the influence of the pre-formed blood clot, new experiments with smaller samples and shorter blood incubation times should be carried out, to avoid blood clot delamination. Additionally, control experiments with the same substrates and HBCs but without the pre-formed blood clot should be carried out simultaneously.

References:

[1] R.G. Harrison, The cultivation of tissues in extraneous media as a method of morpho-genetic study, The Anatomical Record 6(4) (1912) 181-193.

[2] C.J. Wilson, R.E. Clegg, D.I. Leavesley, M.J. Pearcy, Mediation of biomaterial-cell interactions by adsorbed proteins: a review, Tissue engineering 11(1-2) (2005) 1-18.

[3] R.A. Gittens, R. Olivares-Navarrete, Z. Schwartz, B.D. Boyan, Implant osseointegration and the role of microroughness and nanostructures: Lessons for spine implants, Acta Biomaterialia 10(8) (2014) 3363-3371.

[4] D.M. Brunette, P. Tengvall, M. Textor, T. P., Titanium in Medicine, Springer, Berlin 2001.

[5] T.P. Kunzler, T. Drobek, M. Schuler, N.D. Spencer, Systematic study of osteoblast and fibroblast response to roughness by means of surface-morphology gradients, Biomaterials 28(13) (2007) 2175-2182.

[6] A. Wennerberg, T. Albrektsson, Effects of titanium surface topography on bone integration: a systematic review, Clinical Oral Implants Research 20 (2009) 172-184.

[7] D.M. Brunette, B. Chehroudi, The Effects of the Surface Topography of Micromachined Titanium Substrata on Cell Behavior in Vitro and in Vivo, Journal of Biomechanical Engineering 121(1) (1999) 49-57.

[8] C. Zink, H. Hall, D.M. Brunette, N.D. Spencer, Orthogonal nanometer-micrometer roughness gradients probe morphological influences on cell behavior, Biomaterials 33(32) (2012) 8055-8061.

[9] A.B. Faia-Torres, M. Charnley, T. Goren, S. Guimond-Lischer, M. Rottmar, K. Maniura-Weber, N.D. Spencer, R.L. Reis, M. Textor, N.M. Neves, Osteogenic differentiation of human mesenchymal stem cells in the absence of osteogenic supplements: A surface-roughness gradient study, Acta Biomaterialia 28 (2015) 64-75.

[10] M.J. Dalby, N. Gadegaard, R. Tare, A. Andar, M.O. Riehle, P. Herzyk, C.D. Wilkinson, R.O. Oreffo, The control of human mesenchymal cell differentiation using nanoscale symmetry and disorder, Nature materials 6(12) (2007) 997-1003.

[11] R.G. Flemming, C.J. Murphy, G.A. Abrams, S.L. Goodman, P.F. Nealey, Effects of synthetic micro- and nano-structured surfaces on cell behavior, Biomaterials 20(6) (1999) 573-588.

[12] A. Rich, A.K. Harris, Anomalous preferences of cultured macrophages for hydrophobic and roughened substrata, Journal of Cell Science 50(1) (1981) 1-7.

[13] A. Ranella, M. Barberoglou, S. Bakogianni, C. Fotakis, E. Stratakis, Tuning cell adhesion by controlling the roughness and wettability of 3D micro/nano silicon structures, Acta Biomaterialia 6(7) (2010) 2711-2720.

[14] T.P. Kunzler, C. Huwiler, T. Drobek, J. Vörös, N.D. Spencer, Systematic study of osteoblast response to nanotopography by means of nanoparticle-density gradients, Biomaterials 28(33) (2007) 5000-5006.

[15] M.S. Lord, M. Foss, F. Besenbacher, Influence of nanoscale surface topography on protein adsorption and cellular response, Nano Today 5(1) (2010) 66-78.

[16] G. Mendonça, D.B.S. Mendonça, F.J.L. Aragão, L.F. Cooper, Advancing dental implant surface technology – From micron- to nanotopography, Biomaterials 29(28) (2008) 3822-3835.

[17] J.Y. Lim, J.C. Hansen, C.A. Siedlecki, J. Runt, H.J. Donahue, Human foetal osteoblastic cell response to polymer-demixed nanotopographic interfaces, Journal of the Royal Society Interface 2(2) (2005) 97-108.

[18] K. Cai, J. Bossert, K.D. Jandt, Does the nanometre scale topography of titanium influence protein adsorption and cell proliferation?, Colloids and surfaces. B, Biointerfaces 49(2) (2006) 136-44.

[19] R.A. Gittens, T. McLachlan, R. Olivares-Navarrete, Y. Cai, S. Berner, R. Tannenbaum, Z. Schwartz, K.H. Sandhage, B.D. Boyan, The effects of combined micron-/submicron-scale surface roughness and nanoscale features on cell proliferation and differentiation, Biomaterials 32(13) (2011) 3395-3403.

[20] D.A. Puleo, A. Nanci, Understanding and controlling the bone–implant interface, Biomaterials 20(23) (1999) 2311-2321.

[21] B.S. Kopf, A. Schipanski, M. Rottmar, S. Berner, K. Maniura-Weber, Enhanced differentiation of human osteoblasts on Ti surfaces pre-treated with human whole blood, Acta Biomaterialia 19 (2015) 180-190.

[22] D. Di Iorio, T. Traini, M. Degidi, S. Caputi, J. Neugebauer, A. Piattelli, Quantitative evaluation of the fibrin clot extension on different implant surfaces: An in vitro study, Journal of Biomedical Materials Research Part B: Applied Biomaterials 74B(1) (2005) 636-642.

[23] J.E. Davies, Mechanisms of Endosseous Integration, The International Journal of Prosthodontics 11(5) (1998) 391-401.

[24] C. Selhuber-Unkel, M. López-García, H. Kessler, J.P. Spatz, Cooperativity in Adhesion Cluster Formation during Initial Cell Adhesion, Biophysical Journal 95(11) (2008) 5424-5431.

[25] M. Arnold, E.A. Cavalcanti-Adam, R. Glass, J. Blümmel, W. Eck, M. Kantlehner, H. Kessler, J.P. Spatz, Activation of Integrin Function by Nanopatterned Adhesive Interfaces, ChemPhysChem 5(3) (2004) 383-388.

[26] M.J.P. Biggs, R.G. Richards, M.J. Dalby, Nanotopographical modification: a regulator of cellular function through focal adhesions, Nanomedicine: Nanotechnology, Biology and Medicine 6(5) (2010) 619-633.

Chapter **7**

Replication of morphological gradients for biological applications

7.1 Introduction

In order to use the morphological gradients described in Chapter 2 for biological studies, large numbers of samples with identical topographies are needed. Replicating a master gradient offers the advantage that large numbers of samples can be prepared that display exactly the same surface topography. As a result, the time-consuming and cost-intensive fabrication of masters can be reduced and the reproducibility of cell-culture assays on structured surfaces can be increased. Additionally, replication allows the roughness gradient to be transferred to different materials and the surface chemistry to be adjusted by an appropriate coating method. [1, 2]

In this chapter three different replication methods were examined for the replication of micro-, nano- and combined micro- and nanostructures.

In Section 7.2, micro-roughness gradients and samples with homogenous micro-roughness were replicated with the use of the epoxy-resin-based replica technique as described by Wieland *et al.* [2] and Schuler *et al.* [1]. This replication process consists of three steps. First a negative replica is cast from a master (e.g. in polyvinylsiloxane), second a positive epoxy replica is cast from the negative and in the third step the epoxy replica is coated with a material that is appropriate for the application, such as titanium in the case of implantology studies.

Section 7.3 deals with the replication of nanoparticle-density gradients with nanofeatures of diameters of 12, 39 and 72 nm. A two-step PDMS-epoxy-based replication technique previously introduced by Zink *et al.* [3] was used for the replication of 72 nm particle-density gradients. While the replication was possible, the process was very time consuming, not very reproducible and resulted in many faulty samples. Injection molding offers the possibility of being a more efficient and precise method for the production of identical structured samples. Therefore injection molding from polymer molds was applied for the replication of 72 nm particle-density gradients. The replication of smaller nanoparticles with a diameter of 12 and 39 nm was tackled with a new nanoimprint lithography method, called substrate conformal imprint lithography (SCIL) in sol-gel resist previously introduced by Marc Verschuuren [4].

2D orthogonal gradients with combined micro- and nanostructures are challenging due to the more than 3 orders of feature scales that need to be simultaneously replicated with high fidelity. In Section 7.4 the sol-gel-based resist used in SCIL was adapted to replicate 2D orthogonal gradients.

A brief description of the replication methods is presented in the following sections.

7.1.1 Injection molding

Injection molding (IM) is the most important technique for the production of polymer parts. It is the most efficient technology for the mass replication of polymeric parts and usually the cycle time is very short. Hot polymer is injected under high pressure and temperature conditions into a closed mold. The finished product cools down and solidifies inside the mold and is ejected at the end of the manufacturing cycle.

Standard isothermal injection molding (IIM) is able to replicate low-aspect-ratio structures, as small as 18 nm, as shown by Holzer *et al.* [5].

Replication becomes more difficult for complex topographies, particularly for high-aspect-ratio structures and polymers with high melt viscosities. Hong *et al.* [6] determined that the highest potential for accurate replication is offered by variothermal injection compression molding (VICM). In standard isothermal injection molding (IIM), shrinkage is compensated only by holding pressure, while in injection compression molding (ICM) an additional compression stroke reduces the uneven stress distribution obtained in IIM [7]. In IIM the temperature of a mold is maintained constant below the glass-transition temperature of the polymer throughout the molding cycle, while in VICM the mold is rapidly heated above the glass-transition temperature followed by injection and subsequent rapid cooling below the glass-transition temperature [7]. It was shown that a high mold temperature is beneficial for the replication quality of nickel nanostructures [8].

Molds used for the replication of thousands of parts by injection molding need to be highly resistant to thermal and mechanical fatigue. Silicon would be convenient to use as a stamp material, but because of it fragile nature, silicon structures are generally transferred into more ductile materials such as nickel, which can be easily electroplated on the silicon structures to produce negatives. For the production of several hundreds of samples, polymers such as PEEK or PPSU are preferred as mold materials, to avoid the rather slow and expensive process of nickel electroplating. Hot embossing into polymers offers fast and cost-efficient negative production directly replicated from silicon. An additional advantage of polymer inserts is the lower heat transfer, which results in a much higher contact temperature when the polymer melt initially contacts the mold and forms the structures. Therefore the replication quality from injection molding of polymer molds is comparable to results obtained from variothermal injection molding. Hobaek *et al.* [9] showed that ceramic coatings with a lower heat transfer than nickel enhance the contact temperature at the mold-melt interface and improve the replication of nanostructures compared to uncoated nickel. [7]

7.1.2 Substrate conformal imprint lithography (SCIL)

Substrate conformal imprint lithography (SCIL) is a novel wafer-scale nanoimprint technology for large-area patterning with nanometer resolution that was invented by Marc Verschuuren at Philips Research [4]. It combines the nanometer resolution and low pattern distortion characteristic of rigid stamps, with the flexibility and robustness of soft stamps. [10]

Nanoimprint lithography (NIL) creates structures by imprinting a rigid stamp into a low-viscosity resist. It is an embossing tool with nanometer resolution. Thermoplastic, thermo-curing or UV-curing polymers are used as resists. [11] The advantages of NIL are high resolution and low pattern deformation [11-13]. But the use of a rigid stamp causes several disadvantages, the stamp fabrication is expensive and the process is sensitive to contamination, such as dust particles that may inhibit close contact between stamp and resist over large areas [14]. Additionally a non-stick layer is needed to prevent chemical adhesion of the imprint resist to the stamp [4] and the release of the stamp from the cured resist without resist pattern deformation or destruction is difficult [14].

As an alternative to NIL, soft lithography has been developed [15], where an elastomeric stamp is used. The soft stamp can easily make conformal contact with the substrate over large areas, stamp removal is easily accomplished by a peeling action and multiple stamps can be made from one master at low cost. But stamp deformation (pairing, sagging) limits pattern fidelity, placement accuracy and resolution [15, 16].

With the use of a three-layer composite stamp composed of two rubber layers (PDMS) on a thin glass support, SCIL combines the resolution and accuracy of rigid stamps with the flexibility of soft-stamp methods [4]. SCIL offers wafer-scale replication with sub-50 nm resolution, high throughput and minimal pattern deformation [17]. Stamps are composed of a thin glass carrier plate, a soft PDMS intermediate layer and a pattern-containing layer made of

special PDMS with a high Young's modulus [18] (Figure 7.1). The thin glass is flexible in the out-of-plane direction to allow conformal contact to be made, but it is stiff in the in-plane direction, which avoids pattern distortion [18].
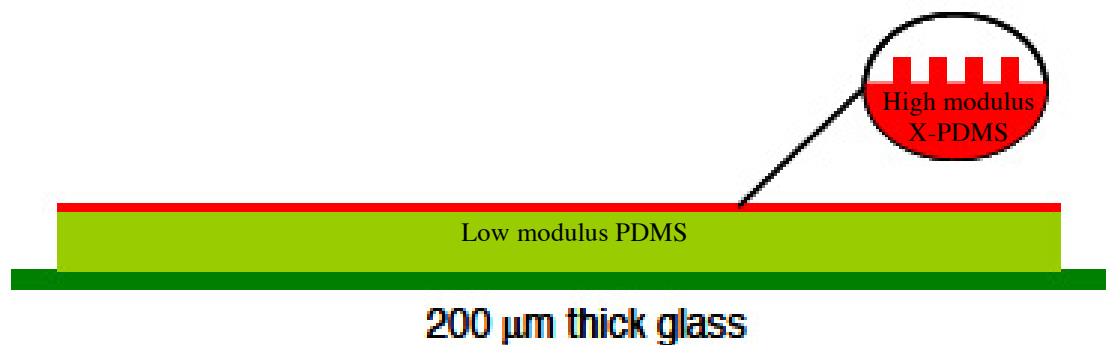

Figure 7.1: Schematic of a SCIL composite stamp consisting of a thin glass plate with two-layer silicone rubber stamp on top. The top PDMS layer consists of high-modulus X-PDMS, which allows accurate replication of nanometer-sized structures and contains the pattern, while the low modulus of the bottom PDMS (Sylgard 184) layer helps to make conformal contact during imprinting. Adapted from [4].

SCIL can be used with conventional NIL resists but for optimal performance Marc Verschuuren [4] developed a new inorganic-silica-forming imprint resist based on a sol-gel route [19, 20], which allows direct patterning of silicon oxide glass with nanometer resolution. The sol-gel resist hardens via the diffusion of solvent into the PDMS stamp material.

The base component of silicon sol-gel chemistry is alkoxide tetra-methyl-ortho-silicate (TMOS), $Si(OCH_3)_4$. TMOS can react with water (hydrolysis) to yield methanol and a silanol group $(CH_3O)_3Si$-OH. Then two silicon hydroxyl groups can react under release of water (condensation) to form a stable Si-O-Si bond, the basis of a silicon oxide glass. [4]

The detailed procedure for the preparation of inorganic sol-gel imprint resist is described in [21].
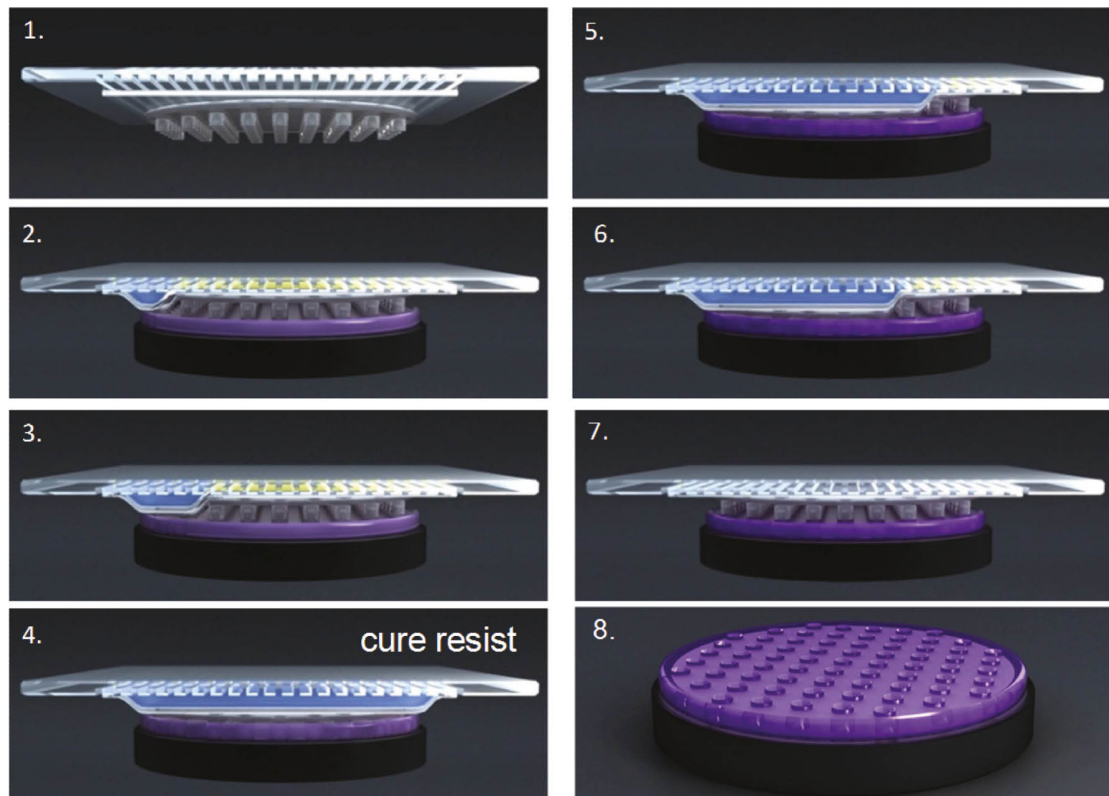
Figure 7.2: SCIL imprint process: (1) Mounting the X-PDMS composite stamp on the groove plate of SCIL tooling. (2) A silicon wafer with a sol-gel resist coating is loaded. (2-4) Sequential pressurizing of the grooves leads to a contact-line that pushes away the air and the stamp becomes sucked into the sol-gel resist by capillary forces. (4) Thermal curing. (5-7) Release of the stamp in a peeling-like action by sequential application of vacuum to the grooves. (8) Imprinted wafer. Reprinted from [22], Copyright (2018), with permission from Elsevier.

After applying the sol-gel based resist on a silicon wafer by spin coating, the stamp is sequentially brought into contact with the resist (see Figure 7.2). For this the stamp is attached to a grooved vacuum plate. The grooves get pressurized stepwise to form full contact on a wafer coated with sol-gel resist. With the sequential pressurizing of the grooves, a line contact pushes away the air and the stamp is sucked into the sol-gel resist by capillary forces. Solvents diffuse into the PDMS stamp and increase the concentration of reactive groups (Si-OH and Si-OR), which condense to form a Si-O-Si bonded 3D network. After curing of the resist, the stamp is released in a smooth peeling-like action by sequential application of vacuum to the grooves. The resulting patterned layer consist of 88 wt% silicon oxide, is transparent and stable in air up to 450 °C. [23, 24]

7.2 Microstructure replication

The fabrication and replication of homogenous micro-roughness masters was previously published in Dental Materials [25].

7.2.1 Experimental

7.2.1.1 Master

Micro-roughness gradients were produced as described in Section 2.3. Additionally, homogenous masters with different roughness values were prepared in a similar way as the gradients [26]. After sandblasting of the aluminum sheets with corundum particles, a uniformly rough surface morphology was achieved. In a second step, the sandblasted substrate was completely immersed into a chemical polishing solution containing 77.5% (v/v) phosphoric acid, 16.5% (v/v) sulfuric acid and 6% (v/v) nitric acid. The substrates were exposed to the chemical polishing solution for 33, 12 or 2 min, resulting in homogenous roughness masters with a R_a value of approximately 1, 2 or 4 µm, respectively. [25]

7.2.1.2 Poly-vinylsiloxane (PVS) negative – epoxy replica (positive)

In order to produce multiple identical samples, the masters were replicated, as previously described by Wieland *et al.* [2] and Schuler *et al.* [1].

Negatives of the micro-roughness gradients or homogenous roughness masters were prepared in polyvinylsiloxane (PVS, PROVIL novo light, Heraeus-Kulzer, Switzerland). Negatives of gradients were directly used to cast epoxy. The two components of the epoxy resin (EPO-TEK 302-3M, Polyscience AG, Switzerland) were thoroughly mixed in a centrifuge tube in the ratio 100:45, as recommended by the manufacturer. The mixture was then degassed in a

centrifuge for 5 min at 4000 RPM. Epoxy resin was cast onto the PVS negatives and cured at 65 °C for at least 24 h. The cured, positive epoxy replicas were then removed from the negative and cleaned for 20 min in 2 vol% Hellmanex solution (HELLMA GmbH & Co, Müllheim, Germany) followed by 20 min in MilliQ water in an ultrasonic bath. Afterwards they were extensively rinsed 10 times in MillQ water, pre-dried in a stream of nitrogen and left to dry completely in air overnight. Epoxy replicas used for cell tests, were sputter-coated with 40 nm of metallic titanium (Reactive magnetron sputtering, Paul Scherrer Institute, Villigen, Switzerland), in order to mimic a bone-implant surface. It has been shown that in order to block the auto-fluorescence of the epoxy sufficiently, the replicas need to be coated with a minimum of 40 nm titanium [27].

7.2.1.3 Characterization

The micrometer-scale roughness of the titanium-coated epoxy replicas and the master was analyzed by an optical profilometer and SEM as described in Section 2.3.1.2.

7.2.2 Results and Discussion

The accuracy of the replica was monitored by comparing its structure (Figure 7.3 b) with the structure on the master (Figure 7.3 a) before replication. The epoxy replica showed the characteristic high fidelity of the process and all features down to the sub-micrometer range were accurately replicated [27].
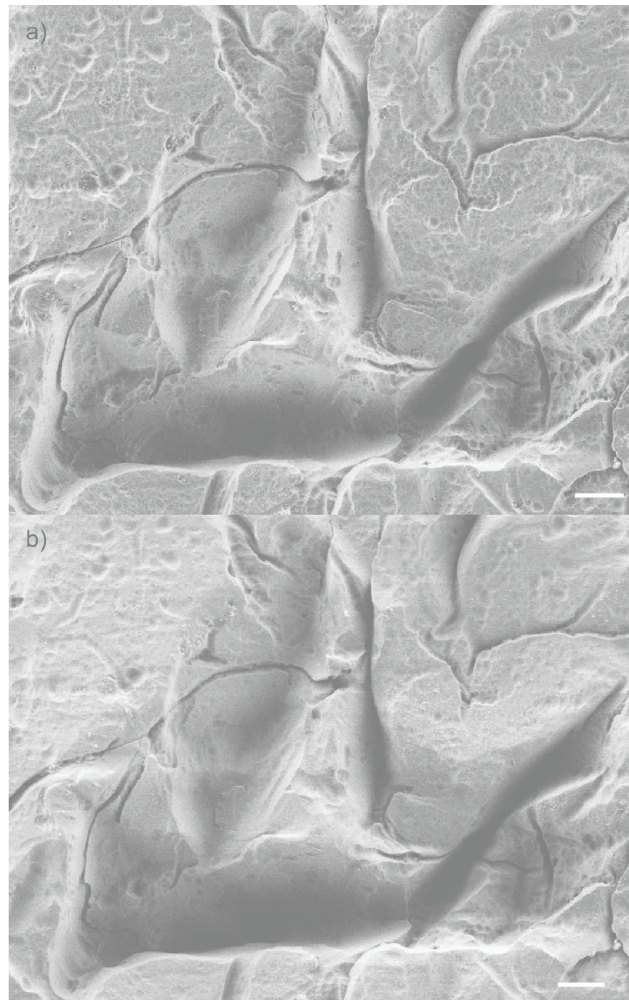

Figure 7.3: SEM images of a feature of a) the aluminum master and b) its epoxy replica. The scale bar is 10 m for all images. Adapted from [27].

The roughness values R_a of epoxy replicas along a 30-mm-long micro-roughness gradient were similar to those of the aluminum master (Figure 7.4).
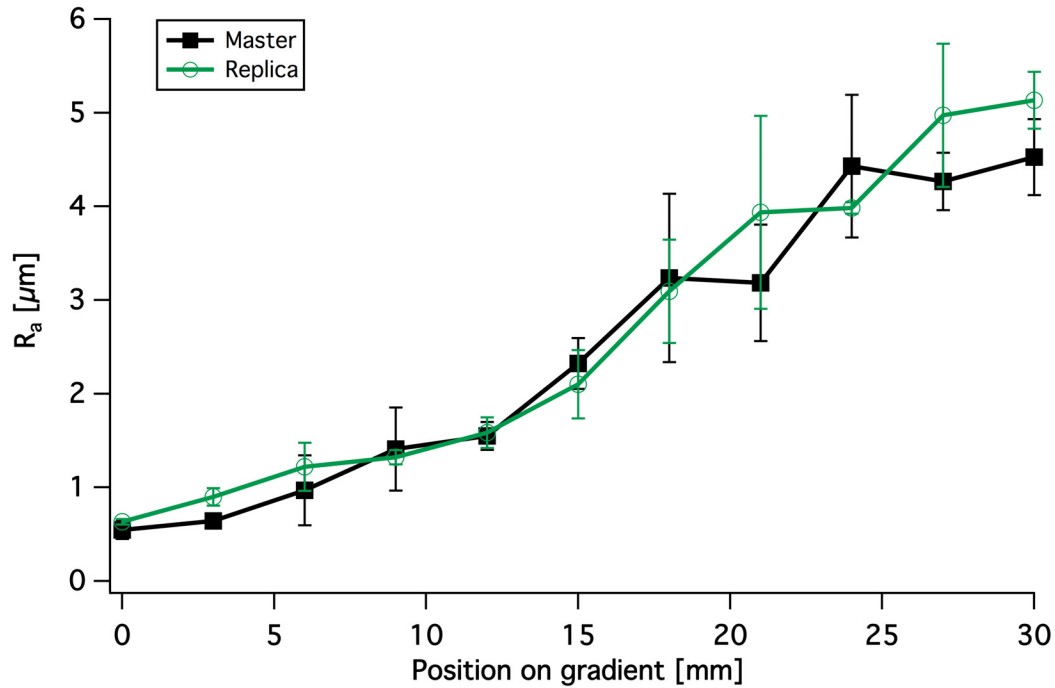
Figure 7.4: Roughness parameter R_a of a 30 mm long micro-roughness gradient on the aluminum master (black) and epoxy replica (green).

The roughness values R_a and R_q of Ti-coated epoxy replicas with homogenous roughness were similar to those found on the corresponding aluminum masters. (Table 7.1)

Table 7.1: Polishing time and standard roughness values calculated from optical profilometer profiles for master and its TiO_2-coated epoxy replica. Replica data was previously published in [25].

Polishing time, min	33 min	12 min	2 min
Master (n=3)			
R_a (m)	1.40 ± 0.26	2.28 ± 0.34	3.91± 0.39
R_q (m)	1.81 ± 0.35	2.95 ± 0.51	5.15 ± 0.69
R_z (m)	9.36 ± 4.88	22.36 ± 6.97	40.92 ± 12.15
Replica (n=9)			
R_a (m)	1.19 ± 0.24	2.30 ± 0.27	4.02 ± 0.27
R_q (m)	1.46 ± 0.31	3.42 ± 0.68	5.25 ± 0.57
R_z (m)	7.07 ± 3.53	36.2 ± 17.38	40.64 ± 19.07

R_a—arithmetic average roughness; R_q—root mean square roughness; R_z—arithmetic average of maximum peak-to-valley height. Data are presented as mean ± D.

The physical-vapor-deposited titanium film observed on top of the epoxy replicas was found to be homogenous. SEM investigation of freeze-fractured cross-sections of Ti-coated epoxy samples with a R_a of approximately 4 m showed that the epoxy surface is entirely covered with a 40 - 55 nm thick layer of Ti (Figure 7.5). There was no evidence of a thinner coating on peaks or thicker coating in valleys. (Data published in Appendix A of [25])
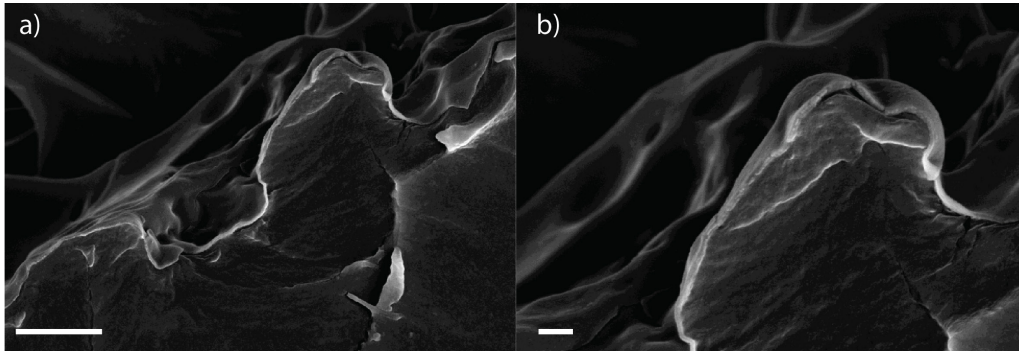

Figure 7.5: SEM images of the physical-vapor-deposited Ti film of an epoxy replica a) 50 kX magnification, scale bar 1 m b) 100 kX magnification, scale bar 200 nm. Reprinted with permission from [25] Appendix A.

250 replicas of each homogenous micro-roughness master (R_a approximately 1, 2 and 4 m) and 250 replicas of an untreated silica wafer were produced with the 2-step PVS-epoxy method. The 1000 replicas were sputter-coated with 40 nm Ti and used to study proliferation, behavior, and differentiation of osteoblasts on surfaces with different microroughness, in a collaboration with Professor Schedle from the Division of Conservative Dentistry and Periodontology, School of Dentistry, Medical University of Vienna, in Austria.

The work resulted in a paper that was published in Dental Materials [25], the corresponding manuscript can be found in Appendix A of this thesis.

7.3 Nanostructure replication

7.3.1 Replication in epoxy

7.3.1.1 Experimental

Master fabrication

Nanoparticle-density gradients made from silica particles with diameters of 12, 39 or 72 nm were produced as previously described in Section 2.2. Homogenous particle-density samples have been produced with the same technique as the gradients, by dipping about 17 mm of a negatively rendered silicon wafer (20 × 20 mm²) for 10, 20 or 40 min into 0.004 wt% 72 nm particle suspension and flushing with 500 ml of MilliQ to end the particle adsorption. The different dipping times resulted in homogenous particle-density masters with particle-densities of 11.02 ± 5.6, 27.72 ± 5.4 or 48.26 ± 4.9 particles/ m² respectively. Prior to the stamp (negative) fabrication, the master surfaces were activated in oxygen plasma (PDC_32G, Harrick Plasma, USA) at high RF-level for 2 min and subsequently coated with a monolayer of perfluorosilanes by vapor-phase deposition (1H,1H,2H,2H-perfluorooctyltrichlorosilane, ABCR, Germany) to prevent the mold material from sticking to the master.

PDMS negative

Replication of nanoparticle-density gradients with 12, 39 or 72 nm features was performed, adapting a technique previously developed by Zink *et al.* [27] where they showed that the conventional replication technique developed earlier in the group [1, 2, 26] for microfeatures was not able to replicate nanoparticles smaller than 100 nm in full detail. Zink *et al.* [27] developed a new 2-step replication protocol in which a high fidelity polydimethylsiloxane (hf-PDMS) [28] was used to produce the negative instead of PVS. With this method Zink and co-workers were able to replicate nanofeatures with a diameter of 72 and 39 nm.

After the perfluorosilane coating of the master gradients (12, 39 and 72 nm) a drop of hf-PDMS (kindly provided by Heiko Wolf; IBM Research, Zurich Research Laboratory, Switzerland) was placed on the gradient and covered with a piece of Sylgard 184 PDMS (Dow Corning, USA) or PVS. The so formed "sandwich" was either exposed to a vacuum in a desiccator for 1 h at approximately 7 mbar prior to curing or immediately cured at 60 °C for 24 h. After curing, the master gradient was removed from the mold and used again for the fabrication of other molds.

POP negative

Negative replicas of the master were prepared as described by Csucs *et al.* [29]. Affinity VP 8770 (Dow Chemical Company, Midland, MI, USA), a polyolefin plastomers (POP) was shown to perform better than PDMS in the nanometer range when used as stamps (negatives) in micro-contact printing [29]. Firstly, POP pellets were melted into bars of $30 \times 90 \times 4 \ mm^3$ at 190 °C under low pressure for 10 min (Figure 7.6A) using an appropriate metal template. To avoid the sticking of the POP to the heated metal plates, thin polyimide foils were placed in between. The solid polymer bars were allowed to cool to room temperature, removed from the template and cut into three $30 \times 30 \times 4 \ mm^3$ bars with a razor blade, rinsed with ethanol and dried under a stream of nitrogen. In a second step, the bars were placed over a stamp master ($25 \times 25 \times 0.5 \ mm^3$) and two spacers ($25 \times 25 \times 0.5 \ mm^3$) and jammed between two silicon wafers. This "sandwich" was then placed between two heated plates at 130 °C. The "sandwich" was allowed to warm up for 30 s without any load, then a 200 g weight was added on top for 5 min, which was later increased to 700 g for 4 min (Figure 7.6B). After cooling, the POP negatives were peeled off the masters. Prior to usage, the POP stamps were cleaned in an ultrasonic bath with toluene and isopropanol for 5 min each and dried in a stream of nitrogen.
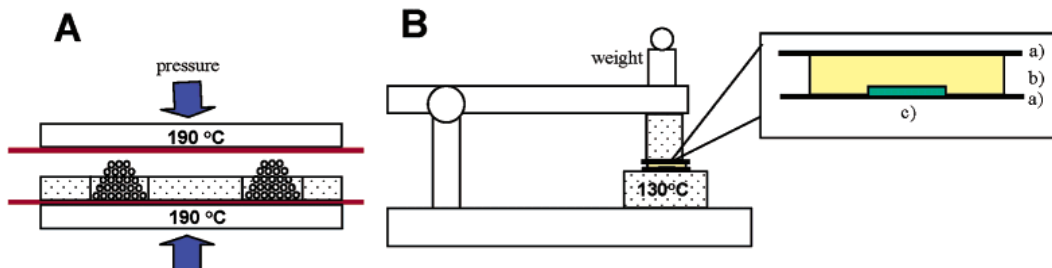
Figure 7.6: Two main steps of POP negative formation. A) Melting the POP pellets into bars. Two polyimide foils indicated by red lines. B) Replicating the master into the POP bar: a) silicon wafer (black line) b) POP bar (yellow) c) master placed on top of a spacer in order to increase the depth of the mold (green). The sandwich was heated from both sides at 130 °C. Reprinted with permission from [29]. Copyright (2018) American Chemical Society.

Epoxy replicas (positives)

The PDMS and POP stamps were used to produces epoxy replicas. The two components of epoxy resin (EPO-TEK 302-3M; Epoxy Technology, Polyscience AG, Switzerland) were mixed in a 100:45 ratio by weight, as recommended by the manufacturer. The mixture was then degassed in a centrifuge for 5 min at 4000 RPM. The epoxy was cast into the molds and the molds were either exposed to a vacuum in a desiccator for 1 h at approximately 7 mbar prior to curing or immediately cured at 65 °C for 24 h. The cured, positive epoxy replicas were then removed from the molds and cleaned for 20 min in 2 vol% Hellmanex solution (HELLMA GmbH & Co, Müllheim, Germany) followed by 20 min in MilliQ water in an ultrasonic bath. Afterwards they were rinsed extensively 10 times in MillQ water, dried in a stream of nitrogen and left to fully dry overnight in air.

Characterization

Replicas of particle-density gradient samples were analyzed by SEM and AFM as described in Section 2.2.1.2.

7.3.1.2 Results and Discussion

With the replication technique introduced by Zink *et al.* [3] it was not possible to replicate nanoparticles smaller than 39 nm in diameter. Figure 7.7 d-f) show AFM images of positive epoxy replicates cast into a high-fidelity PDMS negative. The technique was able to replicate nanoparticles with 72 nm (Figure 7.7 d) and 39 nm (Figure 7.7 e) in diameter. The AFM measurements showed that the height was not preserved fully as the height was reduced by about 15% during the process. There were some particle clusters that were not replicated in full detail and therefore appeared to be bigger beads on the surface (Figure 7.7 d). Nanoparticles with a diameter of 12 nm could not be replicated in full detail - the epoxy positive showed particle clusters with a height of around 6 nm and a width of around 50 nm instead of 12 nm (Figure 7.7 f).

AFM measurements of the epoxy positives made from POP negatives showed no improvement over the use of hf-PDMS negatives (Figure 7.7 g-i). The particle height was reduced drastically (e.g. from 62 nm down to 30 nm) and the particles were not replicated in full detail - bigger clusters were found as well.

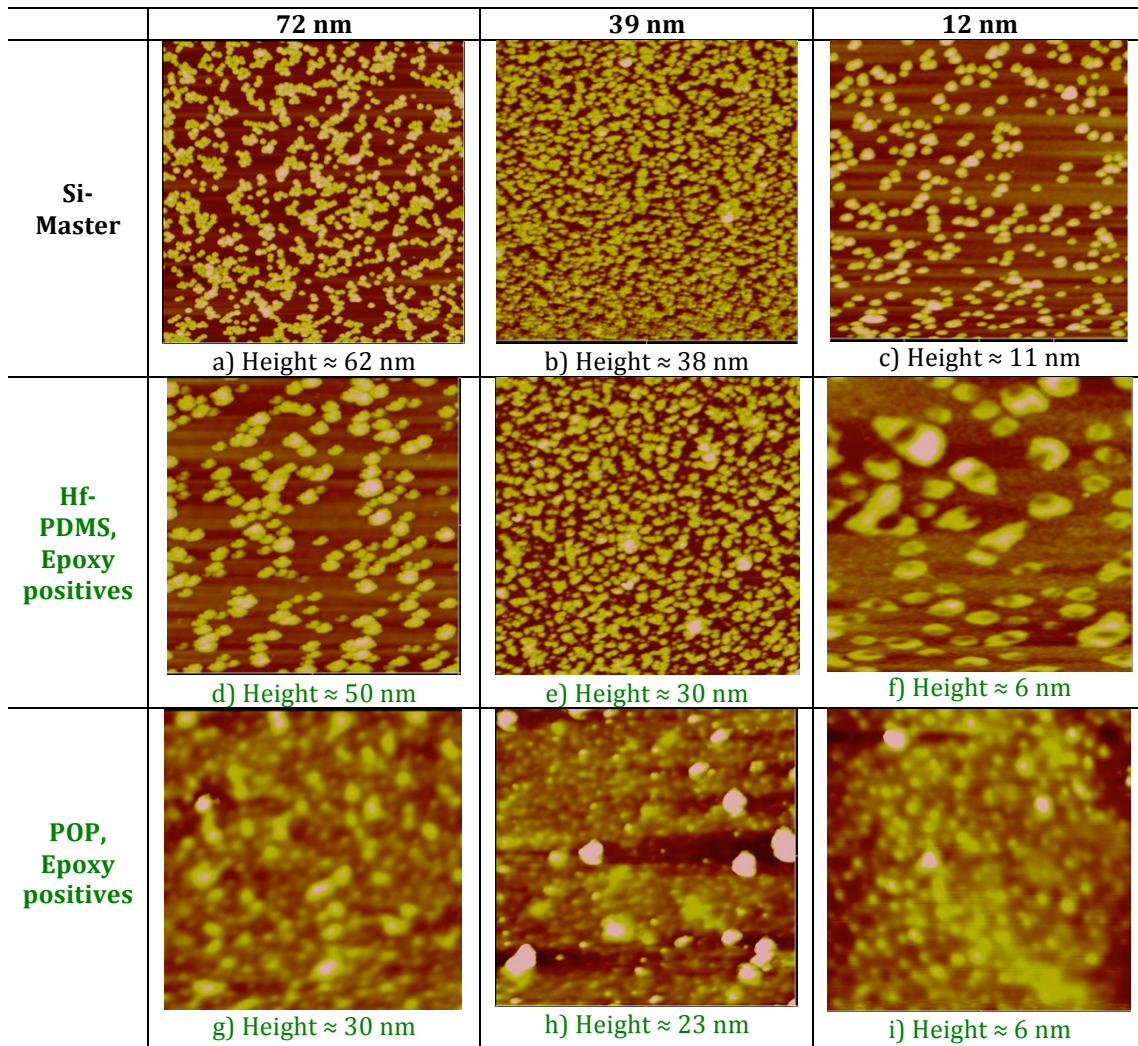|	**72 nm**	**39 nm**	**12 nm**
Si-Master	a) Height ≈ 62 nm	b) Height ≈ 38 nm	c) Height ≈ 11 nm
Hf-PDMS, Epoxy positives	d) Height ≈ 50 nm	e) Height ≈ 30 nm	f) Height ≈ 6 nm
POP, Epoxy positives	g) Height ≈ 30 nm	h) Height ≈ 23 nm	i) Height ≈ 6 nm

Figure 7.7: AFM study comparing hf-PDMS replication technique to POP replication technique. Images a-c) show the Si master of 72, 39 and 12 nm particles. Images d-f) show the epoxy positives of hf-PDMS negatives and images g-i) the epoxy positives of POP negatives. The image size is 5×5 μm^2 for the samples with 72 nm and 39 nm particles (a,b,d,e,g,h) and 1×1 μm^2 for the 12 nm particles (c,f,i).

A possible reason for the bad replication with the two-step process in hf-PDMS and epoxy could be trapped air. Air could be trapped between the master and the hf-PDMS during the negative fabrication, hindering the PDMS to follow the master structure in detail (Figure 7.8 a). Air could also get trapped in the pores of the negative, hindering the epoxy to fill the pores completely (Figure 7.8 b). To overcome this issue, vacuum was applied during negative and positive fabrication. The uncured master/hf-PFMS/PVS "sandwich" or cast epoxy were exposed to a vacuum (~ 7 mbar) in a desiccator for 1 h prior to curing in the oven at 65 °C.
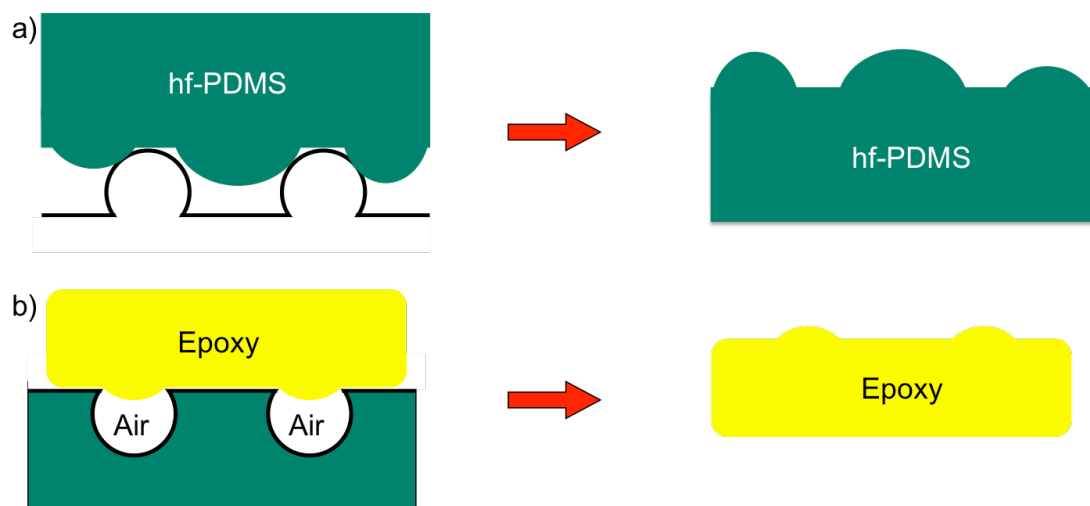
Figure 7.8: Scheme of the possible reasons for bad replication with the two-step replication method. Air might be trapped during a) the negative formation in hf-PFMS or b) the positive formation in epoxy.

Figure 7.9 shows that the replication quality was improved by the addition of a vacuum step for the negative and the positive fabrication. The AFM measurements showed that the height was fully preserved for 72 and 39 nm particles, while the height of the 12 nm particles was reduced by about 15% during the process (from 11 to 9 nm). The round shape of the 12 nm particles was preserved during replication with the added vacuum steps compared to the replication without the vacuum (Figure 7.7 f).

SEM images from two different positions on three consecutive replicas made from the first negative of a homogenous 72 nm particle-density master with a density of 10 particles/ m² showed that the replication quality varies between different positions on the same replica (Figure 7.10 a and b), as well as between the different replicas (Figure 7.10 a-c).

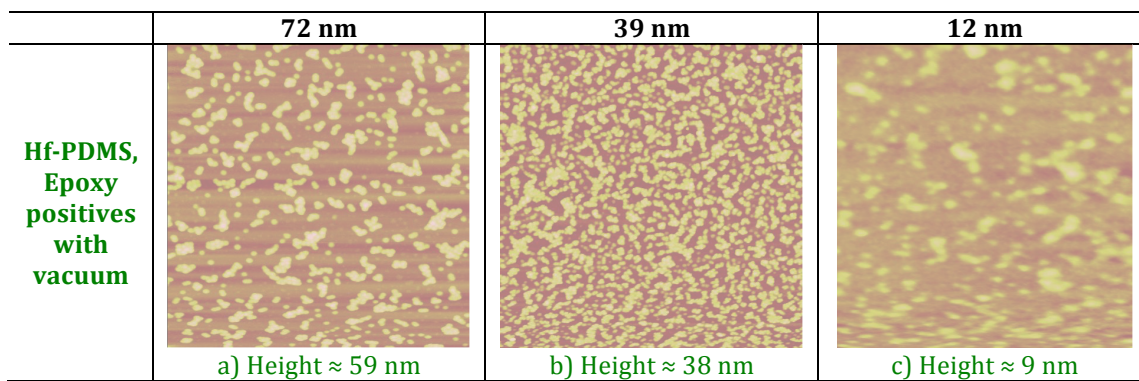|	72 nm	39 nm	12 nm
Hf-PDMS, Epoxy positives with vacuum	a) Height ≈ 59 nm	b) Height ≈ 38 nm	c) Height ≈ 9 nm

Figure 7.9: AFM images of epoxy replicas of a) 72, b) 39 and c) 12 nm particle-density gradients. Vacuum was applied for the negative fabrication in hf-PDMS and the positive fabrication in epoxy. Image size is 5×5 μm^2 for the samples with 72 nm and 39 nm particles (a and b) and 1×1 μm^2 for the 12 nm particles (c).

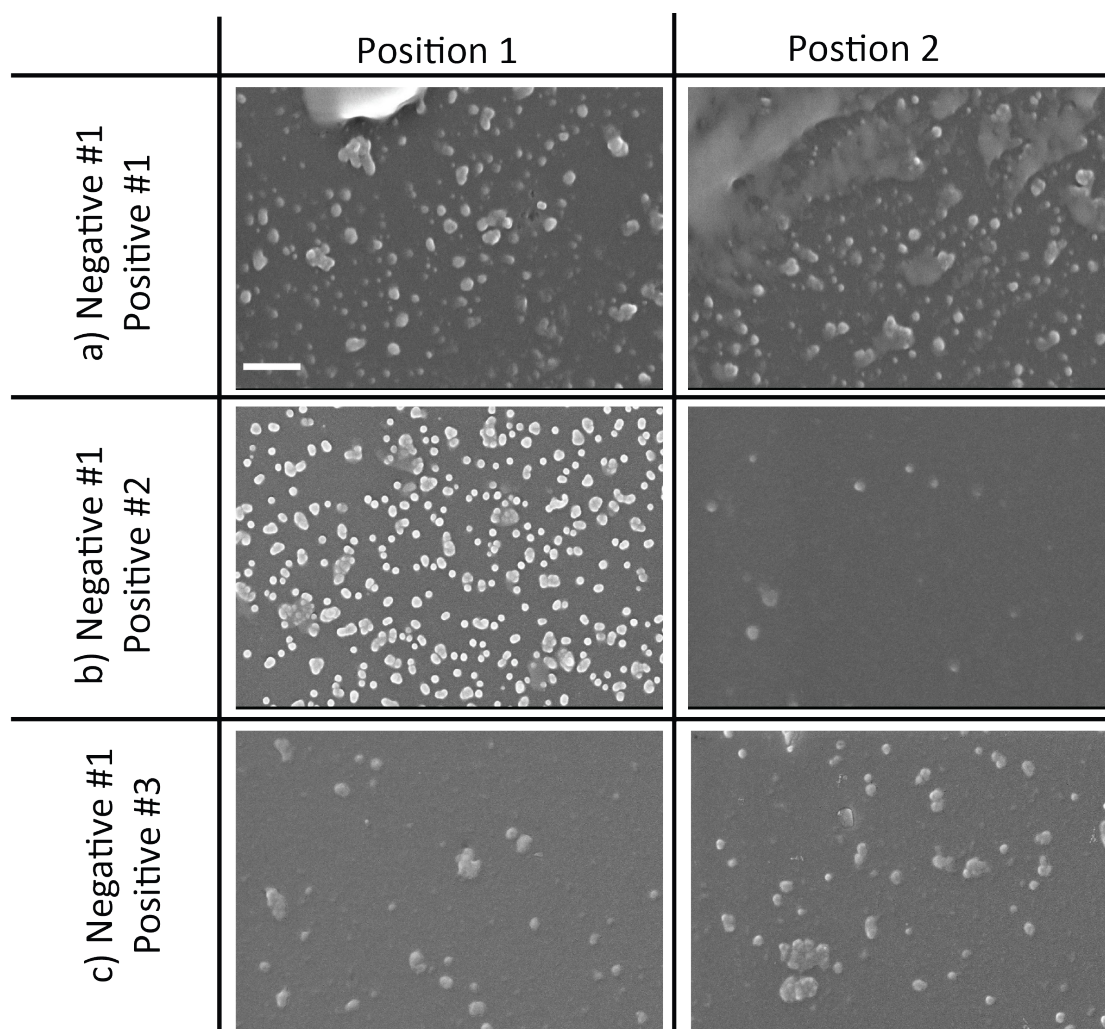|	Position 1	Postion 2
a) Negative #1 Positive #1		
b) Negative #1 Positive #2		
c) Negative #1 Positive #3		

Figure 7.10: SEM images of epoxy replicas of a homogenous 72 nm particle density master with a particle-density of 10 particles/μm^2. SEM images were taken with 50 kX magnification, scale bar 1 μm. SEM images of two different positions on the replica of a) first replica of the first negative, b) second replica of the first negative and c) third replica of the first positive.

SEM images from two different positions on epoxy replicas made from the second (Figure 7.11 a and b) and third negative (Figure 7.11 c) from the same homogenous 72 nm particle-density master with a density of 10 particles/ m2 showed that the replication quality decreases with increasing negative number due to the loss of particles. The replication quality also changes at different positions of the same replica as well as between the different replicas (Figure 7.11 a-c).
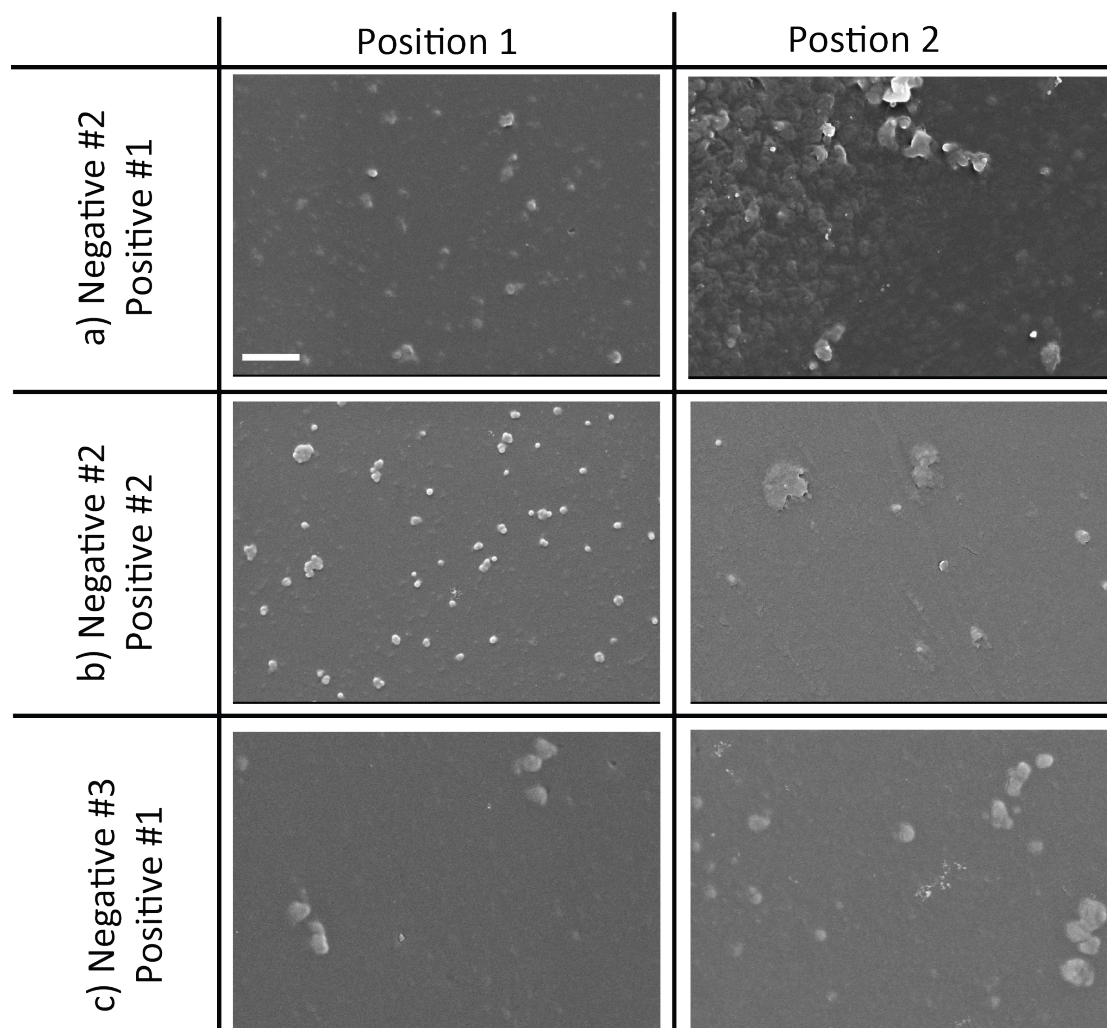

Figure 7.11: SEM images of epoxy replicas of a homogenous 72 nm particle-density master with a particle-density of 10 particles/ m2. SEM images were taken with 50 kX magnification, scale bar 1 m. SEM images of two different positions on the replica of a) first replica of the second negative, b) second replica of the second negative and c) first replica of the third positive.

The two-step replication method with a negative fabrication in hf-PDMs and a positive casting in epoxy involves a lot of steps carried out by hand, thus introducing a large factor of uncertainty. The replication quality varied from replica to replica and at different positions on the same replica. This indicates that every single replica needs to be analyzed extensively by AFM and SEM before any possible use for a biological application. The fabrication of a master particle-density gradient or homogenous master takes 12 h, 1 h for gradient fabrication, 9 h for sintering and 2 h for the cool-down. While the fabrication of one replica takes more than 24 h due to the 24 h curing step in the epoxy replica production. The success of replication was very low, which made the fabrication of replicas more time-consuming than the fabrication of silica masters.

7.3.2 Replication with injection molding

As the replication of nanoparticle-density gradients with hf-PDMS negative and epoxy positive was shown to be very time-consuming and not very reproducible, injection molding was investigated as an alternative replication technique.

In this section, injection compression molding was used to replicate homogenous particle-density samples with particle diameter of 72 nm in high numbers. The work was performed in collaboration with Christian Rytka from the Fachhochschule Nordwestschweiz (FHNW) and the Institut für Nanotechnische Kunststoffanwendung (INKA). The master fabrication and analysis of the master, negatives and positives were performed at ETH Zürich, while the negative and positive fabrication was carried out at FHNW. Christian Rytka [7] fabricated PEEK/PPSU negatives and A-PA and PP positives. Benjamin Rüfenacht [30] who carried out his bachelor thesis on this topic performed the negative fabrication in PPSU. Christian Rytka and Rebecca Huber fabricated the positives by injection molding in COP. Negative fabrication by hot embossing in Moldflon® was carried out at ETH Zürich by Rebecca Huber

7.3.2.1 Experimental

Master fabrication

The masters were produced using the same protocol as described in Section 7.3.1.1.

Injection molding

The injection-molding processes were previously described by Rytka *et al*. [31]. The different experiments were carried out on an injection-molding machine from Arburg 320 A (Lossburg, Germany), with a hydraulic clamping unit with a maximum clamp force of 600 kN, an electrical injection unit with a maximum injection velocity of 142 cm³/s and a 3-zone screw with a diameter of 30 mm. The injection mold was designed internally at INKA/FHNW, produced at AdvalTech FOBOHA, Muri, Switzerland and constructed with changeable inserts for testing different structures.

Polymers used for injection molding were: amorphous polyamide (A-PA, Grilamid TR55LX PA12/MACMI + PA12, EMS-Chemie, Switzerland), Polypropylene (PP, PPC-711, Braskem, Brazil) and cyclo-olefin polymer (COP, Zeonor® 1020R, Zeon Corporation, Japan).

The melt and mold temperatures and the injection velocity were kept constant for all injection molding trials, summarized in Table 7.2.

Table 7.2: Set injection molding parameters applied for all trials.

Material	Cylinder temperature $T_{cyl.}$ [°C]	Injection speed V_{inj} [cm³/s]	Set mold temperature at ejection T_{mold} [°C]
A-PA	280	15	50/60
PP	220	15	35/45
COP	260	30	20/30/40

Mold inserts

On the injection side, two unstructured, highly polished chrome steel (CrNi 1.4301; roughness R_a = 0.013 m) inserts were clamped. On the ejection side polymeric mold-inserts were used for the replication trials. Silicon wafers with sintered SiO_2 nanoparticles (72 nm in diameter) with different homogenous particle densities were transferred by hot embossing into 2 mm thick plates of polyetheretherketone (PEEK, Victrex 450G, Victrex, UK) and polyphenylenesulfone (PPSU, Ultrason P3010, BASF, Germany) to produce the polymeric mold-inserts. Hot embossing in PEEK was performed at 240 °C for 30 min, while hot embossing in PPSU was performed at 260 °C for 40 min with a pressure of 1.1 bar. The inserts were then used for injection-molding trials as schematically shown in Figure 7.12.
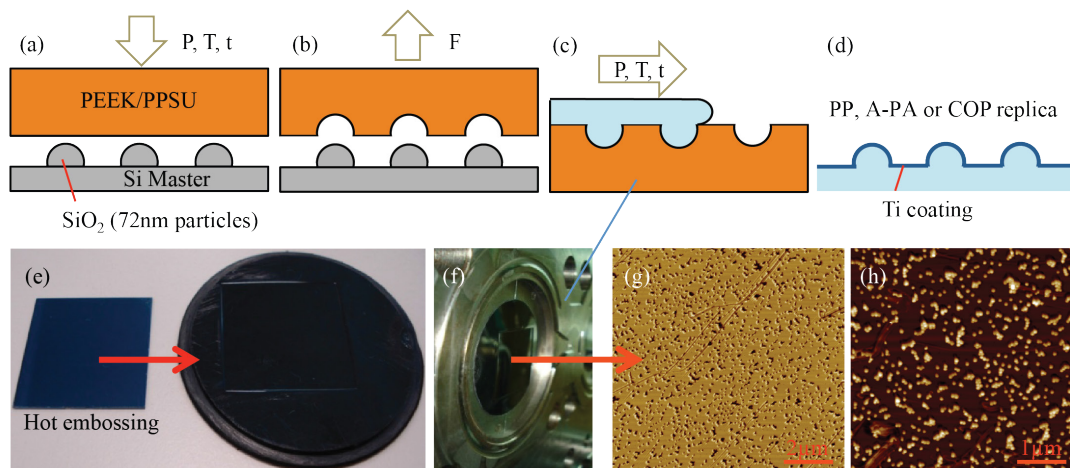

Figure 7.12: Process chain of the fabrication of replica from a silicon master: (a) Hot embossing of sintered Si master into PEEK/PPSU; (b) demolding; (c) injection molding; (d) replicated nanostructured polymer samples in PP, A-PA or COP with Ti-coating; (e) picture of Si master and hot embossed PPSU insert; (f) clamped PPSU insert; (g) AFM picture of PPSU insert with nano-holes; (h) AFM picture of replicated nanostructured polymer sample. Adapted from [7].

Hot embossing in Moldflon® (ElringKlinger Kunststofftechnik GmbH, Germany), a thermoplastic material with a composition largely similar to that of conventional modified polytetrafluoroethylene (PTFE), was performed at 380 °C for 1 min and the negative was cooled down to room temperature before removal of the master. Moldflon® negatives were not used for injection molding trials.

Characterization

The replicas were analyzed by SEM and AFM as described in Section 2.2.1.2.

7.3.2.2 Results and Discussion

SEM and AFM images of the homogenous 72 nm nanoparticle-density masters used for the replication with injection molding are shown in Figure 7.13. ImageJ analysis showed particle densities of 11.02 ± 5.6, 27.72 ± 5.4 or 48.26 ± 4.9 particles/ m^2 for 10, 20 and 40 min dipping in particle suspension, respectively. The AFM images showed that the particle height after sintering was reduced from 72 to 62.07 ± 4.8 nm.

Polymeric mold inserts made by hot embossing into Moldflon® showed nanocavities with a depth of 48.65 ± 8.8 nm and a semi-crystalline morphology. AFM measurements of the roughness of the crystalline structure showed an increase in the R_a (1.69 ± 0.3 nm) and R_q (2.14 ± 0.3 nm) values compared to the roughness measured between particles on the silicon master (R_a 0.24 ± 0.1 nm, R_q 0.32 ± 0.2nm). Additionally, cooling inhomogeneities due to different thermal coefficients of silicon masters and Moldflon® led to warpage of the negatives. It was therefore decided that Moldflon® was less suitable as a mold material (Figure 7.14).

Negatives in PEEK showed a cavity depth of 51.10 ± 2.1 nm. A secondary structure with lines was visible, most probably originating from prepressing the PEEK plaques with machined steel plates prior to hot embossing and hence PEEK inserts were not used for further injection molding trials (Figure 7.15).
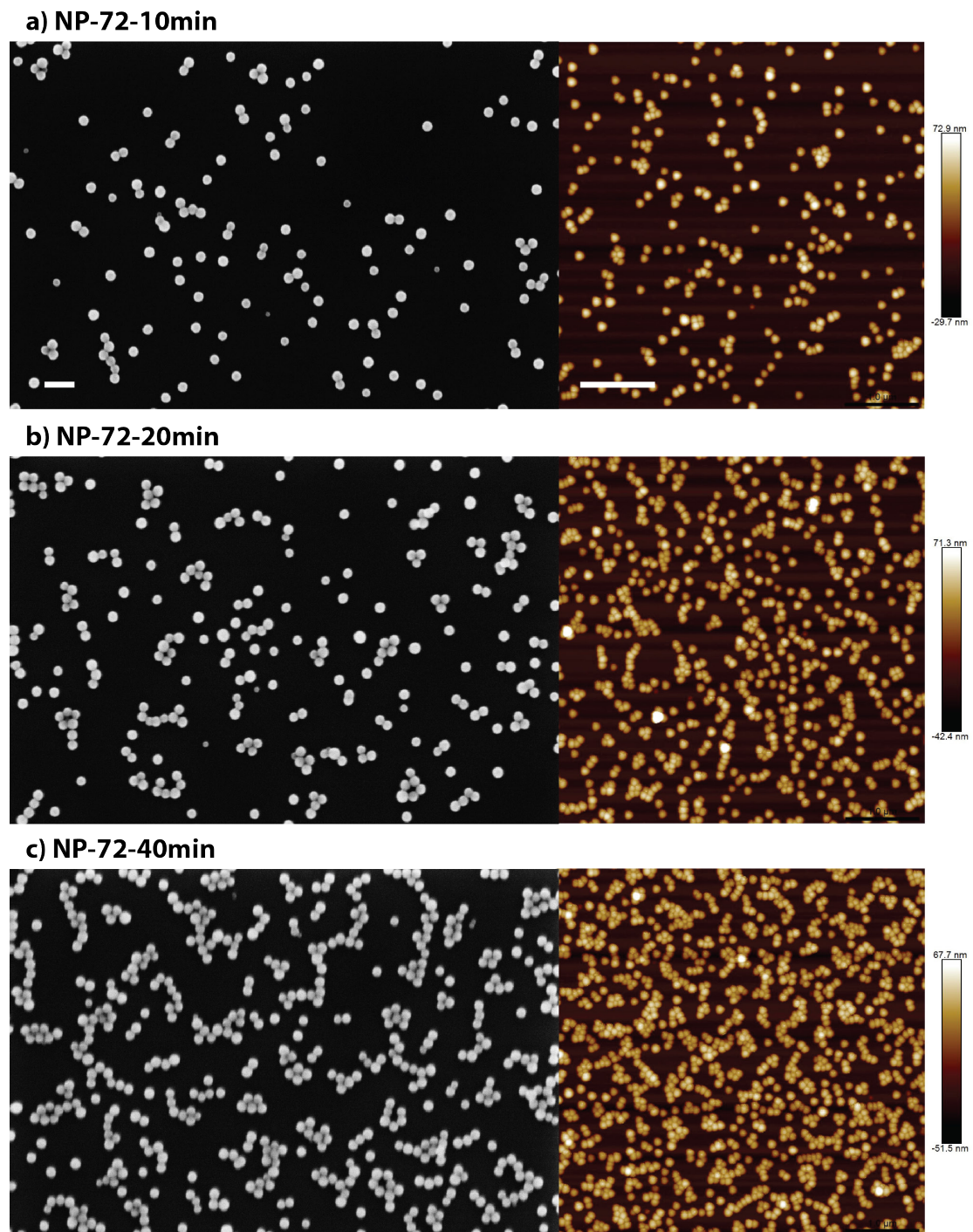
a) NP-72-10min

b) NP-72-20min

c) NP-72-40min

Figure 7.13: SEM and AFM images of sintered homogenous nanoparticle-density samples made by dipping into a 0.004 wt% 72 nm SiO_2 particle suspension for a) 10 min, b) 20 min and c) 40 min. Scale bar for SEM images 200 nm and scale bar for AFM images 1 m.
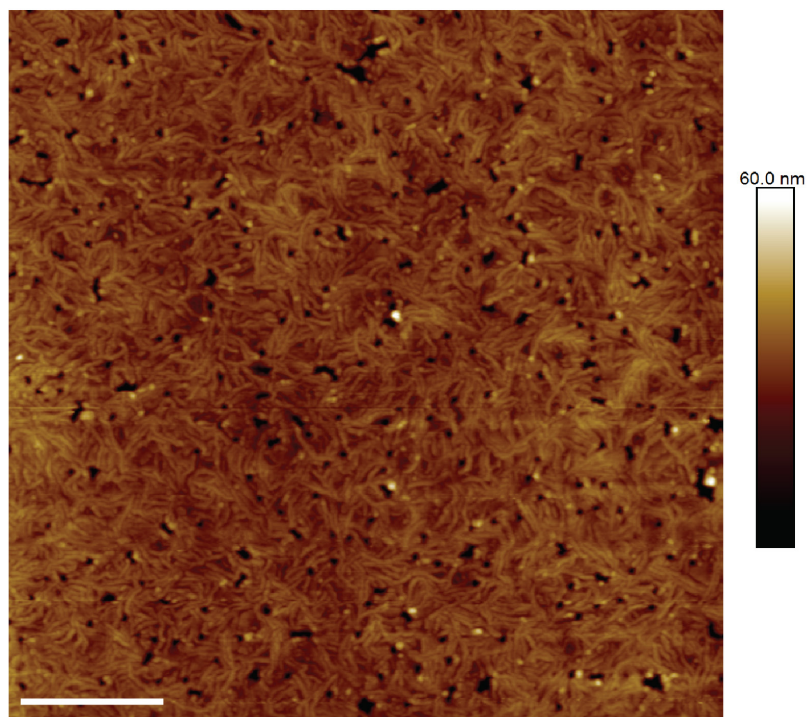
Figure 7.14: AFM image of Moldflon® negative of NP-72-10min. Nanocavities with a depth of 48.65 ± 8.8 nm were observed. Additionally the semi-crystalline structure of Moldflon® can be seen. Scale bar 1 µm.
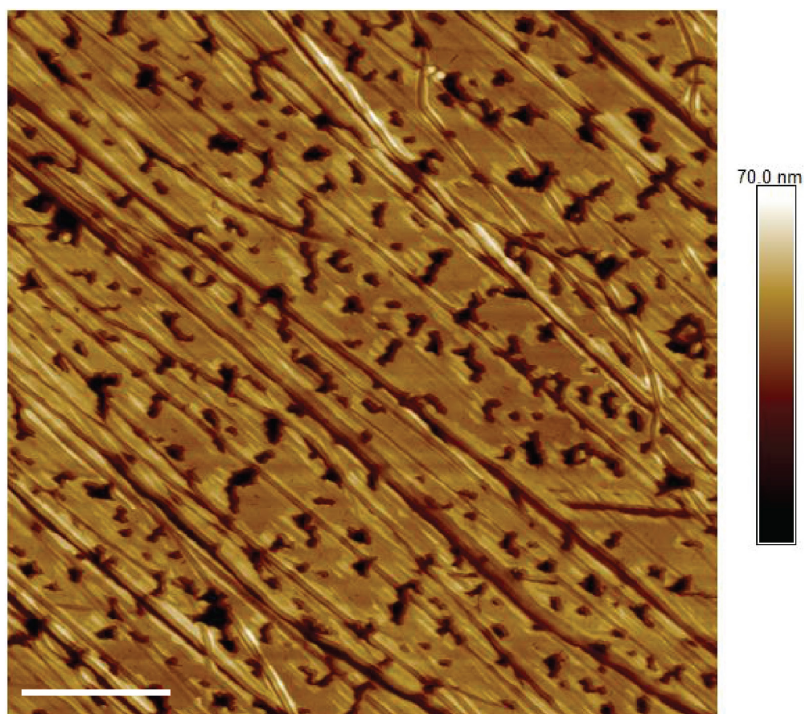

Figure 7.15: AFM image of PEEK negative of NP-72-10min. Nanocavities with a depth of 51.10 ± 2.1 nm were observed. Additionally a secondary line structure originating from prepressing of the PEEK plaque with machined steel plates can be seen. Scale bar 1 µm.
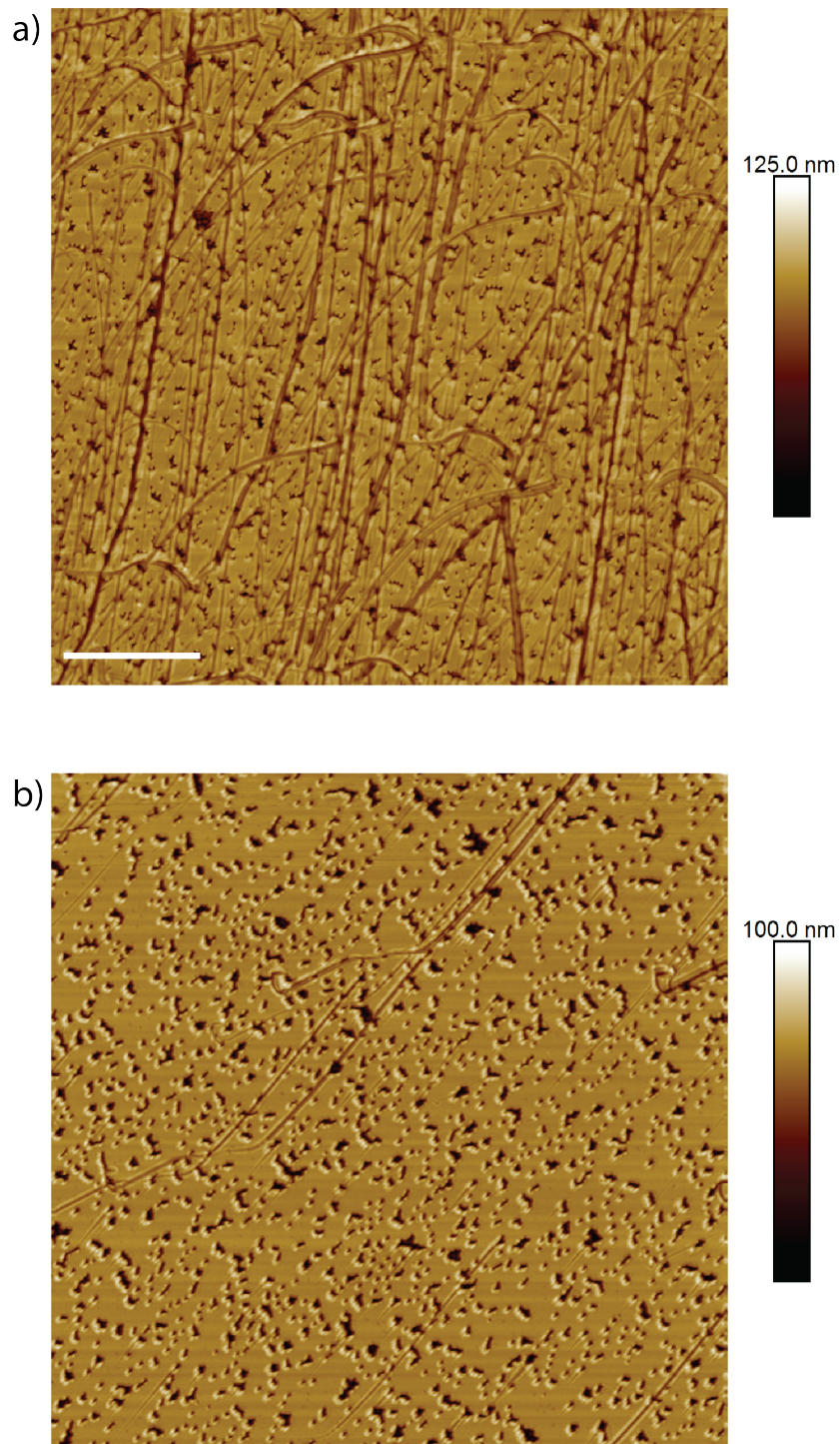
Figure 7.16: AFM image of PPSU negatives of NP-72-20min. Nanocavities with a depth of 50.84 ± 2.9 nm were observed. a) AFM image of first hot embossing trial in PPSU, scratches with a depth of approximately 10 nm are visible. Scratches originate from particles, most probably due to in-plane movements during release of the master from the negative. b) New hot embossing trial with less in-plane movement during release of the master. Scale bar 2 m

Negatives in PPSU showed a cavity depth of 50.84 ± 2.9 nm (Figure 7.16). AFM images of the first embossing trial showed that scratches originating from particles were present all over the surface. The scratches might arise due to in-plane movements during demolding of the master (Figure 7.16 a). The scratches had a depth of approximately 10 nm. In order to reduce the number of scratches, masters were treated with a second perfluorosilane coating, to reduce sticking of the PPSU to the silicon and more attention was paid to a careful release of the master from the negative. However, even then scratches could not be completely prevented (Figure 7.16 b).

The structured PPSU inserts were replicated in PP and A-PA by injection molding. Figure 7.17 a) shows that replication in A-PA with a mold temperature of 50 °C resulted in a good replication quality with nearly round particles. The particle height of 63 nm was nearly identical to that on the master at 62 nm (Table 7.3). Injection molding in A-PA at T_{mold} 60 °C led to sticking of the PPSU negative to the A-PA negative during demolding and caused deformation of the replicated particles that led to an increased particle height of 82 nm (Figure 7.17 b, Table 7.3). This might be due to a contact temperature higher than the T_g of A-Pa. The mold temperature is essential for the replication quality of nanostructures and is usually set to a constant temperature—as low as possible to get short cycle times. While metals have a very high thermal effusivity and can transport heat from the polymer melt away quickly, polymer inserts are less efficient at heat transfer, resulting in a much higher contact temperature at the interface of the polymer melt and the polymer insert [7].

Figure 7.18 shows slightly elongated particles for replication in PP. AFM measurements showed that the particle height was reduced from 62 to 41 nm or 37 nm at mold temperatures of 35 °C or 45 °C, respectively (Table 7.3). PP undergoes crystallization that is associated with a substantial shrinkage, which could be an explanation for the small particle height as well as the sample deformation. Another possible reason for the incomplete replication of the particle heights with PP could be that the polymer melt could not be maintained

at its flow temperature for a long-enough duration, resulting in a premature solidification before the filling of the nanostructure was complete.

Table 7.3: Replicated particle heights and demolding characteristics from different mold temperatures.

Material	Set mold temperature at ejection T_{mold} [°C]	Particle height measured in AFM [nm]	Demolding
A-PA	50	63.26 ± 18.0	good
	60	82.50 ±15.6	sticking, defects
PP	35	41.46 ± 10.9	good
	45	36.69 ± 9.9	good
COP	30	64.81 ± 6.4	good

a) A-PA - 50 °C   **b) A-PA - 60 °C**

Figure 7.17: SEM images of A-PA replica prepared by injection molding with a PPSU master, applying different mold temperatures T_{mold}: a) 50 °C, b) 60 °C. Top: 50 kX magnification, white scale bar 1 µm, bottom: 300 kX magnification, red scale bar 100 nm.
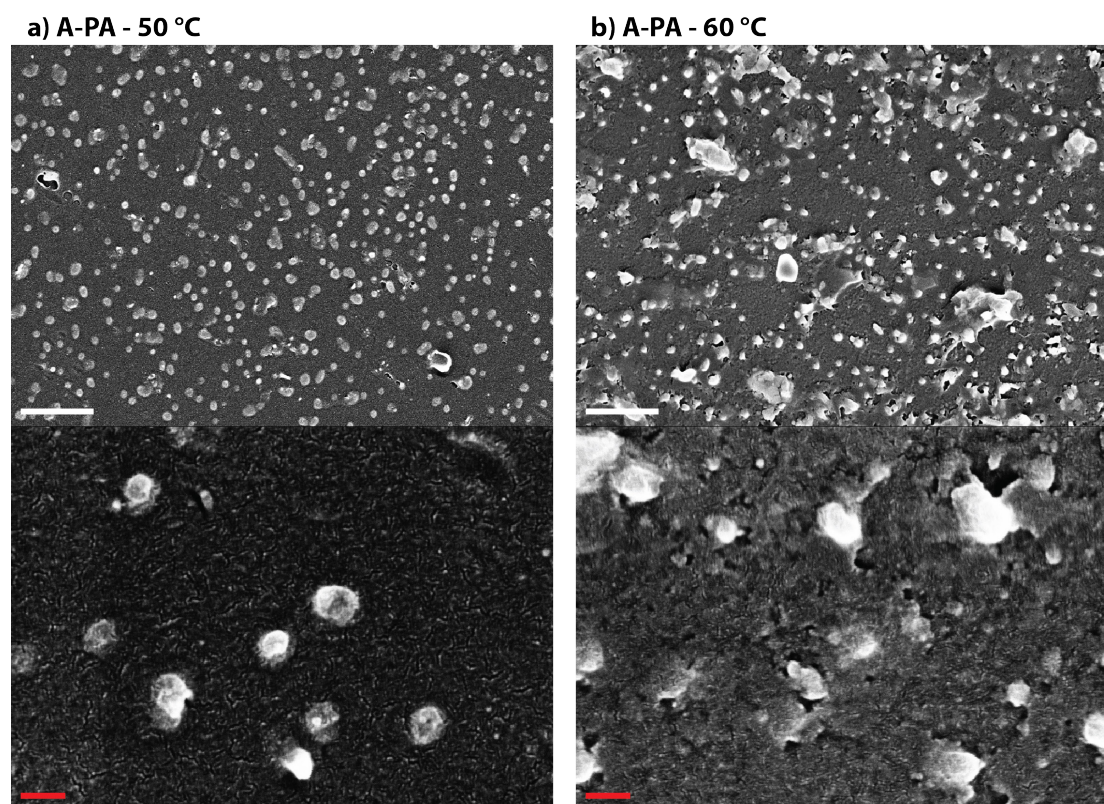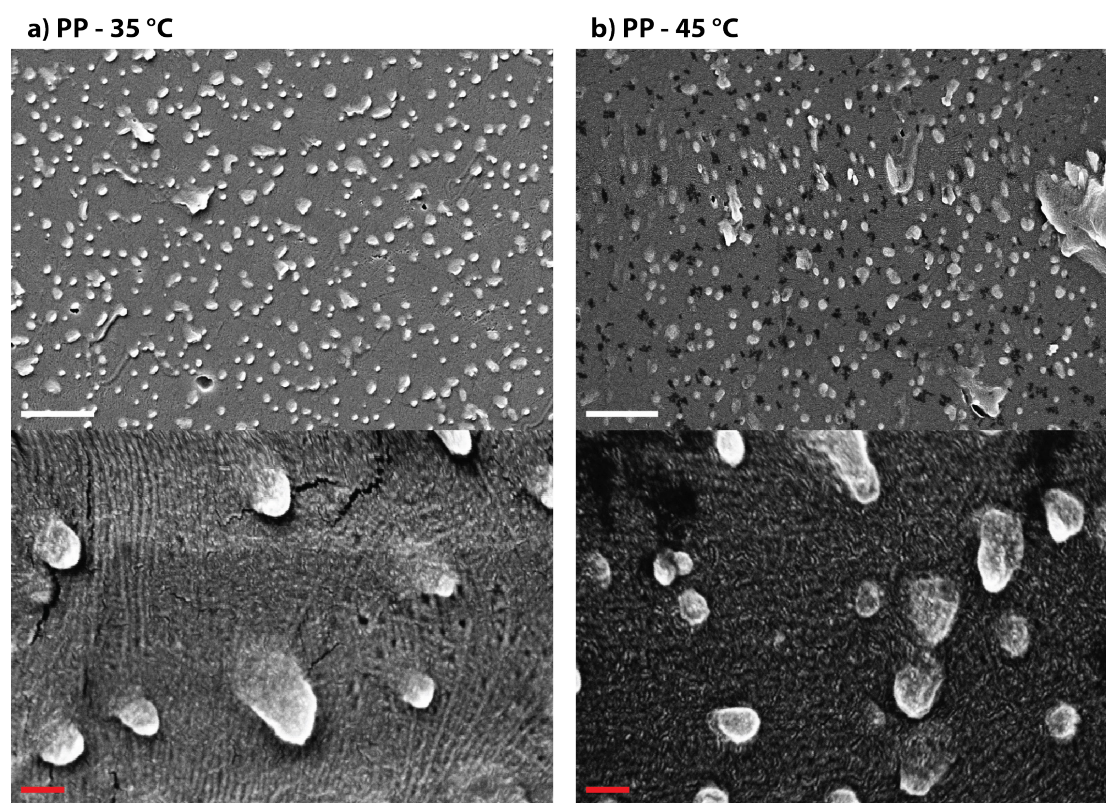
Figure 7.18: SEM images of PP replica prepared by injection molding with a PPSU master, applying different mold temperatures T_{mold}: a) 35 °C, b) 45 °C. Top: 50 kX magnification, white scale bar 1 m, bottom: 300 kX magnification, red scale bar 100 nm

The best replication quality and roundest particles were achieved by replication in COP at a mold temperature of 30 °C (Figure 7.19). The measured particle height was 64.81 ± 6.4 nm (Table 7.3). Replication in COP with a PPSU master was chosen for mass production of samples with three different densities. A PPSU negative of each master was produced. 300 COP replicas were fabricated with each negative and no loss in replication quality was observed with increasing replication number (data not shown). Scratches that were present on the PPSU negative were replicated in the COP negative with a height of approximately 10 nm (Figure 7.19 a). Particle-agglomerates on higher density samples were nicely replicated in COP. Single-particle features could be distinguished on the COP replicas (Figure 7.19 c).

a) COP replica of NP-72-10min
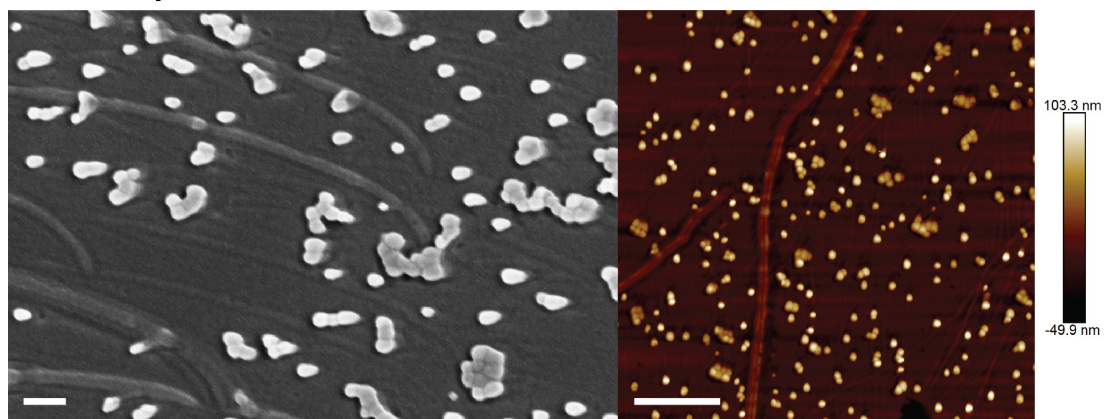
b) COP replica of NP-72-20min
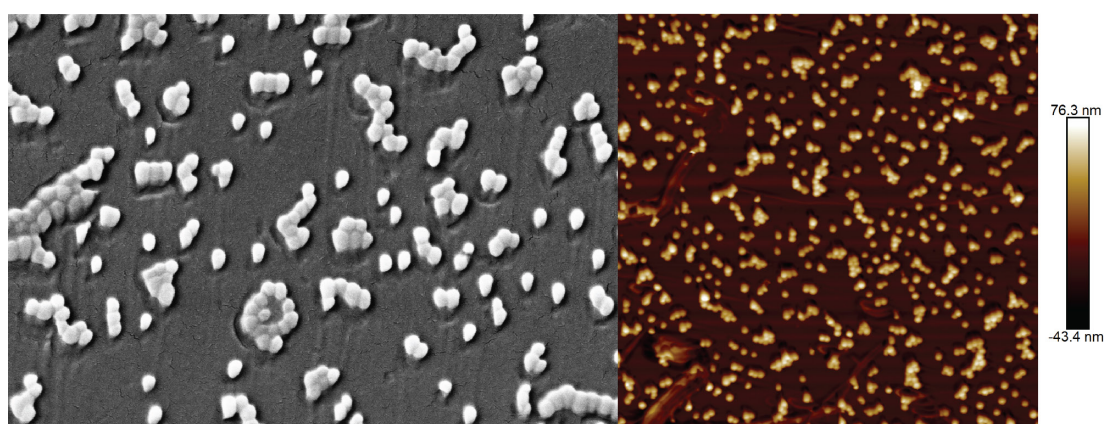
c) COP replica of NP-72-40min
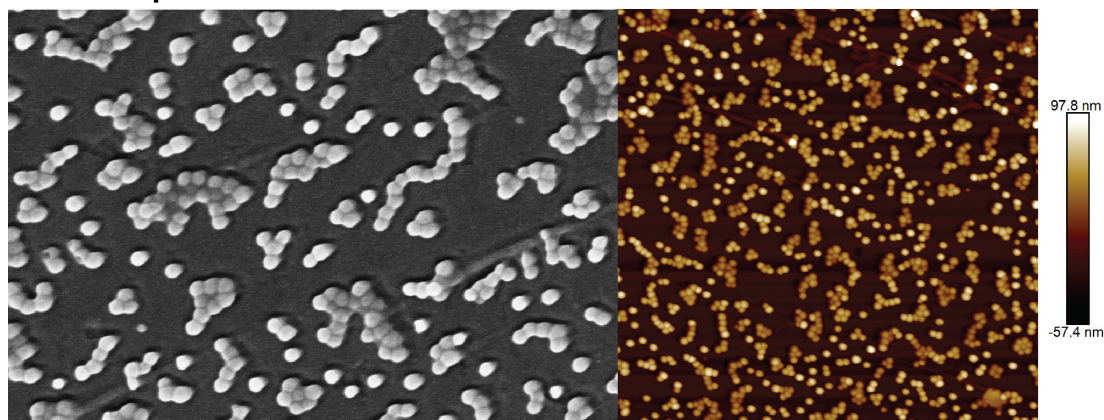
Figure 7.19: SEM and AFM images of COP replicas prepared by injection molding with a PPSU master. COP replicas of sintered homogenous nanoparticle-density samples made by dipping into a 0.004 wt% 72 nm SiO_2 particle suspension for a) 10 min, b) 20 min and c) 40 min. Scale bar for SEM images 200 nm and scale bar for AFM images 1 m.

7.3.3 Replication with substrate conformal imprint lithography (SCIL)

Injection molding was shown to be a good replication technique for nanofeatures with a size of 72 nm; smaller particles were not replicated with this technique. Substrate conformal imprint lithography (SCIL) offers nanoscale resolution and the advantage that the positive is formed on a silica wafer—the same material as the masters.

In this section SCIL was used to replicate nanoparticle-density gradients with particle diameter of 12, 39 and 72 nm. The work was performed during a two-month internship at SCIL Nanoimprint Solutions in Eindhoven under the supervision of Marc Verschuuren. The master fabrication and analysis of the master, negatives and positives were done at ETH Zürich, while the negative and positive fabrication was performed at SCIL Nanoimprint Solutions.

7.3.3.1 Experimental

The SCIL method was developed by Marc Verschuuren for Philips Research and is described in detail in his PhD thesis [4].

Master fabrication

The masters were produced using the same protocol as described in Section 7.3.1.1.

X-PDMS composite negative fabrication

X-polydimethylsiloxane (X-PDMS, kindly provided by Marc Verschuuren; SCIL Nanoimprint Solutions, Philips Intellectual Property & Standards, the Netherlands) is a Q-siloxane modified PDMS rubber with high Young's modulus (60-80 MPa). After the perfluorosilane coating of the master gradients (12, 39 and 72 nm), composite X-PDMS negatives are molded from the masters. The X-

PDMS is thoroughly mixed, degassed and spin-coated at 2000 rpm for 10 s over the masters resulting in a 50-100 m thick X-PDMS layer. The X-PDMS was pre-cured for 6 min at 50 °C on a heating plate and left resting for 3 min at room temperature before an intermediate Sylgard 184 PDMS (Dow Corning, USA) layer with an adapted mixing ratio of 2:1 (base:curing agent) was spin-coated on top, and cured over night at 75 °C. As a last step a 2 mm thick Sylgard 184 layer was poured on top of the X-PDMS and the intermediate layer and cured for 1 h at 60 °C. After curing, the master gradient was removed from the negative and used again for the fabrication of other negatives.

For large-area imprints (larger than a few square cm), composite X-PDMS negatives were grafted onto a thin glass plate (AF45 glass, thickness 150- 200 m).

Imprint in sol-gel resist

For imprint experiments, the Si-based sol-gel resist from SCIL Nanoimprint Solutions was used. The preparation of such silica-based sol-gel resist was previously described in [21]. For the preparation of 88 wt% inorganic sol-gel resist, methyl-tri-methoxy-silane (MTMS, 97% Acros, Germany) and tetra-methoxy-ortho-silicate (TMOS, 98% Aldrich, USA) were mixed in a 1:1 molar ratio with 7 mol of water acidified to pH 1.5 by adding formic acid. After 15 minutes stirring in a cooled water-bath 12 mol water was added, later isopropanol was used to dilute the sol to a concentration of 0.78 mol Si/kg hydrolysis mixture and kept at room temperature for 20 min. The mixture was kept at -20 °C until further use. Imprint resist was always prepared freshly prior to imprinting by mixing a 1:1 ratio of isopropanol with the previously prepared sol-gel hydrolysis mixture and adding 1 wt% 1,2-propanediol. [21]

The resist was open-bowl spin coated on 100 mm Si-wafers (layer thickness approximately 200 nm). During the spin coating the volatile resist components evaporate and only silicon oxide oligomers and 1,2-propanediol are left behind [21]. Prior to the spin coating, Si-wafers were cleaned by oxygen

plasma (barrel geometry, 200 W, 0.5 mbar, 2 min) to ensure good wetting and adhesion of the sol-gel layer to the substrates. Within one minute after spin coating the sol-gel layer was imprinted using the patterned X-PDMS negative. The negative was imprinted by hand by slowly pressing it down from one side and letting the wetting edge move forward. The negative and the sol-gel were left in contact and cured at 50 °C for 2 min on a heating plate. The negative was carefully removed from the hardened sol-gel layer by gently peeling it from one side. The imprinted silicon wafer was baked for an additional 10 min at 150 °C. The released X-PDMS composite negative could be used for further imprints.

Characterization

The replicas were analyzed by SEM and AFM as described in Section 2.2.1.2.

7.3.3.2 Results and Discussion

Replication of nanoparticle-density gradients with 12, 39 and 72 nm silica particles with an X-PDMS negative and a positive imprint in a silicon-based sol-gel resist were tested.

AFM images along a replicated 39 nm particle-density gradient showed that the SCIL technique was able to replicate nanofeatures with a size of 39 nm (Figure 7.20). The particle height of the master gradient of 39.95 ± 6.9 nm was reduced to 37.39 ± 2.5 nm on the replica.

AFM images along a replicated 12 nm particle-density gradient showed that the SCIL technique was also able to replicate nanofeatures with a size of 12 nm (Figure 7.21). The particle height of the master gradient of 11.81 ± 1.6 nm was reduced to 9.26 ± 3.1 nm on the replica.

Figure 7.20: Replication of NP-39-BB4, a 39 nm particle-density gradient in a silicon-based sol-gel resist. a) Scheme of a gradient sample, b) particle-density measured from AFM images along the master gradient (black) and the replica (green), c) AFM images with a size of 5×5 μm² at different position of the master (top) and replica (bottom).
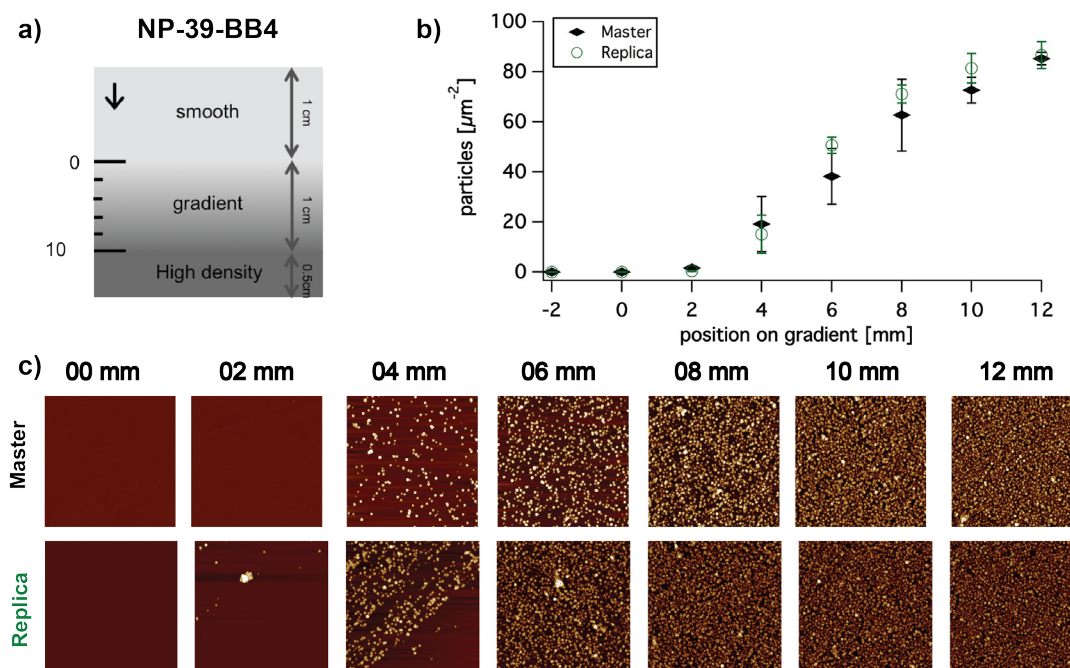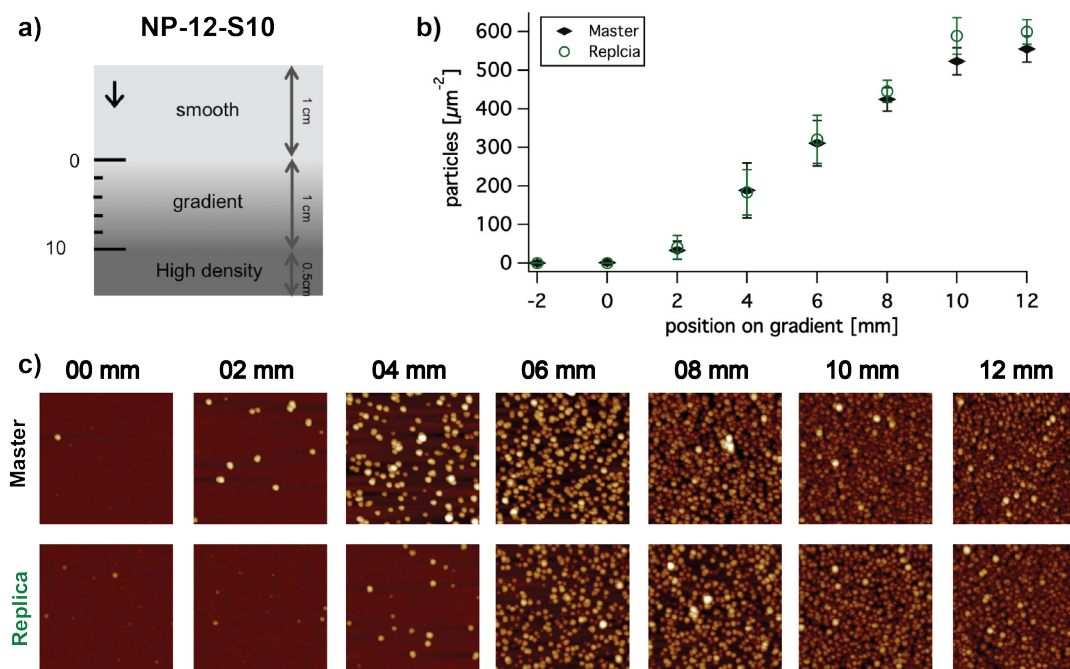

Figure 7.21: Replication of NP-12-S10, a 12 nm particle-density gradient in a silicon-based sol-gel resist. a) Scheme of a gradient sample, b) particle-density measured from AFM images along the master gradient (black) and the replica (green), c) AFM images with a size of 1×1 μm² at different position of the master (top) and replica (bottom).

AFM measurements of replicated 72 nm particle-density gradients showed that the particle height of the master gradient of 62.07 ± 4.8 nm was reduced to 52.90 ± 8.4 nm on the replica. (Data not shown)

The reduced particle height after replication can be explained by the post-cure shrinkage of the imprinted sol-gel patterns. Verschuuren found a 6% shrinkage in height for a sintering temperature of 200 °C [4]. The silicon sol-gel resists consisting of tetra-methyl-ortho-silicate (TMOS) and methyl-tri-methoxy-silane (MTMS) was mixed with alcohol and acidified water to catalyze the hydrolysis reaction. The partly hydrolyzed TMOS and MTMS molecules can subsequently condense with release of water and alcohols to form Si-O-Si bonds, which leads to the shrinkage.

The SCIL technique was able to replicate nanofeatures with a size of 12 nm and bigger, although the imprint process was carried out by hand. In order to produce many identical replicas an automated lithography tool, developed by SCIL Nanoimprint Solutions, capable of manufacturing up to 60 wafers per hour, can be used [32].

To be able to use the automated tool, masters with a diameter of at least 2 inches (approx. 5 cm) are needed. Nanoparticle-density gradients with a size of 2.5×2.5 cm^2 were glued on top of a 6-inch silicon wafer by spin-coating an X-PDMS layer on top of the wafer and aligning particle-density gradients on top. Gaps between the gradients and the surrounding area were filled up with Sylgard 184 to achieve a flat surface. The as-prepared large master was treated with a perfluorosilane coating and used for the fabrication of an X-PDMS negative. A first imprint by hand in sol-gel resist with the negative showed good reproduction (Figure 7.22) but further improvements for the fabrication of a large master from multiple small gradients are needed before the automated tool can be used for mass production of gradients.

Figure 7.22: Photograph of the first sol-gel imprint on a 6'' wafer with X-PDMS negative obtained from 12 nanoparticle-density gradients assembled on a 6'' wafer.

7.4 2-dimensional roughness gradient replication with substrate conformal imprint lithography (SCIL)

Replicating 2D-orthogonal roughness gradients is challenging due to the more than 3 orders of feature scales that need to be simultaneously replicated with high fidelity. SCIL was used to replicate 2-dimensional micrometer-roughness vs. nano-feature density gradients during a two-month internship at SCIL Nanoimprint Solutions in Eindhoven under the supervision of Marc Verschuuren.

Earlier, it was demonstrated that SCIL was able to replicate nanoparticle-density gradients with 12 nm particles (see Section 7.3.3). In order to replicate 2D-gradients a higher sol-gel resist thickness was required. Therefore, the sol-gel resist recipe was adapted in this sub-chapter.

7.4.1 Experimental

7.4.1.1 Master fabrication

2-dimensional micrometer-roughness vs. nano-feature density gradients were prepared as described in Section 2.4.

7.4.1.2 X-PDMS composite negative fabrication

Composite X-PDMS negatives were fabricated using the same protocol as described in Section 7.3.3.1.

7.4.1.3 Imprint in sol-gel resist

In order to be able to replicate 2D-gradients, a higher sol-gel resist thickness was required. Three different commercially available colloidal silica suspensions in water were chosen as filler material to increase the resist thickness:

- Nyacol® 1430 colloidal silica 30 wt% in H_2O, particle diameter of 14 nm, pH 8.0 (Eka Chemicals Inc., USA)
- LUDOX® AS-40 colloidal silica, 40 wt% in H_2O, particle diameter 22 nm, pH 9.1 (Sigma Aldrich, USA)
- BINDZIL® 40 NH3/80 colloidal silica, 40 wt% in H_2O, wide particle size range, pH 9.3 (Akzo Nobel, Sweden)

5 g of colloidal silica suspension were mixed with 1.06 g acetic acid (glacial, MERCK, Germany), 0.53 g methanol (analytical grade, Fisher Scientific, Switzerland) and 0.6 g trimethoxymethylsilane (MTMS, 98%, Aldrich, USA) in a glass vial, stirred with a magnetic stirrer and cooled in a water bath for 5 min. 0.4 g diethylene glycol diethyl ether (98%, Sigma Aldrich, USA) and 3.5 g MTMS was added drop wise. In a last step the pH was set to 3.5-4 by adding acetic acid. The sol-gel resist was stored in the freezer until further use.

Additionally a resist with colloidal silica in isopropanol was used:

- ORGANOSILICASOL™ IPA-ST colloidal silica, 30 wt% in isopropanol, particle diameter 10-15 nm, pH 2-4 (Nissan Chemical America Corporation, USA)

ORGANOSILICASOL™ was mixed with MTMS and 4 wt% diethylene glycol diethyl ether (EEE) was added. The sol-gel resist was stored in the freezer until further use.

A seven-stage spin-coat cycle was used to apply a thick sol-gel resists layer. A typical spin-coat cycle is described in Table 7.4. During the pre-drying step most of the alcohol and water will evaporate while the EEE remains in the sol-gel coating and lowers the viscosity of the sol-gel layer to allow time between the spin coating of the sol-gel layer and the application of the X-PDMS negative [4].

Table 7.4: Seven-stage spin-coat cycle used for spin coating of thick sol-gel resist layers.

Step	Time [s]	Speed [rpm]	Acceleration [rpm/s]	Use
#1	1	1000	2000	resist application
#2	4	150	2000	achieving a homogenous thick resist layer at rather low speed
#3	3	400	2000	
#4	30	350	2000	
#5	10	600	2000	
#6	2	2000	2000	removal of thick liquid on substrate edge
#7	20	700	2000	pre-drying: evaporation of water and alcohols

Within one minute after spin-coating the sol-gel layer was imprinted using a patterned X-PDMS negative. The negative was left in contact with the sol-gel and baked on a heating plate for 15 min at 50 °C. Sol-gel resist made with ORGANOSILICASOL™ was hardened at this point and the negative could be removed by gently peeling it off from one side. Sol-gel resist made from colloidal silica in H_2O was baked overnight at 75 °C to ensure a complete hardening of the sol-gel before removal of the negative. The released X-PDMS composite negative was cleaned in isopropanol, dried in a stream of nitrogen and used for further imprints.

7.4.1.4 Characterization

The replicas were analyzed by SEM and AFM as described in Section 2.2.1.2. AFM images were analyzed with Gwydion (http://gwyddion.net).

7.4.2 Results and Discussion

AFM measurement of imprints with X-PDMS composite stamps of 2D-roughness gradients with a 10 mm long micro-roughness gradient (MR-10) and 12 nm particle density gradient (NP-12) in Nyacol® 1430 and LUDOX® AS-40 sol-gel resists showed replicated nanoparticles on top of the microstructure (Figure 7.23). The hardening time of the Nyacol® 1430/ LUDOX® AS-40 sol-gel resist to form a rigid glass-like structure that did not deform during removal of the stamp was more than 24 h at 75 °C and was most probably due to a high amount of acetic acid that was added to the resist to reach a pH of 3.5–4. Therefore, it was decided to try out different colloidal-silica suspensions to achieve thick resist layers.

a) MR-10-NP-12 imprinted in Nyacol 1430 resist   **b) MR-10-NP-12 imprinted in LUDOX AS resist**
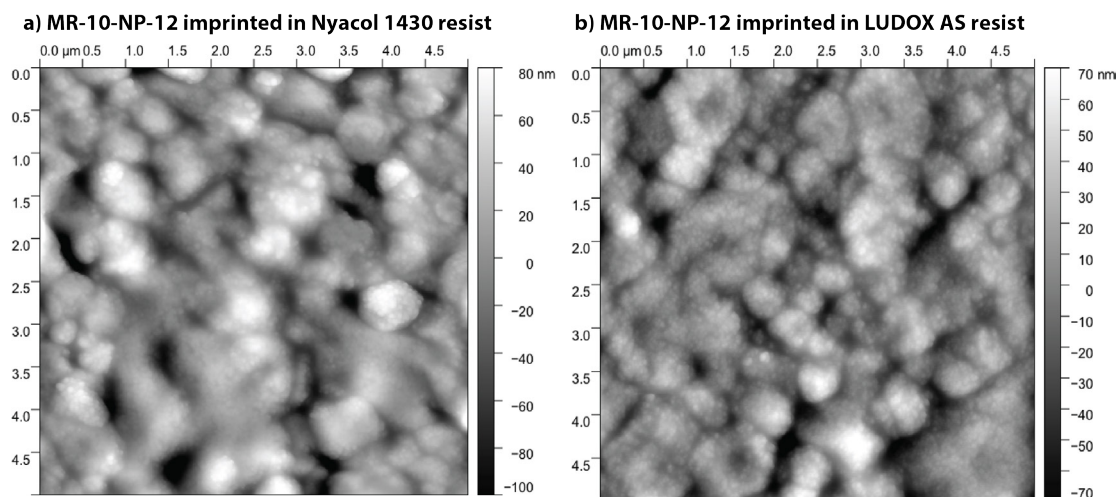

Figure 7.23: AFM images of the 2D orthogonal gradient MR-10-NP-12 with a 10 mm long micro-roughness gradient and an orthogonal 12 nm particle-density gradient imprinted in sol-gel resist with MTMS and a) Nyacol® 1430 and b) LUDOX® AS-40. The AFM images were taken at low roughness end of the micrometer roughness gradient with high nanoparticle-density. The grain structure originating from the ceramic alumina master with nanoparticles on top can be seen. Size of AFM image: 5×5 μm².

First experiments with sol-gel resist with MTMS and BINDZIL® 40 NH3/80 showed that the amount of MTMS was not sufficient to fill up the space between filler particles and the filler particles were visible at the surface (data not shown). In order to cover-up the filler particles, the amount of MTMS was doubled during resist fabrication for all further experiments (1.2 g instead of 0.6 MTMS in the first step and 7 g instead of 3.5 g MTMS in the second step).

In Figure 7.24 AFM images of 2D-orthogonal gradients imprinted in sol-gel resist with MTMS and BINDZIL® 40 NH3/80 are shown. Nanoparticles with a size of 72 nm (Figure 7.24 a), 39 nm (Figure 7.24 b) and 12 nm (Figure 7.24 c) were nicely replicated on top of the micro-features. A more quantitative analysis of the replica fidelity was performed by measuring particle heights. Due to the grainy nature of alumina used to fabricate the 2D orthogonal masters, performing meaningful AFM measurements was rather difficult. Therefore, the particle height was determined from replicas of nanoparticle-density gradients. AFM measurements of replicated particle-density gradients showed that the particle height of the 72 nm master gradient was reduced from 62.07 ± 4.8 nm to 56.20 ± 2.4 nm, that of a 39 nm master gradient was reduced from 39.95 ± 6.9 nm to 34.60 ± 8.3 nm while that of 12 nm master gradient was reduced from

11.81 ± 1.6 nm to 9.6 ± 1.7 nm on the replica. The MTMS and BINDZIL® 40 NH3/80 sol-gel resist nicely replicates the particles in full detail.
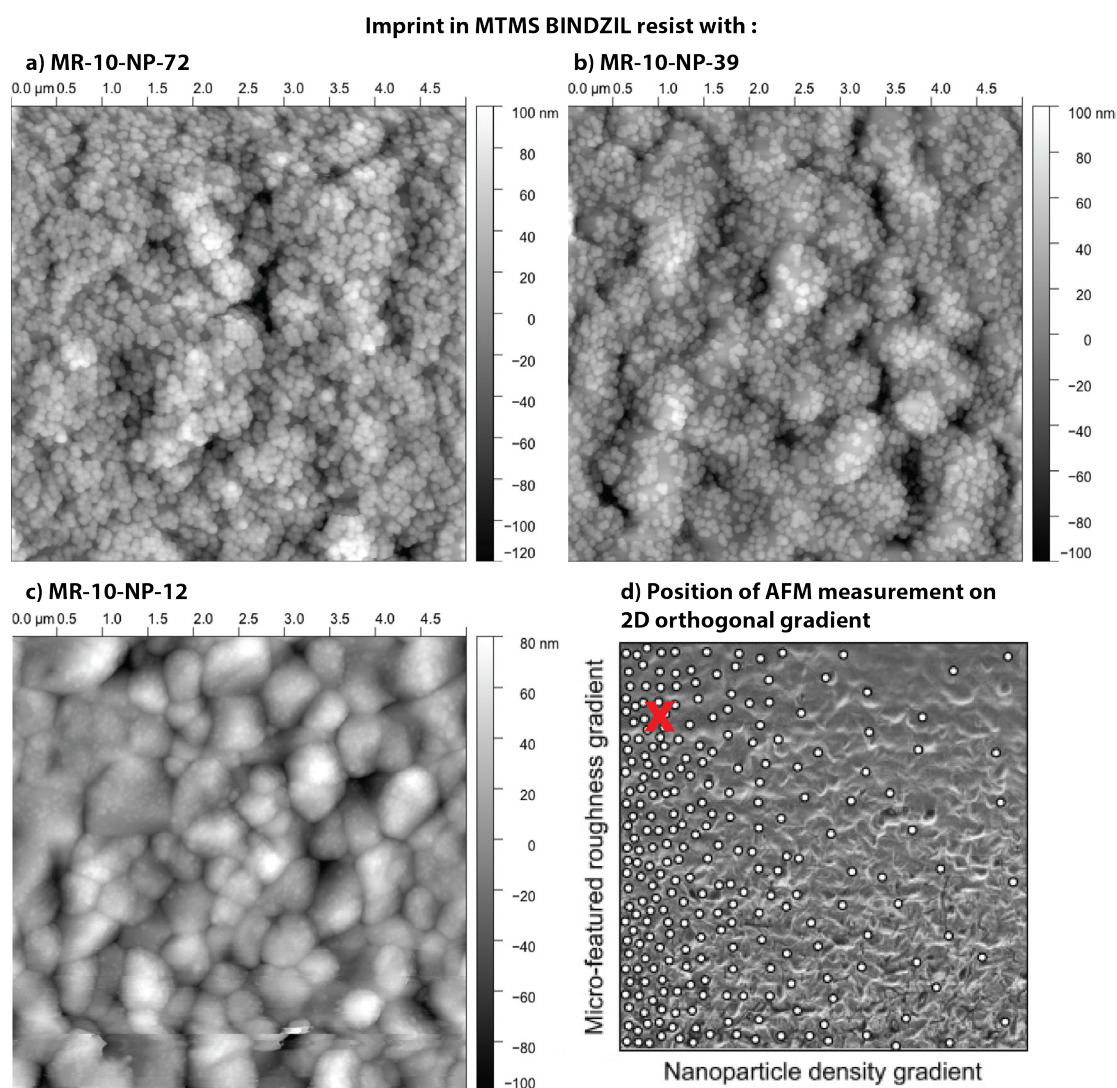

Figure 7.24: AFM images of 2D orthogonal gradients imprinted in sol-gel resist with MTMS and BINDZIL® 40 NH3/80 of a) MR-10-NP-72 with 72 nm particles, b) MR-10-NP-39 with 39 nm particles and c) MR-10-NP-12 with 12 nm particles. d) Scheme of the 2D orthogonal gradient indicating the position where the AFM images were taken at low-roughness end of the micrometer-roughness gradient with high nanoparticle-density. The grain structure originating from the ceramic alumina master with nanoparticles on top can be seen. Size of AFM image: 5×5 m². Scheme adapted from [3].

smooth   rough
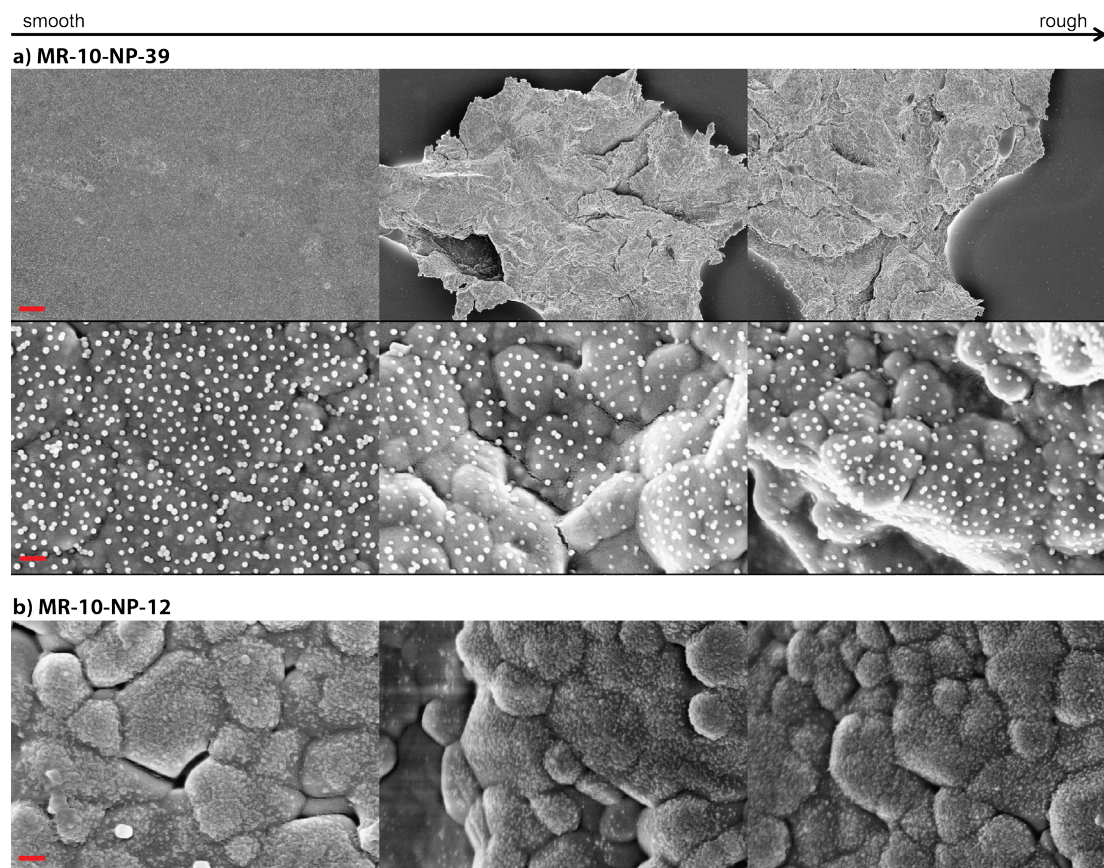
a) MR-10-NP-39

b) MR-10-NP-12

Figure 7.25: SEM images along micro-roughness gradient of 2D orthogonal gradients imprinted in BINDZIL® sol-gel resist. a) MR-10-NP-39 with 39 nm particles. Top row: 2 kX magnification showing the well replicated micro-roughness. With increasing roughness the sol-gel resist started to dewet and islands were formed. Scale bar 10 m. Bottom row: 100 kX magnification images showing the well-replicated 39 nm particles along the micro-roughness gradient. Scale bar 200 nm. b) MR-10-NP-12 with 12 nm particles, 100 kX magnification showing the well-replicated 12 nm particles along the micro-roughness gradient. Scale bar 200 nm.

SEM images along the micro-roughness gradient of 2D orthogonal gradients imprinted BINDZIL® sol-gel resist showed that with higher surface roughness the sol-gel resist started to dewet (Figure 7.25 a top row). On small sol-gel resist islands, both the micro- and the nanostructure were neatly replicated for 39 nm (Figure 7.25 a bottom row) and 12 nm particles (Figure 7.25 b), indicating that SCIL would be capable of replicating a 2D-gradient if higher resist thicknesses could be reached.
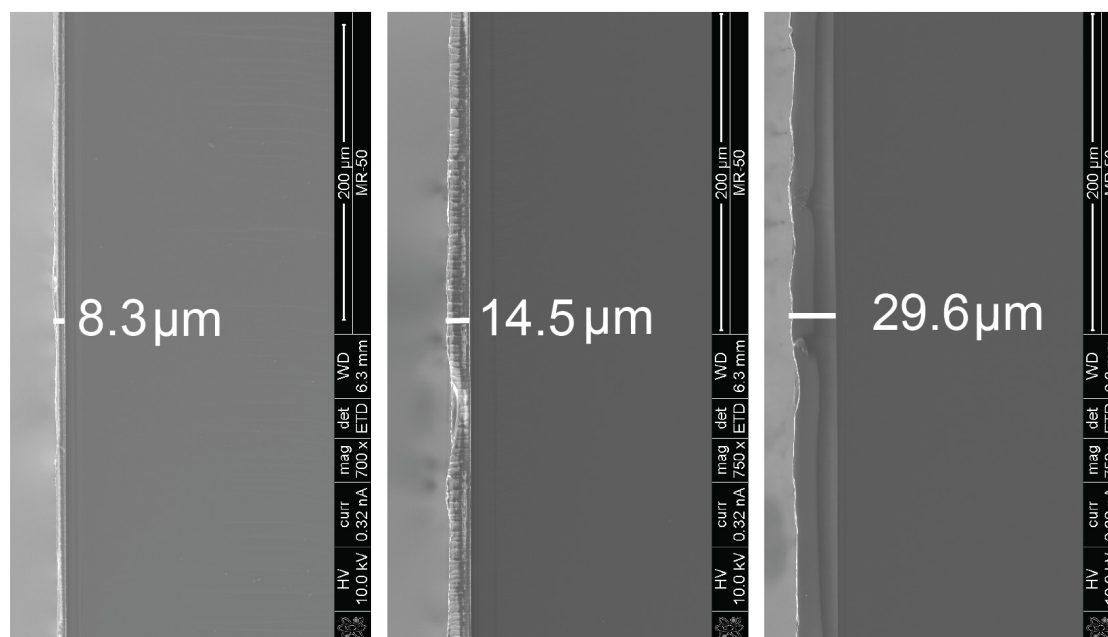
Figure 7.26: SEM images of cross-sections of MTMS BINDZIL® sol-gel resist.

SEM images of the cross-section of MTMS BINDZIL® sol-gel resist layer showed that the thickness varies from 8.3 to 29.6 m (Figure 7.26). The maximum peak-to-valley height measured for the highest roughness area of the 2D orthogonal gradient was $R_z = 40.64 \pm 19.07$ m, which was much higher than the resist thickness and could explain the dewetting behavior of the resist.

The hardening time of the MTMS BINDZIL® sol-gel resist to form a rigid glass-like structure that did not deform during removal of the stamp was about 12 h at 75 °C—a big improvement compared to the 24 h needed for the Nyacol® 1430/ LUDOX® AS-40 to harden. But a 12 h drying time would be still not feasible for the automated production of replicas. In order to reduce the drying time, the amount of water in the resist needed to be decreased and hence the colloidal silica suspension in water was replaced by ORGANOSILICASOL™ IPA-ST colloidal silica in isopropanol.

In Figure 7.27, AFM images of 2D-orthogonal gradients imprinted in sol-gel resist with MTMS and ORGANOSILICASOL™ IPA-ST are shown. At a low micro-roughness ($R_a \sim 1$ m), neat replication of 72 nm (Figure 7.27 a) and 39 nm (Figure 7.27 b) was possible, while 12 nm (Figure 7.27 c) particles were not replicated. AFM measurements of replicated particle-density gradients showed

that the particle height of the 72 nm master gradient was reduced from 62.07 ± 4.8 nm to 51.50 ± 4.5 nm and that of the 39 nm master gradient was reduced from 39.95 ± 6.9 nm to 30.20 ± 8.3 nm on the replica.
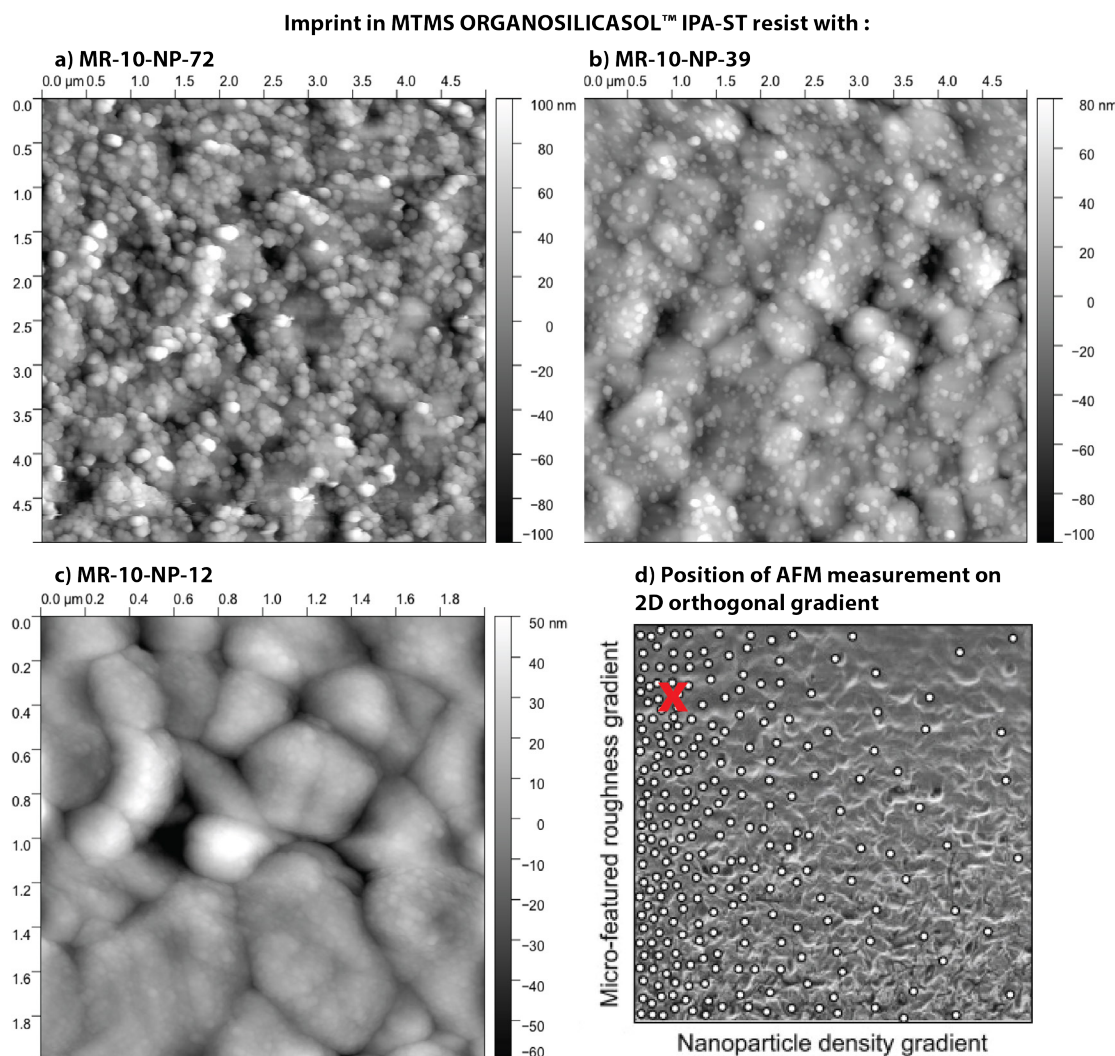

Figure 7.27: AFM images of 2D orthogonal gradients imprinted in sol-gel resist with MTMS and ORGANOSILICASOL™ IPA-ST of a) MR-10-NP-72 with 72 nm particles, b) MR-10-NP-39 with 39 nm particles and c) MR-10-NP-12 with 12 nm particles. d) Scheme of the 2D orthogonal gradient indicating the position where the AFM images were taken at low roughness-end of the micrometer-roughness gradient with high nanoparticle-density. Size of AFM image: 5×5 µm² for a), b) and 2×2 µm² for c). Scheme adapted from [3].

SEM images along the micro-roughness gradient of 2D orthogonal gradients imprinted into ORGANOSILICASOL™ IPA-ST sol-gel resist showed that with higher surface roughness the sol-gel resist started to dewet (Figure 7.28a top row) to a higher degree than for the BINDZIL® sol-gel resist (Figure 7.25a top row). On the small sol-gel resist islands, both the micro- and the

nanostructure were replicated nicely for 39 nm particles, but the small 15 nm filler particles from the resist were visible on the surface of the replica (Figure 7.28 bottom row). Figure 7.28b shows SEM images along MR-10-NP-12. The whole surface is covered in nanoparticles, indicating that the filler nanoparticles of ORGANOSILICASOL™ IPA-ST are not covered with MTMS and are revealed on the surface. The used filler particles had a diameter of 15 nm and therefore had a similar size to the particles that were to be replicated (12 nm). The replicated nanoparticles could not be distinguished from the filler nanoparticles.
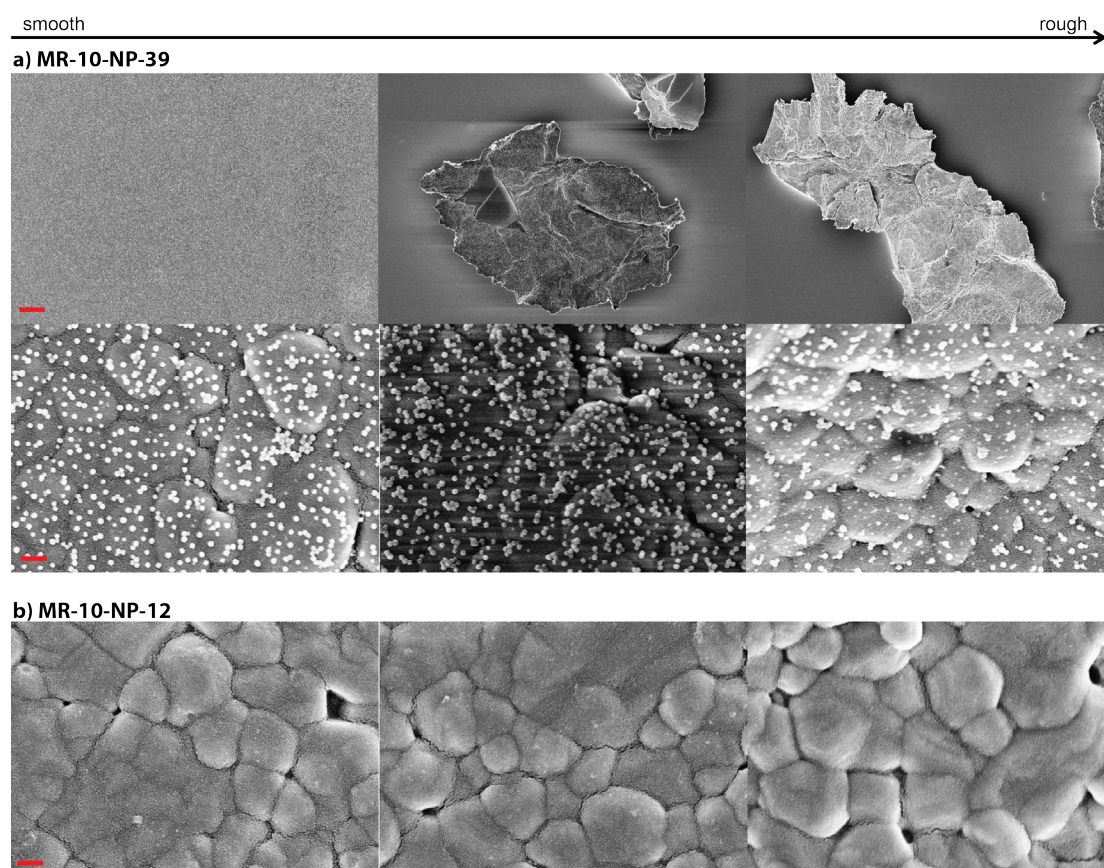

Figure 7.28: SEM images along micro-roughness gradient of 2D orthogonal gradients imprinted in ORGANOSILICASOL™ IPA-ST sol-gel resist. a) MR-10-NP-39 with 39 nm particles. Top row: 2 kX magnification showing that the micro-roughness was well replicated, but with increasing roughness the sol-gel resist started to dewet and islands were formed. Scale bar 10 µm. Bottom row: 100 kX magnification images showing that the 39 nm particles were nicely replicated along the micro-roughness gradient. Scale bar 200 nm. b) MR-10-NP-12 with 12 nm particles, 100 kX magnification showing that 12 nm particles are nicely replicated along the micro-roughness gradient. Scale bar 200 nm.

SEM images of the cross-section of the MTMS ORGANOSILICASOL™ IPA-ST sol-gel resist layer showed that the thickness varies from 2.5 to 5.8 m (Figure 7.29), which was much lower than that of the MTMS BINDZIL® sol-gel resist (Figure 7.26) and therefore explains the higher degree of dewetting of this resist.
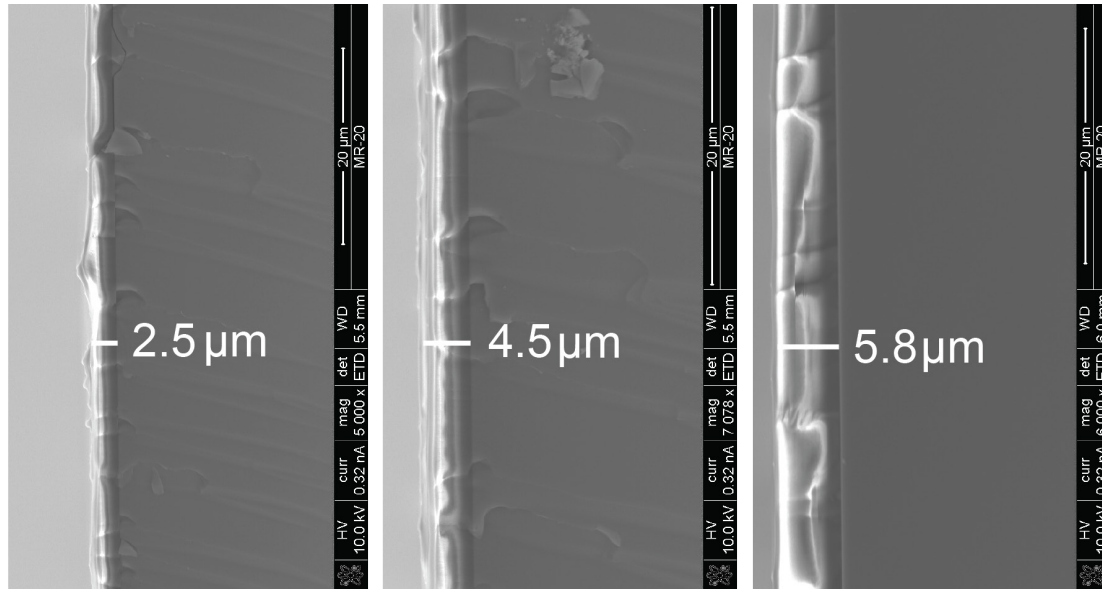

Figure 7.29: SEM images of cross-sections of MTMS ORGANOSILICASOL™ IPA-ST sol-gel resist.

The reduced water content in the MTMS ORGANOSILICASOL™ IPA-ST sol-gel resist resulted in a reduced drying time for the sol-gel to harden. The sol-gel reached a glass-like solid state in only 15 min at 50 °C and the negative could be released.

The study showed that the sol-gel resist thickness can be increased by adding silica nanoparticles as filler particles. At a low micro-roughness ($R_a \sim 1$ m), good replication of 12, 39 and 72 nm particles was possible with the MTMS BINDZIL® sol-gel resist, with the drawback that the drying time was about 12 h. The drying time could be drastically decreased to 15 min by the use of colloidal silica in isopropanol, but the resist thickness was much lower and 12 nm particles could not be replicated.

In order to fully replicate a 2D orthogonal gradient along the whole micro-roughness gradient, the sol-gel resist needs to be further improved. One possible way might be to increase the viscosity of the resist by aging it. The older the

resists become, the greater the degree of condensation. This could have the consequence that the replication quality might also be reduced as the molecules become larger, potentially reaching the size of the nanofeatures that need to be replicated. Other colloidal-silica suspensions in different solvents and with higher particle content should be tested in order to find the ideal resist thickness with an acceptable drying time.

7.5 Conclusions

Different replication techniques have been shown to successfully replicate micro- or nanoscale features.

The two-step technique with a PVS negative and an epoxy positive was shown to be an effective method for the replication of micro-featured surfaces (Section 7.2), while epoxy seemed to be not ideal for nanometer-scale feature replication (Section 7.3.1).

Nanofeatures with a size of 72 nm were nicely replicated with injection molding in COP or A-PA. It was possible to replicate more than 300 parts with injection molding in COP from a PPSU insert (negative). The transfer was simple, cheap and took less than a day and is therefore ideal for the fabrication of identical samples for applications where many identical samples are needed, e.g. cell studies. (Section 7.3.2)

SCIL was shown to be able to replicate nanofeatures down to a size of 12 nm (Section 7.3.3) and was proven to be able to replicate combined nano- and micro featured structures as long as the resist thickness was in the same range as the maximum peak-to-valley distance of the micro-roughness (R_z) (Section 7.4). In order to be able to fully replicate 2D orthogonal gradients and to use the automated SCIL process, further improvements in the resist chemistry are needed.

This newly worked out replication technique which works equally well for 12, 39 and 72 nm particles has tremendous potential to be used for biological experiments like protein-adsorption, blood-interaction and cell studies. However, because of the time constraints of the current PhD project, these experiments were performed on master gradients that had similar density profiles but were not completely identical, as described in Section 2.2.

References:

[1] M. Schuler, T.P. Kunzler, M. De Wild, C.M. Sprecher, D. Trentin, D.M. Brunette, M. Textor, S.G.P. Tosatti, Fabrication of TiO_2-coated epoxy replicas with identical dual-type surface topographies used in cell culture assays, Journal of Biomedical Materials Research - Part A 88(1) (2009) 12-22.

[2] M. Wieland, B. Chehroudi, M. Textor, D.M. Brunette, Use of Ti-coated replicas to investigate the effects on fibroblast shape of surfaces with varying roughness and constant chemical composition, Journal of Biomedical Materials Research 60(3) (2002) 434-444.

[3] C. Zink, H. Hall, D.M. Brunette, N.D. Spencer, Orthogonal nanometer-micrometer roughness gradients probe morphological influences on cell behavior, Biomaterials 33(32) (2012) 8055-8061.

[4] M.A. Verschuuren, Substrate Conformal Imprint Lithography for Nanophotonics, Utrecht University, 2010.

[5] C. Holzer, J. Gobrecht, H. Schift, H. Solak, Replication of Micro- and Nanostructures on Polymer Surfaces, Macromolecular Symposia 296(1) (2010) 316-323.

[6] S. Hong, I. Min, K. Yoon, J. Kang, Effects of adding injection–compression to rapid heat cycle molding on the structure of a light guide plate, Journal of Micromechanics and Microengineering 24(1) (2014) 015009.

[7] C. Rytka, Replication of functional polymeric micro- and nanostructures, Fakultät Elektrotechnik und Informationstechnik, TU Dortmund, 2016.

[8] H. Schift, C. David, J. Gobrecht, A.D. Amore, D. Simoneta, W. Kaiser, M. Gabriel, Quantitative analysis of the molding of nanostructures, Journal of Vacuum Science & Technology B: Microelectronics and Nanometer Structures Processing, Measurement, and Phenomena 18(6) (2000) 3564-3568.

[9] T.C. Hobæk, M. Matschuk, J. Kafka, H.J. Pranov, N.B. Larse, Hydrogen silsesquioxane mold coatings for improved replication of nanopatterns by injection molding, Journal of Micromechanics and Microengineering 25(3) (2015) 035018.

[10] A. Verschuuren Marc, M. Megens, Y. Ni, H. van Sprang, A. Polman, Large area nanoimprint by substrate conformal imprint lithography (SCIL), Advanced Optical Technologies, 2017, p. 243.

[11] B. Tobias, S.M. Spearing, M. Andrew, An assessment of the process capabilities of nanoimprint lithography, Journal of Physics D: Applied Physics 41(17) (2008) 174001.

[12] S.Y. Chou, P.R. Krauss, P.J. Renstrom, Nanoimprint lithography, Journal of Vacuum Science & Technology B: Microelectronics and Nanometer Structures Processing, Measurement, and Phenomena 14(6) (1996) 4129-4133.

[13] M.D. Austin, H. Ge, W. Wu, M. Li, Z. Yu, D. Wasserman, S.A. Lyon, S.Y. Chou, Fabrication of 5nm linewidth and 14nm pitch features by nanoimprint lithography, Applied Physics Letters 84(26) (2004) 5299-5301.

[14] F.v. Delft, R.v.d. Laar, M. Verschuuren, E. Platzgummer, H. Loeschner, Template masters for substrate conformal imprint lithography generated by charged particle nanopatterning techniques, 26th European Mask and Lithography Conference, SPIE, 2010, p. 12.

[15] Y. Xia, G.M. Whitesides, Soft Lithography, Angewandte Chemie International Edition 37(5) (1998) 550-575.

[16] J.A. Rogers, K.E. Paul, G.M. Whitesides, Quantifying distortions in soft lithography, Journal of Vacuum Science & Technology B: Microelectronics and Nanometer Structures Processing, Measurement, and Phenomena 16(1) (1998) 88-97.

[17] M.A. Verschuuren, P. Gerlach, H.A.v. Sprang, A. Polman, Improved performance of polarization-stable VCSELs by monolithic sub-wavelength gratings produced by soft nano-imprint lithography, Nanotechnology 22(50) (2011) 505201.

[18] R. Fader, M. Rommel, A. Bauer, M. Rumler, L. Frey, M.A. Verschuuren, R.v.d. Laar, R. Ji, U. Schömbs, Accuracy of wafer level alignment with substrate conformal imprint lithography, Journal of Vacuum Science & Technology B, Nanotechnology and Microelectronics: Materials, Processing, Measurement, and Phenomena 31(6) (2013) 06FB02.

[19] C.J. Brinker, G.W. Scherer, Sol-Gel Science: The Physics and Chemistry of Sol-Gel Processing, Elsevier Science2013.

[20] L.L. Hench, J.K. West, The sol-gel process, Chemical Reviews 90(1) (1990) 33-72.

[21] M. Verschuuren, H.V. Sprang, 3D Photonic Structures by Sol-Gel Imprint Lithography, MRS Proceedings 1002 (2007) 1002-N03-05.

[22] M.J. Haslinger, M.A. Verschuuren, R. van Brakel, J. Danzberger, I. Bergmair, M. Mühlberger, Stamp degradation for high volume UV enhanced substrate conformal imprint lithography (UV-SCIL), Microelectronic Engineering 153 (2016) 66-70.

[23] V.E. Ferry, M.A. Verschuuren, H.B.T. Li, R.E.I. Schropp, H.A. Atwater, A. Polman, Improved red-response in thin film a-Si:H solar cells with soft-imprinted plasmonic back reflectors, Applied Physics Letters 95(18) (2009) 183503.

[24] F. van Delft, R. van de Laar, M. Verschuuren, E. Platzgummer, H. Loeschner, Charged Particle Nanopatterning (CHARPAN) of 2D and 3D masters for flexible replication in Substrate Conformal Imprint Lithography (SCIL), Microelectronic Engineering 87(5) (2010) 1062-1065.

[25] O. Andrukhov, R. Huber, B. Shi, S. Berner, X. Rausch-Fan, A. Moritz, N.D. Spencer, A. Schedle, Proliferation, behavior, and differentiation of osteoblasts on surfaces of different microroughness, Dental Materials 32(11) (2016) 1374-1384.

[26] T.P. Kunzler, T. Drobek, C.M. Sprecher, M. Schuler, N.D. Spencer, Fabrication of material-independent morphology gradients for high-throughput applications, Applied Surface Science 253(4) (2006) 2148-2153.

[27] C. Zink, Morphological Gradients for Biomedial Applications, ETH Zürich, 2011.

[28] M. Geissler, H. Wolf, R. Stutz, E. Delamarche, U.-W. Grummt, B. Michel, A. Bietsch, Fabrication of metal nanowires using microcontact printing, Langmuir 19(15) (2003) 6301-6311.

[29] G. Csucs, T. Künzler, K. Feldman, F. Robin, N.D. Spencer, Microcontact Printing of Macromolecules with Submicrometer Resolution by Means of Polyolefin Stamps, Langmuir 19(15) (2003) 6104-6109.

[30] B. Rüfenacht, Polymerinserts für kürzere Entwicklungszeiten, Institut für Nanotechnische Kunststoffanwendungen, Fachhochschule Nordwestschweiz, 2015.

[31] C. Rytka, P.M. Kristiansen, A. Neyer, Iso- and variothermal injection compression moulding of polymer micro- and nanostructures for optical and medical applications, Journal of Micromechanics and Microengineering 25(6) (2015) 065008.

[32] Website, SCIL Nanoimprint Solutions. <http://www.ip.philips.com/data/static/scil/index.php>, 7. Februar 2018 17:01:23 MEZ).

Chapter 8

Particle-size gradients by dewetting of noble metals

In this chapter, the fabrication and characterization of particle-size gradients, obtained by dewetting of silver as previously described by Clément Cremmel [1] are discussed. The goal of a master project conducted by Vera Voney [2] and a 6-month internship conducted by Yoan Boussès [3] was to find a fabrication protocol that can reproduce particle-size gradients by dewetting of silver and to use the gradients for biological experiments.

8.1 Introduction

In 1966, Brandon *et al.* [4] discovered solid-state dewetting of metals at temperatures below their melting point on surfaces. In the as-deposited state, thin films are metastable. If a thin film is heated, agglomerates start to form and the film breaks up into islands. This process is called dewetting [5]. The driving force for the dewetting process is interface energy minimization and can occur in the solid state though capillary-driven surface self-diffusion [6]. With elevated temperatures, but still below the melting temperature of the metal, the mobility of the atoms increases and they start to move into more favorable positions by diffusion along the surface, interfaces and grain boundaries. Holes are formed, which grow in size and eventually start to overlap to form dewetted regions [5]. Since atomic transport is required for dewetting, the rate of dewetting strongly depends on temperature. It was shown that the temperature at which dewetting is observed decreases with decreasing film thickness [7, 8]. Kojima *et al.* [9] investigated nanoparticle formation in thin (5-30 nm) Au films on smooth SiO_2 substrates. They showed that the diameter and spacing of Au islands that form through dewetting decrease with decreasing film thickness. The equilibrium

shape of small particles in contact with a foreign substrate can be predicted by the Winterbottom construction [10]. Through their modeling studies, Zucker *et al.* [6] showed that certain crystallographic planes may be favored during the dewetting process due to their higher stability, which leads to faceted particles or faceted dewetting structures.

Dewetting limits the reliability of integrated circuits and other microsystems and much research has been carried out to characterize and suppress dewetting [11-16]. However, there is an increasing number of examples in which dewetting has been used on purpose to make particles and interconnected structures [5]. Solid-state dewetting is used to make particle arrays in sensor [17], for the generation of nanocrystals for electrical and optical memory devices [18, 19] and for use as catalyst templates for the growth of carbon nanotubes [20, 21].

The aim of this work was to reproduce the silver particle-size gradients previously introduced by Clément Cremmel [1] made by solid-state dewetting of silver-thickness gradients and to study protein adsorption on them. Results from Clément Cremmel are shown in Figure 8.1 and Figure 8.2. Gold and silver particle-size gradients were investigated by AFM and SEM. The particle height was found to vary between a few nm and 300 nm, the particle diameter from a few nm to 650 nm and the particle density was decreasing from 120×10^9 to a few particles per cm^2, along the gradient.
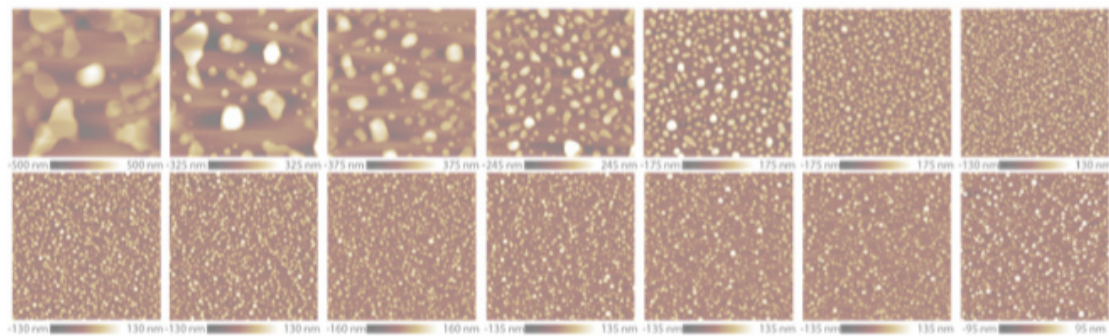

Figure 8.1: AFM images of Clément Cremmel's silver gradient. Images were taken every 5 mm with decreasing silver thickness from left to right, and top to bottom. Image size 10 m. Taken from [1].
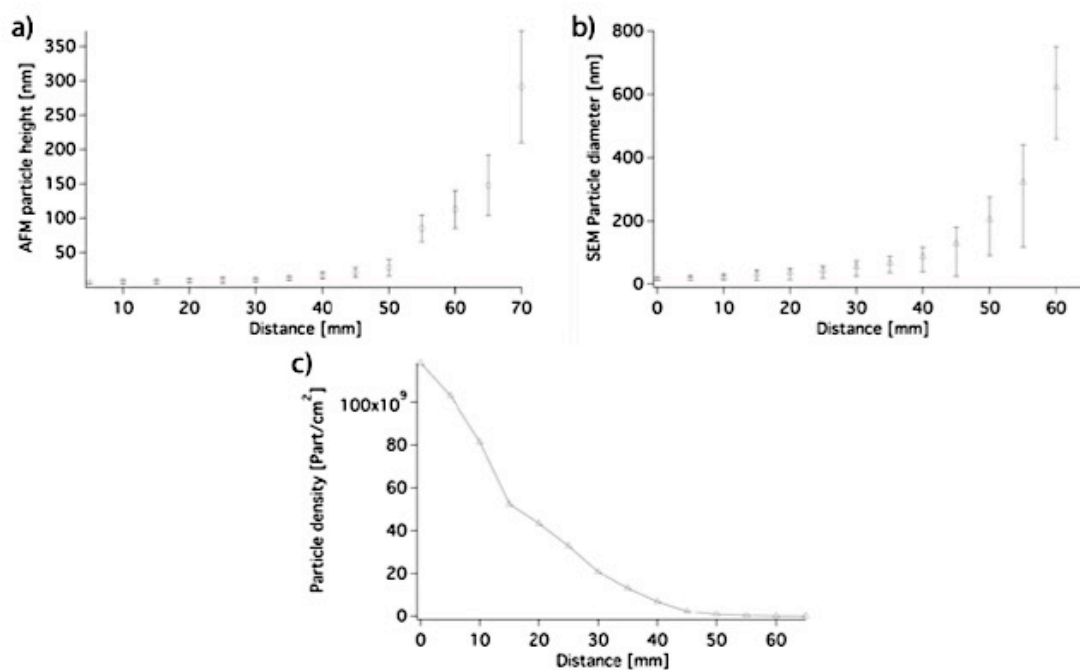
Figure 8.2: Particle analysis of Clément Cremmel's gold gradient. a) Particle height measured by AFM. b) Particle diameter and c) particle density measured from SEM images. Taken from [1].

8.2 Experimental

8.2.1 Gradient fabrication

For all the experiments, 76×26 mm² silicon wafers (<100> orientation, Si-mat, Germany) were used. The wafers were ultra-sonicated in toluene (puriss. P.a., ≥ 99.7%, Fluka Chemicals, Germany) for 20 minutes with solvent exchange after the first 10 minutes and dried with nitrogen (5.0 purity). Subsequently the wafers were ultra-sonicated for 20 minutes in 2-propanol (ACS grade, min 99.8%, Fluka Chemicals, Germany) with a solvent exchange after 10 min, and dried with nitrogen. To remove any organic contamination, wafers were immersed into hot piranha (3:1 sulphuric acid/hydrogen peroxide) solution for 20 minutes. The samples were then transferred to a beaker filled with MilliQ water, rinsed with MilliQ water and dried with nitrogen.

As a last cleaning step and to activate the surface, the samples were further cleaned in a radio-frequency (RF) oxygen plasma (PDC_32G, Harrick Plasma, USA), pumping the plasma chamber down to 2.5×10^{-2} mbar, and maintaining a constant pressure at $3 \cdot 10^{-2}$ mbar under oxygen. The plasma was ignited at high RF level (100 W) for 2 min. Immediately after plasma-cleaning, the samples were coated with hexamethyldisilazane (HMDS, Sigma-Aldrich, USA) by placing them in a desiccator. 0.2 ml HMDS was dropped onto a fresh glass slide next to the samples and the desiccator was closed without applying vacuum and left for 1 hour.

Silver was deposited using an evaporator (Balzer MED20, Baltec AG, Liechtenstein). To achieve a gradient in coating thickness, the samples were mounted upright with a cross-section SEM holder (G301S, Plano GmbH, Germany) (Figure 8.3). Samples were either mounted in a radial or tangential alignment with the HMDS-coated side facing inside. Silver deposition was performed at a pressure below 2.5×10^{-5} mbar and an evaporation rate lower than 0.1 mm/s. To improve homogeneity of the coating, the samples were rotated during the evaporation process. The coating was stopped when the horizontal quartz crystal microbalance measurement at the bottom of the wafer corresponded to 50 nm thickness.

For dewetting of the silver coating, the samples were placed in aluminum oxide crucibles and heated in an oven (Heraeus M110, Heraeus Instruments) to 600 °C at a rate of 1 °C/min in air, maintained at 600 °C for 2 hours and cooled down to room temperature at a rate of 1 °C/min.
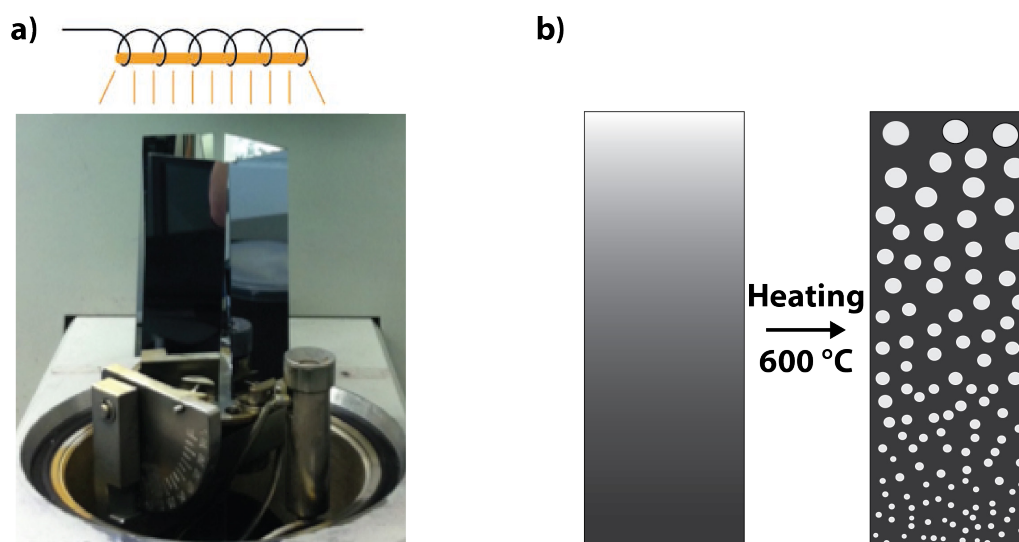
Figure 8.3 a) Silver deposition on the wafer. The wafers are kept upright in the evaporator towards the source and rotated during the evaporation. b) Dewetting step. The silver coated wafer is heated up to 600 °C for 2 h, silver islands form along the gradient. Adapted from [1].

For protein-adsorption experiments, the gradients were coated with 6 nm of TiO_2 to mimic the surface of titanium implants. The coating was performed at the Paul Scherrer Institute by magnetron sputtering and a growth rate of 1 nm/min.

8.2.2 Characterization

To analyze the diameter, height and density of the silver particles along the gradient, the samples were investigated by atomic force microscopy (AFM, Dimension Icon AFM, Bruker, UK) in tapping mode. Olympus tapping-mode tips (OMCL-AC160TS-R3, Olympus, Japan) were used with a nominal resonance frequency of 300 kHz and a nominal spring constant of 26.1 N/m. To measure the particle height, AFM images were analyzed by NanoScope Analysis 1.5.

Silver gradient samples were analyzed by scanning electron microscopy (SEM, LEO 1530, Zeiss, Germany) by taking SEM pictures along the gradient with an acceleration voltage of 3 kV with the in-lens detector. A Matlab code was written by Vera Voney [2] to measure the particle diameter and density. The function *imfindcircles* was used to find all circles in an image. The code gives a

list of all the particles and their diameters as an output. For the Matlab analysis, SEM images with 20 kX magnification were used.

To estimate the thickness of the deposited silver layer, some samples were half covered with adhesive tape during evaporation and were analyzed with ellipsometry (Variable Angle Spectroscopic Ellipsometer M-2000F).

8.2.3 Protein experiments

For protein experiments, fetal bovine serum (FBS, qualified, E.U.-approved, South American origin, Invitrogen, USA) was spiked with 5 g/ml fluorescently labeled albumin (albumin from bovine serum (BSA), Alexa Fluor 647 conjugate, Invitrogen, USA) and 5 g/ml fibrinogen (fibrinogen from human plasma (HPF), Alexa Fluor 546 conjugate, Invitrogen, USA).

Before use, the particle-size gradients were cleaned in oxygen plasma for 2 min to remove hydrocarbon contamination and get a hydrophilic TiO_2 surface. Protein adsorption was carried out by immersing the whole samples into 8 ml protein suspension. After 10 min the gradient was transferred into 8 ml HEPES 2 buffer (10 mM 4-(2-hydroxyethyl) piperazine-1-ethanesulfonic acid (HEPES) and 150 mM NaCl, pH 7.4) and rinsed three times with HEPES 2, followed by a transfer into 400 ml Milli-Q water and one rinse with Milli-Q water. Subsequently the gradients were dried in a stream of nitrogen.

The fluorescently labeled albumin and fibrinogen were mapped with a fluorescence microarray scanner (Axon Genepix 4200A, Molecular Devices, USA). The resolution was set to 5 μm/pixel. Image analysis was performed using ImageJ software (version 1.44p for Mac). A line plot of intensity along the particle-size gradient was created by averaging the gray values of all pixels along the lines perpendicular to the gradient. As the real surface area changes along the particle-size gradient, the measured intensity values were corrected for the

increase in surface area by the presence of silver islands by normalizing the intensity values to the real surface area (measured by AFM).

8.2.4 Fabrication of epoxy replicas

Negatives of the silver particle-size gradients were prepared in polydimethylsiloxane (PDMS, Sylgard 184, Dow Corning, USA). The gradient was mounted with double-sided tape to the bottom of a petri dish and the PDMS mixture was poured over the gradient. In order to remove air bubbles from the interface, a low vacuum (~ 7 mbar) was applied for 1 h prior to curing at 60 °C for 24 h.

Negatives of gradients were used directly to cast the epoxy. The two components of the epoxy resin (EPO-TEK 302-3M, Polyscience AG, Switzerland) were thoroughly mixed in a centrifuge tube in the ratio 100:45, as recommended by the manufacturer. The mixture was then degassed in a centrifuge for 5 min at 4000 RPM. Epoxy resin was cast onto the PDMS negatives and cured at 65 °C for 24 h. The cured, positive epoxy replicas were then removed from the negative and cleaned for 20 min in 2 vol% Hellmanex solution (HELLMA GmbH & Co, Müllheim, Germany) followed by 20 min in MilliQ water in an ultrasonic bath. Afterwards they were extensively rinsed 10 times in MillQ water, pre-dried in a stream of nitrogen and left to dry completely in air overnight.

8.3 Results and Discussion

In order to improve the gradients, small changes in the preparation procedure have been made. An overview of these changes and the results are displayed in Table 8.1.

Table 8.1: Summary of first experiments of the master project of Vera Voney [2]. The samples were named SG for Silver Gradient and a letter for the batch.

Batch	Differences from standard protocol	Results
SG-A	HMDS with vacuum	Nice round particles
SG-B	No plasma cleaning and no HMDS	Different results depending on position in oven
SG-C	As SG-A but HMDS without vacuum. First time new sample positioning in evaporator	Round particles but smaller than in SG-A
SG-D	No piranha cleaning	No round particles in thick part, smaller particles than in SG-C
SG-E	Reproduction of SG-C	Similar to SG-C

a) SG-A1+ Piranha + O2 Plasma + HMDS (with vacuum)

b) SG-B2 + Piranha - O2 Plasma - HMDS

c) SG-C1 + Piranha + O2 Plasma + HMDS (without vacuum)

d) SG-D2 - Piranha + O2 Plasma + HMDS (without vacuum)

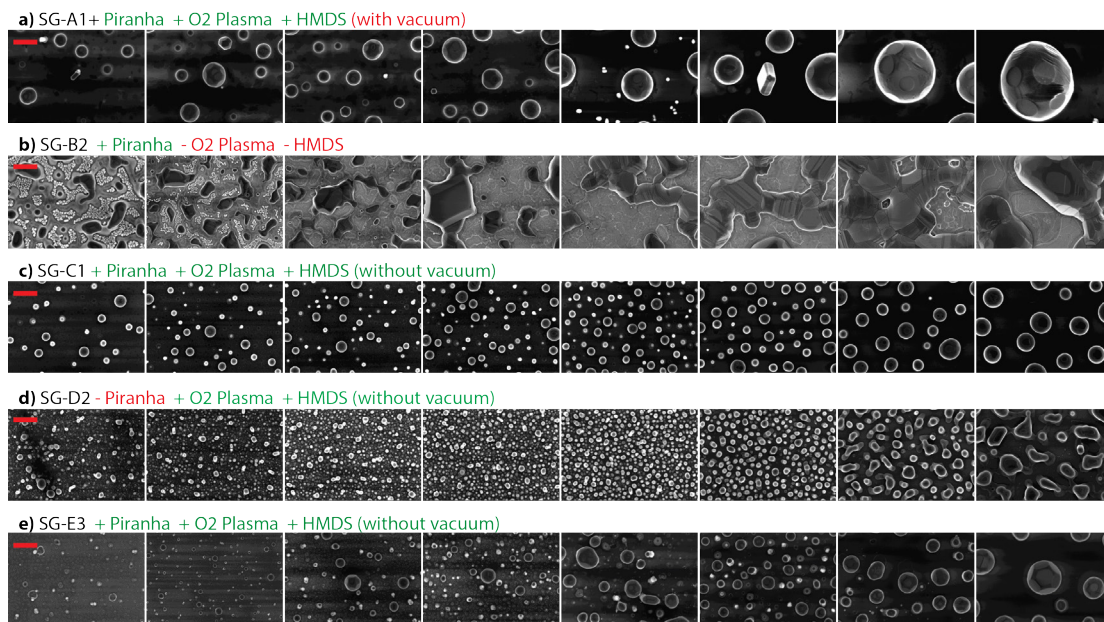**e)** SG-E3 + Piranha + O2 Plasma + HMDS (without vacuum)

Figure 8.4: SEM images taken every 10 mm along silver particle-size gradients with increasing silver thickness from left to right with a magnification of 100 kX. Scale bar for all images 500 nm. a-e) different batches of silver particle-size gradients with slightly altered fabrication protocols. Alterations from standard protocol are marked in red.

Slight changes in the fabrication protocol resulted in significant changes in the appearance of the particle-size gradients as can be seen in Figure 8.4.

The SG-A batch was prepared as described by Clément Cremmel [1] with the exception that HMDS was deposited with applied vacuum ($\sim$ 7 mbar). This resulted in gradients (see Figure 8.5 and Figure 8.6) with perfectly round-shaped particles (Figure 8.7) with diameters between 200 and 1200 nm (Figure 8.8 b), and heights between 100 and 550 nm (Figure 8.8 a) with increasing coating thickness. The particle density starts at 1.6×10^8 particles/cm^2, increases initially, stays constant and then decreases to 0.2×10^8 particles/cm^2 (Figure 8.8 c). Comparing the results to the gold gradient data that Clément Cremmel obtained (see Figure 8.2), it can be seen that the silver particles were larger in diameter and height, whereas the density was lower.
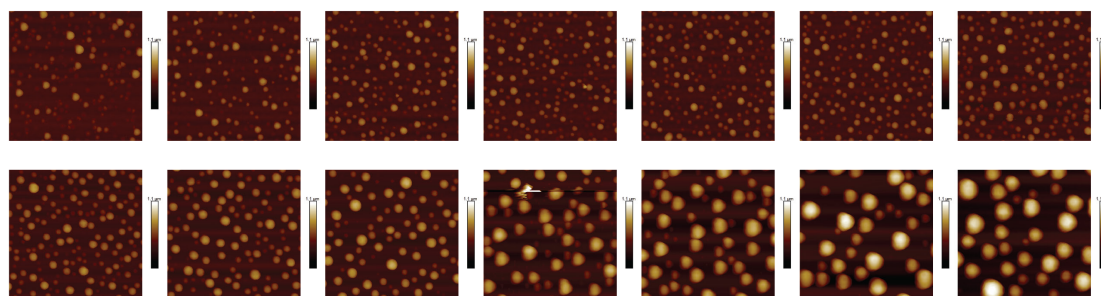

Figure 8.5: AFM images of SG-A1, taken every 5 mm along the gradient with increasing silver thickness from left to right, and top to bottom. Image size is 10 m.
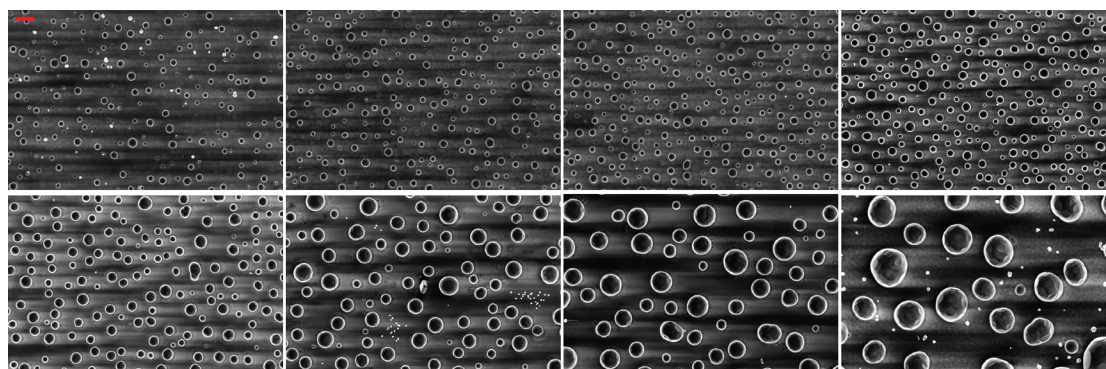

Figure 8.6: SEM images of SG-A1, taken every 10 mm along the gradient with increasing silver thickness from left to right, and top to bottom with a magnification of 20 kX. Scale bar 1 m.
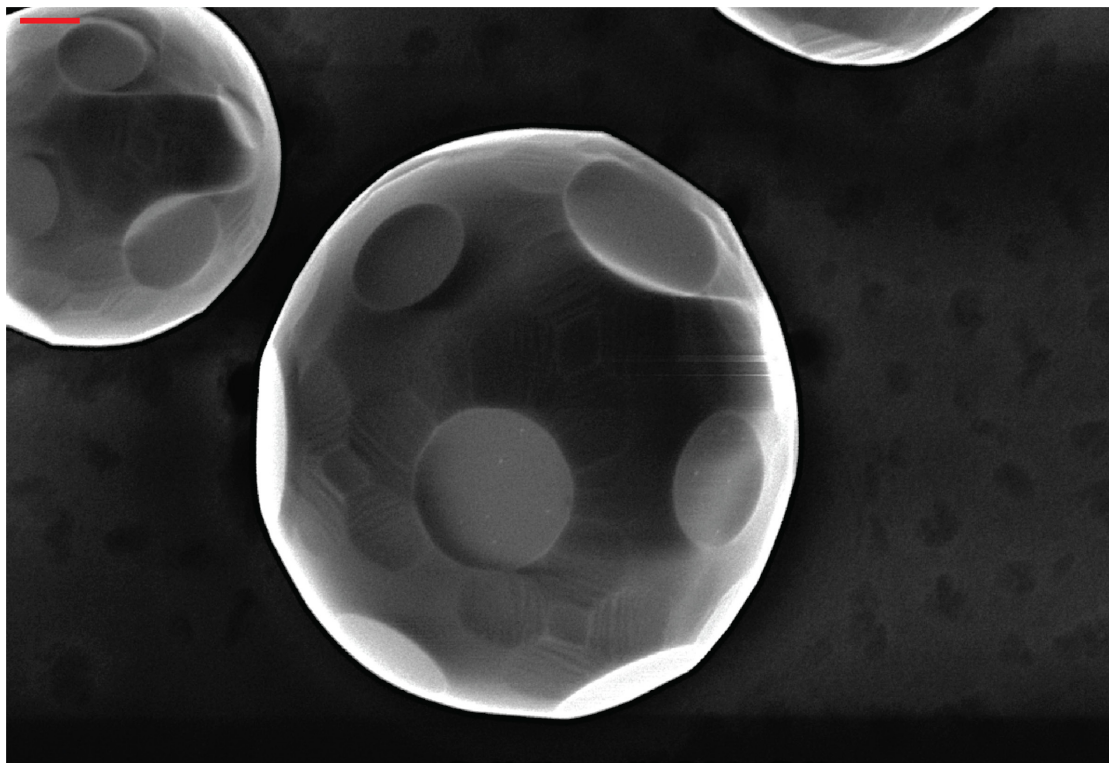
Figure 8.7: In-lens SEM images of a silver particle at the thick end of the SG-A1 gradient with 100 kX magnification. Scale bar 200 nm.
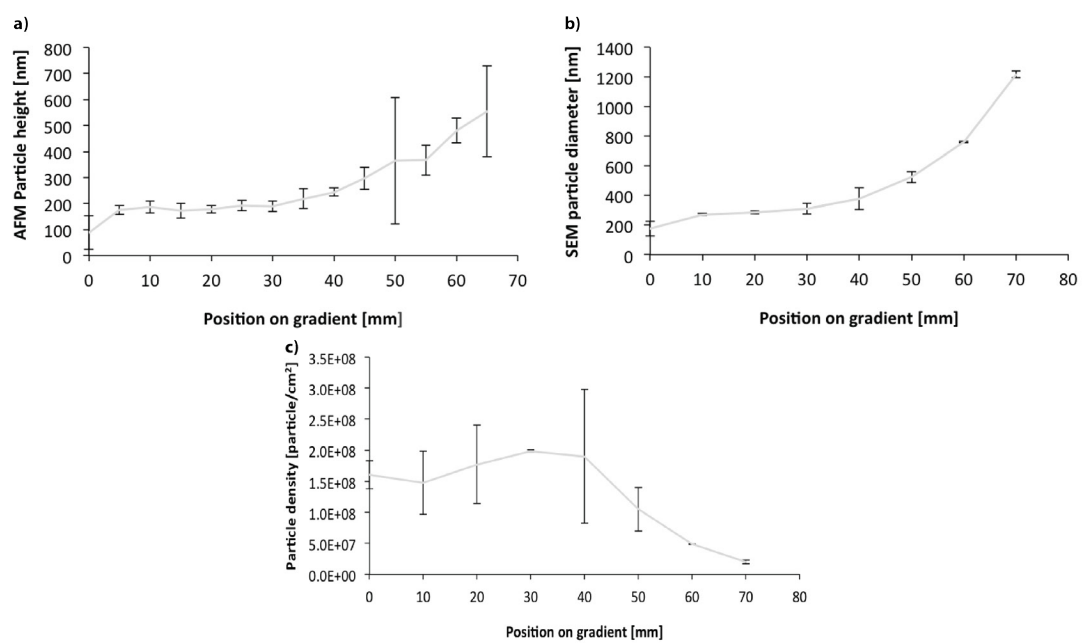

Figure 8.8: AFM and SEM analysis of SG-A. a) Particle height measured by AFM. b) Particle diameter measured from SEM images. c) Particle density calculated from SEM images.

Influence of position in oven during dewetting

To understand the importance of the HMDS coating in the gradient formation, a batch without HMDS and without plasma cleaning was prepared. The AFM images of this batch showed that the position in the oven during dewetting played an important role. SG-B1 and SG-B2 were placed in a large ceramic tray in the bottom and covered with a second tray. AFM images of these two samples showed that the silver did not dewet completely and no round particles were formed at the high-coating-thickness end of the gradient (Figure 8.9 and Figure 8.10). SG-B3 which was placed in the top tray and covered with a third tray during dewetting in the oven, showed round particles (Figure 8.11) with diameter between 200 and 300 nm (Figure 8.12 b), and heights between 115 and 145 nm (Figure 8.12 a) with increasing coating thickness. The particle density started at 5.7×10^8 particles/cm^2 and decreased to 0.6×10^8 particles/cm^2 (Figure 8.12 c). Comparing the results to SG-A (Figure 8.8), it can be seen that the silver particles were smaller in diameter and height, whereas the density was higher.
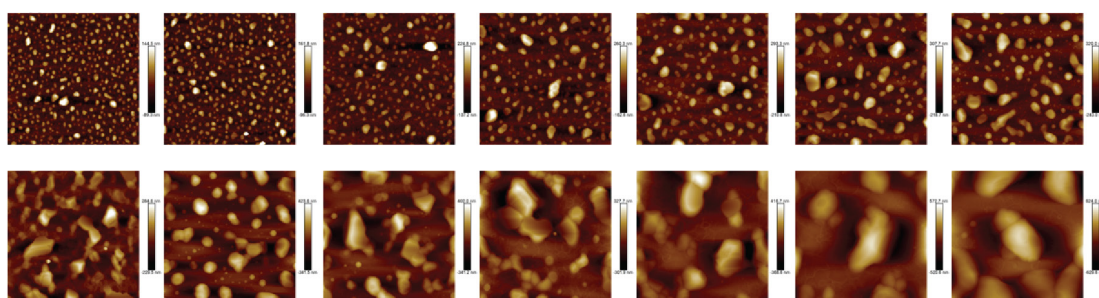

Figure 8.9: AFM images of SG-B1, taken every 5 mm along the gradient with increasing silver thickness from left to right, and top to bottom. Image size is 10 m. Gradient was positioned in bottom tray during dewetting.

Figure 8.10: AFM images of SG-B2, taken every 5 mm along the gradient with increasing silver thickness from left to right, and top to bottom. Image size is 10 m. Gradient was positioned in bottom tray during dewetting.
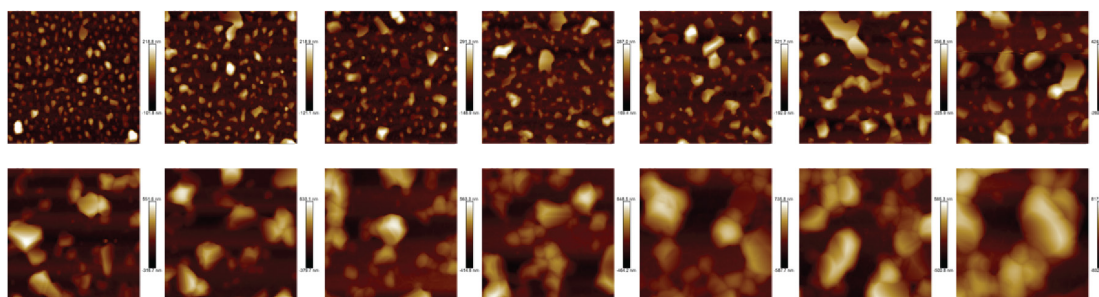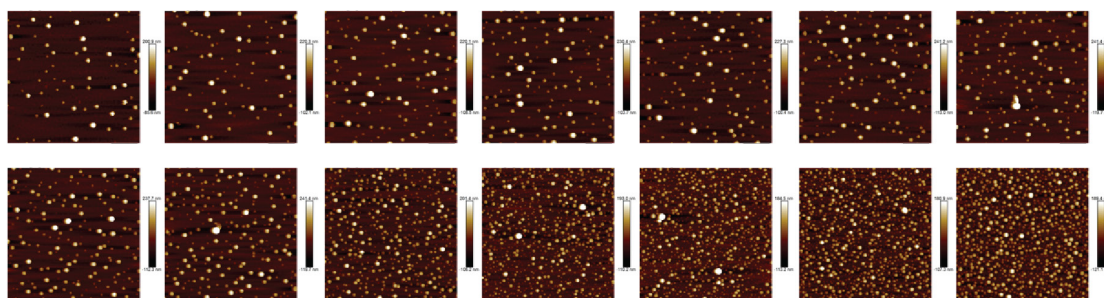
Figure 8.11: AFM images of SG-B3, taken every 5 mm along the gradient with increasing silver thickness from left to right, and top to bottom. Image size is 10 m. Gradient was positioned in top tray during dewetting.
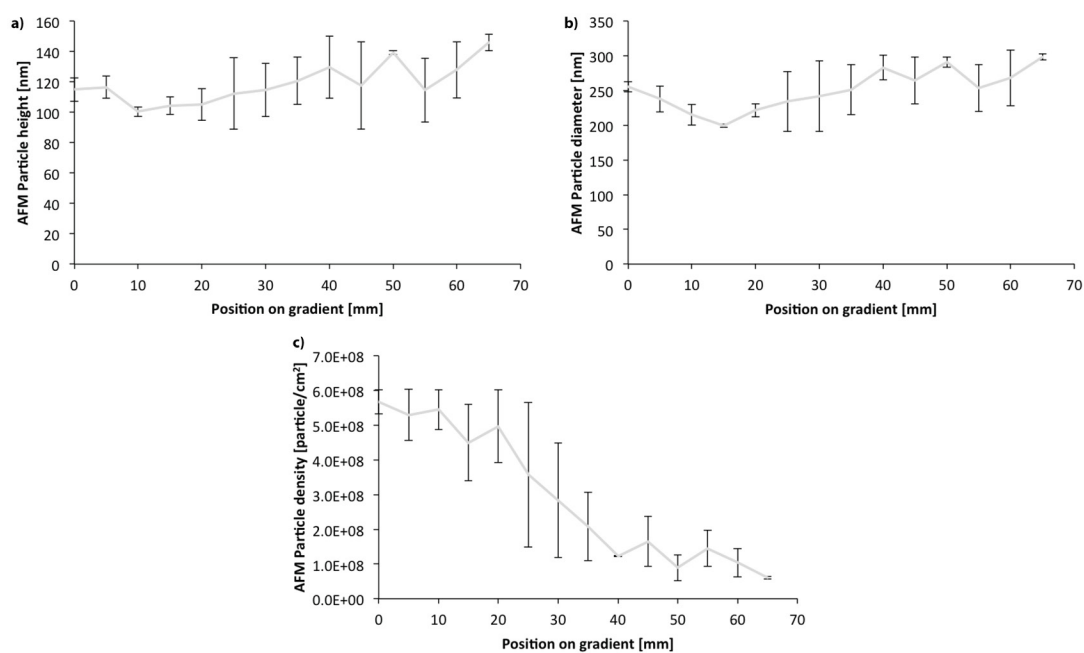

Figure 8.12: AFM measurements of SG-B3 a) mean particle height, b) mean particle diameter and c) mean particle density.

The different dewetting behaviors of the silver gradients in the top and bottom trays can be explained by temperature differences, which will change the mobility of the silver atoms. Thermocouple measurements of the temperature inside the ceramic trays in the oven during dewetting showed that the temperature development was different in the bottom and in the top tray (Figure 8.13). The temperature in the top tray (green) increased faster than that in the bottom tray (red) during heating and decreased faster than the temperature in the bottom tray during cooling. At 650 °C the effect was more pronounced; a temperature difference between the top and the bottom box of approximately 30 °C was measured.
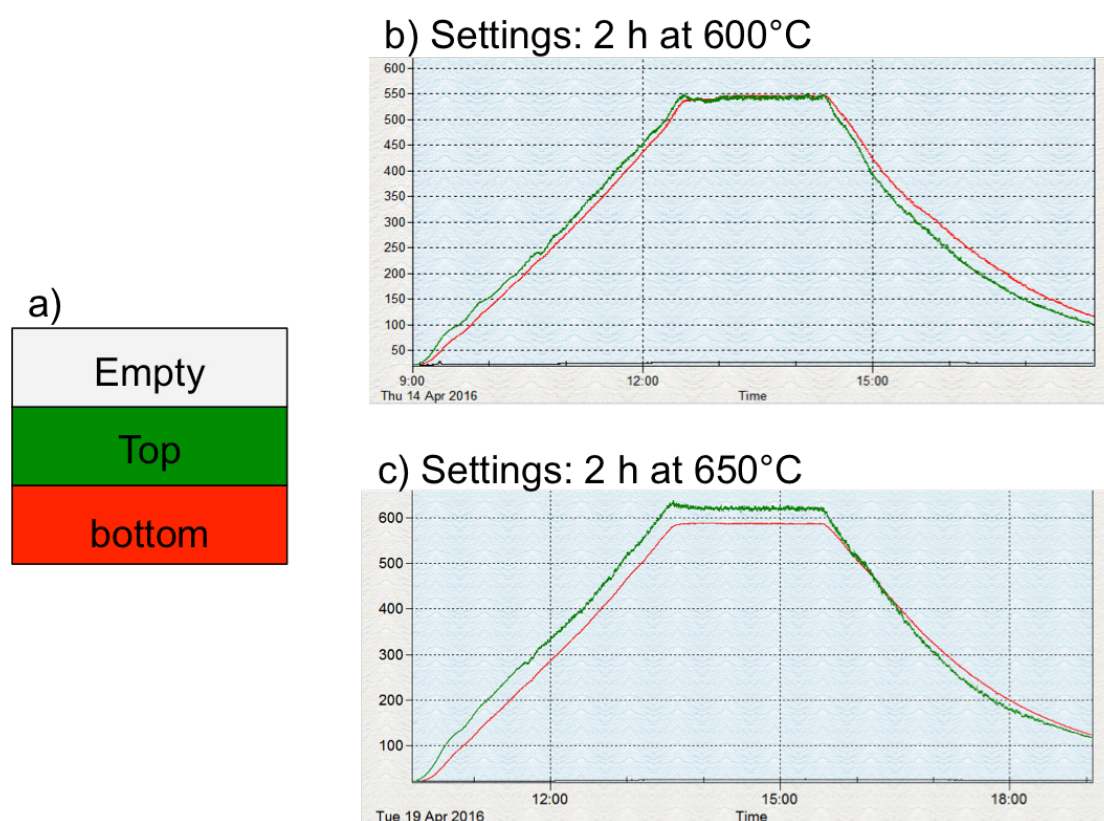
Figure 8.13: Thermocouple measurement of the temperature development in the oven. a) Scheme of ceramic tray alignment. Temperature development in bottom (red) and top (green) tray at b) 600 °C and c) 650 °C for 2 h.

Influence of alignment in evaporator chamber

In the first two experiments the samples were mounted in a radial alignment. In this configuration the wafers shielded each other and only three samples could fit. There was also a gradient in coating thickness in the lateral direction, since one side of the sample was closer to the evaporation source than the other. The setup was changed to a tangential arrangement in which it was possible to fit four samples at a time and a more uniform coating in the lateral direction was achieved. The ellipsometry measurements (Figure 8.14) of the coating thickness showed that the placement in the evaporator did influence the coating thickness. In the radial placement (SG-A, red), the thickness stayed almost constant until the middle of the sample and then increased to a thickness that was too thick to be measured by ellipsometry. The tangential placement (SG-C, blue) showed a nearly linear increase with a lower thickness on the thick end of the gradient.
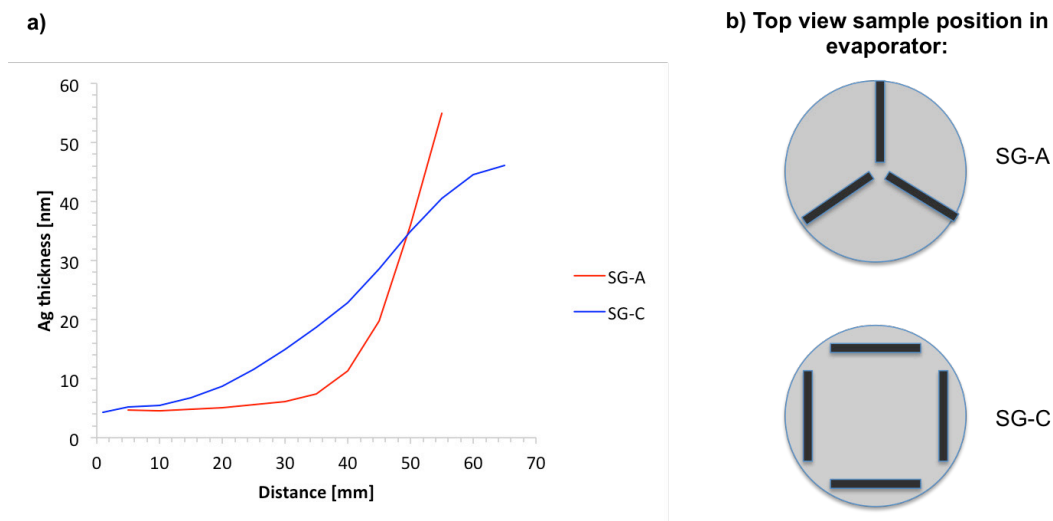
a)

b) Top view sample position in evaporator:

Figure 8.14: a) Ellipsometer measurements of silver coating thickness depending on sample alignment in the evaporator chamber. b) Sample position in the evaporator. SG-A with radial and SG-C with tangential alignment.

The SG-C batch was prepared as described by Clément Cremmel [1], but with a tangential aligning of the wafers in the evaporator chamber. The gradients showed round particles (Figure 8.15 and Figure 8.16) with an increase in particle diameter from 110 nm to 380 nm (Figure 8.17 b) and in particle height from 100 to 250 nm. The particles were therefore much smaller in diameter than observed for SG-A. The density had a maximum of 9.9×10^8 particles/cm^2 in the middle of the gradient (Figure 8.17 c). Compared to Clément Cremmel's gradients the particle height and diameter distribution of this gradient was narrower because of the different placement in the evaporation chamber, which led to a smaller coating thickness. The smaller coating-thickness also explains the difference in particle size to the SG-A batch.
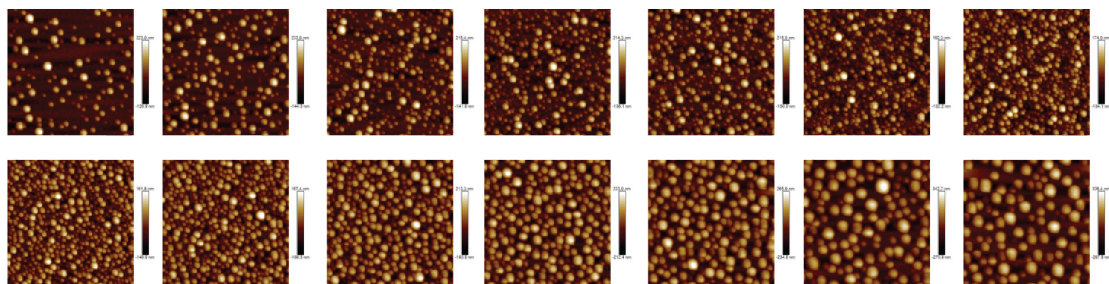

Figure 8.15: AFM images of SG-C4, taken every 5 mm along the gradient with increasing silver thickness from left to right, and top to bottom. Image size is 10 m.
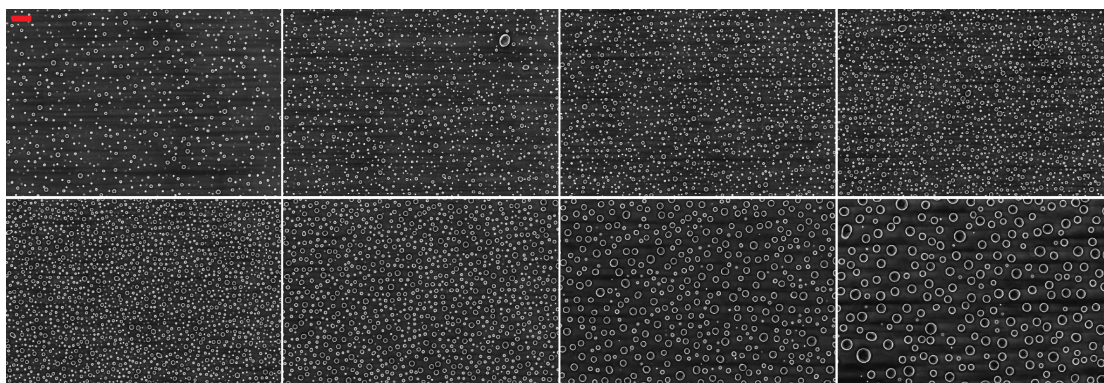
Figure 8.16: SEM images of SG-C1, taken every 10 mm along the gradient with increasing silver thickness from left to right, and top to bottom with a magnification of 20 kX. Scale bar 1 m.
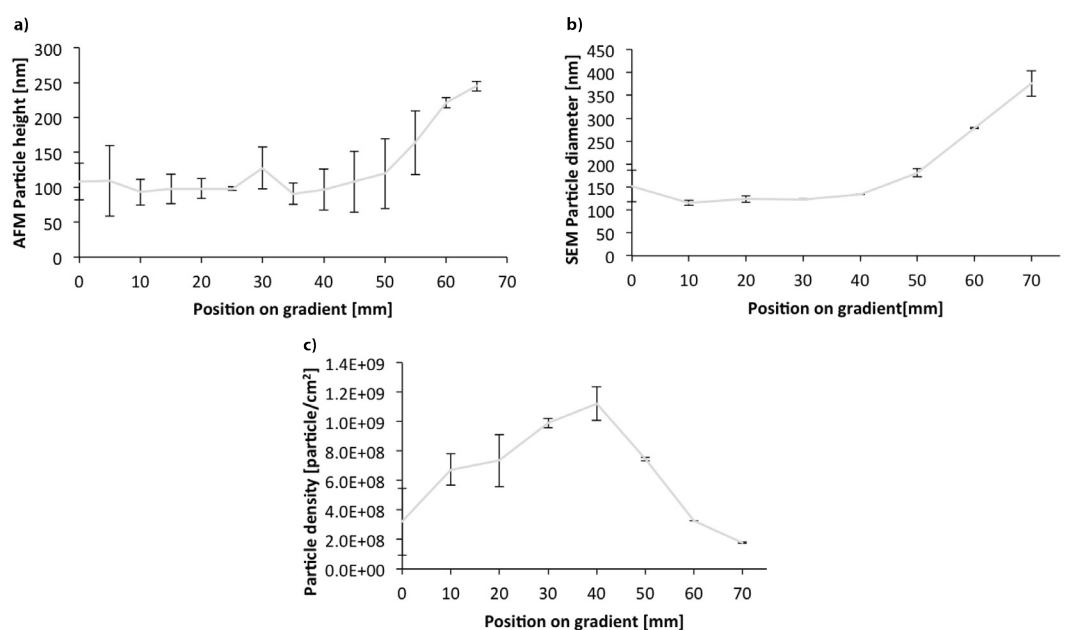
Figure 8.17: AFM and SEM analysis of SG-C. a) Particle height measured by AFM. b) Particle diameter measured from SEM images. c) Particle density calculated from SEM images.

Influence of piranha cleaning

To investigate the influence of piranha cleaning on the dewetting process, the samples were produced with the same protocol as for batch SG-C, but without piranha cleaning. AFM (Figure 8.18) and SEM images (Figure 8.19) along the gradient revealed that a particle-size gradient was formed. But a closer look at SEM images with 100 kX magnification in Figure 8.20 showed that the silver coating was not fully dewetted. Without the piranha cleaning, organic residues contaminate the silicon wafer surface, which change the dewetting behavior of the silver. Due to the interconnection of the particles, no complete particle

analysis was possible. The AFM measurements of SG-D2 showed particle heights between 80 and 140 nm (see Figure 8.21), which was lower than the heights obtained before. A possible reason for the lower particle height might be the incomplete island formation.

Figure 8.18: AFM images of SG-D2, taken every 5 mm along the gradient with increasing silver thickness from left to right, and top to bottom. Image size is 10 m.

Figure 8.19: SEM images of SG-D2, taken every 10 mm along the gradient with increasing silver thickness from left to right, and top to bottom with a magnification of 20 kX. Scale bar 1 m.
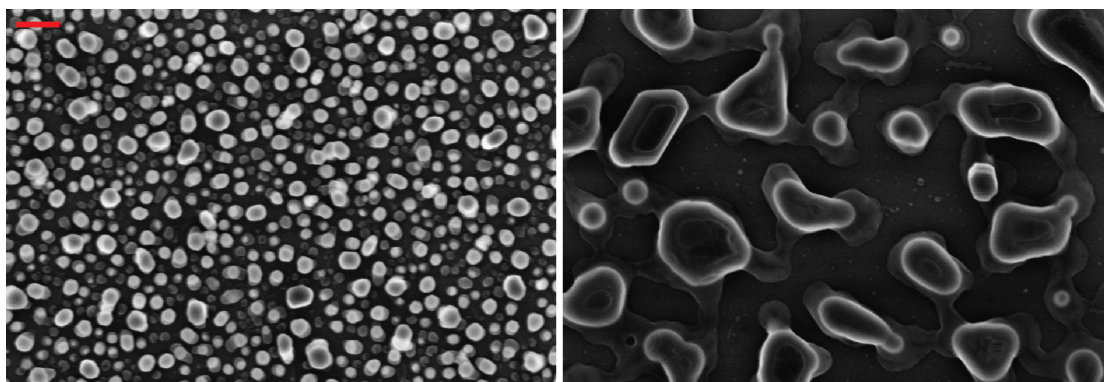

Figure 8.20: SEM images of SG-D2 at 40 and 70 mm distance from the thin end of the gradient. 100 kX magnification. Scale bar 200 nm.
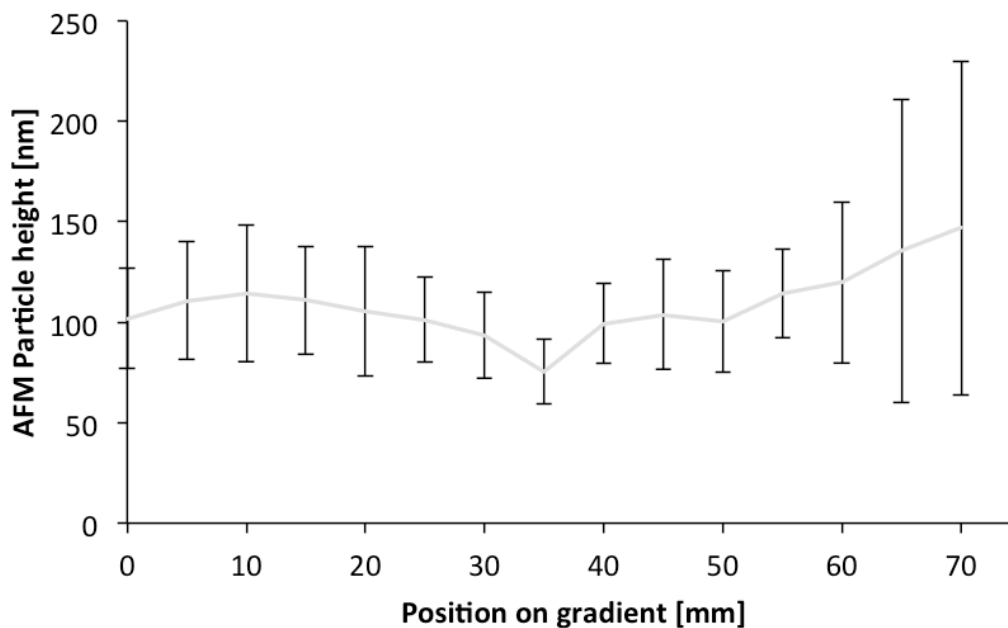
Figure 8.21: Particle height measured by AFM along SG-D2 gradient.

Reproducibility of gradients

Batch SG-E was a reproduction of SG-C with exactly the same fabrication protocol. AFM (Figure 8.22) and SEM images (Figure 8.23) showed that a particle-size gradient was achieved with round particles. An increase in particle diameter from around 50 nm to 380 nm (Figure 8.24a) was measured that was very similar to the one measured for SG-C3 (110 to 380 nm). The density had a maximum of 4.07×10^9 particles/cm^2 in the middle of the gradient (Figure 8.24b), which was much higher than that measured for SG-C3 of 9.9×10^8 particles/cm^2.
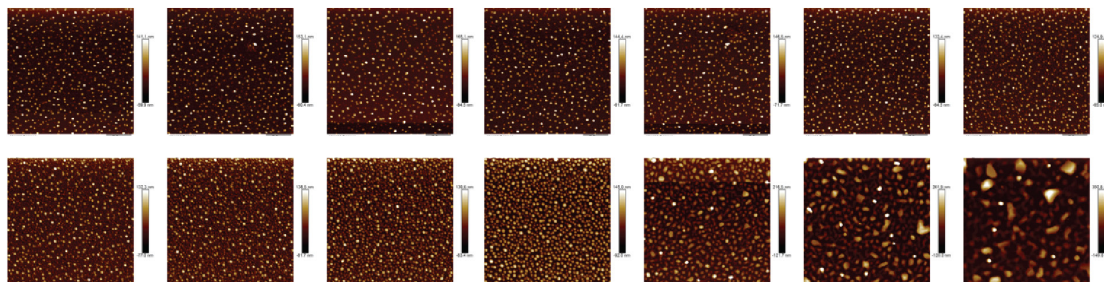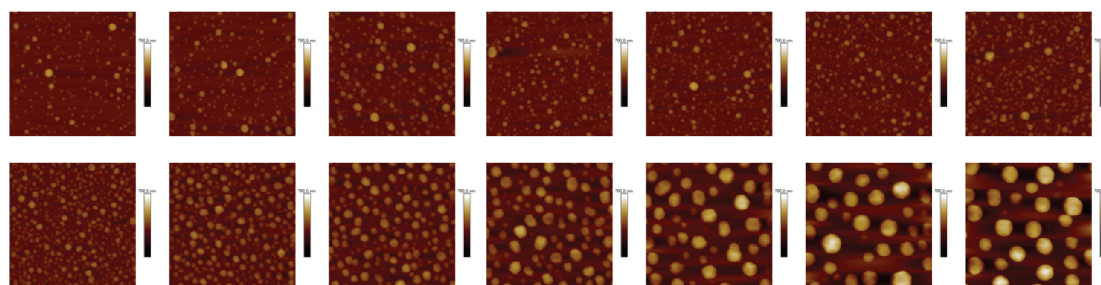

Figure 8.22: AFM images of SG-E3, taken every 5 mm along the gradient with increasing silver thickness from left to right, and top to bottom. Image size is 10 m.
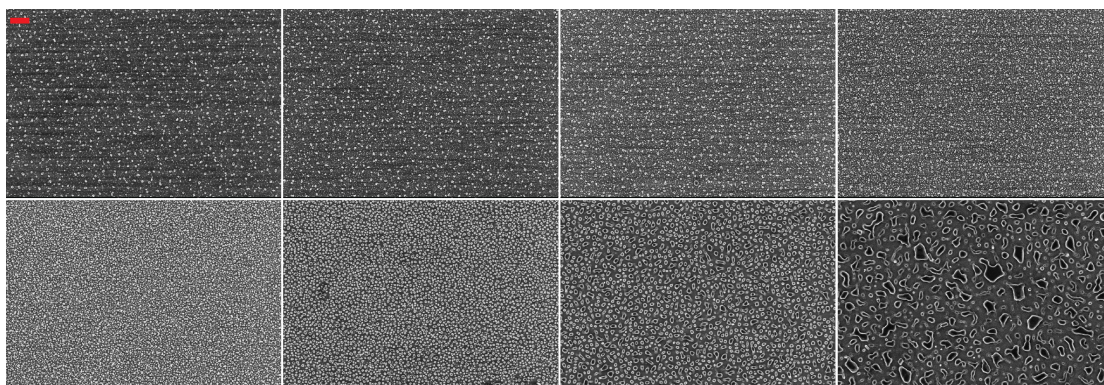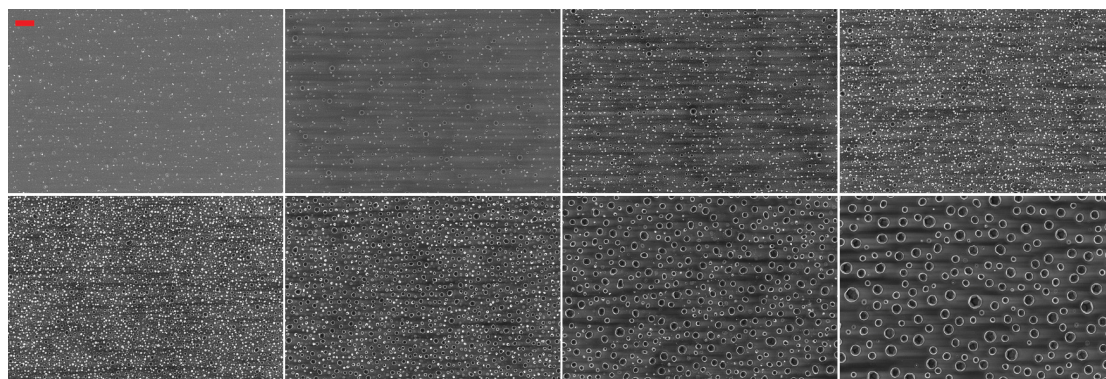
Figure 8.23: SEM images of SG-E3, taken every 10 mm along the gradient with increasing silver thickness from left to right, and top to bottom with a magnification of 20 kX. Scale bar 1 m.
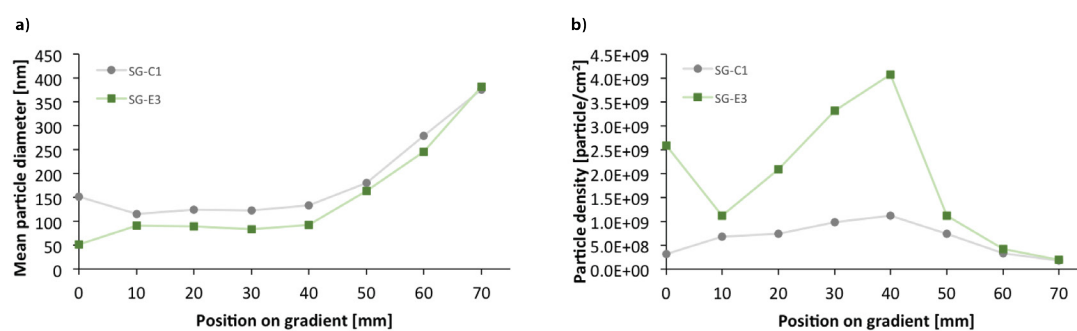

Figure 8.24: a) Mean particle diameter and b) density of SG-E3 (green squares) compared with SG-C3 (gray circles) measured from SEM images.

Figure 8.25 compares AFM images along different silver gradient batches that were produced with identical protocols. It can be seen that a particle-size gradient was always achieved, but the particles' shape, size and density varied from batch to batch and also between different samples from the same batch (Figure 8.25 a) and b), c) and d), e) and f), i) and j)).

a) SG-C1

b) SG-C4

c) SG-E3

d) SG-E4

e) SG-G1

f) SG-G3

g) SG-H2

h) SG-I4

i) SG-J1

j) SG-J2

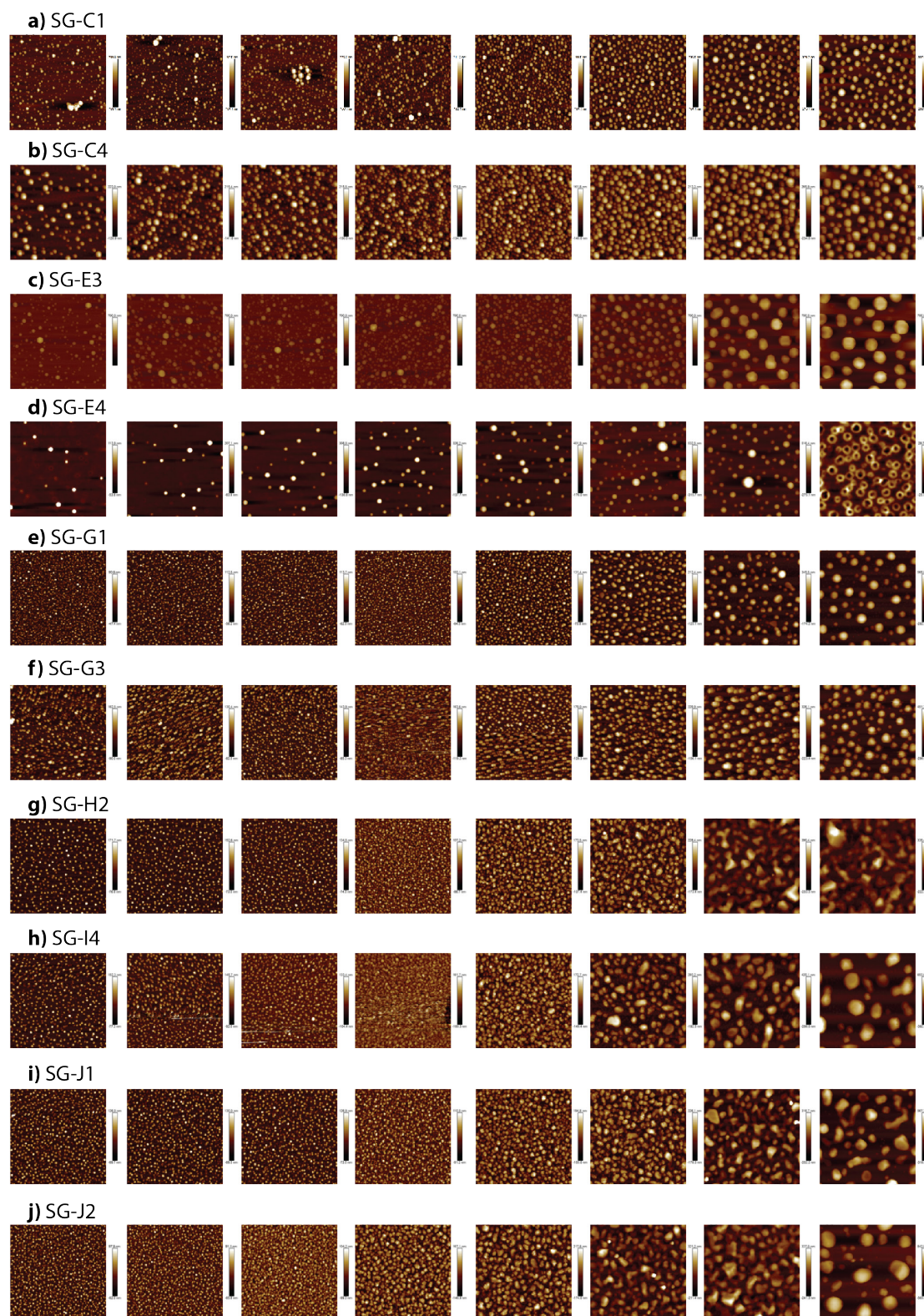Figure 8.25: AFM images taken every 10 mm along silver gradients with increasing silver thickness from left to right. a) SG-C1, b) SG-C4, c) SG-E3, d) SG-E4, e) SG-G1, f) SG-G3, g) SG-H2, h) SG-I4, i) SG-J1 and j) SG-J2. Image size is 10 m.

8.3.1 Protein experiment

To mimic the real physiological situation, protein-adsorption experiments were carried out in competition with fetal bovine serum (FBS) by spiking pure FBS with 5 g/ml fluorescently labeled albumin and 5 g/ml fluorescently labeled fibrinogen.

Line plots of gray values measured with the microarray scanner and normalized to the real surface area showed an increase in fluorescence intensity of fibrinogen adsorption at the thick end of the SG-A gradients, while the fluorescence intensity for albumin adsorption stayed nearly constant with slightly higher signal in the middle part of the gradient (Figure 8.26). The SG-I gradients showed a maximum in intensity in the middle of the sample for both albumin and fibrinogen adsorption (Figure 8.27). Microarray-scanner images of the SG-I2 gradient before protein adsorption indicated that the silver particle-size gradient itself showed some fluorescence signal (Figure 8.28). An increase in intensity measured during excitation with the 635 nm laser was observed on the gradient without adsorbed proteins, indicating that the formed silver particles on the gradient that are coated with 6 nm or TiO_2 exhibit self-fluorescence.

SEM investigation of the TiO_2-coated silver gradients used for protein experiments showed that the coating led to the creation of a nano-roughness on top of the silver particles (Figure 8.29). This phenomenon did not occur on TiO_2 coated gold gradients, fabricated with the same dewetting protocol, as the silver gradients (Data not shown), indicating that there was a reaction between the silver and titanium oxide during the sputtering process. Oxygen plasma is present during the sputter coating process and it is known that silver reacts readily with atomic oxygen. Silver films can be significantly altered or damaged by oxygen plasma [22, 23]. This additional roughness was not considered for the protein-experiments and the further AFM analysis would be needed to analyze the increase in surface area after TiO_2 coating.

a) SG-A1 Albumin

b) SG-A1 Fibrinogen

SG-A2 Albumin

SG-A2 Fibrinogen
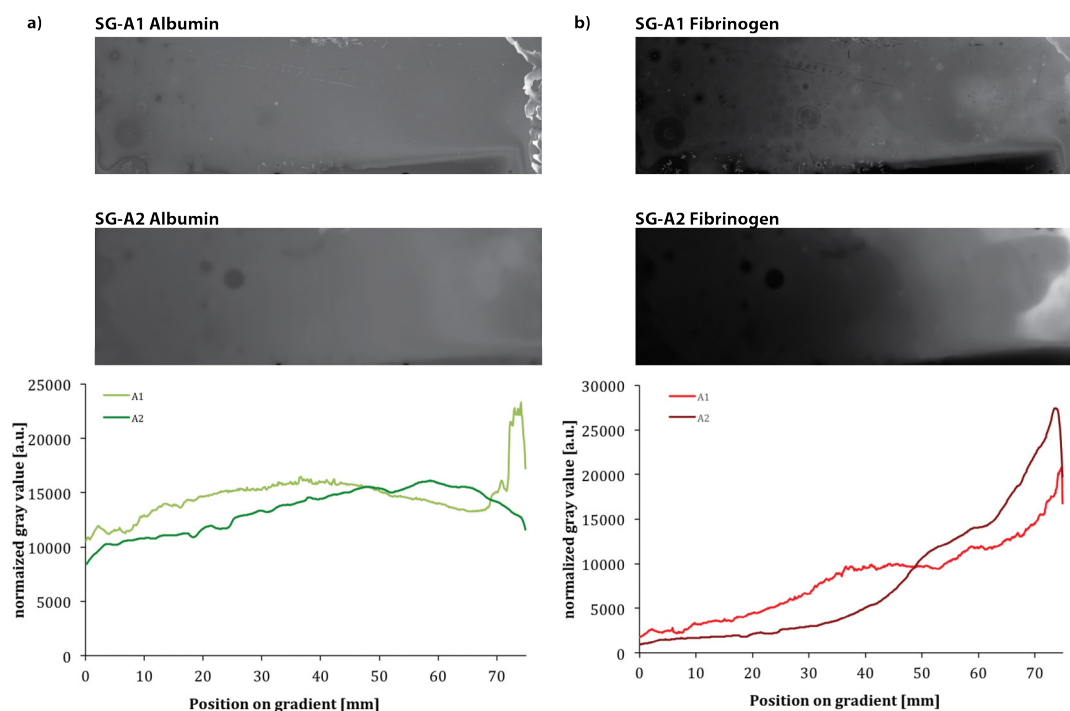
Figure 8.26: Results from competitive protein adsorption in fetal bovine serum (BSA + HPF in FBS) for SG-A1 and SG-A2. On top microarray scanner images and below line plots of intensity along the particle-size gradient created by averaging the gray values of all pixels along the lines perpendicular to the gradient and normalized to the real surface area are presented. Normalized gray values of a) albumin (green) and b) fibrinogen (red) adsorption along silver particle gradients with increasing silver thickness from left (0 mm) to right (75 mm).

a) SG-I3 Albumin

b) SG-I3 Fibrinogen

SG-I4 Albumin

SG-I4 Fibrinogen
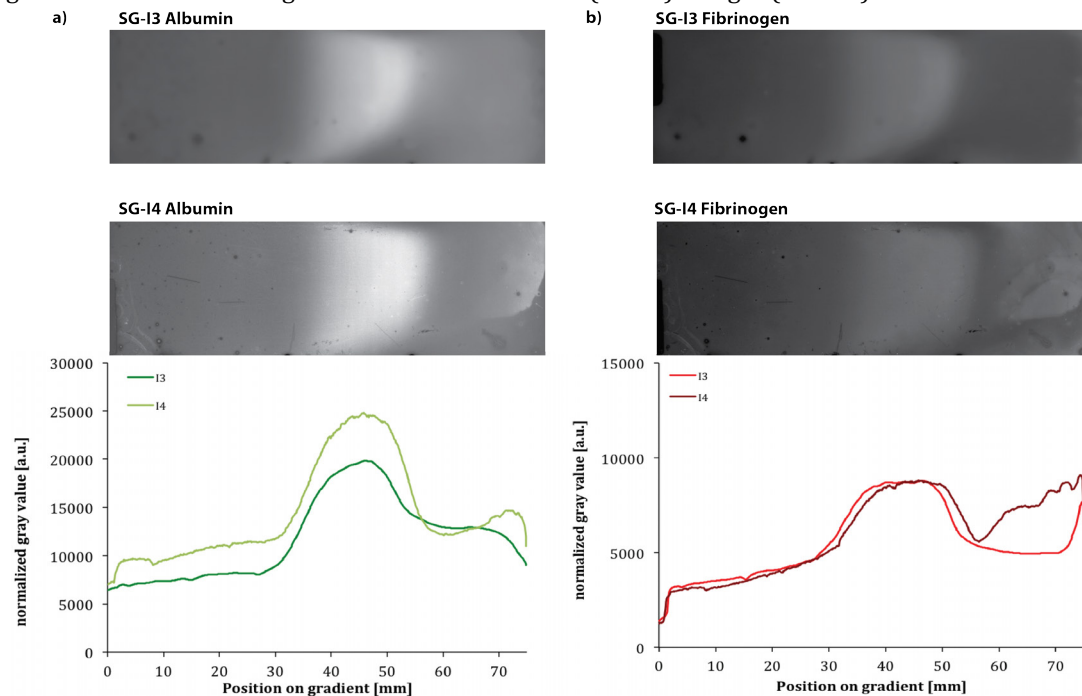
Figure 8.27: Results from competitive protein adsorption in fetal bovine serum (BSA + HPF in FBS) for SG-I3 and SG-I4. On top microarray scanner images and below line plots of intensity along the particle-size gradient created by averaging the gray values of all pixels along the lines perpendicular to the gradient and normalized to the real surface area are presented. Normalized gray values of a) albumin (green) and b) fibrinogen (red) adsorption along silver particle gradients with increasing silver thickness from left (0 mm) to right (75 mm).

a)   SG-I3 measured with 635 nm laser (albumin)   **b)**   SG-I3 measured with 532 nm laser (fibrinogen)
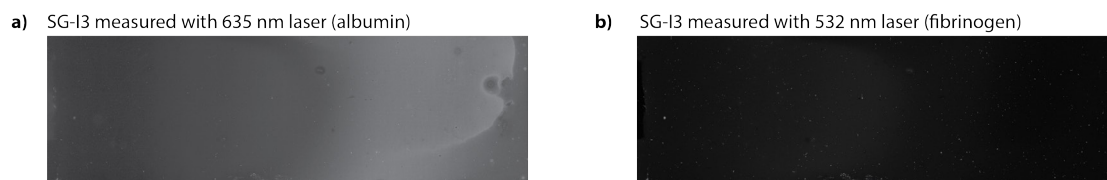
Figure 8.28: Microarray scanner images form SG-I3 without previous protein adsorption. a) Gray value image measured with 635 nm and b) 532 nm laser.

It was decided not to further investigate the protein adsorption on the silver particle-size gradients due to the self-fluorescence of the gradients, the reaction of the silver with oxygen during TiO_2 sputter coating and the rather complex change of the three particle parameters, height, diameter and density, which all might influence the protein-adsorption behavior.
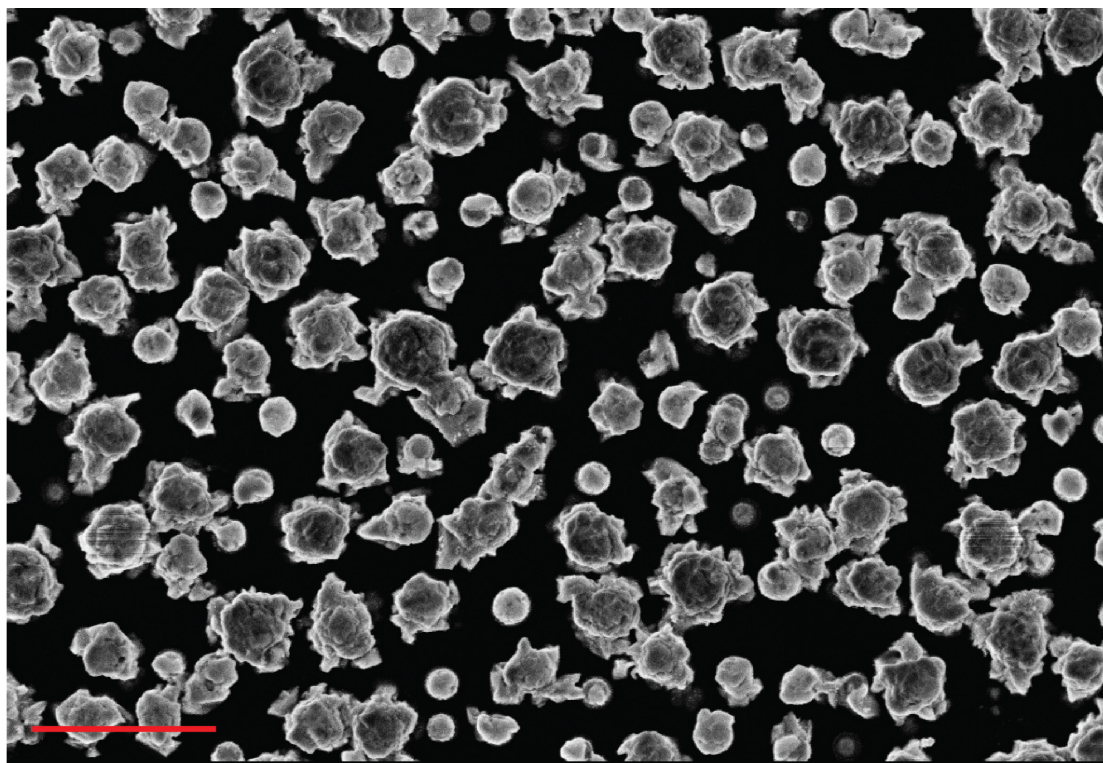
Figure 8.29: SEM image of SG-C1 coated with 6 nm titanium oxide. 50 kX magnification, scale bar 1 μm.

8.3.2 Fabrication of epoxy replicas

The change in particle size, height and density of the formed silver particles during the dewetting process was different for every sample, even for samples from the same batch. Therefore extensive analysis of every fabricated silver-particle gradient was needed. In order to perform meaningful biological experiments, many identical samples would be needed. Replicating one master gradient offers the advantage that large number of samples can be prepared that display the same surface topography [24, 25]. Additionally, replication in epoxy and a subsequent coating with TiO_2 eliminates the self-fluorescence issue observed with the master silver gradients and avoids the reaction of silver with oxygen during the sputter-coating process.

AFM images along SG-C1 master (Figure 8.30 a) and epoxy replica (Figure 8.30 b), as well as SEM images along SG-AB3 master (Figure 8.31 a) and epoxy replica (Figure 8.31 b) showed qualitatively that the shape and density of the silver particles along the gradients were preserved during replication.
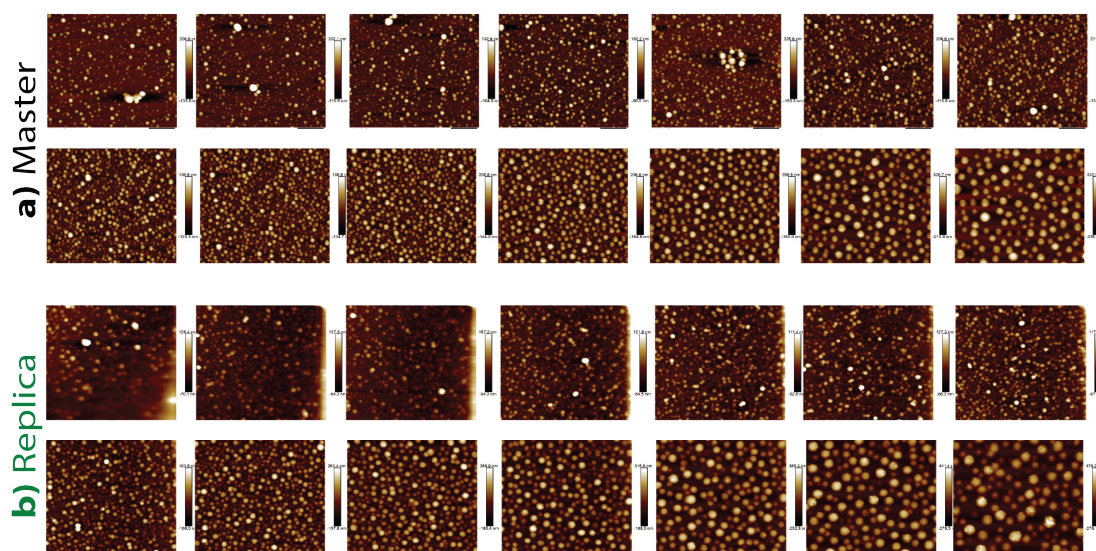
Figure 8.30: AFM images of a) master SG-C1 and b) epoxy replica of SG-C1, taken every 5 mm along the gradient with increasing silver thickness from left to right, and top to bottom. Image size is 10 m.
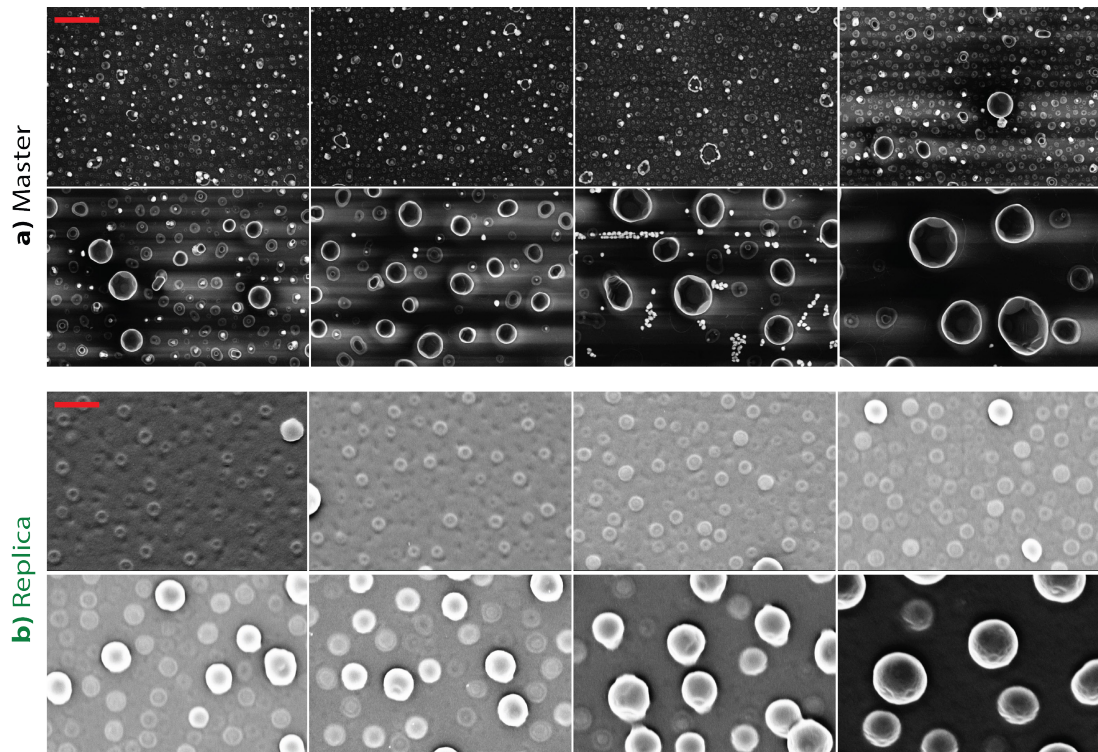
Figure 8.31: SEM images of a) master SG-AB3 and b) epoxy replica of SG-AB3, taken every 10 mm along the gradient with increasing silver thickness from left to right, and top to bottom. 50 kX magnification, scale bar 1 m.

In Figure 8.32 it can be seen that particle height was well replicated along the gradient for SG-AB3. Replication of the silver-particle gradients in epoxy was successful, but more experiments and quantitative analysis of particle height, diameter and density are needed to confirm these first experiments.
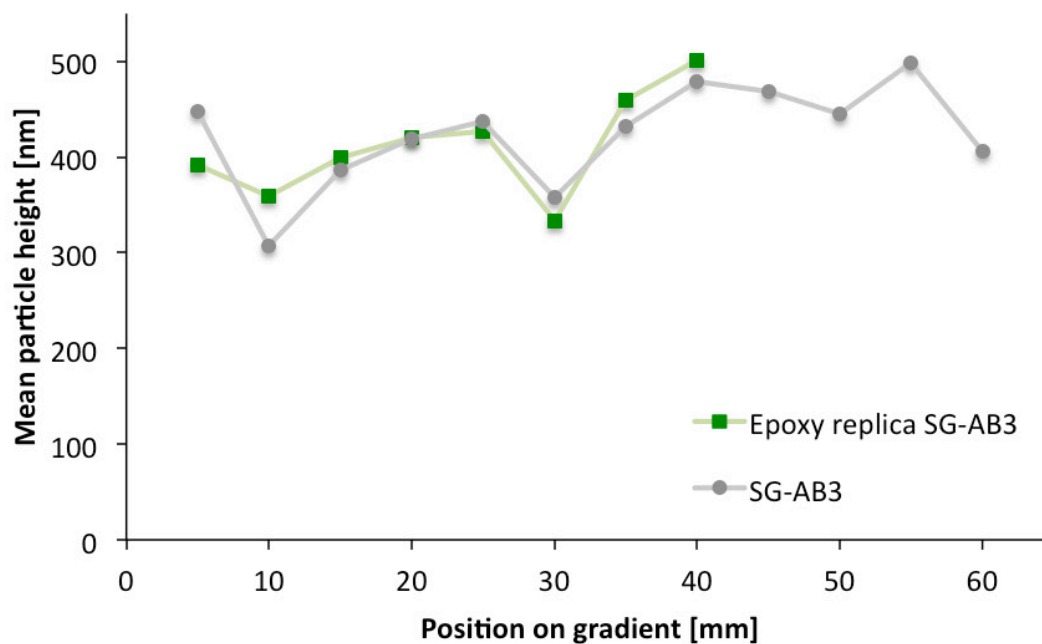
Figure 8.32: Mean particle height of a) SG-AB3 (gray circles) compared with b) epoxy replica of SG-AB3 (green squares). Measured from AFM images.

8.4 Conclusion

Silver dewetting allows for an easy fabrication of silver-particle gradients with changing particle size, height and density along the gradient, but exact reproducibility was not possible. It was observed that the positioning of the samples in the evaporator influences the silver layer thickness and its distribution over the gradient. Additionally, depending on the position in the oven the temperature that the gradient experiences during dewetting varied, resulting in different dewetting behavior. To achieve a better reproducibility of the production process, one would need to assure the exact same position of the silver gradient in the evaporator as well as the oven for every dewetting process.

Protein experiments showed a different protein attachment along the gradients, but these results were biased by the fact that the TiO_2-coated silver gradients exhibit self-fluorescence. Additionally, the creation of a nano-roughness on top of the silver particles was observed after the sputter coating

with TiO_2, which induced a change in real surface area. Therefore, no clear conclusion of the protein adsorption behavior was possible.

First replication experiments in PDMS and epoxy showed that the replication of the silver particle-size gradients is possible. Replication is a possible solution for the observed problems with the silver particle-size gradients. TiO_2 coated epoxy replicas do not show self-fluorescence and the unwanted reaction of silver and oxygen during the sputtering process can be avoided. Master gradients were not exactly reproducible even when no changes in the fabrication protocol were made.

References:

[1] C.V.M. Cremmel, Roughness-size gradients for biomedical applications, ETH-Zürich, 2015.

[2] V. Voney, Particle-size Gradients by Dewetting of Silver, ETH Zürich, 2016.

[3] Y. Boussès, Production of particle-size gradients by silver dewetting for biomedical applications and tribological studies, ETH Zürich, 2016.

[4] R. Brandon, F.J. Bradshaw, R.A.E. FARNBOROUGH, The Mobility of the Surface Atoms of Copper and Silver Evaporated Deposits, Defense Technical Information Center1966.

[5] C.V. Thompson, Solid-State Dewetting of Thin Films, Annual Review of Materials Research 42(1) (2012) 399-434.

[6] R.V. Zucker, G.H. Kim, W. Craig Carter, C.V. Thompson, A model for solid-state dewetting of a fully-faceted thin film, Comptes Rendus Physique 14(7) (2013) 564-577.

[7] J. Mizsei, V. Lantto, In situ AFM, XRD and Resistivity Studies of the Agglomeration of Sputtered Silver Nanolayers, Journal of Nanoparticle Research 3(4) (2001) 271-278.

[8] P.R. Gadkari, A.P. Warren, R.M. Todi, R.V. Petrova, K.R. Coffey, Comparison of the agglomeration behavior of thin metallic films on SiO_2, Journal of Vacuum Science & Technology A: Vacuum, Surfaces, and Films 23(4) (2005) 1152-1161.

[9] Y. Kojima, T. Kato, Nanoparticle formation in Au thin films by electron-beam-induced dewetting, Nanotechnology 19(25) (2008) 255605.

[10] W.L. Winterbottom, Equilibrium shape of a small particle in contact with a foreign substrate, Acta Metallurgica 15(2) (1967) 303-310.

[11] S.-L. Zhang, M. Östling, Metal Silicides in CMOS Technology: Past, Present, and Future Trends, Critical Reviews in Solid State and Materials Sciences 28(1) (2003) 1-129.

[12] D. Deduytsche, C. Detavernier, R.L.V. Meirhaeghe, C. Lavoie, High-temperature degradation of NiSi films: Agglomeration versus NiSi2 nucleation, Journal of Applied Physics 98(3) (2005) 033526.

[13] C. Jahan, O. Faynot, L. Tosti, J.M. Hartmann, Agglomeration control during the selective epitaxial growth of Si raised sources and drains on ultra-thin silicon-on-insulator substrates, Journal of Crystal Growth 280(3) (2005) 530-538.

[14] B. Legrand, V. Agache, J.P. Nys, V. Senez, D. Stievenard, Formation of silicon islands on a silicon on insulator substrate upon thermal annealing, Applied Physics Letters 76(22) (2000) 3271-3273.

[15] U. Schmid, The impact of thermal annealing and adhesion film thickness on the resistivity and the agglomeration behavior of titanium/platinum thin films, Journal of Applied Physics 103(5) (2008) 054902.

[16] R.M. Tiggelaar, R.G.P. Sanders, A.W. Groenland, J.G.E. Gardeniers, Stability of thin platinum films implemented in high-temperature microdevices, Sensors and Actuators A: Physical 152(1) (2009) 39-47.

[17] J. Mizsei, Activating technology of SnO_2 layers by metal particles from ultrathin metal films, Sensors and Actuators B: Chemical 16(1) (1993) 328-333.

[18] J.-H. Chen, T.-F. Lei, D. Landheer, X. Wu, J. Liu, T.-S. Chao, Si Nanocrystal Memory Devices Self-Assembled by In Situ Rapid Thermal Annealing of Ultrathin a -Si on SiO_2, Electrochemical and Solid-State Letters 10(10) (2007) H302-H304.

[19] S. Rath, M. Heilig, H. Port, J. Wrachtrup, Periodic Organic Nanodot Patterns for Optical Memory, Nano Letters 7(12) (2007) 3845-3848.

[20] M. Chhowalla, K.B.K. Teo, C. Ducati, N.L. Rupesinghe, G.A.J. Amaratunga, A.C. Ferrari, D. Roy, J. Robertson, W.I. Milne, Growth process conditions of vertically aligned carbon nanotubes using plasma enhanced chemical vapor deposition, Journal of Applied Physics 90(10) (2001) 5308-5317.

[21] G.D. Nessim, A.J. Hart, J.S. Kim, D. Acquaviva, J. Oh, C.D. Morgan, M. Seita, J.S. Leib, C.V. Thompson, Tuning of Vertically-Aligned Carbon Nanotube Diameter and Areal Density through Catalyst Pre-Treatment, Nano Letters 8(11) (2008) 3587-3593.

[22] C. Ma, M.J. Trujillo, J.P. Camden, Nanoporous Silver Film Fabricated by Oxygen Plasma: A Facile Approach for SERS Substrates, ACS Applied Materials & Interfaces 8(36) (2016) 23978-23984.

[23] L.A.A. Pettersson, P.G. Snyder, Preparation and characterization of oxidized silver thin films, Thin Solid Films 270(1) (1995) 69-72.

[24] M. Schuler, T.P. Kunzler, M. De Wild, C.M. Sprecher, D. Trentin, D.M. Brunette, M. Textor, S.G.P. Tosatti, Fabrication of TiO_2-coated epoxy replicas with identical dual-type surface topographies used in cell culture assays, Journal of Biomedical Materials Research - Part A 88(1) (2009) 12-22.

[25] M. Wieland, B. Chehroudi, M. Textor, D.M. Brunette, Use of Ti-coated replicas to investigate the effects on fibroblast shape of surfaces with varying roughness and constant chemical composition, Journal of Biomedical Materials Research 60(3) (2002) 434-444.

Chapter 9

Conclusions and Outlook

9.1 Conclusions

The aim of this thesis was to understand the early interaction between blood and the implant and how this further steers osseointegration, by following the natural processes that occur after implantation of an osseous implant.

Nanoparticle-density gradients were produced by a simple dip-coating process. A silicon wafer was rendered positively charged by poly(ethylene imine) adsorption and then slowly immersed into a diluted silica-particle suspension with particle diameter of 12, 39 or 72 nm. The gradients were heat-treated at 1050 °C to sinter the particles on to the surface and adjust their shape. TiO_2-coated gradients were employed for biological applications.

An easy and fast method was implemented to study protein adsorption on surfaces of varying nano-roughness by using nanoparticle-density gradients and a fluorescence micro-array scanner for analysis. Protein-adsorption studies from single and mixed protein solutions on nanoparticle-density gradients showed no influence of nano-features on the amount of protein adsorption for gradients with 39 and 72 nm nanoparticles. In contrast, for 12 nm gradients, fibrinogen in competition with albumin and fibronectin or serum, showed a higher adsorption in the high-particle-density region of the gradient. It is suggested that the increase in fibrinogen adsorption is a consequence of the *Vroman effect* and the particle surface curvature induced "side on" adsorption of the fibrinogen in a denatured state. The denatured fibrinogen displays a very high surface affinity

and is thus less likely to be displaced by other proteins that follow the *Vroman sequence*.

Blood-coagulation studies in Chapter 4 revealed that nanostructures with a size of 39 nm seem to enhance blood coagulation. With an increase in 39 nm particle-density a faster fibrin network formation was observed, while smaller (12 nm) and larger (72 nm) nanoparticles did not influence the activation of platelets and the fibrin network formation.

In order to find the correlation between the protein and blood experiments, fibrinogen-antibody experiments were carried out. Preliminary results in Chapter 5 showed a decrease in the ratio of amount of antibody binding to the amount of surface-bound fibrinogen with increasing density of particles with a diameter of 39 nm. The decrease in ratio of antibody binding and adsorbed fibrinogen is an indicator for conformational changes in adsorbed fibrinogen and might explain the different blood-clotting behavior found on 39 nm particle-density gradients.

In Chapter 6, human bone cell (HBC) experiments performed on nano-roughness gradients exhibited a gradual change in the cell behavior along the gradient. On 39 nm particle-density gradients, the number of HBCs was seen to decrease with decreasing inter-particle distance. The observation of a decreased cell number on areas with high particle coverage could be of interest in regard to potential applications in cell engineering and could be used as a simple approach to reduce cell adhesion on a surface in a permanent way.

Unfortunately it was not possible to study the role of pre-adsorbed blood components on human bone cell behavior by means of particle-density gradients due to an observed loss of blood clot prior to cell seeding. Therefore no conclusion about the influence of the pre-formed blood clot on the HBC behavior on nanostructured surfaces could be drawn.

In Chapter 7 different replication techniques have been shown to successfully replicate micro- or nanoscale features. Injection molding from PPSU inserts proved to be a successful replication technique for the mass production of samples with nanostructures with a size of 72 nm. For smaller nanoparticles a novel replication method called substrate conformal imprint lithography (SCIL) demonstrated the replication of nanofeatures down to a size of 12 nm and was proven to be able to replicate combined nano- and micro-featured structures. This new replication technique works equally well for 12, 39 and 72 nm particles and has tremendous potential to be used for biological experiments such as protein-adsorption, blood-interaction and cell studies.

Silver dewetting was demonstrated to provide an easy fabrication approach for silver-particle gradients with changing particle size, height and density along the gradient, but exact reproducibility was very challenging. Replication of the silver-particle gradients in PDMS and epoxy was shown to be a possible way to produce identical particle-size gradients and TiO_2 coated epoxy replicas could be used for biological applications.

9.2 Outlook

In this PhD thesis, a new replication technique, SCIL, was shown to be able to replicate nano-features down to 12 nm. Additionally, replicas are made in the same material as the master (silica). SCIL replicas should be used instead of master gradients for further protein-adsorption, blood-interaction and cell studies. With the use of replicas instead of master gradients, differences in the outcome of biological experiments due to slight variations of the gradient samples could be excluded and the reproducibility would be increased.

In order to find the correlation between protein adsorption and blood coagulation experiments on nanoparticle gradients, antibody-binding experiments on nanoparticle-density gradients pre-adsorbed with full serum spiked with fluorescently labeled fibrinogen should be measured, followed by platelet-interaction studies on the very same substrates. Additionally antibodies for the other potential platelet-binding peptide sequences, the two RGD sequences in each of the Aα chains, should be employed.

Gaebel and Feuerstein [1] showed that adherent platelets cause redistribution of adsorbed fibrinogen, indicating that the tightness with which the fibrinogen is held could also influence platelet behavior. To find direct evidence for the relationship between changes in the tightness of fibrinogen binding and platelet adhesion, AFM studies could be carried out to test the binding strength of adsorbed fibrinogen on the nano-roughness gradients [2, 3].

In order to examine the influence of the pre-formed blood clot on human bone-cell behavior, experiments with smaller samples and shorter blood-incubation times should be carried out to avoid blood clot delamination. To understand osseointegration and mineralization depending on the surface roughness, more studies that look at different factors for osseointegration, such as a time-dependent study of bone-marker molecules that could reveal the onset and speed of mineralization, should be carried out.

An aspect of surface topography that was not covered in this thesis is pore size and pore density. The influence of nanopores on protein-adsorption, blood-coagulation and HBC behavior could give more insight into processes involved in successful osseointegration. A nanopore-density gradient could be fabricated from a nanoparticle-density gradient by template-stripping [4, 5].

By combining the nanoparticle-density gradient with a gradient in hydrophobicity [6] or a gradient in surface functionalization [7], possible synergetic effects of combined chemical modification of a surface with nano-roughness on protein adsorption, blood coagulation and osseointegration could be examined.

Recently it was demonstrated that artificial Au nanostructures mimicking native nanopatterns of Cacada's wings exhibit excellent biocidal property against methicillin-resistant *Staphylococcus aureus* (MRSA) [8]. It would be interesting to use nanoparticle-density gradients to investigate how the spatial characteristics of the nanostructures such as density and height influence the antimicrobial activity. In collaboration with Qun Ren from Empa, St.Gallen, the influence of 72 nm particle samples on *Pseudomonas aeruginosa* was investigated. A preliminary test on a 72 nm particle-density gradient showed that fewer bacterial cells adhere on the high-particle-density end of the gradient compared to the smooth end.

In non-biological systems, the silver particle-density gradients could be further used for tribology experiments. Experiments on nanoparticle-density gradients showed already an influence of the nano-roughness on adhesion and friction properties [9, 10].

References:

[1] K. Gaebel, I.A. Feuerstein, Platelets process adsorbed protein: a morphological study, Biomaterials 12(6) (1991) 597-602.

[2] L.-C. Xu, C.A. Siedlecki, A.C.f.t.H.a.B.I.R. Group, Atomic Force Microscopy Studies of the Initial Interactions Between Fibrinogen and Surfaces, Langmuir : the ACS journal of surfaces and colloids 25(6) (2009) 3675-3681.

[3] A. Sethuraman, M. Han, R.S. Kane, G. Belfort, Effect of Surface Wettability on the Adhesion of Proteins, Langmuir 20(18) (2004) 7779-7788.

[4] M. Hegner, P. Wagner, G. Semenza, Ultralarge atomically flat template-stripped Au surfaces for scanning probe microscopy, Surface Science 291(1) (1993) 39-46.

[5] S.N. Ramakrishna, Adhesion and tribology on well-defined, nano-scale rough surfaces. A gradient approach, ETH, 2013.

[6] S. Morgenthaler, S. Lee, S. Zürcher, N.D. Spencer, A Simple, Reproducible Approach to the Preparation of Surface-Chemical Gradients, Langmuir 19(25) (2003) 10459-10462.

[7] S. Morgenthaler, C. Zink, B. Städler, J. Vörös, S. Lee, N.D. Spencer, S.G.P. Tosatti, Poly(l-lysine)-grafted-poly(ethylene glycol)-based surface-chemical gradients. Preparation, characterization, and first applications, Biointerphases 1(4) (2006) 156-165.

[8] S. Wu, F. Zuber, J. Brugger, K. Maniura-Weber, Q. Ren, Antibacterial Au nanostructured surfaces, Nanoscale 8(5) (2016) 2620-2625.

[9] S.N. Ramakrishna, P.C. Nalam, L.Y. Clasohm, N.D. Spencer, Study of Adhesion and Friction Properties on a Nanoparticle Gradient Surface: Transition from JKR to DMT Contact Mechanics, Langmuir 29(1) (2013) 175-182.

[10] S.N. Ramakrishna, L.Y. Clasohm, A. Rao, N.D. Spencer, Controlling Adhesion Force by Means of Nanoscale Surface Roughness, Langmuir 27(16) (2011) 9972-9978.

Appendix A

Proliferation, behavior, and differentiation of osteoblast on surfaces of different microroughness

Oleh Andrukhov, Rebecca Huber, Bin Shi, Simon Berner, Xiaohui Rausch-Fan, Andreas Moritz, Nicholas D. Spencer, Andreas Schedle

Rebecca Huber prepared the micro-roughness samples and performed the analysis of the samples with optical profilometry and SEM. The cell studies were conducted by Oleh Andrukhov, Bin Shi, Xiaohui Rausch-Fan and Andreas Moritz. Simon Berner, Nicholas D. Spencer and Andreas Schedle supervised the work. Rebecca Huber, Oleh Andrukhov, Nicolas D. Spencer and Andreas Schedle wrote the manuscript, which was approved by all authors.

10.1 Introduction

Dental implantation is a safe and long-term approach for restoring edentulous patients [1-3]. The formation of a bone-implant interface — a process known as osseointegration — is a key requirement for stable implant anchoring and clinical success. Titanium is largely used as a material for dental implants, because it causes no tissue reaction and exhibits the ability to fuse with bone [4]. Promoting the rate and extent of osseointegration immediately after dental implantation is crucial for the success of implant therapies. The modification of titanium surfaces is a key instrument to enhance osseointegration and improve the clinical outcome of implant therapy. Titanium (Ti) implant surface characteristics, such as chemical composition, surface topography, roughness,

surface energy, nanostructures as well as coating of Ti implants with different bioactive materials are considered to have a substantial impact on the osseointegration process during initial wound healing after implantation [5-8].

The micrometer-scale roughness of Ti surfaces is one of the key parameters influencing osseointegration [9]. The roughness of Ti surfaces can be increased by several methods, such as sand blasting, acid etching, laser etching, and anodic oxidation [9]. Most studies describe surface micrometer-scale roughness in terms of either R_a or S_a parameters, which represent mean arithmetic profile roughness and mean arithmetic 2D roughness, respectively. Nowadays, surfaces with moderate roughness with S_a parameters of about 1–2 μm are widely used in implant dentistry and exhibit improved osseointegration and clinical outcome [6]. Arithmetic roughness, however, does not provide information about spatial characteristics of surface and roughness profiles. These topographical surface features are characterized by parameters such as average width of profile elements (R_{Sm}), profile asymmetry parameter surface skewness (R_{Sk}), and surface kurtosis describing peaks' sharpness. These parameters are differently affected by different roughening procedures [10] but their influence on osseointegration is not known. Furthermore, different roughening protocols might influence surface structures not only at the micrometer scale, but also at the nanometer scale. Therefore, further studies that can discriminate the effect of different surface characteristics on osseointegration and specify the relationship between mean arithmetic roughness and osseointegration are required.

Improved osseointegration of Ti surfaces with micro-scale roughness could be related to its positive effect on osteoblasts, which are directly involved in the process of bone formation. Previous in vitro studies show that Ti surfaces with moderate microroughness inhibit proliferation and promote differentiation of osteoblasts [11, 12]. This effect of surface microroughness on osteoblasts seems to be associated with activation of $\alpha_2\beta_1$ integrin signaling in osteoblasts [13, 14]. Nevertheless, the effect of a large range of micro-scale roughness values on osteoblast behavior still remains to be investigated. Most previous studies

have compared two Ti surfaces with defined microscale roughness values, whereas studies with controlled micrometer-scale roughness are rather rare. Notably, Kunzler *et al.* showed, in a study with titanium-coated microroughness gradient replicas with R_a values in the range 0–4 μm, that the proliferation of rat calvarial osteoblasts increases with increasing surface roughness [15]. Another study with controlled microroughness shows that osteogenic differentiation of bone marrow mesenchymal stem cells is promoted by surfaces with R_a values of about 2–3 μm [16]. A relationship between surface micrometer-scale roughness and osteoblast differentiation is investigated in two studies with controversial results: one study suggests an improved osteoblast differentiation with an increased surface roughness [17]; the other study suggests a biphasic relationship, where surfaces with moderate roughness better support osteoblast differentiation compared to very smooth or very rough surfaces [18]. Therefore, additional studies on the relationship between the controlled micrometer-scale roughness and osteoblast response would be highly desirable. Therefore, in the present study, we have investigated the behavior, proliferation, and differentiation of osteoblast-like MG-63 cells grown on Ti-coated replicas with R_a parameters of about 0, 1, 2, and 4 μm. The workflow of the present study is shown in Figure 10.1.
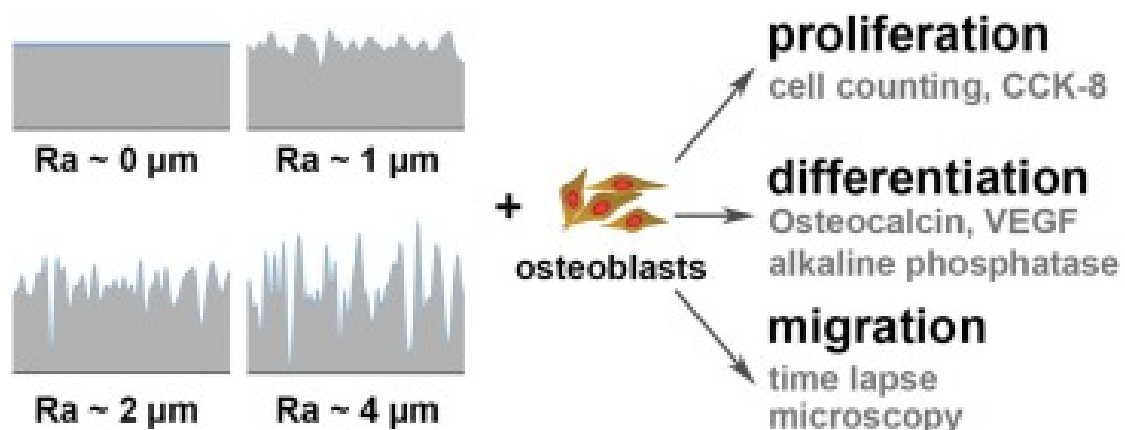

Figure 10.1: Workflow of the study.

10.2 Materials and methods

10.2.1   Production of Ti surfaces with different micrometer-scale roughness values

10.2.1.1   Micrometer-featured roughness masters

Micrometer-featured masters with different roughness values were prepared in a similar way as described previously [19]. A two-step process was used to create micrometer-scale-featured roughness masters. Rolled aluminum sheets (purity 99.5%, dimensions: 20 mm × 40 mm × 2 mm (Metall Service Menzikon AG, Switzerland)) were sand-blasted with corundum particles (81500-826-074, Sablux, Switzerland) to achieve a uniformly rough surface morphology. In a second step, the roughened substrate was fully immersed into a chemical polishing solution (77.5% (v/v) phosphoric acid, 16.5% (v/v) sulfuric acid and 6% (v/v) nitric acid), which preferentially removes small and sharp features as a function of time. The substrates were exposed to the chemical polishing solution for 33, 12 or 2 min. The different polishing times result in homogenous roughness masters with a R_a value of approximately 1, 2 or 4 μm, respectively (referred as surfaces **1**, **2** and **4**). A flat silicon wafer ($\langle 1\,0\,0 \rangle$ orientation, Si-mat, Germany) was also used as a master with a R_a value of approximately 0 μm (referred as surface **0**).

10.2.1.2   Replication

In order to produce multiple identical samples for reproducibility reasons, the masters were replicated, as described by Wieland et al. [20] and Schuler *et al.* [21]. Impressions of the different roughness masters were prepared in polyvinylsiloxane (PROVIL novo light, Heraeus-Kulzer, Switzerland). A 24-well plate (TPP, Switzerland) was used as a mold to achieve cylindrical negatives with a diameter of 16.2 mm. Negative replicas were inserted into a

polytetrafluoroethylene (PTFE) template with holes of a diameter of 15 mm, leaving a rim of 1 mm height. Epoxy resin (EPO-TEK 302-3M, Polyscience AG, Switzerland) was cast onto the polyvinylsiloxane negatives and cured at 65 °C for at least 24 h. The epoxy samples were cleaned for 10 min in an ultrasonic bath containing a 2 vol% Hellmanex solution (HELLMA GmbH & Co, Müllheim, Germany) and extensively rinsed in ultra-pure water 10 times. Samples were pre-dried with a jet of nitrogen and air dried overnight. Clean epoxy replicas were sputter-coated with 40 nm of metallic titanium (Reactive magnetron sputtering, Paul Scherrer Institute, Villigen, Switzerland). SEM investigation of freeze-fractured cross-sections of epoxy samples with highest roughness ($R_a \sim 4\,\mu m$) showed that the epoxy surface is entirely covered with a 30–50 nm thick layer of TiO_2. No tendency of a thinner coating on peaks and thicker coating in valleys could be observed (see also exemplary images in Supplementary material). The replicas were cleaned in a plasma cleaner (Harrick, PDC-32G, USA) for 2 min in an oxygen atmosphere of roughly 2×10^{-3} mbar at high RF level. The replicas were sterile packed under laminar flow in containers containing ultra-pure water and stored at room temperature until further use.

10.2.1.3   Characterization

The micrometer-scale roughness of the titanium-coated epoxy replicas was analyzed by an optical profilometer (Sensofar Plu Neox, Sensofar, Spain) in confocal mode. 2.75 mm long strips were stitched together by using the 20× objective. The evaluation was carried out with the SensoMap software (v.6.0, Sensofar, Spain) according to the DIN EN ISO 4287 standard.

The contribution of different wavelength windows to the overall surface roughness was determined using a fast-Fourier-transformation (FFT)-based analysis method [22]. With this method, contributions in different wavelength windows can be individually evaluated. Three different windows with wavelengths between 3–10 μm, 10–50 μm and 50–250 μm were used to calculate the arithmetic roughness value R_a.

10.2.2   Cell culture

Osteoblast-like MG-63 cells (American Type Culture Collection, Rockville, USA) were used in the present study. MG-63 is a cell line that exhibits osteoblastic features and has constant properties [11, 23-25], whereas characteristics of primary osteoblasts may differ depending on the source, donor, and isolation method [26-28]. The cells were cultured in modified Eagle's minimum essential medium (MEM, Gibco®, Carlsbad, USA) supplemented with 10% fetal bovine serum, penicillin (100 U/ml) and streptomycin (50 µg/ml) at 37 °C in a humidified atmosphere containing 5% CO_2. Cells were grown in culture up to passage four, in order to obtain sufficient cell numbers for experiments. Cells between the fourth and the seventh passage were used in the experiments.

10.2.3   Measurements of cell proliferation and viability

Cell proliferation was measured by two methods: manual cell counting and cell counting kit 8 (CCK-8, Dojindo Laboratories, Japan). In proliferation experiments, 2×10^4 cells were seeded on each Ti-coated (diameter 15 mm, cylinder height 1 mm) surface in 500 µl MEM. Cells seeded at similar density on tissue culture plastic (TCP) were used as control. Each group included three different wells. Cell proliferation was measured after 2, 5, and 9 days of culture. For manual cell counting, cells were collected by accutase and counted in blind fashion using a cell-counting chamber under a microscope. Cell viability/proliferation was determined using the cell counting kit-8 (CCK-8; Dojindo Laboratories, Japan) assay. After incubation, 50 µl of CCK-8 reagent were added into each well and culture plates were incubated in 5% CO_2 at 37 °C for 4 h. Thereafter 100 µl of each well were transferred to a separate 96-well plate and the optical density (OD) was measured at 450 nm using a microplate reader (Spectramax Plus 384; Molecular Devices, USA).

10.2.4 Time-labse microscopy

The behavior of MG-63 cells on different surfaces was observed using time-lapse microscopy, as described in our previous studies [29, 30]. Cells were stained with CellTracker™ Orange CMRA (Molecular Probes™, Invitrogen, UK) according to manufacturer's instructions and 1×10^5 stained cells, resuspended in 800 µl of MEM, were seeded on Ti discs with different surface treatments. Experiments for each surface were repeated at least three times. Cells were observed with an upright fluorescence microscope (Nikon Eclipse E 800 M microscope; Nikon Instruments Europe B.V, Badhoevedorp, Netherlands), and photographed with a digital imaging system (Photometrics1, Cascade 512F, Germany) every 30 min for over 120 h with the aid of NIS-elements software (Nikon Instruments). Cell motility was analyzed using the tracking module in manual tracking mode. For each experiment, 10 randomly selected cells per well/group were tracked in the time period from 6 h until 12 h after seeding. Cell motility was described by average migration speed.

10.2.5 Alkaline phosphatase activity

MG-63 cells were seeded at an initial density of 5×10^4 cells per well in 0.5 ml of MEM on Ti surfaces with different micrometer-scale roughness values, as well as on tissue-culture plastic. After 2, 5, or 9 days of culture, the activity of alkaline phosphatase was measured with a similar method to that described in our previous studies [30]. In brief, culture cells were collected by accutase and lysed in 200 µl phosphate-buffered saline (PBS) containing 0.2% Triton X-100, which facilitates the destruction of the plasma membranes, and then homogenized by sonication. The total protein content in cell homogenates was determined using a commercially available kit (Micro/Macro BCA; Pierce Chemical Co., Rockford, IL, USA). The ALP activity was assayed using the conversion of a colorless *p*-nitrophenyl phosphate to a colored *p*-nitrophenol according to the manufacturer's protocol (Sigma, St. Louis, MO, USA). The color changes were measured spectrophotometrically at 405 nm. The amounts of released

phosphate were quantified by comparison with a standard curve and normalized to the total protein content in cell homogenates. ALP activity experiments were repeated three times.

10.2.6   Real-time PCR

The expression levels of different osteogenesis-related proteins in MG-63 cells were quantified by means of real time PCR, applying a similar method to those described earlier [31]. MG-63 cells were seeded at a density of 5×10^4 cells per well in 0.5 ml MEM and cultured for 2, 5, or 9 days. Isolation of mRNA and transcription into cDNA was performed using the TaqMan® Gene Expression Cells-to-CT™ kit (Ambion/Applied Biosystems, Foster City, CA, USA) according to the manufacturer's instructions. This kit provides high accuracy and superior sensitivity in gene-expression analysis [32]. qPCR was performed on an ABI StepOnePlus device (Applied Biosystems) in paired reactions using TaqMan®gene expression assays with the following ID numbers (all from Applied Biosystems): alkaline phosphatase (ALP), Hs01029141_g1; osteocalcin (OC), Hs00609452_g1; VEGF, Hs00900055_m1; Hs; β-actin, Hs99999903_m1. β-actin was used as a house-keeping gene. The PCR reactions were performed in triplicate under the following thermocycling conditions: 95 °C for 10 min; 40 cycles, each for 15 s at 95 °C and at 60 °C for 1 min. The point at which the PCR product was first detected above a fixed threshold (cycle threshold, C_t), was determined for each sample. Changes in the expression of target genes were calculated using the $2^{-\Delta\Delta Ct}$ method, where $\Delta\Delta C_t = (C_t^{target} - C_t^{\beta-actin})_{sample} - (C_t^{target} - C_t^{\beta-actin})_{control}$, taking MG-63 cells grown on plastic as a control.

10.2.7   Measurement of osteocalcin and BEGF in conditioned medium

Commercially available ELISA kits were used for osteocalcin (Ebioscience, San Diego, USA) and VEGF (BosterBio, Pleasanton, USA) assays in the conditioned media after 5 days of culturing. Undiluted samples were used for measurements

10.2.8   Statistical analysis

The normal distribution of all data was tested with the Kolmogorov–Smirnov test. For normally distributed data, the statistical differences between different groups were analyzed by one-way analysis of variance (ANOVA) followed by a post-hoc LSD test. Data are expressed as mean ± S.E.M. Differences were considered to be statistically significant at $p < 0.05$.

10.3 Results

10.3.1   Ti surface with different micrometer-scale roughness

The topography of the titanium-coated replicas was characterized using optical profilometry. Table 10.1 shows an overview of different roughness values. The amplitude parameters R_a, R_q and R_z decrease with increasing polishing time. The spacing parameter R_{Sm} increases with decrease in roughness. The skewness value R_{Sk} oscillates around zero, indicating that the profile remains symmetrical.

Table 10.1: Polishing time and standard roughness values calculated from non-contact laser profilometer profiles (n = 9).

	Surface 0	Surface 1	Surface 2	Surface 4
Polishing time, min	–	33 min	12 min	2 min
R_a	0.05 ± 0.01	1.19 ± 0.24	2.30 ± 0.27	4.02 ± 0.27
R_q	0.06 ± 0.01	1.46 ± 0.31	3.42 ± 0.68	5.25 ± 0.57
R_z	0.39 ± 0.07	7.07 ± 3.53	36.2 ± 17.38	40.64 ± 19.07
R_{Sm}	19 ± 2	213 ± 36	131 ± 28	67 ± 15
R_{Sk}	0.16 ± 0.42	−0.09 ± 0.33	0.52 ± 2.49	0.05 ± 0.57
S_a	0.07 ± 0.01	−1.89 ± 0.44	2.96 ± 0.27	4.46 ± 0.35

R_a—average 2D roughness; R_q—root mean square roughness; R_z—mean roughness depth; R_{Sm}—mean width of profile elements; R_{Sk}—skewness of roughness profile; S_a—average 3D roughness. Data are presented as mean ± SD.

Fine-roughness features may be of particular importance for the performance of the surface in cell-surface interactions. Such fine features are often hidden by the coarser contribution to roughness. Using the FFT method to split the microroughness into windows of different wavelength reveals the contribution of different feature sizes to the overall morphology. The results of the arithmetic average R_a for different roughness windows are shown in Table 10.2. The wavelength-dependent evaluation reveals that small features (3–10 µm), such as peaks and sharp ridges, are initially attacked by the polishing solution and are only evident for surface **4**, while large features (10–50 µm) are removed only after longer polishing times and remain for surfaces **4** and **2**.

Table 10.2: Roughness values R_a calculated for different wavelength windows (n = 9).

Replica surface	Unfiltered	Wavelength (50–250 µm)	Wavelength (50–250 µm)	Wavelength (50–250 µm)
Surface 0	0.05 ± 0.01	0.02 ± 0.01	0.03 ± 0.01	0.02 ± 0.00
Surface 1	1.19 ± 0.24	0.77 ± 0.18	0.10 ± 0.03	0.03 ± 0.00
Surface 2	2.30 ± 0.27	1.66 ± 0.25	0.82 ± 0.24	0.24 ± 0.13
Surface 4	4.02 ± 0.27	2.96 ± 0.29	1.79 ± 0.16	0.64 ± 0.11

The results of the arithmetic average R_a for different roughness windows are presented as mean ± SD.

10.3.2 Cell counting

Cell numbers were significantly higher after culturing on tissue-culture plastic, compared to all Ti surfaces ($p < 0.05$, Figure 10.2). This was observed after 2, 5 and 9 days of culture. Amongst the Ti surfaces, cell numbers gradually decreased with increasing surface roughness. Cell numbers after culturing on surfaces **0, 1** and **2** were significantly higher compared to values on surface **4** ($p < 0.05$). In addition, cell numbers after culturing on the surface **0** were significantly higher compared to results on surface **2** ($p < 0.05$).
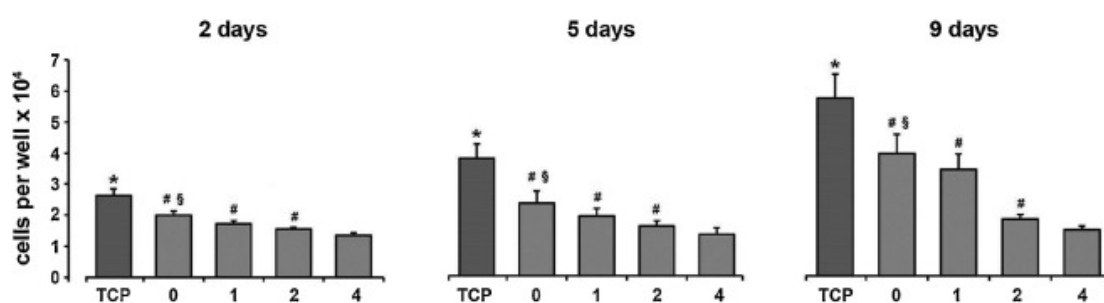

Figure 10.2: Number of MG-63 cells grown on Ti surfaces with different micrometer-scale roughness values. Total cell numbers were measured by manual cell counting. Data are presented as mean ± S.E.M. of five different experiments.
*Means significantly higher compared to all Ti surfaces, $p < 0.05$.
#Means significantly higher compared to surface with R_a 4 μm, $p < 0.05$.
§Means significantly higher compared to surface with R_a 2 μm, $p < 0.05$.

10.3.3 Proliferation/viability of MG-63 cells measured by CCK-8 kit

Cell proliferation/viability was significantly higher for cells grown on tissue-culture plastic compared to those grown on Ti surfaces ($p < 0.05$, Figure 10.3). Amongst the Ti surfaces, a gradual decrease in cell proliferation/viability with increasing R_a parameter was observed. Proliferation/viability of cells grown on surfaces **0** and **1** was significantly higher compared to results on surface **4** after all observation time points ($p < 0.05$). In addition, proliferation/viability for cells grown on surface **0** was significantly higher compared to results on surface **2** after 5 and 9 days of culture.
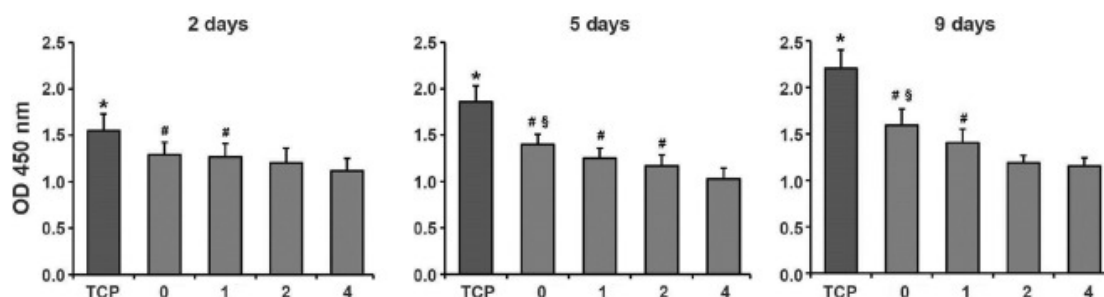
Figure 10.3: Proliferation/viability of MG-63 cells grown on Ti surfaces with different micrometer-scale roughness values. Proliferation/viability was measured by CCK-8 after 2, 5, or 9 days of the culture. Data are presented as mean ± S.E.M. of five independent experiments.
*Means significantly higher compared to all Ti surfaces, $p < 0.05$.
#Means significantly higher compared to surface **4**, $p < 0.05$.
§Means significantly higher compared to surface **2**, $p < 0.05$

10.3.4   Time-lapse microscopy

The migration speed of MG-63 cells on surface **4** was markedly lower than that on surfaces with lower roughness (Figure 10.4). Significant differences in migration speed were observed between surfaces **0** and **4** ($p < 0.05$). A similar tendency was observed between surfaces **1** vs. **4** ($p = 0.53$) and between surfaces **2** vs. **4** ($p = 0.56$).
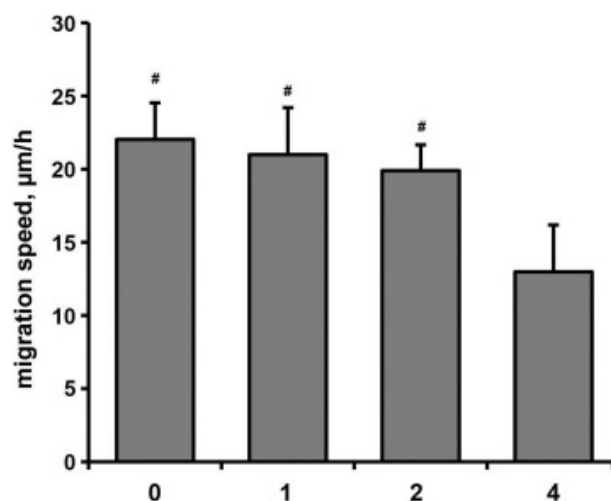

Figure 10.4: Migration of MG-63 cells on Ti surfaces with different micrometer-scale roughness values, measured in time-lapse microscopy experiments. The migration speed of HUVECs was determined in the time-lapse microscopy experiments within the time interval from 6 to 12 h after seeding. Data are presented as mean ± S.E.M. of six independent experiments.
*Means significantly lower compared to surface **4**, $p < 0.05$.

10.3.5 Expression of osteogenic markers

The effect of micrometer-scale roughness on the expression of the alkaline phosphatase and osteocalcin osteogenesis markers is shown in Figure 10.5. During the entire observation period, the highest mRNA expression of alkaline phosphatase and osteocalcin was observed on surfaces **1** and **2**, compared to surfaces **0** and **4** (Figure 10.5A). No significant difference was observed in the expression of any of the osteogenic markers between surfaces **1** and **2**. The data on gene-expression levels were generally supported by protein analysis (Figure 10.5B). The highest alkaline phosphatase activity was observed in cells grown on surface **2**, which was significantly higher compared to those observed for surfaces **0** and **4**. The alkaline phosphatase activity values for surface **1** were significantly higher than those for surface **4**. The production of osteocalcin by cells grown on surface **2** was significantly higher than that on surfaces **0** and **4** ($p < 0.05$).
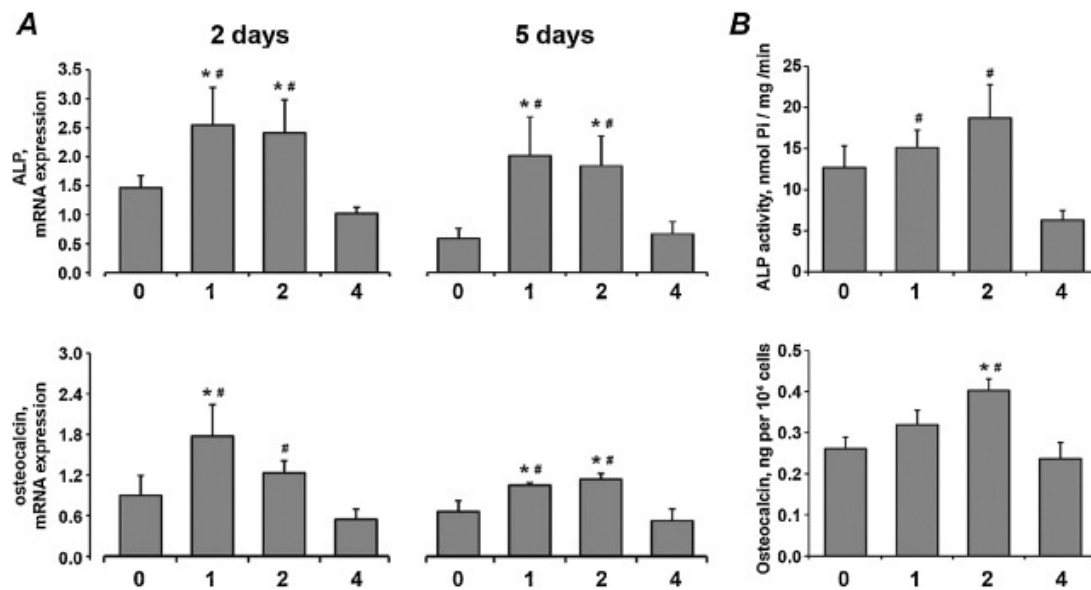
Figure 10.5: Expression of osteogenesis-related factors in MG-63 cells grown on Ti surfaces with different micrometer-scale roughness values. MG-63 cells were grown on Ti surfaces with different micrometer-scale roughness values. A—expression of alkaline phosphatase and osteocalcin measured by qPCR after 2, and 5 days of culture. Ordinate axes represent the n-fold expression levels of the target gene in relation to cells grown on tissue-culture plastic ($n = 1$). B— alkaline phosphatase activity of MG-63 cell lysates (upper panel) and osteocalcin production by MG-63 cells measured after 5 days of culture. ALP activity was determined by measuring the release of p-nitrophenol from p-nitrophenylphosphate per minute per total amount of protein. The content of osteocalcin in conditioned media was determined by commercially available ELISA kits and normalized to the total cell number determined by manual cell counting. Data are presented as mean ± S.E.M. of 5 independent experiments.
*Means significantly higher compared to surface **0**, $p < 0.05$.
#Means significantly higher compared to surface **4**, $p < 0.05$.

10.3.6 VEGF production

The effect of micrometer-scale roughness on VEGF production is shown in Figure 10.6. After 2 days of culture, the expression of VEGF was significantly higher in cells grown on surfaces **1** and **2** compared to those grown on surface **4** ($p < 0.05$, Figure 10.6A, left panel). After 5 days of culture, the expression of VEGF was significantly higher in cells grown on surfaces **1** and **2** compared to those grown on surfaces **0** and **4** ($p < 0.05$, Figure 10.6A, right panel). A similar tendency was also observed for the VEGF protein content in conditioned media measured after 5 days of culturing (Figure 10.6B). The production of VEGF by cells grown on surfaces **1** and **2** was significantly higher compared to surface **0** ($p < 0.05$). In addition, cells grown on surface **2** produced significantly more VEGF compared to those grown on surface **4**.
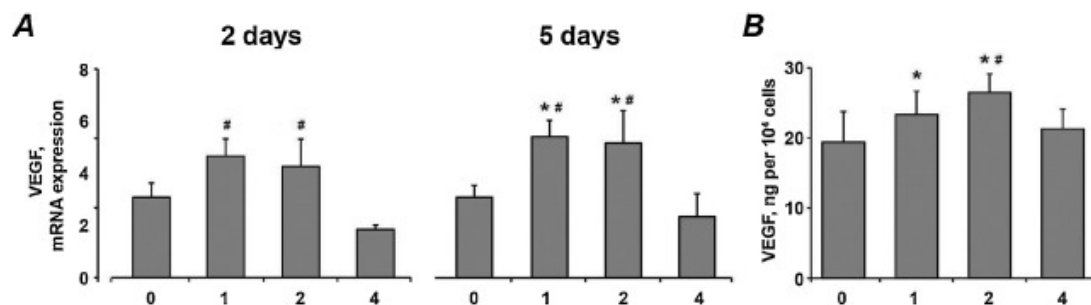

Figure 10.6: Expression of VEGF in MG-63 cells grown on Ti surfaces with different micrometer-scale roughness values. MG-63 cells were grown on Ti surfaces with different micrometer-scale roughness values. A—expression of vascular endothelial growth factor (VEGF) measured by qPCR after 2 and 5 days of culture. Ordinate axes represent the n-fold expression levels of the target gene in relation to cells grown on tissue culture plastic ($n = 1$). B—production of VEGF protein by MG-63 cells measured after 5 days of culture. The content of VEGF in conditioned media was determined by commercially available ELISA kits and normalized to the total cell number determined by manual cell counting. Data are presented as mean ± S.E.M. of 5 independent experiments.
*Means significantly higher compared to surface **0**, $p < 0.05$.
#Means significantly higher compared to surface **4**, $p < 0.05$.

10.3.7   Gene expression of OPG/RANKL

No significant effect of surface roughness on the expression of OPG and RANKL was observed after 2 and 5 days of culture (Figure 10.7).
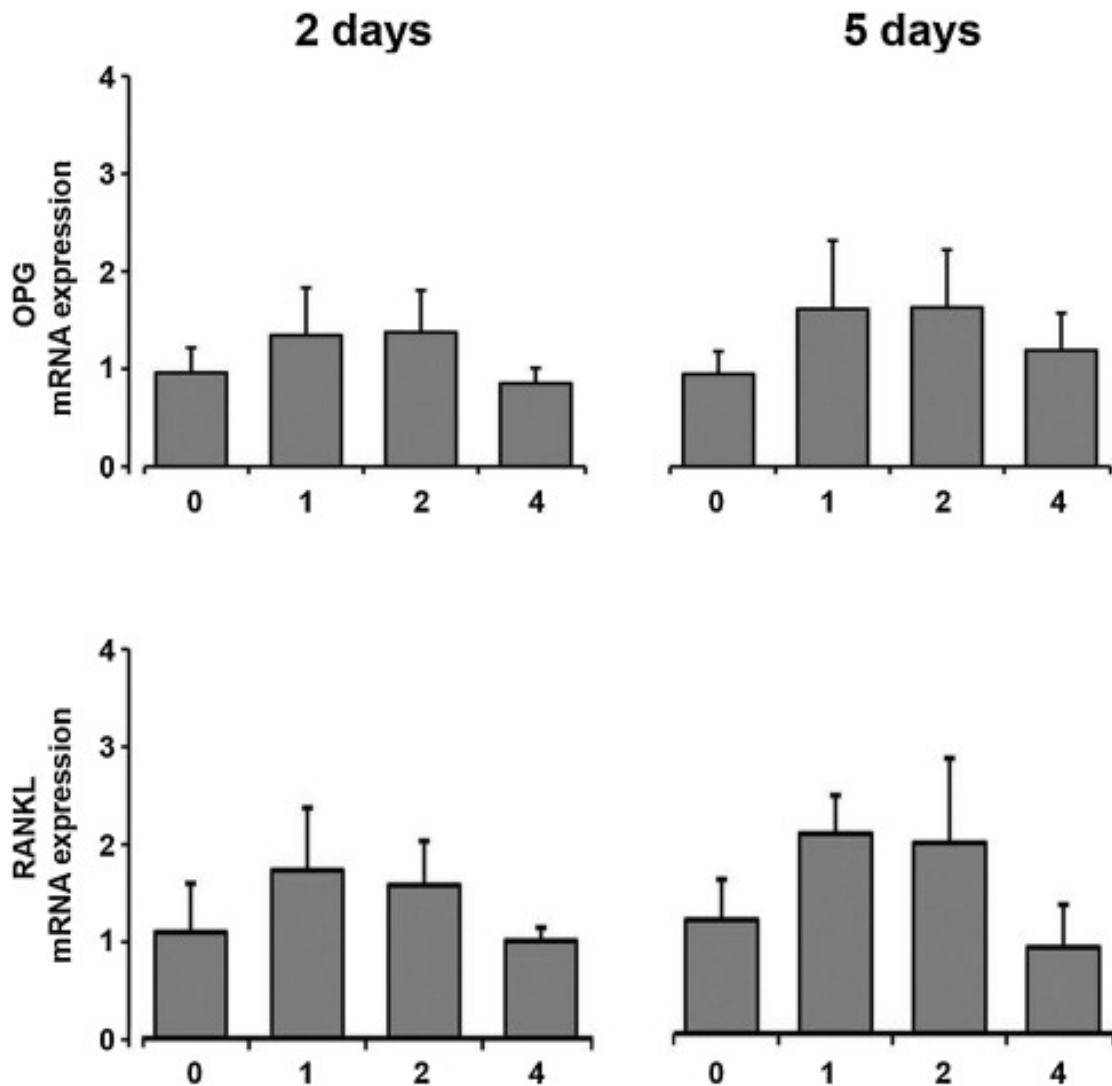

Figure 10.7: Gene expression of OPG and RANKL in MG-63 cells grown on Ti surfaces with different micrometer-scale roughness values. MG-63 cells were grown on Ti surfaces with different micrometer-scale roughness values. The expression of osteoprotegerin (OPG) and receptor activator of nuclear factor κB (RANKL) was measured by qPCR after 2 and 5 days of culture. Ordinate axes represent the n-fold expression levels of the target gene in relation to cells grown on tissue-culture plastic (n = 1). Data are presented as mean ± S.E.M. of 4 independent experiments.

10.4 Discussion

Osteoblast proliferation was inversely related to surface roughness. This was revealed by both cell-counting and MTT experiments. The literature data on the effect of surface micrometer-scale roughness on osteoblast proliferation is rather contradictory. In our previous studies we found that proliferation of MG-63 cells and alveolar osteoblasts decreases on Ti surfaces with higher roughness [11, 33, 34], which is also supported by studies of other groups [17, 35-37]. In contrast, some studies report a stimulating effect of surface roughness on human osteoblast-like SaOS-2 cells [38] and human mandibular alveolar bone cells [39, 40]. In a previous study with controlled micrometer-scale roughness, a stimulating effect of surface roughness on proliferation of rat calvarial osteoblasts was observed [15]. The reason for this discrepancy is not entirely clear. Several factors, such as the precise nature of the roughness resulting from the surface-production procedure, the initial cell seeding density, the method of proliferation measurement, or the presence of serum during experiments, might influence the results on osteoblast proliferation on Ti surfaces. It should be noted that in most of these studies, surfaces with non-controlled micrometer-scale roughness were used, which means that these surfaces might also contain components of submicrometer- and nanoscale roughness. As shown in some studies, micrometer-scale and nanoscale features might have a synergistic effect on MG-63 proliferation [41, 42].

One of the most interesting findings in our study is that the speed of cell migration on Ti surfaces with R_a of about 4 µm (surface **4**) was significantly lower compared to that on surfaces with R_a up to 2 µm (surfaces **0**, **1** and **2**). No effect of surface roughness on cell migration was observed for surfaces with R_a in the range of 0–2 µm (surfaces **0**, **1** and **2**). We assume that very deep valleys in the surface **4** might interfere with osteoblast migration. To date, no systematic study on the effect of Ti surface roughness on osteoblast migration has been performed. In a study by Li *et al.*, the migration of human osteosarcoma Saos-2 cells measured in a wound-healing assay on acid-etched Ti surfaces with the highest peak at R_{max} of 3.3 µm was slower than that on polished Ti surfaces with

R_{max} 0.92 µm [43]. Our finding on the effect of surface roughness on cell migration is also indirectly supported by a recent study showing that cell spreading was greater on rough Ti surfaces compared to that on glass slides and smoother Ti surfaces [44]. Another study showed that osteoblast spreading is inversely related to migration speed [45]. Our time-lapse-microscopy data strongly suggest that osteoblast migration is strongly inhibited by surfaces with increased micrometer-scale roughness. Cell migration in wounded areas is a crucial process in tissue regeneration and a prerequisite for new tissue formation [46]. The decreased cell migration observed in our *in vitro* study could account for the poor clinical outcome observed in clinical trials with titanium plasma-sprayed surfaces with high roughness (reviewed in [9]).

Our data suggest a biphasic relationship between surface micrometer-scale roughness and osteoblast differentiation. This is based on the observation that the highest expressions of alkaline phosphatase and osteocalcin, which are markers of early and late osteoblast differentiation, were observed on surfaces with R_a values of approximately 1–2 µm (surfaces **1** and **2**) compared to surfaces with R_a values of 0 and 4 µm. This finding is in agreement with numerous previous studies showing that moderately rough surfaces, with R_a of about 1–2 µm, promote osteoblast differentiation *in vitro* (reviewed in [6]). However, osteoblast differentiation, as suggested by the expression of alkaline phosphatase and osteocalcin, was not promoted by surfaces with R_a of about 4 µm (surface **4**). To date, the effect of extremely rough surfaces on osteogenic differentiation was investigated rather rarely. In a recent study, osteogenic differentiation of bone marrow mesenchymal stem cells was investigated depending on a micrometer-scale roughness gradient ranging from R_a 0 µm to R_a 5 µm [16]. In that study, the intensity of alkaline phosphatase and alizarine red was gradually increased with increasing R_a up to about 2 µm, but further R_a increase resulted in lower staining intensities. A biphasic relationship between surface micrometer-scale roughness and osteoblast differentiation is also shown in a recently published study, in which differentiation of osteoblasts was investigated on carbon fiber-reinforced polyetheretherketone nanohydroxyapatite composites (PEEK/n-HA/CF) with different roughness [18].

Here, the differentiation of osteoblasts was promoted by the surface with R_a about 2 μm compared to the surfaces with R_a about 0, 1, and 3 μm. Another study investigates the response of MG-63 osteoblasts to Ti_6Al_4V surfaces with R_a values 0.2, 2.0, 3.0, and 3.3 μm and shows that osteoblast differentiation as suggested by osteocalcin production is higher for surfaces with higher roughness [17]. However, this finding does not exclude a biphasic relationship between surface micrometer-scale roughness and osteoblast differentiation, because in this study no surfaces with higher R_a values were tested.

The biphasic relationship between surface roughness and implant osseointegration is also implied by some *in vivo* studies. The strongest bone response to sand-blasted surfaces with S_a ranging from 0.6 to 2.1 μm was found for surfaces with S_a about 1.5 μm (for review, see Ref. [6]). Rønold and Ellingsen show that the tensile force required for implant loosening from the rabbit tibia is gradually increased up to S_a parameter of 3.6 μm, and decreases for surfaces with higher S_a parameters [47]. Although the biphasic relationship between surface roughness and bone response can be seen in both *in vitro* and *in vivo* studies, there are some discrepancies in the optimal values of surface roughness for bone formation. We assume that the optimal surface roughness might depend on the surface material and the roughening procedure and must be evaluated individually.

The expression of VEGF in MG-63 cells was affected by Ti surface micrometer-scale roughness. VEGF is a crucial stimulator of the angiogenesis process [48]. Previous studies show that rough hydrophilic SLActive surfaces stimulate the release of vascular endothelial growth factor (VEGF) by osteoblasts, which in turn might promote endothelial cell differentiation and angiogenesis [11, 49]. Our data show that h surfaces with moderate roughness stimulate the release of VEGF by osteoblasts, whereas this process is not supported by surfaces with high micrometer-scale roughness. This finding suggests that extremely rough Ti surfaces do not support the angiogenesis process *in vivo*.

We did not observe any effect of surface micrometer-scale roughness on the expression of OPG and RANKL. OPG and RANKL are important factors involved in bone metabolism [50]. RANKL is known to activate bone-resorbing osteoclasts and OPG is known to bind to RANKL and thus inhibits its ability to activate osteoclasts. Our data suggest that Ti surface microroughness influences osteoblast differentiation rather than the processes of bone resorption regulation by osteoblasts. However, a possible effect of surface roughness on monocyte differentiation into osteoclasts cannot be excluded [51].

The reasons why very rough surfaces do not support the differentiation of osteoblasts are not entirely clear. The interaction of osteoblasts with Ti surfaces is mediated through the interaction of cell-surface integrins with proteins adsorbed to the surface and these integrins are "sensors" of surface roughness [52]. In particular, MG-63 cells grown on rougher Ti surface exhibit higher expression of integrin subunits $\alpha 2$, $\alpha 3$, $\alpha 5$, $\beta 1$, and $\beta 3$ compared to cells grown on smoother surfaces [53]. A recent study shows that knocking-out of integrin $\alpha 2$ and $\beta 1$ subunits by shRNA switches off the stimulating effect of moderately rough SLA surfaces on the differentiation of MG-63 cells [14]. However, no systematic study on the effect of surface roughness on integrin expression is known, especially in the range of high surface roughness. The decreased osteogenic differentiation of MG-63 cells observed in our study for surface **4** might also be explained by decreased cell-to-cell interaction. As we have seen, cell migration was inhibited on surfaces with a R_a value of approximately 4 μm (surface **4**), which might result in decreased interaction between different cells. At the same time, it is known that cell-to-cell interaction through gap junctions plays an important role in osteoblast differentiation [54]. A recent study on PEEK/n-HA/CF shows that protein adsorption by the surface with R_a about 3 μm is lower compared to the surfaces with lower R_a values [18]. Since the interaction of osteoblasts with Ti surfaces is mediated by adsorbed proteins, this also might influence the differentiation of osteoblasts.

The influence of spatial roughness characteristics and roughness profiles on osteoblast differentiation is poorly understood. A recent study showed that

the skewness and kurtosis surface-profile parameters are important in influencing osteogenic differentiation of osteoblasts and mesenchymal stem cells [55]. In particular, osteogenic differentiation seems to be inhibited by increased skewness, which implies asymmetry in profile peaks and valleys, as well as by increased kurtosis, which implies sharp peaks. In contrast, *in vivo* studies on rabbits show using pull-out test that surfaces with high skewness and kurtosis exhibit the strongest implant-to-bone contacts [56]. The surfaces used in our study did not exhibit any significant differences in the skewness parameter. This parameter was not significantly different from 0 for all surfaces, which suggest a symmetrical distribution of hills and valleys in the roughness profile. Therefore, the differences in cell behavior on the different surfaces observed in our study cannot be attributed to these different roughness-profile characteristics. The spatial roughness characteristic R_{Sm}, which characterizes the width of single peaks, was different on the different surfaces used in the present study. On the rough surfaces (**1**, **2**, and **4**), the R_{Sm} parameter decreased with increased surface roughness, suggesting that rougher surfaces had a higher density of peaks. It cannot be excluded that the differences in spatial roughness characteristics might also account for differences in osteoblast behavior on the different surfaces investigated in our study. However, this question still needs to be investigated in further studies using well-controlled surface-production protocols.

10.5 Conclusion

In summary, proliferation, migration and differentiation of osteoblasts on Ti surfaces with different controlled micrometer-scale roughness values were investigated in the present study. Our data suggest that the relationship between micrometer-scale roughness and osteoblast response is biphasic. Osteoblast differentiation is supported by surfaces with moderate roughness, whereas surfaces with very low or very high roughness values seem to be sub-optimal for osteoblasts. The optimal micrometer-scale roughness for dental implant surfaces might be specific for surface material and surface treatment. Further *in vitro* and *in vivo* studies must address the effect on osteoblasts of combinations of controlled micrometer-scale roughness with other structural features, such as spatial surface roughness, roughness profile characteristics, submicrometer and nanoscale roughness.

10.6 Acknowledgements

References:

[1] R.J. Blanes, J.P. Bernard, Z.M. Blanes, U.C. Belser, A 10-year prospective study of ITI dental implants placed in the posterior region. I: Clinical and radiographic results, Clinical Oral Implants Research 18(6) (2007) 699-706.

[2] J.T. Lambrecht, A. Filippi, A.R. Künzel, H.J. Schiel, Long-term Evaluation of Submerged and Nonsubmerged ITI Solid-Screw Titanium Implants: A 10-year Life Table Analysis of 468 Implants, International Journal of Oral and Maxillofacial Implants 18(6) (2003) 826-834.

[3] A. Ridell, K. Gröndahl, L. Sennerby, Placement of Brånemark implants in the maxillary tuber region: Anatomical considerations, surgical technique and long-term results, Clinical Oral Implants Research 20(1) (2009) 94-98.

[4] H. Tschernitschek, L. Borchers, W. Geurtsen, Nonalloyed titanium as a bioinert metal-a review, Quintessence International 36(7) (2005) 523-530.

[5] Y.T. Sul, B.S. Kang, C. Johansson, H.S. Um, C.J. Park, T. Albrektsson, The roles of surface chemistry and topography in the strength and rate of osseointegration of titanium implants in bone, Journal of Biomedical Materials Research - Part A 89(4) (2009) 942-950.

[6] A. Wennerberg, T. Albrektsson, Effects of titanium surface topography on bone integration: A systematic review, Clinical Oral Implants Research 20(SUPPL. 4) (2009) 172-184.

[7] F. Schwarz, D. Ferrari, M. Herten, I. Mihatovic, M. Wieland, M. Sager, J. Becker, Effects of surface hydrophilicity and microtopography on early stages of soft and hard tissue integration at non-submerged titanium implants: An immunohistochemical study in dogs, Journal of Periodontology 78(11) (2007) 2171-2184.

[8] J.B.S. Schmid, M. Bertl, H. Ulmer, V. Kuhn, A.G. Crismani, Biofunctionalization of onplants to enhance their osseointegration, J Stomat Occ Med 7 (2014) 105-110.

[9] P.G. Coelho, R. Jimbo, N. Tovar, E.A. Bonfante, Osseointegration: Hierarchical designing encompassing the macrometer, micrometer, and nanometer length scales, Dental Materials 31(1) (2015) 37-52.

[10] C.N. Elias, Y. Oshida, J.H.C. Lima, C.A. Muller, Relationship between surface properties (roughness, wettability and morphology) of titanium and dental implant removal torque, Journal of the mechanical behavior of biomedical materials 1(3) (2008) 234-242.

[11] X. Rausch-fan, Z. Qu, M. Wieland, M. Matejka, A. Schedle, Differentiation and cytokine synthesis of human alveolar osteoblasts compared to osteoblast-like

cells (MG63) in response to titanium surfaces, Dental Materials 24(1) (2008) 102-110.

[12] G. Zhao, O. Zinger, Z. Schwartz, M. Wieland, D. Landolt, B.D. Boyan, Osteoblast-like cells are sensitive to submicron-scale surface structure, Clinical Oral Implants Research 17(3) (2006) 258-264.

[13] R. Olivares-Navarrete, P. Raz, G. Zhao, J. Chen, M. Wieland, D.L. Cochran, R.A. Chaudhri, A. Ornoy, B.D. Boyan, Z. Schwartz, Integrin α2β1 plays a critical role in osteoblast response to micron-scale surface structure and surface energy of titanium substrates, Proceedings of the National Academy of Sciences of the United States of America 105(41) (2008) 15767-15772.

[14] M. Lai, C.D. Hermann, A. Cheng, R. Olivares-Navarrete, R.A. Gittens, M.M. Bird, M. Walker, Y. Cai, K. Cai, K.H. Sandhage, Z. Schwartz, B.D. Boyan, Role of α2β1 Integrins in Mediating Cell Shape on Microtextured Titanium Surfaces, Journal of biomedical materials research. Part A 103(2) (2015) 564-573.

[15] T.P. Kunzler, T. Drobek, M. Schuler, N.D. Spencer, Systematic study of osteoblast and fibroblast response to roughness by means of surface-morphology gradients, Biomaterials 28(13) (2007) 2175-2182.

[16] A.B. Faia-Torres, S. Guimond-Lischer, M. Rottmar, M. Charnley, T. Goren, K. Maniura-Weber, N.D. Spencer, R.L. Reis, M. Textor, N.M. Neves, Differential regulation of osteogenic differentiation of stem cells on surface roughness gradients, Biomaterials 35(33) (2014) 9023-9032.

[17] Z. Schwartz, P. Raz, G. Zhao, Y. Barak, M. Tauber, H. Yao, B.D. Boyan, Effect of micrometer-scale roughness of the surface of Ti6Al4V pedicle screws in vitro and in vivo, Journal of Bone and Joint Surgery - Series A 90(11) (2008) 2485-2498.

[18] Y. Deng, X. Liu, A. Xu, L. Wang, Z. Luo, Y. Zheng, F. Deng, J. Wei, Z. Tang, S. Wei, Effect of surface roughness on osteogenesis in vitro and osseointegration in vivo of carbon fiber-reinforced polyetheretherketone– Nanohydroxyapatite composite, International journal of nanomedicine 10 (2015) 1425-1447.

[19] T.P. Kunzler, T. Drobek, C.M. Sprecher, M. Schuler, N.D. Spencer, Fabrication of material-independent morphology gradients for high-throughput applications, Applied Surface Science 253(4) (2006) 2148-2153.

[20] M. Wieland, B. Chehroudi, M. Textor, D.M. Brunette, Use of Ti-coated replicas to investigate the effects on fibroblast shape of surfaces with varying roughness and constant chemical composition, Journal of Biomedical Materials Research 60(3) (2002) 434-444.

[21] M. Schuler, T.P. Kunzler, M. De Wild, C.M. Sprecher, D. Trentin, D.M. Brunette, M. Textor, S.G.P. Tosatti, Fabrication of TiO$_2$-coated epoxy replicas with identical dual-type surface topographies used in cell culture assays, Journal of Biomedical Materials Research - Part A 88(1) (2009) 12-22.

[22] M. Wieland, P. Hänggi, W. Hotz, M. Textor, B.A. Keller, N.D. Spencer, Wavelength-dependent measurement and evaluation of surface topographies: Application of a new concept of window roughness and surface transfer function, Wear 237(2) (2000) 231-252.

[23] C. Pautke, M. Schieker, T. Tischer, A. Kolk, P. Neth, W. Mutschler, S. Milz, Characterization of osteosarcoma cell lines MG-63, Saos-2 and U-2 OS in comparison to human osteoblasts, Anticancer Research 24(6) (2004) 3743-3748.

[24] R. Moreau, R. Aubin, J.Y. Lapointe, D. Lajeunesse, Pharmacological and biochemical evidence for the regulation of osteocalcin secretion by potassium channels in human osteoblast-like MG-63 cells, Journal of Bone and Mineral Research 12(12) (1997) 1984-1992.

[25] B.D. Boyan, R. Batzer, K. Kieswetter, Y. Liu, D.L. Cochran, S. Szmuckler-Moncler, D.D. Dean, Z. Schwartz, Titanium surface roughness alters responsiveness of MG63 osteoblast-like cells to $1\alpha,25$-(OH)2D3, Journal of Biomedical Materials Research 39(1) (1998) 77-85.

[26] K.B. Jonsson, A. Frost, O. Nilsson, S. Ljunghall, Ö. Ljunggren, Three isolation techniques for primary culture of human osteoblast-like cells. A comparison, Acta Orthopaedica Scandinavica 70(4) (1999) 365-373.

[27] H. Declercq, N. Van Den Vreken, E. De Maeyer, R. Verbeeck, E. Schacht, L. De Ridder, M. Cornelissen, Isolation, proliferation and differentiation of osteoblastic cells to study cell/biomaterial interactions: Comparison of different isolation techniques and source, Biomaterials 25(5) (2004) 757-768.

[28] M.E. Martínez, M.T. Del Campo, S. Medina, M. Sánchez, M.J. Sánchez-Cabezudo, P. Esbrit, P. Martínez, I. Moreno, A. Rodrigo, M.V. Garcés, L. Munuera, Influence of skeletal site of origin and donor age on osteoblastic cell growth and differentiation, Calcified Tissue International 64(4) (1999) 280-286.

[29] O. Andrukhov, A.C. Gemperli, Y. Tang, N. Howald, M. Dard, F. Falkensammer, A. Moritz, X. Rausch-Fan, Effect of different enamel matrix derivative proteins on behavior and differentiation of endothelial cells, Dental Materials 31(7) (2015) 822-832.

[30] L. Fleischmann, A. Crismani, F. Falkensammer, H.P. Bantleon, X. Rausch-Fan, O. Andrukhov, Behavior of osteoblasts on TI surface with two different coating designed for orthodontic devices, Journal of materials science. Materials in medicine 26(1) (2015) 5335.

[31] O. Andrukhov, O. Andrukhova, U. Hulan, Y. Tang, H.-P. Bantleon, X. Rausch-Fan, Both 25-Hydroxyvitamin-D3 and 1,25-Dihydroxyvitamin-D3 Reduces Inflammatory Response in Human Periodontal Ligament Cells, PLOS ONE 9(2) (2014) e90301.

[32] G. Van Peer, P. Mestdagh, J. Vandesompele, Accurate RT-qPCR gene expression analysis on cell culture lysates, Scientific Reports 2 (2012) 222.

[33] Z. Qu, X. Rausch-Fan, M. Wieland, M. Matejka, A. Schedle, The initial attachment and subsequent behavior regulation of osteoblasts by dental implant surface modification, Journal of Biomedical Materials Research - Part A 82(3) (2007) 658-668.

[34] Y.X. Zhang, H. Gu, Intersection of a homogeneous symmetric cantor set with its translations, Acta Math. Sinica (Chin. Ser.) 54(6) (2011) 1043-1048.

[35] H.J. Kim, S.H. Kim, M.S. Kim, E.J. Lee, H.G. Oh, W.M. Oh, S.W. Park, W.J. Kim, G.J. Lee, N.G. Choi, J.T. Koh, D.B. Dinh, R.R. Hardin, K. Johnson, V.L. Sylvia, J.P. Schmitz, D.D. Dean, Varying Ti-6A1-4V surface roughness induces different early morphologic and molecular responses in MG63 osteoblast-like cells, Journal of Biomedical Materials Research - Part A 74(3) (2005) 366-373.

[36] J.Y. Martin, Z. Schwartz, T.W. Hummert, D.M. Schraub, J. Simpson, J. Lankford, Jr., D.D. Dean, D.L. Cochran, B.D. Boyan, Effect of titanium surface roughness on proliferation, differentiation, and protein synthesis of human osteoblast‑like cells (MG63), Journal of Biomedical Materials Research 29(3) (1995) 389-401.

[37] C.H. Lohmann, R. Sagun Jr, V.L. Sylvia, D.L. Cochran, D.D. Dean, B.D. Boyan, Z. Schwartz, Surface roughness modulates the response of MG63 osteoblast-like cells to 1,25-(OH)2D3 through regulation of phospholipase A2 activity and activation of protein kinase A, Journal of Biomedical Materials Research 47(2) (1999) 139-151.

[38] I. Degasne, M.F. Baslé, V. Demais, G. Huré, M. Lesourd, B. Grolleau, L. Mercier, D. Chappard, Effects of roughness, fibronectin and vitronectin on attachment, spreading, and proliferation of human osteoblast-like cells (Saos-2) on titanium surfaces, Calcified Tissue International 64(6) (1999) 499-507.

[39] K. Mustafa, A. Wennerberg, J. Wroblewski, K. Hultenby, B.S. Lopez, K. Arvidson, Determining optimal surface roughness of TiO 2 blasted titanium implant material for attachment, proliferation and differentiation of cells derived from human mandibular alveolar bone, Clinical Oral Implants Research 12(5) (2001) 515-525.

[40] L. Marinucci, S. Balloni, E. Becchetti, S. Belcastro, M. Guerra, M. Calvitti, C. Lilli, E.M. Calvi, P. Locci, Effect of titanium surface roughness on human osteoblast proliferation and gene expression in vitro, International Journal of Oral and Maxillofacial Implants 21(5) (2006) 719-725.

[41] C. Zink, H. Hall, D.M. Brunette, N.D. Spencer, Orthogonal nanometer-micrometer roughness gradients probe morphological influences on cell behavior, Biomaterials 33(32) (2012) 8055-8061.

[42] O. Zinger, K. Anselme, A. Denzer, P. Habersetzer, M. Wieland, J. Jeanfils, P. Hardouin, D. Landolt, Time-dependent morphology and adhesion of osteoblastic cells on titanium model surfaces featuring scale-resolved topography, Biomaterials 25(14) (2004) 2695-2711.

[43] C.Y. Li, S.Y. Gao, T. Terashita, T. Shimokawa, H. Kawahara, S. Matsuda, N. Kobayashi, In vitro assays for adhesion and migration of osteoblastic cells (Saos-2) on titanium surfaces, Cell and Tissue Research 324(3) (2006) 369-375.

[44] T. Osathanon, K. Bespinyowong, M. Arksornnukit, H. Takahashi, P. Pavasant, Human osteoblast-like cell spreading and proliferation on Ti-6Al-7Nb surfaces of varying roughness, Journal of oral science 53(1) (2011) 23-30.

[45] K. Webb, V. Hlady, P.A. Tresco, Relationships among cell attachment, spreading, cytoskeletal organization, and migration rate for anchorage-dependent cells on model surfaces, Journal of Biomedical Materials Research 49(3) (2000) 362-368.

[46] K.H. Frosch, F. Barvencik, C.H. Lohmann, V. Viereck, H. Siggelkow, J. Breme, K. Dresing, K.M. Stürmer, Migration, matrix production and lamellar bone formation of human osteoblast-like cells in porous titanium implants, Cells Tissues Organs 170(4) (2002) 214-227.

[47] H.J. Rønold, J.E. Ellingsen, Effect of micro-roughness produced by TiO_2 blasting-tensile testing of bone attachment by using coin-shaped implants, Biomaterials 23(21) (2002) 4211-4219.

[48] A.K. Olsson, A. Dimberg, J. Kreuger, L. Claesson-Welsh, VEGF receptor signalling - In control of vascular function, Nature Reviews Molecular Cell Biology 7(5) (2006) 359-371.

[49] A.L. Raines, R. Olivares-Navarrete, M. Wieland, D.L. Cochran, Z. Schwartz, B.D. Boyan, Regulation of angiogenesis during osseointegration by titanium surface microstructure and energy, Biomaterials 31(18) (2010) 4909-4917.

[50] G.N. Belibasakis, N. Bostanci, The RANKL-OPG system in clinical periodontology, Journal of Clinical Periodontology 39(3) (2012) 239-248.

[51] S. Makihira, Y. Mine, E. Kosaka, H. Nikawa, Titanium surface roughness accelerates RANKL-dependent differentiation in the osteoclast precursor cell line, RAW264.7, Dental Materials Journal 26(5) (2007) 739-745.

[52] M.C. Siebers, P.J. Ter Brugge, X.F. Walboomers, J.A. Jansen, Integrins as linker proteins between osteoblasts and bone replacing materials. A critical review, Biomaterials 26(2) (2005) 137-146.

[53] R. Lange, F. Lüthen, U. Beck, J. Rychly, A. Baumann, B. Nebe, Cell-extracellular matrix interaction and physico-chemical characteristics of titanium surfaces depend on the roughness of the material, Biomolecular Engineering 19(2-6) (2002) 255-261.

[54] Y. Hashida, K.I. Nakahama, K. Shimizu, M. Akiyama, K. Harada, I. Morita, Communication-dependent mineralization of osteoblasts via gap junctions, Bone 61 (2014) 19-26.

[55] R. Olivares-Navarrete, S.L. Hyzy, M.E. Berg, J.M. Schneider, K. Hotchkiss, Z. Schwartz, B.D. Boyan, Osteoblast Lineage Cells Can Discriminate Microscale Topographic Features on Titanium–Aluminum–Vanadium Surfaces, Annals of Biomedical Engineering 42(12) (2014) 2551-2561.

[56] S.F. Lamolle, M. Monjo, S.P. Lyngstadaas, J.E. Ellingsen, H.J. Haugen, Titanium implant surface modification by cathodic reduction in hydrofluoric acid: Surface characterization and in vivo performance, Journal of Biomedical Materials Research - Part A 88(3) (2009) 581-588.

Acknowledgments

This work would not have been possible without the help of many people. I am happy that I can finally thank them all for their support.

First, I would like to thank Prof. Nic Spencer for accepting me as a PhD student in his group, for giving me an interesting project to work on and for his support, guidance, good ideas and his incredible speed-reading skills.

I also would like to thank Katharina Maniura for supervising me, welcoming me in her group at Empa and supporting me with biological questions.

Thanks also to Dr. Simon Berner and Prof. Janos Vörös for being co-examiner and critically reading my thesis, and to Prof. Ralph Spolenak for representing the Department of Materials.

During my time as PhD student, I was supported by a number of students. Thank you Ben Hartmeier, Yvonne Gombert, Vera Voney and Yoan Boussés for being a great help in the lab and contributing to this thesis.

I would like to express my sincere thanks to Christian Rytka from FHNW for helping me with the replication of nanoparticle-density gradients, introducing me to injection molding and for his patience. Special thanks goes also to Benjamin Rüfenacht, who made negatives of 72 nm structures in PPSU and made the replication and mass production possible.

Rok Simic for introducing me to the mountain-bike world, for our adventures in Iceland, skiing trips, coffee breaks and many good drinks and conversations.

Andrea Arcifa, also known as sad Andrea, for always being confused, funny and not sad at all. And of course for his amazing dance moves.

My sport-buddy Fabiana Spadaro for joining me to Kondi, running and rowing, to make sure someone is speaking louder than me and her friendship.

Alok Goel for being a great "bro", for the panda, good Indian food, smooth whiskey and nice conversations.

Adrienne Nelson for teaching me some rowing skills, joining me to a lot of different sport events and good dinners.

Szymon Bernat and Federica Cocco for a legendary summer full of Limmat tubing, pub-crawls, good drinks and BBQs.

Yvonne Gombert, Manjesh Singh, Cathrein Limacher and Robert Bielecki for being great office mates.

Everybody for the great atmosphere at the SOLA, fondue evenings, pub-crawls, off-site group meetings, Christmas-, Nerd- and Bollywood-parties and of course also in the lab.

Many thanks to Marianne Sommer for your friendship and becoming my running buddy.

Thanks to Dimitri Kokkinis and Roman Engeli for being great flat mates, having open ears and to understanding the PhD life.

Vera Voney for coming with me to every sport ASVZ offers, for your friendship and for joining me making a fool of oneself with stupid surf- and Kondi-moves on the dance floor.

I would also like to thank my friends outside of ETH. They didn't contribute a lot scientifically to my thesis; however the ensured that I stayed sane. Thank you Florian and Katrin for taking me to adventures all over the world and in Switzerland. Thanks to the Tuesday-dinner crew: Sylvie, Raffi, Fabian, Katja, Martin, Vera, Flo, Kati, André, Seline, Annette, Urs, Carlo, Adi, Roman and Tina for amazing evenings. Ben, Zami and Silvan for climbing, wakesurfing and biking adventures. Padi and Jessi, the best flat mates in the world, for their friendship and open ears. Selina and Flavia for making sure that I don't forget where I come from and for their friendship.

Last but not least, I would like to thank my family, especially my parents for supporting me during all those years and trying to understand what I'm actually doing. Without them this thesis would not have been possible! And of course, thanks to Greg for your support, for cheering me up and for accepting me the way I am.